

**DOCTORAL THESIS**

# Additive Manufacturing of TiC-based Cermets with Fe-based Binders using Novel Laser Scan Techniques

Himanshu Singh Maurya

TALLINN UNIVERSITY OF TECHNOLOGY  
DOCTORAL THESIS  
61/2023

**Additive Manufacturing of TiC-based  
Cermets with Fe-based Binders using  
Novel Laser Scan Techniques**

HIMANSHU SINGH MAURYA



TALLINN UNIVERSITY OF TECHNOLOGY

School of Engineering

Department of Mechanical and Industrial Engineering

This dissertation was accepted for the defence of the degree 01/11/2023

**Supervisor:**

Fjodor Sergejev  
Tenure Associate Professor  
Department of Mechanical and Industrial Engineering  
Tallinn University of Technology  
Tallinn, Estonia

**Co-supervisor:**

Dr. Kristjan Juhani  
Department of Mechanical and Industrial Engineering  
Tallinn University of Technology  
Tallinn, Estonia

**Opponents:**

Dr.-Ing. Jurgen Eckert, Professor  
Department of Material Physics  
University of Leoben  
Leoben, Austria

Dr. Knut Sorby, Professor  
Department of Mechanical and Industrial Engineering  
Norwegian University of Science and Technology  
Trondheim, Norway

**Defence of the thesis:** 04/12/2023, Tallinn

**Declaration:**

Hereby I declare that this doctoral thesis, my original investigation, and achievement, submitted for the doctoral degree at Tallinn University of Technology has not been submitted for a doctoral or equivalent academic degree.

Himanshu Singh Maurya

-----  
signature



European Union  
European Regional  
Development Fund



Investing  
in your future

Copyright: Himanshu Singh Maurya, 2023

ISSN 2585-6898 (publication)

ISBN 978-9916-80-065-2 (publication)

ISSN 2585-6901 (PDF)

ISBN 978-9916-80-066-9 (PDF)

Printed by Koopia Niini & Rauam

TALLINNA TEHNIKAÜLIKOOL  
DOKTORITÖÖ  
61/2023

**Titaankarbiidsete Fe-baasil sideainega  
kermiste valmistamine uudse  
laserskaneeriva kihtlisandustehnoloogia teel**

HIMANSHU SINGH MAURYA





# Contents

List of publications .....	7
Author's contribution to the publications .....	8
Introduction .....	9
Abbreviations and symbols .....	11
1 Literature review .....	12
1.1 Cermets and hardmetals .....	12
1.2 Additive Manufacturing of Cermets .....	13
1.2.1 Indirect Additive Manufacturing technologies .....	17
1.2.2 Direct Additive Manufacturing technologies .....	18
1.3 Fabrication of TiC-based cermets via Additive Manufacturing route .....	23
1.4 Research gap .....	25
1.5 Aim and objective of the thesis .....	26
2 Experimental methodology .....	27
2.1 Investigated materials .....	27
2.2 Feedstock preparation .....	27
2.3 SLM/LPBF fabrication .....	28
2.3.1 Laser Pulse shaping .....	29
2.3.2 Multiple Laser scanning technique .....	30
2.4 Test methods .....	31
2.4.1 Metallographic preparation .....	31
2.4.2 Microstructure and phase analysis .....	31
2.5 Characterization of physical and mechanical properties .....	31
2.5.1 Density .....	31
2.5.2 Hardness and microhardness testing .....	31
2.5.3 Tribological characterization .....	32
3 Results and discussion .....	33
3.1 Development of optimal process parameters to fabricate parts with lower process-induced defects .....	33
3.1.1 Standard laser pulse .....	33
3.1.2 Laser pulse shaping .....	34
3.1.3 Multiple laser scanning .....	37
3.2 Effect of adapted laser scan techniques on the microstructural formation .....	39
3.3 Effect of laser process parameters on the phase formation .....	40
3.4 Process induced defects .....	42
3.4.1 Keyhole effect .....	43
3.4.2 Spattering effect .....	43
3.4.3 Entrapped gas .....	44
3.4.4 Low energy density .....	44
3.5 Mechanical properties .....	44
3.5.1 Hardness .....	44
3.5.2 Fracture toughness .....	46
3.6 Tribological properties .....	48
3.7 TiC -Fe-based cermets via Conventional sintering route .....	52

3.7.1 Microstructural formation .....	53
3.7.2 Mechanical properties .....	55
4 Conclusion .....	57
5 Kokkuvõte .....	59
6 Future work .....	61
References .....	62
List of other publications .....	73
Acknowledgments.....	74
Abstract.....	75
Lühikokkuvõte.....	77
Appendix .....	79
Curriculum vitae.....	129
Elulookirjeldus.....	131

## List of publications

The list of author's publications, based on which the thesis has been prepared:

- I **H.S. Maurya**, L. Kollo, Marel Tarrate, K. Juhani, F. Sergejev, K.G. Prashanth. Selective Laser Melting of TiC-Fe via Laser Pulse Shaping: Microstructure and Mechanical Properties. *3D Printing and Additive Manufacturing* (2021).
- II **H.S. Maurya**, L. Kollo, K. Juhani, F. Sergejev, K.G. Prashanth. Effect of preheating and cooling of the powder bed by laser pulse shaping on the microstructure of the TiC-based cermets. *Ceramics International* 48 (2022) 20612–20618.
- III **H.S. Maurya**, K.Kosiba, K. Juhani, F. Sergejev, K.G. Prashanth. Effect of powder bed preheating on the crack formation and microstructure in ceramic matrix composites fabricated by laser powder-bed fusion process. *Additive Manufacturing* 58 (2022) 103013.
- IV **H.S. Maurya**, J. Jayaraj, Z. Wang, K. Juhani, F. Sergejev, K.G. Prashanth. Investigation of the tribological behavior of the additively manufactured TiC-based cermets by scratch test. *Journal of Alloy and Compound* 959 (2023) 170496.

## **Author's contribution to the publications**

Contribution to the papers in this thesis are:

- I First and corresponding author. Methodology. Design of experiments. Conducting experiments. Formal analysis. Data analysis. Manuscript preparation.
- II First and corresponding author. Methodology. Design of experiments. Conducting experiments. Formal analysis. Data analysis. Manuscript preparation.
- III First and corresponding author. Methodology. Design of experiments. Conducting experiments. Formal analysis. Data analysis. Manuscript preparation.
- IV First and corresponding author. Methodology. Design of experiments. Conducting experiments. Formal analysis. Data analysis. Manuscript preparation.

## Introduction

Cemented carbide, Hardmetals, and Cermets with Co and Ni-based binder (5–25 wt.%) have been widely used in industries for decades for high wear-resistant parts, molds, mining parts, drilling and cutting tools, etc (Aramian, Razavi, Sadeghian, & Berto, 2020; Ettmayer, 1989; R. S. Khmyrov, Safronov, & Gusarov, 2017; Kübarsepp & Juhani, 2020; Son, 2021). This material exhibits excellent mechanical properties, including hardness, fracture toughness, transverse rupture strength (TRS), and compressive strength (Ettmayer, 1989; Heydari, Lietor, Corpas-Iglesias, & Laguna, 2021; Kübarsepp & Juhani, 2020). Moreover, these materials possess better wear and corrosion resistance for such applications (Enneti & Prough, 2019b, 2019c; Kübarsepp, Klaasen, & Pirso, 2001). However, there are some limitations to such materials especially poor oxidation behavior and deterioration of the mechanical properties at elevated temperatures (Lofaj & Kaganovskii, 1995; Voitovich, Sverdel, Voitovich, & Golovko, 1996). In general, cemented carbides can be classified into three types: cemented carbides based on WC with Co binder phase, WC in combination with NbC and TaC, and TiC with Co binder phase and cermets (TiC and TiCN).

W and Co have both been added to the 2019 list of critical raw materials (CRMs) (Kolnes et al., 2018; Kübarsepp & Juhani, 2020; Tarraste et al., 2018). There is a high economic importance and a high supply risk associated with both metals. It is therefore vital that these CRMs are replaced completely or partially to benefit the hard metal industry. Recycling of waste, the substitution of critical raw materials, and resource efficiency will be essential in the future manufacturing chain (Kolnes et al., 2018). Moreover, these CRMs is also declared as a carcinogen to human health in both the powder and sintered forms according to the European Union REACH program (Registration, Evaluation, Authorization, and Restriction of Chemical Substances) and U.S NTP (National Toxicology Program)(Kübarsepp & Juhani, 2020). In WC-based hard metals, Ni has been proven to be a promising replacement for Co, however, it is also deemed to be toxic to human health according to the EU REACH and US NTP program (Tarraste et al., 2018).

TiC-based cermets have been considered to be the most important metal carbides for manufacturing a new generation of cermets and have the potential to substitute these hard metals in certain applications that require wear at high temperatures under corrosive conditions (Akinribide et al., 2019; Aramian, 2020a; L. Wang, Liu, Huang, Zou, & Liu, 2014; Zhuang, Lin, He, & Kang, 2017). The TiC-based cermets have a low coefficient of friction (CoF), a high level of solvency with other carbides, excellent thermal stability, high elastic modulus (410–450 GPa), better melting point (3067 °C). In addition, these cermets are more thermodynamically stable and have a higher hardness than WC (33% more than WC) and much lower density than commercial WC-Co hard metals (WC density is ~ 3 times of TiC), making them extremely suitable for hot rolling equipment roller guides as well as other components subjected to high inertial loads (Aramian, Sadeghian, Narimani, Razavi, & Berto, 2023).

Furthermore, TiC-based cermets are generally less expensive to fabricate than WC, which could lead to many applications replacing WC with TiC-based cermets (Tarraste M.; Kolnes, M.; Kübarsepp, J.; Juhani, K.; Viljus, M.; Külaviir, 2020). Several types of metal alloys are used to control the properties of cermet, including Ni, Fe, and Co alloys. The various alloys will provide specific benefits to the cermet, such as improving the sintering response and toughness, increasing corrosion resistance, improving thermal

conductivity, and/or enhancing thermal shock resistance. A Ni or Co-based binder phase exhibits the best wetting properties when used in conjunction with (Ti, X) (C, N) phases (Kübarssepp & Juhani, 2020). Research efforts are currently being directed at developing Ni-Co-free TiC-based cermets with low-cost Fe-based binders.

Die casting and Powder metallurgy techniques have been extensively adapted over the decades to manufacture WC-based Hard metals and Cermet parts by different solidification/fusion/diffusion processes (Heydari, 2021; Yang et al., 2020). Although both manufacturing processes can fabricate near-net-shaped parts, die-casting manufacturing has many limitations, including higher production cost on average, restrictions on nonferrous metals (especially for materials with high melting points), and the lower quality final product (with process defects like porosity), which affects the quality and performance of the final product (Konyashin, 2023).

Powder metallurgy can eliminate these challenges by providing new material possibilities and enabling intricate designs with better-quality parts (Konyashin, 2023). Cermets are manufactured via conventional methods such as spark plasma sintering (SPS), hot isostatic pressing (HIP), hot pressing (HP), and self-propagating high-temperature synthesis (SHS) that have been adapted for several decades (Aramian et al., 2020). These conventional methods adopted for the fabrication of cermets are time and energy-consuming. In addition, the other limitations are the need for several post-processing steps to achieve the final product, restriction to fabricating complex geometry in a single step, waste of energy and scarp material, etc. in terms of being sustainable and environmentally friendly (Aramian et al., 2023).

Compared to conventional methods, the fabrication of cermets using additive manufacturing technologies (AM) overcomes these limitations and aids in improving/modulating the microstructure and properties of the fabricated parts (Aramian et al., 2020). With increased competitiveness, AM has attracted a great deal of attention and is under intensive investigation for fabricating cermets with improved density and mechanical properties.

The novel aspect of this research work is the fabrication of TiC-based cermets using different Fe-based binder via Additive manufacturing route based on Laser Powder Bed Fusion (LPBF) such as Selective Laser Melting. Fabrication of cermets poses a stiff challenge when processed by any of the solidification processes like the laser-based powder fusion technique due to their brittle nature, high thermal residual stresses, and process defects such as cracks, pores, delamination, etc. Therefore, in this work, novel laser processing techniques have been adapted to fabricate the cermet parts with lower process defects by controlling the melt pool/powder bed temperature. Furthermore, the effect of laser process parameters and laser scanning techniques adapted to fabricated TiC-Fe-based cermets has a significant impact on microstructural formation, mechanical properties, density, and tribological characteristics, as a result of the adapted SLM process rapid melting and unique solidification conditions that have been studied in detail.

## Abbreviations and symbols

AM	Additive Manufacturing
LPBF	Laser Powder Bed Fusion
SLM	Selective Laser Melting
AISI	American Iron and Steel Institute
ISO	International Organization of Standardization
a.u.	arbitrary unit
CAD	Computer-Aided Design
CoF	Coefficient Of Friction
EDS	Energy Dispersive X-Ray Spectroscopy
3DP	Three-Dimensional Printing
SEM	Scanning Electron Microscope
HV	Hardness Value (Vickers Hardness)
FSS	Ferritic Stainless Steel
LPS	Laser Pulse Shaping
MLS	Multiple Laser Scanning
CALPHAD	CALculation of PHAse Diagrams
IFT	Indentation Fracture Toughness
DED	Directed Energy Deposition
EBM	Electron Bean Melting
TRS	Transverse Rapture Strength
RD	Relative Density
PHS	Preheating Scan
MS	Melting Scan
PS	Pulse Shaping
HIP	Hot Isostatic Pressing
CPS	Conventional Pressureless Sintering

# 1 Literature review

This chapter describes the cermets materials and their development. Moreover, different direct Additive manufacturing routes are adapted to fabricate cermets specimens. The LPBF AM method such as the Selective laser melting process will be discussed in detail, followed by describing the process parameters and its shortcomings for the fabrication of such brittle materials. Finally, the latest development of the TiC-based Cermet fabricated by Direct additive manufacturing will be reviewed, as well as the research gaps that need to be addressed in future research.

## 1.1 Cermets and hardmetals

A Cermet is an acronym derived from **CER**amic and **MET**al, both of which are the major phases of this material, and it exhibits excellent mechanical properties such as hardness and toughness, which are characteristic of ceramics (reinforcement phase) and metals (binder phase), respectively (Jose, 2022). Among the most common ceramic phases are titanium, tungsten, niobium, tantalum, vanadium carbides and carbonitrides, while molybdenum, cobalt, and nickel alloys are used as metallic binder components (Fig. 1) (Chang, Chang, & Huang, 2015; Kenneth J. A. Brookes, 1992; Sabatello, Frage, & Dariel, 2000). The wear and corrosion resistance of the carbide phases is enhanced with the toughness of the metallic phase by combining both hardness and toughness to determine the wear behavior of cermet materials (D’Errico, Bugliosi, Cuppini, & Guglielmi, 1997; Jin, Onuoha, Farhat, Kipouros, & Plucknett, 2017; Pirso, Viljus, Letunovitš, Juhani, & Joost, 2011).

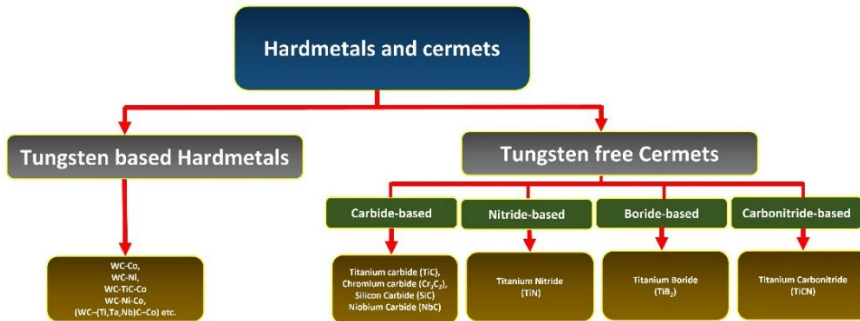


Figure 1. Classification of Cermets and Hardmetals (Ettmayer, 1989; Kulu, 2001).

The first hardmetals (WC-Co) were introduced in 1927, and Cermets, containing titanium carbide/molybdenum carbide with nickel as a binder, were first manufactured in Germany in 1929. This class of cermet materials also contains ceramic phases like WC or Mo<sub>2</sub>C to improve the wetting of the hard phase and improve the mechanical performance of the fabricated specimens. Since then, Cermets have been combined with ceramics and metals in various combinations to enhance their densification and mechanical properties. There is a wide variety of applications for Cermets consisting of TiC, Ti (C, N), and WC-Co with binders such as Co, Fe, Mo, Ni, and alloys. For the preparation of such cermets, powder metallurgy techniques such as Vacuum sintering, Reactive sintering, sintering under pressure such as Hot Isostatic Pressing, and Field assisted sintering techniques such as Spark plasma sintering (SPS) are most commonly used.

## 1.2 Additive Manufacturing of Cermets

3D printing (3DP) or Additive manufacturing (AM) is a revolutionary material fabrication technology that has been developing rapidly over the past 30 years (Aramian et al., 2020; Berman, 2012; Lele, 2019). As opposed to traditional manufacturing techniques (or Subtractive manufacturing), AM uses 3D CAD models to construct parts by adding material layers at a time, rather than removing them. This fabrication technique fulfills the demand for parts that have intricate geometric shapes, are highly accurate, and are easy to assemble. American Society for Testing and Materials (ASTM) defines AM as “a process of joining materials to make objects from 3D model data, usually layer upon layer, as opposed to subtractive manufacturing technologies”.

Through the development of this precision manufacturing process from rapid prototyping to ready-to-use parts, manufacturing constraints have been significantly relieved and design freedom has been significantly increased (Berman, 2012). Compared to conventional manufacturing methods, AM is considered a green technology that allows the fabrication of a variety of complex-shaped parts and offers advantages such as high design flexibility, customization, shortened lead time, no assembly or molds needed, and reduced energy consumption (R. S. Khmyrov et al., 2017; Lengauer et al., 2020; Santos, Shiomi, Osakada, & Laoui, 2006). Additive manufacturing consists of different technologies, which can be categorized into two major categories; the “direct” way is where the metal powder melts and solidifies to create the final dense part (Azam, 2018). And secondly, the “indirect” way, involves the joining of the feedstock powder particles with a binder and then post-processing steps adapted to achieve desired dense fabricated parts (Guo & Leu, 2013). Fig.2 illustrates the classification of AM processes adapted for the fabrication of the cermets.

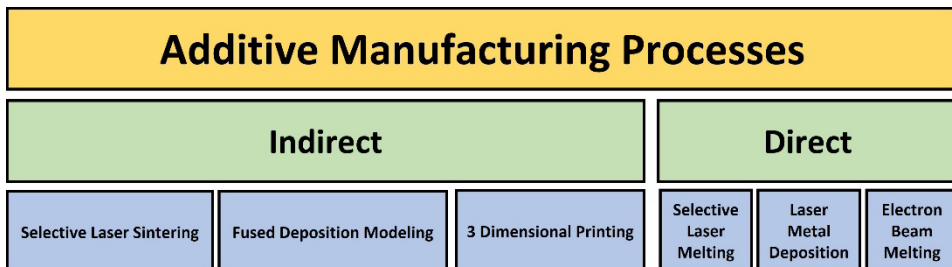


Figure 2. Classification of Additive manufacturing processes (Azam, 2018).

So far both the indirect and direct methods have been employed for the fabrication of the Cermets and Hardmetals (Aramian et al., 2020; Jose, 2022). The most commonly used methods include Selective laser sintering/melting, Laser engineering net shaping (LENS), binder jet (3D printing), and direct laser deposition (DLD). Moreover, the 3D gel/robocasting/direct-ink-write printing AM method, combining gel casting and material extrusion, has also been applied recently to cermet production (Lengauer et al., 2019; Sing et al., 2017). Table 1. summarizes recent developments in the fabrication of Hardmetals and Cermets via Additive manufacturing routes.

Table 1. Table illustrating the relative density and various properties of the Cermets and Hardmetals fabricated via Additive manufacturing routes.

AM Process	Powder Composition	Structural characteristics	Properties		Ref.
		Relative density (%) / density (g/cm <sup>3</sup> )	Hardness	Fracture toughness (MPa·m <sup>1/2</sup> )	
LPBF/ SLM	WC/W <sub>2</sub> C-Ni-Cu	85-97.5%	34-47 HRC	7-12	(Tan et al., 2022)
	WC-Co	-	-	-	(Uhlmann, Bergmann, & Gridin, 2015)
	WC-W <sub>2</sub> C-8.3 wt.% Ni	97.5% /14.69	-	-	(C. W. Li, 2018)
	WC-Co	97%	-	-	(Uhlmann, Bergmann, & Bolz, 2018)
	WC-Co	-	-	-	(Yang et al., 2020)
	TiC-Ni-Cr	88-97.5%	1027-1289 HV1	-	(Aramian, 2020c)
	WC-Co	-	-	-	(Yang et al., 2020)
	WC-Co	-	-	-	(Roman S. Khmyrov, Shevchukov, Gusarov, & Tarasova, 2017)
	WC-12Co	Near theoretical density	1496-1515 HV0.3	-	(Domashenkov, Borbély, & Smurov, 2017)
	WC-Ni	82-96 %	1000-1871 HV0.1	-	(Gu & Meiners, 2010)
	WC-27.9 wt.% Co	-	964 ± 49 HV0.5	-	(Son, 2021)
	TiC-Ni-Cr	93-98%	1250-1370 HV1	19- 26	(Aramian, 2020b)
	WC-10 wt.% Co-4 wt.% Cr	~98 %	2001±29 8 HV1	-	(Campanelli, Contuzzi, Posa, & Angelastro, 2019)
	TiC-NiCr	~97%	1300-1500 HV1	-	(Aramian, 2021)

WC-20 wt.% Co	86-96%	>10 GPa	-	(J. Chen et al., 2019)
WC-12 wt.% Co	4-72%	870-1400 HV	-	(Bricin & Kriz, 2019)
WC-11Co W <sub>5</sub> C11Co (HIP) W <sub>5</sub> C17Co W <sub>5</sub> C17Co (HIP)	14.27 14.64 13.64 14.04	- 77 HRA - 86 HRA	-	(Fortunato, Valli, Liverani, & Ascari, 2019)
WC-12 wt.% Co	99.5%	1315- 1397 HV0.3		(Picas et al., 2009b)
B <sub>4</sub> C-Co	67%	2900- 3200 HV0.3	-	(Davydova et al., 2016)
WC-6 wt.% Co	-	2500	7	(Grigoriev, Tarasova, Gusarov, Khmyrov, & Egorov, 2019)
WC-10 wt.% Fe- Ni-Zr	78-96%	-	-	(Ku, Pittari, Kilczewski, & Kudzal, 2019)
WC- 12 wt.% Co	84-92%	1080- 1425 HV0.2	9-11	(L. Zhang, 2022)
Ti- 28% B <sub>4</sub> C	-	-	-	(Kühnle & Partes, 2012)
WC- CO	98.5-99.9%	1000- 1200 HV1	-	(Ibe, 2021)
WC-Co	>90%	1150- 1350 HV30	-	(J. Liu et al., 2021)v
WC – 12Co	-	-	-	(Xing et al., 2022)
WC- 13Co	90-96%	-	-	(Y. Li, Bai, Wang, Hu, & Guo, 2009)
WC-20 HEA (Ni- Al-Co-Cr- Cu-Fe)	99.35%/13.46	988-1396 HV	9-11	(C. W. Li, 2019)
WC-17Co	96-97%	1410- 1484 HV	-	(D. Liu, Yue, Kang, & Wang, 2022)
WC-17Co	97%	-	-	(D. Liu, Yue, Kang, & Wang, 2021)
WC-12Co	83.5-96%	-	-	(Kim, 2021)

<b>DED/ LENS/ DLF</b>	WC – 13 wt.% Co	96-97%	-	-	(Y. Xiong, Smugeresky, Lavernia, & Schoenung, 2008)
	WC-12Co	>99.5%	86-92.5 HRA	-	(X. Li et al., 2022)
	WC-10 wt.% Co	96%	1300-1350 HV	-	(Xiong, 2009)
	TiC-20 vol.% Ni TiC-30 vol.% Ni TiC-40 vol.% Ni	-	2200 HV0.3 2000 HV0.3 1900 HV0.3	-	(Y. Li et al., 2009)
	(Ti, W) C– Ni	94-95%	17 GPa	6-7	(Y. Xiong, 2010)
	WC-17 wt.% Co	95-97%/12.95-13.70	584-663 HV10	-	(Fries et al., 2020)
	WC-10 wt.% FeCr	-	1300-600 HV30	-	(Molobi, Sacks, & Theron, 2022)
	<b>Binder jet 3D printing</b>	WC-10%Co	14.52 g/cc	-	-
WC-12% Co		Near theoretical density	1256 HV 30	17	(Enneti & Prough, 2019d)
WC-12% Co		-	-	-	(Enneti & Prough, 2019a)
TiCN-Ni-Mo <sub>2</sub> C		> 98%	-	-	(Berger, 2022)
<b>Extrusion-based 3D printing</b>	WC-10Co & (Ti(C, N), WC, (Ta,Nb)C, Cr <sub>3</sub> C <sub>2</sub> , Co, Ni)	-	-	-	(Lengauer et al., 2019)
<b>3D gel printing</b>	WC-20%Co	99.93 %	87.7 HRA	-	(X. Zhang, Guo, Chen, & Yang, 2018)
<b>Thermo plastic 3D Printing (T3DP)</b>	WC-10%Co	~100	-	-	(Scheithauer et al., 2017)

### **1.2.1 Indirect Additive Manufacturing technologies**

The indirect Additive manufacturing process for the fabrication of the cermets parts uses an organic binder to temporarily fix the feedstock particles during fabrication. By layering three-dimensional objects, the binder is removed, and the powder is sintered to produce the final parts. For indirect additive manufacturing of cermets, a number of shaping technologies can be used, including binder jetting, material extrusion, and material jetting. A generic Indirect AM process follows the concept of Shaping-Debinding-Sintering as a sequential processing route. Hence, they are sometimes referred to as “sinter-based” Additive Manufacturing technologies. Following are some of the indirect additive manufacturing processes employed to fabricate cermets parts.

#### **1.2.1.1 Extrusion-based 3D printing**

Extrusion-based 3D-printing is used for producing hard metals and cermets parts using the SDS (shaping-debinding-sintering) process. This technique uses wire or powder-based feedstock to fabricate fused-filament structures (FFF) or composite-extrusion structures (CEM). In both methods, the feedstock is fused, and nozzles are used to print free-form structures. In some recently developed extrusion-based AM technologies for the cermets and hard metal, the feedstock material is already in a liquid or soft state (e.g., inks, pastes, etc.) before insertion. Lengauer et al. fabricated a cermet based on (Ti(C, N), WC,(Ta, Nb)C, Cr<sub>3</sub>C<sub>2</sub>)-Co, Ni by using a FFF AM technologies (Lengauer et al., 2019). However, the fabricated parts exhibit a microstructure similar to conventional sintered cermets parts. In addition, fabricated cermet parts exhibit an insufficient density and relatively high surface roughness as a result of non-optimal process parameters.

Fabrication of the Hard metals and cermets using Extrusion based 3D printing technologies has some limitations such as raw material must meet several stringent requirements, including maintaining shape and supporting the next layer’s weight without deforming or collapsing. Consequently, extrusion-based 3DP techniques cannot be utilized for specimens with complex hollows or irregular geometries. Thus, future efforts need to be made to fabricate parts with better surface quality and improved density by optimizing printing parameters and using the appropriate feedstock.

#### **1.2.1.2 Binder jet 3D printing**

Binder jet 3D Printing (BJ3DP) has emerged as a promising alternative to overcome the limitation of extrusion-based AM (Aramian et al., 2020). As a result of this AM process, Cermets and hard metal parts with complex geometries can be manufactured. Powder and binder are the two types of materials used in BJ3DP. An adhesive pattern is commonly printed by binder-jet 3D printers in order to bind the feedstock powders into 3D structures (Enneti & Prough, 2019b; Enneti et al., 2020). A major disadvantage of the binder jet 3DP process is the volume change from green specimens to fully consolidated parts, along with the need to remove the binder by extensive post-processing, which results in distortion and shrinkage of the printed cermets parts (Enneti et al., 2020, 2018). Until now, only limited work has been done on BJT3D of cermets or super hard composites. Recently Berger et al. investigated the fabrication of TiCN based with different Ni and Mo<sub>2</sub>C contents (Berger, 2022). To improve the printing of cermets parts, spray granulation techniques have been adapted in order to produce spherical powder. Therefore, the printed parts have a higher density (98%) as a result of the spray granulation techniques. As a result, further efforts need to be focused on improving the density of the final parts and achieving homogeneous microstructures.

### 1.2.2 Direct Additive Manufacturing technologies

Direct AM methods such as laser-based powder bed fusion technology (L-PBF) also known as selective laser melting (SLM), laser-based powder-fed process also known as directed energy deposition (DED), and Electron beam melting (EBM) that offers the fabrication of high-performance materials with intricate structures with unprecedented properties (Hu, 2018). The direct/single-step AM methods combine the forming and densification procedures in a single step and fabricate the final components without the need for post-sintering or post-processing processes. Therefore, direct/single-step AM processes as compared to the indirect/multi-step AM methods can produce components with improved mechanical properties, higher density, and greater purity by adapting less time and energy. In addition, the direct laser-based AM method employs a laser or electron beams as a heat source, where these heat sources have high directionality and high energy intensity and hence, can deliver an intense amount of energy to a micro-scale focused region (Kruth, 2007). Fig. 3 exhibits the cermets parts fabricated via a direct Additive manufacturing route. Due to the intense amount of energy offered by the laser, even materials like Mo/W with high melting points can be fabricated with ease. The following article section briefly describes direct additive manufacturing technologies.

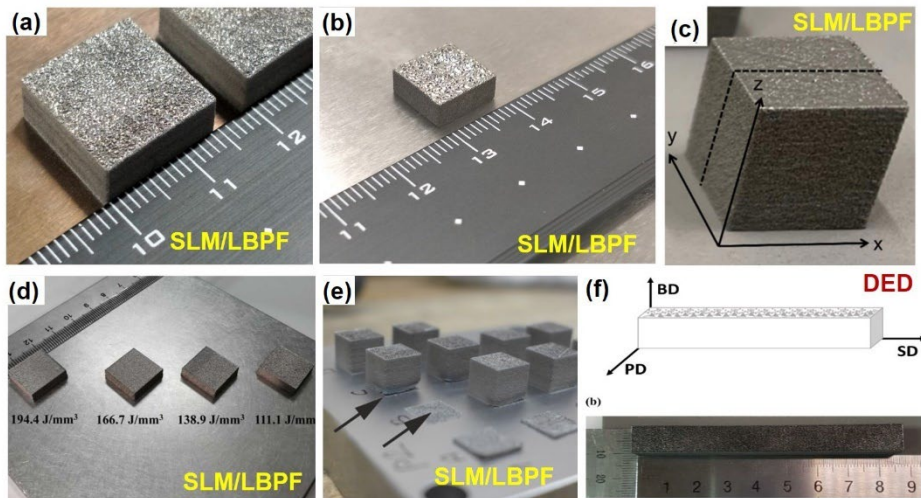


Figure 3. Cermets parts fabricated via a direct Additive Manufacturing process. (a) WC-HEA (C. W. Li, 2019), (b) WC-W<sub>2</sub>C-8.3 wt.% Ni (C. W. Li, 2018), (c) WC-25Co (Ibe, 2021), (d) WC-Co (L. Zhang, 2022), (e) WC-13Co (Bricin, 2020), (f) WC-12Co (Kim, 2021).

#### 1.2.2.1 Electron Beam Melting /Selective Electron beam melting

Electron Beam melting is a direct additive manufacturing (AM) technology that fabricates the 3D printed parts in one step by full melting of feedstock powder particles. The heat source is the primary difference between laser-based additive manufacturing technologies and EBM. In EBM, an electron beam instead of a laser is used as a heat source to melt the powder bed, which requires that the procedure be conducted under a vacuum to prevent electromagnetic dissipation (Nickels, 2016; Wysocki et al., 2017). In the EBM printer, as shown in Fig. 4, the feedstock powder material is spread on the build platform by the machine, and based on the CAD data provided to it, the electron beam melts the material powder selectively (also known as Selective electron beam melting (SEBM)).

A layer of powder is spread on top of the build platform. By tracing the cross-section of the next layer, the beam melts the powder until the 3D part is built, and the process is repeated.

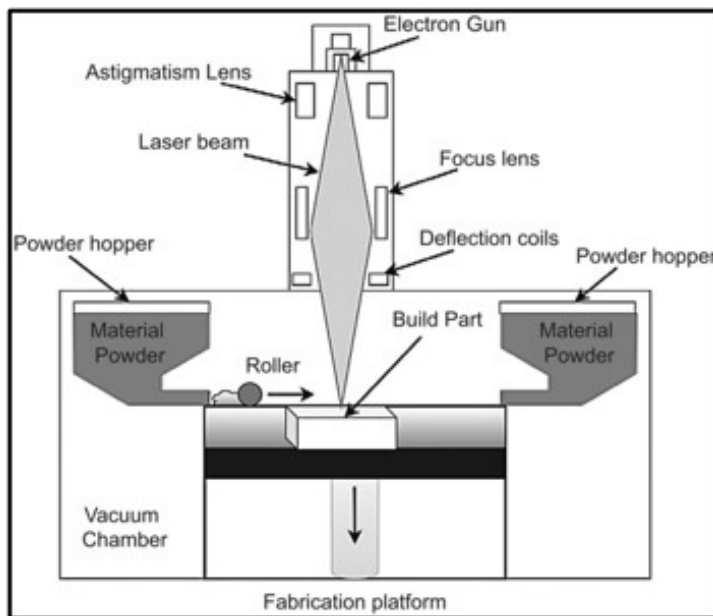


Figure 4. Schematics of the Electron beam melting process (Azam, 2018).

### 1.2.2.2 Directed energy deposition

Directed energy deposition is a powder-based additive manufacturing method used to create 3D parts, repair metal components that are deemed unreparable by conventional methods, or modify existing components (Gibson, Rosen, & Stucker, 2015; Svetlizky et al., 2021; B. Zheng et al., 2019). DED is a 3D printing/AM technology that operates on different sources of energy such as laser beam, electron beam, and electric/plasma arc. The energy source will directly melt the metal powder/wire that comes coaxially with the energy beam, which meets each other near the workpiece as shown in Fig. 5. The melt is then deposited directly on the workpiece or substrate to fabricate 3D parts layer by layer manner. A melt pool is generated when the feedstock powder is heated to a precise temperature with concentrated energy, usually surrounded by an atmosphere of inert gases.

Like other AM processes, DED also involves layer-by-layer fabrication of parts based on a CAD model. During layer-by-layer deposition, DED-deposited parts are subjected to rapid and repeated heating-cooling cycles that can result in microstructural inhomogeneities, residual stresses, solidification cracks, delamination, porosity, and warping (Gibson et al., 2015; Kim, 2021; Svetlizky et al., 2021). DED can deposit high-performance materials such as stainless steel, tool steel, alloy steels, titanium-based alloys, aluminum alloys, cobalt-based alloys, high-entropy alloys, nickel-based alloys, intermetallic, functionally graded materials (FGMs), ceramics, composites, and shape memory alloys (SMAs) (Svetlizky et al., 2021). However, the DED process has some drawbacks, such as local deformation due to the local temperature gradient, high surface roughness, problems with powder recyclability when multiple materials are used, etc

(Picas et al., 2009a; Y. Xiong, 2010). Compared to other AM processes, DED offers a unique advantage, which is site-specific deposition and repair such as in wind turbines, automotive parts, or other industrial parts (Svetlizky et al., 2021).

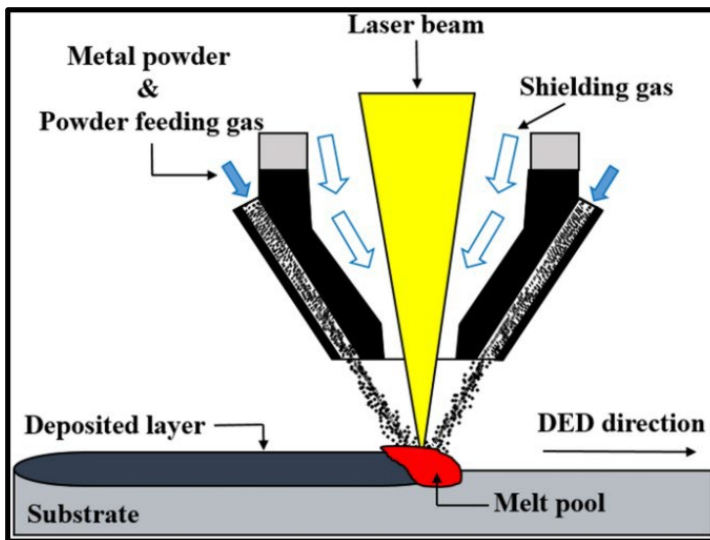


Figure 5. Schematics of the Directed energy deposition process (DED) (Lim, 2021).

### 1.2.2.3 Selective laser melting /Laser powder-bed fusion process

SLM/ L-PBF is an AM process that uses a laser (as an energy source) to fabricate 3-D intricate parts layer-by-layer fashion using a feedstock powder bed as dictated by 3D CAD data. Generally, the process is carried out in an inert atmosphere to protect the melt pool against contamination/oxidation during the solidification process. The layers are printed by scanning the powder bed with the exposure of a laser on a cross-sectional area to melt the powder particles together as an even-thin layer. The melt pool solidifies in a rapid fashion with extremely high cooling rates. However, the melt pool experiences different cooling rates in different directions leading to inhomogeneity in the microstructure along different length scales. After the solidification of the single layer of the powder bed, the subsequent layer of the powder is spread, and the iterative process continues until the entire part is fabricated as shown in Fig. 6. Adapting the SLM process in industrial settings, critical and intricate components that are not feasible to produce with conventional methods can be manufactured in a one-step process.

SLM/ L-PBF process finds its applications in a variety of sectors including the aerospace industry, automotive industry, medical sector, gas and oil plants, jewelry industries, etc (De Wild et al., 2019; Olakanmi, Cochrane, & Dalgarno, 2015; Rahmani, Antonov, Kollo, Holovenko, & Prashanth, 2019; T. Zheng, Pan, Murali, Li, & Li, 2022). However, there exist issues and problems that prevent this technology from being used in a widespread application in mass production. SLM is green technology as it's used to fabricate parts with minimum raw material, creates less waste/scrap, and reduces the overall time of processing as it doesn't require/require minimal machining/post-processing of the fabricated parts. The use of post-processing treatments such as hardening, heat treatment, and hot isostatic pressing (HIP) has been known to improve the microstructure and overall mechanical properties of the SLM finished parts.

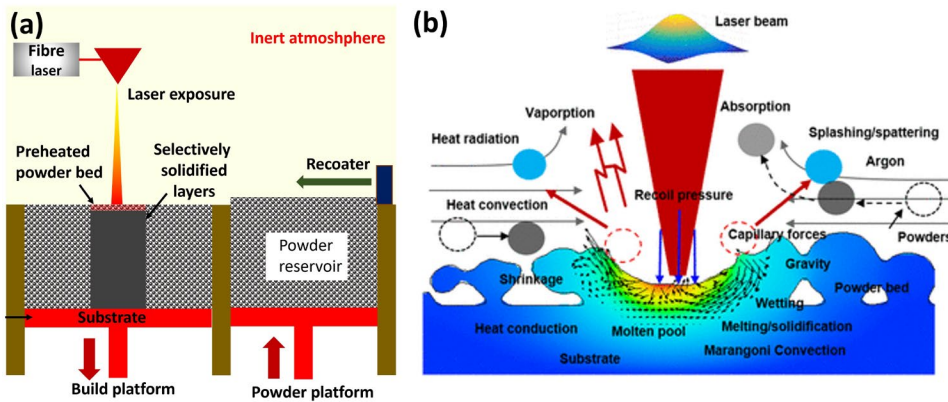


Figure 6. (a) Overview of the laser powder-bed fusion process/ Selective laser melting, and (b) Schematics illustrating the physical processes involved in Selective laser melting (Z. Chen, 2018).

The gas-atomized spherical powder has typically been used for SLM due to its better flowability and homogeneity. In addition to the mechanical mixing method, the milling process can also be used to prepare the composite powders as SLM powder feedstock. The unique advantage of the SLM/ L-PBF process is its ability to utilize unmelted metal powder particles efficiently as it allows for re-use and recycling up to 20 times. The morphological characteristics of the reused powder and fabricated test parts did not change significantly until 14 cycles, validating the methodology of powder recycling for its use in SLM manufacturing (Ardila et al., 2014; Olakanmi et al., 2015). Among other outstanding environmental benefits of SLM, the processing of novel design with weight reduction (topology optimization) leads to reduced emissions in the automobile and aerospace sectors.

In addition, the present methodology eliminates/minimizes the use of toxic chemicals such as lubricants. A major disadvantage of the SLM process is its lower productivity and inferior fatigue performance compared to that of its wrought counterpart. In addition, wider temperature gradients can cause cracking and significant residual stresses (due to high cooling rates  $\sim 10^5$ - $10^6$  K/s) in the SLM fabricated components, making it challenging to process brittle materials like cermets (Hooper, 2018; Jung et al., 2015). A variety of process parameters play a crucial role in the fabrication of the parts including their microstructure and properties, which will be discussed in detail in the coming sections.

### 1.2.2.3.1 Process parameters

The quality of a part fabricated using laser-based additive manufacturing processes depends on several factors including the process parameters. Some of the important process parameters are laser power, laser scan speed, hatch distance, hatch style, laser focus, layer thickness, etc (Hanzl, 2015; Oyesola, 2021). In addition, the powder characteristics including, powder morphology, rheology of the powder, layer thickness, etc. also influence the quality of the fabricated parts (Y. Wang, 2023; Yu, 2022). Laser-based fusion processes (SLM/L-PBF) are controlled by a set of process parameters and changing any of these parameters can adversely affect the fabrication process and densification of the final component, and result in process defects such as delamination, warpage, porosity, micro cracks, etc. which can be avoided by optimizing these parameters. Fig. 7 outlines the different factors (including the process parameters) that affect the fabrication of cermets in the LPBF/SLM process.

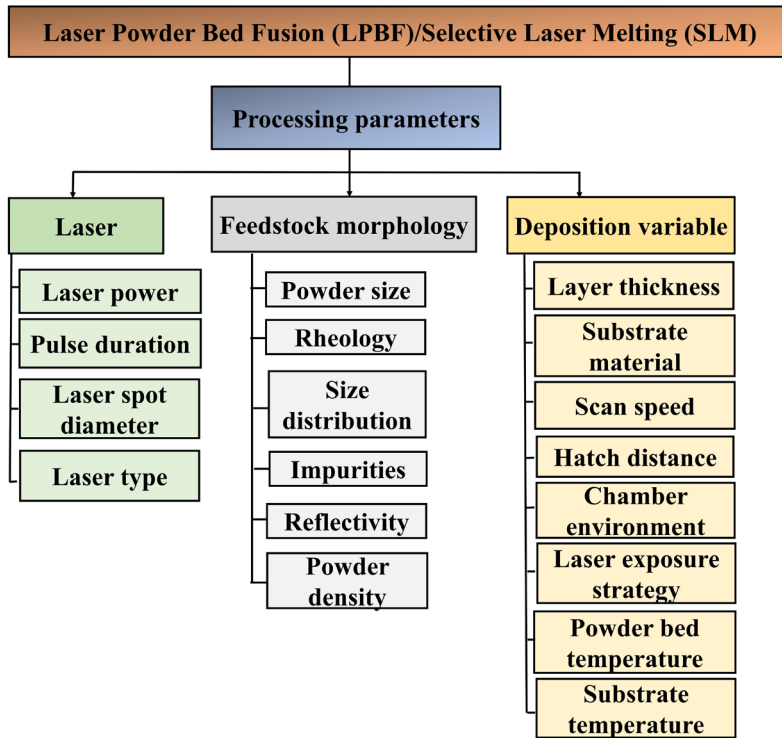


Figure 7. An outline of the process parameters that affect the laser powder bed fusion / Selective laser melting process.

One of the equations that need to be accounted for when discussing the process parameters is the laser energy density or volumetric energy density ( $J/mm^3$ ), which can be calculated as(Aramian, 2020a; Tonelli, Fortunato, & Ceschini, 2020):

$$VED = \frac{P \cdot ET}{PD \cdot HD \cdot d} \quad \dots\dots\dots (1)$$

where VED represents the volumetric laser energy density,  $P$  denotes a laser power in Watts,  $ET$  represents the exposure time in seconds,  $PD$  represents point distance in mm,  $HD$  denotes the hatch distance in mm and  $d$  represents the layer thickness in mm. Even though the equation does not include many parameters that are crucial for the fabrication of defect-free parts, they are widely used as an empirical formula for the parameter optimization process. Many parameters such as laser focus diameter, laser offset at the corners, hatching style, gas flow direction, etc. must also be considered to calculate the overall energy transferred to the powder bed (Prashanth, 2017).

Several reports have focussed on the influence of process parameters on microstructural formation and in turn their mechanical properties. For instance, Aramian et al. have studied the effect of the process parameters for the fabrication of the TiC-NiCr-based cermets by SLM. Aramian et al have varied the laser scan speed, and thus the Volumetric laser energy density to evaluate their influence on the microstructures. The changes in the process parameters influence the thermal behavior of the melt pool and density, which significantly influences the microstructure of the fabricated part.

### 1.2.2.3.2 Process-induced defects

Fabrication of the cermets through laser-based fusion processing such as LPBF/SLM is challenging to produce without any external defects. During the fabrication of cermets, the inherent brittleness and the difference existing between the thermal conductivity of the ceramic and the binder phases, the samples readily crack (Campanelli et al., 2019; R S Khmyrov, Safronov, & Gusarov, 2017). In addition, due to the rapid heating of the powder bed during the laser-based fusion processing, the melt pool temperature rises rapidly, causing thermal residual stress in the fabricated part, which also leads to the cracking of the parts (Yadroitsev & Yadroitsava, 2015). The process defects are not limited to the laser processing condition, but also the morphology and rheology of the powder particles. L-PBF/SLM processes require good powder rheology and flowability (J. Chen et al., 2019; J. Liu et al., 2021). A wide variation in particle size distribution in the feedstock powder can lead to defects that ultimately affect the density/porosity of the as-built parts. Even though, processing defects can be minimized by altering the processing conditions, eliminating the process defects completely is rather a challenge (Aramian et al., 2020; Ku et al., 2019). Cracks and porosity are the two major defects that are often found in laser-processed materials (Campanelli et al., 2019; Xing et al., 2022). Fig. 8 summarizes the different process defects that may be observed during the processing of the laser-based solidification process.

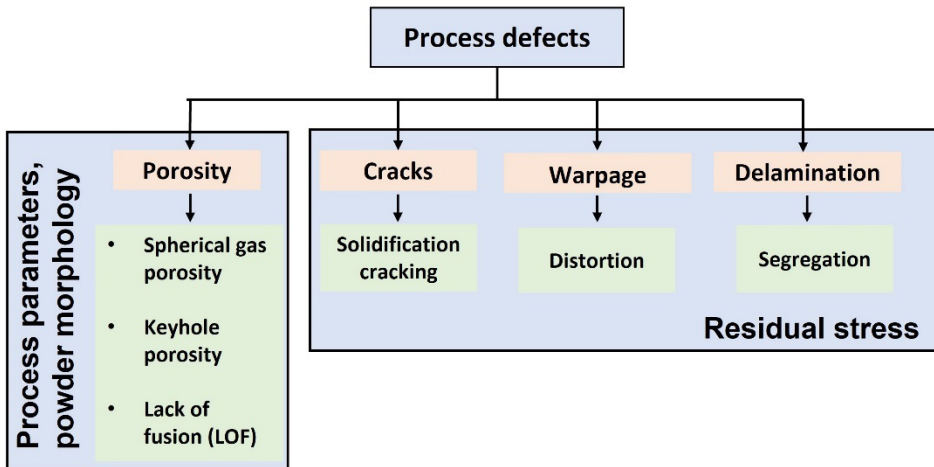


Figure 8. Schematics illustrating the different process defects observed during the fabrication of cermets by laser-based solidification processes.

## 1.3 Fabrication of TiC-based cermets via Additive Manufacturing route

Recently, several efforts have been made to widen the range of materials used in AM, including polymers, metals, ceramics, and their combinations (such as cermets), and several publications have been published in the field of AM of carbide-based cermets via different AM fabrication techniques. By far the most common carbides fabricated using the L-PBF/SLM process are WC and TiC with different metals and alloys as binders. Cermets are one of the most challenging materials for the solidification-based 3D printing/AM process to be fabricated without defects like porosity and cracks as they combine the desirable toughness and thermal conductivity of metals with high hardness (source of cracks), excellent wear resistance, and oxidation resistance of ceramics.

In addition, the wider temperature difference between the carbides and metal/alloy reinforcement makes the additive fabrication process more challenging.

A high cooling rate during the laser-based process and the characteristics of the feedstock affected the fabrication process and the mechanical properties of the final product. Table 1 and Table 2 provide a summary of the recent research and development of the TiC-based cermets (highlighted) and the adapted laser process parameters fabricated via Direct Additive manufacturing processes respectively. This review is mostly focused on the cermets having ( $\geq 50$  wt.%) of the ceramic or hard phase.

To the best of the author’s knowledge, a few studies have been conducted on the fabrication of TiC-based cermets via a direct additive manufacturing route with Ni-based binder. Due to the paucity of research on the development of low-cost TiC -Fe-based cermets by AM, this Ph.D. work focuses on developing and advancing laser-based fusion processing of such cermets.

*Table 2. Laser process parameters adapted to fabricate TiC-based cermets parts via different laser-based Additive manufacturing routes.*

AM Process	Composition	Process parameters					Ref.
		Laser Power	Hatch distance	Scan speed	Layer thickness	Energy density	
SLM	TiC- 40wt. %NiCr	62.4 W	0.06 mm	50-150 mm/s	0.05 mm	138.7 - 416 J/mm <sup>3</sup>	(Aramian, 2020a, 2020c, 2021; Aramian et al., 2021)
DED/ LENS	TiC-20 vol.%Ni		-				
	TiC-30 vol.% Ni	2400–2600 W	-	200 mm/min	1.5–1.8 g/min		(Y. Li et al., 2009)
	TiC-40 vol.% Ni						
	(Ti, W) C-20 wt.%Ni	260–300 W	-	2–4 mm/s	3–5 g/min		(Y. Xiong, 2010)

## 1.4 Research gap

Cermets fabricated via AM processes such as L-PBF /SLM show different microstructural characteristics due to high cooling rates, which in turn could be beneficial to get the final parts with improved mechanical properties. However, the presence of process defects due to materials' inherent brittleness, large thermal expansion coefficient, thermal residual stresses, powder rheology, etc. makes the fabrication of the cermets through laser-based processing challenging. Many open issues need to be considered to improve the quality of the fabricated cermets. The factors that need to be considered in the upcoming years to widen the research area in the field of cermets via AM processing have been discussed below.

- A major challenge in fabricating cermets via laser-based AM processes is attaining fully dense consolidated parts. In most research projects, the density of the samples achieved varies between 96–98%, which is low in comparison to the parts fabricated by conventional methods. To fabricate dense parts, various factors such as the rheology of powder, laser energy density, process defects, etc. must be taken into consideration one at a time. The process parameters need to be optimized to fabricate dense parts and the parameters need to be considered one at a time to have a better output. Novel laser pulse modification techniques should be adopted and explored to carefully tune the microstructure both in terms of morphology and porosity content.
- Preheating the powder bed using laser pulse shaping/laser beam optimization and laser rescanning methods are considered as some options to mitigate crack formation, which is one of the most challenging effects in the fabrication of brittle materials such as cermets. Extensive research should be carried out on laser shaping/modulation and standards should be established using laser modulation to fabricate defect-free cermets.
- Several research studies have been conducted on the fabrication of WC-based cermets with Co or Ni as a binder material. The toxic nature of these elements and the rising price of Co warrants the research towards the development of green/low-cost cermets. TiC-based cermets prove to be an alternating solution and show better mechanical properties at higher temperatures. TiC-based cermets with Fe-based binder show promising results through conventional methods but research in the field of laser-based fusion of AM is still in its infancy.

## 1.5 Aim and objective of the thesis

Due to the limited availability of critical raw materials like tungsten, cobalt, or, more recently, nickel, the hard metal industry is challenged to discover alternatives to WC-based cermets. Therefore, the main **aim** of the present thesis is to investigate the fabrication of TiC-based cermets with different Fe-based binders adapting advanced fabrication routes such as Additive Manufacturing. In addition, to fabricates the cermet parts with improved mechanical properties and lower process-induced defects such as cracks.

**Hypothesis** of the study is that TiC-based cermets could be a potential replacement in applications involving high temperatures and harsh environments. Compared to conventional methods, the fabrication of cermets using additive manufacturing technologies (AM) overcomes some limitations (restriction to fabricating complex geometry in a single step, waste of energy and scarp material, etc. in terms of being sustainable and environmentally friendly) and aids in improving/modulating the microstructure and properties of the fabricated parts. Laser-based processing of cermets parts can be challenging because of the complex thermal history of the fabrication process, inherent ceramic brittleness, variations in thermal expansion coefficients of ceramics and binder materials, etc. Previous studies suggest lowering the thermal gradient of the powder bed may result in fewer defects during laser processing of cermets.

Based on this, the main **objectives** of this thesis can be formulated as.

- Fabrication of TiC-based cermets with different Fe-based binder compositions (such as Fe and Fe-Cr (AISI 430L FSS)), that offer low-cost, nontoxic alternatives to conventional WC-based Hardmetals.
- To lower the process-induced defects by adapting Novel laser scan strategies (Laser Pulse Shaping and Multiple Laser Scanning) that can control the melt pool/powder bed temperature during the laser scan of the powder bed.
- To investigate the influence of adapted laser scan techniques on phase formation, morphological inhomogeneity, and anisotropy in the microstructure of the fabricated TiC-based cermets.
- To improve the physical and mechanical properties of the fabricated cermets (microhardness, fracture toughness) and tribological properties (wear) by adapting optimal laser process parameters.
- A comparison study of conventionally sintered cermet w.r.t laser-processed cermet to evaluate microstructural and mechanical properties via different fabrication routes.

## 2 Experimental methodology

This chapter of the dissertation describes the experimental methodology for fabricating and characterizing cermet parts. The AM LPBF/SLM process, microstructure characterizations (SEM, EDS), Phase composition (XRD), mechanical tests (Hardness and Fracture toughness), and Wear behavior via scratch test were discussed in detail.

### 2.1 Investigated materials

For the fabrication of the TiC-based cermet parts with different Fe-based binders, two different cermet compositions were investigated via a direct additive manufacturing process (LPBF/SLM) (Table 3). TiC powder (purity  $\geq 99.9$ ) as a reinforcement material supplied by Pacific Particulate Materials Ltd. with an average particle size of 2.10  $\mu\text{m}$ . For the binder system, pure Fe (purity  $\geq 99.8$ ) and ferritic stainless-steel (AISI 430L-FSS) (purity  $\geq 99.9$ ) have been used, supplied by TLS Technik GmbH, and Sandvik Osprey Ltd. respectively with an average particle size in the range of 10–45  $\mu\text{m}$ . Fig. 9. exhibits the SEM micrograph of the initial powders. The particle size distribution for TiC powder exhibits an irregular morphology with a small average particle size, while the particle size distribution for the binder materials (Fe and AISI 430L FSS) exhibits a spherical morphology with wide variations in particle size.

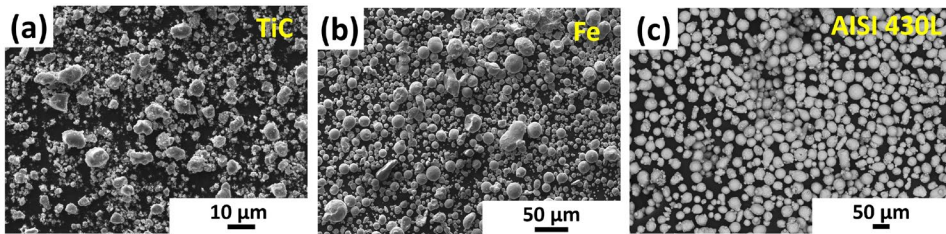


Figure 9. Scanning electron microscopy images of the initial powder particle (a) TiC, (b) Fe, and (c) 430L FSS.

### 2.2 Feedstock preparation

Table 3. Feedstock composition adapted for the fabrication of the cermet parts via laser powder bed fusion/Selective laser melting technology (in vol.%).

Samples designation	TiC	Fe	AISI 430L FSS
			X2Cr17 (EN 1.4016)
Cermet Composition 1 (CC1)	70	30	-
Cermet Composition 2 (CC2)	65	-	35

To prepare the feedstock powder, mechanical mixing was adapted to the composition indicated in Table 3. The powder was mixed in a jar using a Yttria Stabilized Zirconia (YSZ) ball as a mixing media to provide attrition during the mixing. Low powder-to-ball ratios were used to prevent the mechanical milling of powders, which can affect the morphology of the powder and its rheology during printing (Bricin & Kriz, 2019; Gómez, Gordo, &

Torralba, 2006). SEM micrograph of the prepared feedstock powder has been depicted in Fig. 10 (a, c). The binder powders exhibit a spherical morphology, whereas the ceramic phase exhibits irregular morphology after mixing. As a result of the initial powder provided, the mixed feedstock powder in both cermet compositions has a wide particle size distribution. Fig. 10 (b, d) shows the XRD pattern of the mixed feedstock powder of both the cermet compositions. The high-intensity peaks of the TiC and  $\alpha$ -Fe phases in both the CC1 and CC2 compositions suggest that no new phase formation occurred during mixing.

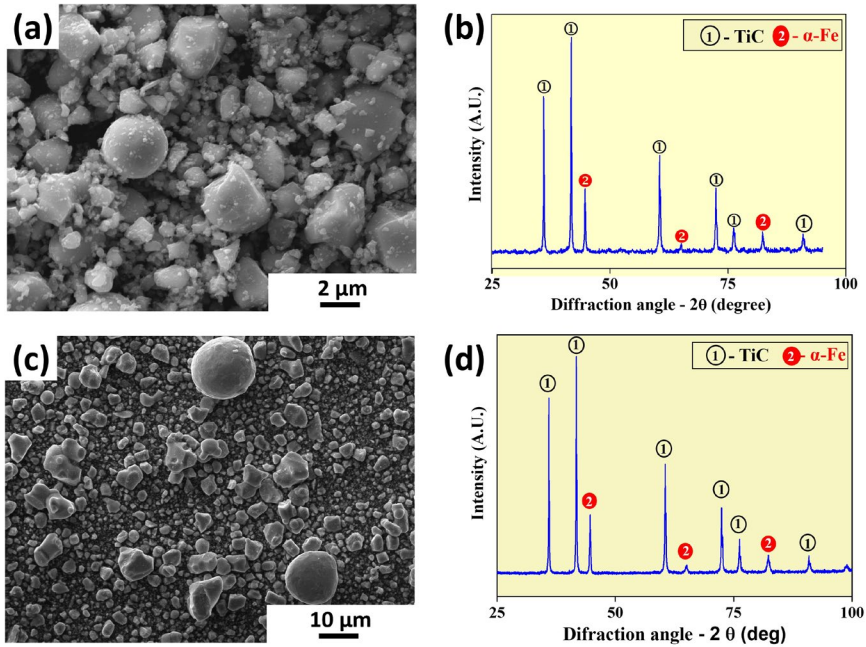


Figure 10. (a) Scanning electron microscopy images of the mixed feedstock powder CC1, (b) X-ray diffraction pattern of the mechanically mixed feedstock powder CC1, (c) Scanning electron microscopy images of the mixed feedstock powder CC2, and (d) X-ray diffraction pattern of the mechanical mixed feedstock powder CC2.

### 2.3 SLM/LPBF fabrication

Fabrication of the cermet parts was performed by using a Realizer SLM 50 (SLM Solutions GmbH, Germany). It was equipped with a 120-watt Nd-YAG pulse fiber laser with a spot size of  $\sim 39 \mu\text{m}$ . The system was designed to produce 3D components up to a diameter and height of 70 and 80 mm, respectively. In this work, the focal diameter of the laser beam on the work surface was fixed at 0.0134 mm, and in order to avoid contamination and melt pool oxidation, parts were fabricated under an Argon atmosphere (Bricin & Kriz, 2019). These cermets parts were printed on stainless-steel substrates, oriented vertically toward the building direction. For the fabrication of the cermet parts with different Fe-based binders (Table 3), two laser scanning techniques have been adapted to control the melt pool/powder bed temperature during the fabrication.

### 2.3.1 Laser Pulse shaping

During a pulsed laser operation, a specific amount of energy is emitted for an associated period. Laser pulse shaping is a technique of distributing energy within a single laser pulse in a controlled manner. It can also be defined as the modification of the power supplied to a laser in order to change the shape of the output pulse and, as a consequence, to change its heat distribution (K. A. Mumtaz & Hopkinson, 2010; K. Mumtaz & Hopkinson, 2010). A material's melting behavior can be completely changed by changing the energy distribution within a pulse. Laser Pulse shaping can be achieved by dividing the laser pulse's current that is used to excite a laser's flash lamp into multiple events and detailing the peak power and duration of each event. Each laser pulse in this work is adapted to 5 different events with variations in laser peak power and exposure times (Fig. 11 (b)).

Multiple events have been adapted during the pulse shaping to preheat, melt, and cool the powder bed at the laser exposure point of the powder bed to lower the thermal gradient or control the cooling rate. Fig. 11 (b) depicts different laser events adapted for single laser scans at each exposure point. Event 1 and 2 with lower laser power and small exposure time act as pre-heating of the powder bed while Event 3 with high laser peak power and exposure time act as a melting laser scan to melt and fuse the powder bed and at the end, Event 4 and 5 with lower laser power and wide exposure time act as a controlled cooling of the melt pool/powder bed. The point scanning strategy has been adapted to scan the laser at the exposure point (Fig. 11 (a)). This variation in the laser process parameters during the laser exposure helps to control the melt pool temperature and thus lowers the process defects in the parts. The laser process parameters adapted to fabricate the TiC-30 vol.% Fe cermets parts vis LPS are depicted in Table 4.

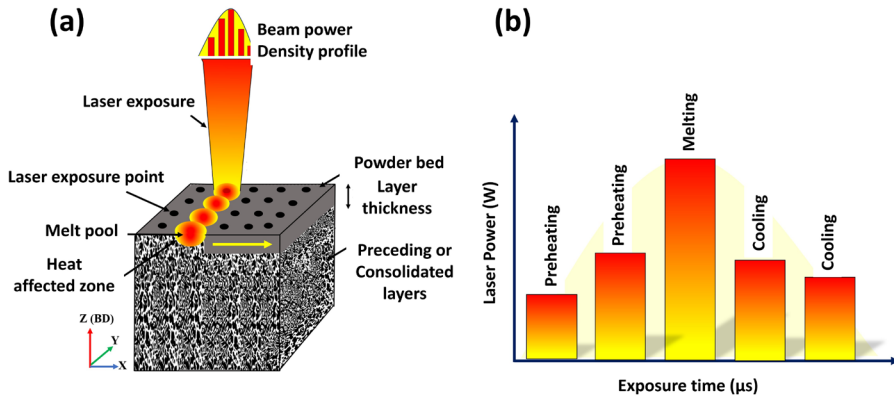


Figure 11. Schematics of (a) laser pulse shaping technique adapted for the fabrication of the TiC-Fe-based cermets, (b) An illustration of various laser peaks adapted to a laser pulse shaping.

Table 4. The laser process parameters adapted to fabricate TiC-30 vo.% Fe via Laser Pulse shaping.

Sample designation	Laser Pulse-type	Laser power (W)	Exposure time (μs)
SP-1	Standard pulse	60	200
SP-2	Standard pulse	72	200
CC1-1	Laser Pulse shaping	12-24-60-19.2-14.4	100-200-200-500-200
CC1-2	Laser Pulse shaping	12-24-72-19.2-14.4	100-200-200-500-200

### 2.3.2 Multiple Laser scanning technique

Another strategy technique adapted for the fabrication of the cermet parts are multiple laser scan strategy. In general, this approach is similar to laser pulse shaping, where the melt pool/powder bed temperature is controlled, and the thermal gradient is lowered. In this technique, the powder bed was scanned twice with different laser process parameters in each laser scanning of the powder bed. Initially, a high laser scan speed with a lower laser energy density is used to preheat the powder bed, followed by a high laser energy density but lower scan speed to melt and fuse the powder as shown in Fig. 12. Between two consecutive powder layers, a 60° scan rotation was employed. Scanning the powder bed with different laser process parameters helps to lower the thermal gradient of the melt pool and consequently lower the thermal residual stress and help to fabricate the parts with lower process defects such as thermal cracks. The effect of laser energy density and laser scan speed on the fabrication of the cermet parts has been studied through the variation of these parameters. All the laser process parameters involved in the MLS for the fabrication of the cermet composition 2 are shown in Table 5.

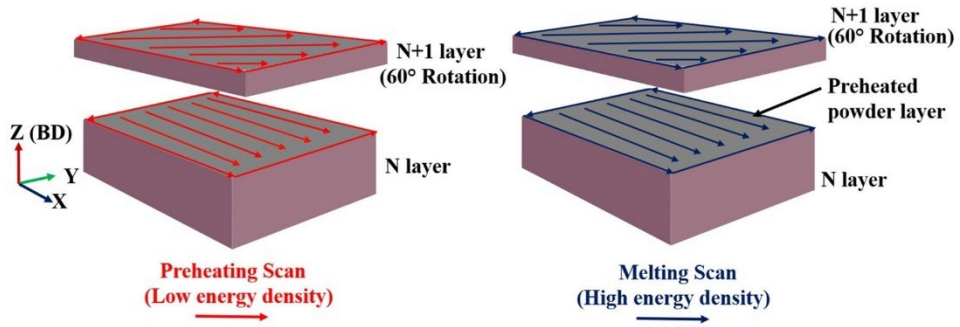


Figure 12. Schematics of Multiple laser scanning techniques adapted for the fabrication of the TiC-Fe-based cermet (adapted from publication III).

Table 5. The laser process parameter adapted to fabricate cermets parts (TiC-35 vol.% 430I FSS) with variation in laser scan speed and energy density employed for both pre-heating scan and melting scan during the selective laser melting process.

Sample designation	Pre-heating scan (PHS)		Melting Scan (MS)	
	Scan speed (mm/s)	Energy Density (J/mm <sup>3</sup> )	Scan speed (mm/s)	Energy Density (J/mm <sup>3</sup> )
CC2-1	488	80.4	99	844.7
CC2-2	203	84.5	81	958.7
CC2-3	176	97	56	1127.6

## 2.4 Test methods

### 2.4.1 Metallographic preparation

To prepare bulk samples for microstructural analysis, standard metallographic processing according to hard metal procedures, such as grinding and polishing, was employed.

### 2.4.2 Microstructure and phase analysis

The phase constituents of the initial and mixed feedstock powder as well as the SLM fabricated parts of both cermet compositions were determined using X-ray diffraction (XRD) methods by Rigaku Smart lab X-Ray Diffractometer (XRD) equipped with Cu-K $\alpha$  radiation ( $\lambda = 0.1542$  nm) at room temperature. Scanning electron microscopy (SEM) (Zeiss EVO MA15) coupled with the EDS system INCA was used to observe the microstructure and elemental distribution of the as-built parts.

Process defects in the fabricated parts (pores and cracks) were analyzed through  $\mu$ -X-ray computed tomography (CT – Phoenix nanotom, General Electric). The scanning was performed at 120 kV and 100 mA with a voxel size of 2.75  $\mu$ m. Additionally, the distribution and size of phases in both fabricated samples were examined using Image J software, using contrast difference measurements.

## 2.5 Characterization of physical and mechanical properties

### 2.5.1 Density

Archimedes' method was adapted to calculate the density of the fabricated parts at room temperature by using an Analytical balance (Mettler Toledo ME204) with a precision of  $\pm 0.0001$  g. Initially, each sample was weighed in air, then immersed in distilled water for an adequate amount of time, and then weighed again at a constant temperature. The rule of the mixture has been adapted to calculate the theoretical density of the present cermet compositions. A minimum of 10 readings were recorded for each sample, and the average value was reported.

### 2.5.2 Hardness and microhardness testing

The Vickers microhardness using a microhardness testing machine (Buehler Micromet) of SLM processed samples (both longitudinally and cross-sectionally) was determined at room temperature according to standard EN-ISO-6507 at 1000 g load with a dwell time of 10 s. For fracture toughness measurement, the fracture by indentation method (Indentation fracture toughness (IFT)) has been adapted according to (EN-ISO 28079:2009) by using a 30 kgf load (Vickers INDENTEC 5030SKV) with a dwell time of 10 s and by subsequently measuring the crack length (Palmqvist method) using optical micrography (Zeiss Axiovert 25). Calculation of fracture toughness values was performed using the following equation (Tarraste et al., 2018; Wu et al., 2011).

$$K_{IC} = 0.15 \sqrt{\frac{HV}{\sum l}} \quad \dots\dots\dots (2)$$

where  $K_{IC}$  (MPa·m<sup>1/2</sup>) denotes fracture toughness,  $\sum l$  (mm) represents the sum of crack tip length from the hardness indent, and  $HV$  (N/mm<sup>2</sup>) denotes Vickers microhardness.

### 2.5.3 Tribological characterization

To assess the tribological properties, scratch tests were conducted on polished as-built cermets by using the CSM Revetest device (Anton Paar GmbH, Austria). An indenter (Rockwell C diamond) with a radius of 200  $\mu\text{m}$  and 120° cone angle has been used for scratch testing. A variation in a normal load of 10, 30, and 50 N is used for all scratches at a scratch length of 2 mm and a scratching speed of 10 mm/min. Fig. 13 (a) shows a schematic diagram of the performed scratch test. In order to assess the wear behavior of additively manufactured cermets, scratch tests were conducted with single and multiple passes (5 passes) of the indenter. The direction of scratching in the multi-pass scratch test was not reversed, i.e., unloading the indenter load at the final scratch position, and applying the same load from the initial scratch position for the next pass. A 3D optical surface profilometer (WYKO NT9100) was used to analyze the macroscopic appearance of scratched surfaces. In order to measure the groove depth and scratch width, the vision 4.10 software was used to make 2D profiles of the scratch track. To evaluate the reproducibility of the results, all tests were repeated three times.

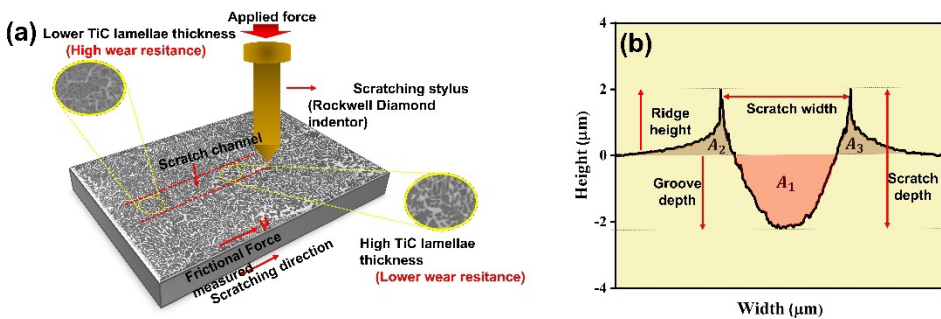


Figure 13. Schematics illustrating (a) scratch test used to study the wear behavior of the additively manufactured cermet parts, (b) 2D profile of the cermets scratch test where  $A_1$  represents the groove area and  $A_2$  and  $A_3$  corresponds to ridge area due to pile-up of the plowing material. (Adapted from publication IV)

### 3 Results and discussion

#### 3.1 Development of optimal process parameters to fabricate parts with lower process-induced defects

##### 3.1.1 Standard laser pulse

A study on the effectiveness of laser exposure with standard laser pulse or without laser pulse shaping has been conducted to determine the effect on the fabrication of the TiC-30 vol. % Fe-based cermets. In a single scan strategy single pulse laser with high laser power and exposure time has been applied to a powder bed (Fig. 14 (a)). The powder bed has only been exposed to one Laser event with the variation in laser melting peak power (60 and 72 watts). In both cases, the exposure time/scan speed was kept the same ( $200 \mu\text{s}/250\text{mm}\cdot\text{s}^{-1}$ ).

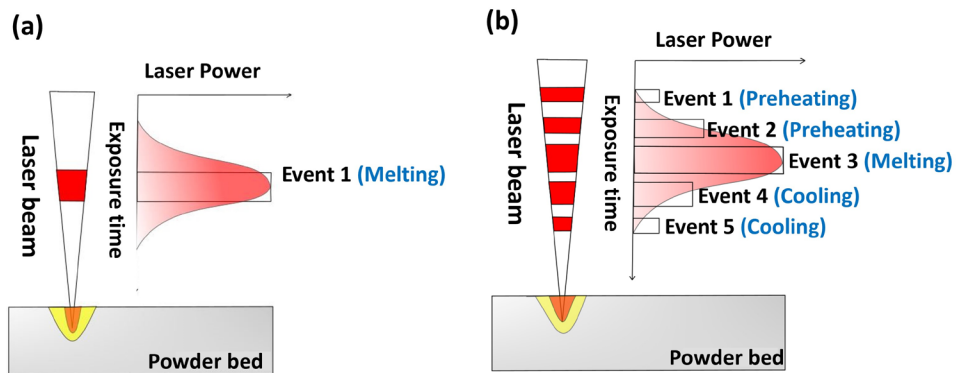


Figure 14. Schematics of the (a) standard laser pulse and, (b) laser pulse shaping adapted for the cermets fabrication (*adapted from publication I*).

Fig. 15 depicts the SEM microstructure of the cermet samples fabricated using a standard laser pulse and variation in laser melting peak power (60 and 72 watts). Cracks were evident in all the fabricated cermet parts as shown in Fig 15. Due to the high-temperature gradient caused by the adaptation of single laser scanning (Event 1), the melt pool may induce a high thermal residual stress in the parts during fabrication, failing the parts during printing. As built cermets parts have cracks, so they gradually weaken from the base, and the material deteriorates after a few layers of printing. As a result, to prevent such process defects (thermal cracks), it is quite important to control the temperature gradient of the melt pool to lower the thermal residual stress in the cermet parts during fabrication. The use of laser pulse shaping could be an optimal method of reducing these process defects by allowing the laser energy to be distributed temporally depending on the duration of exposure time and laser power, thereby reducing the melt pool's thermal gradient.

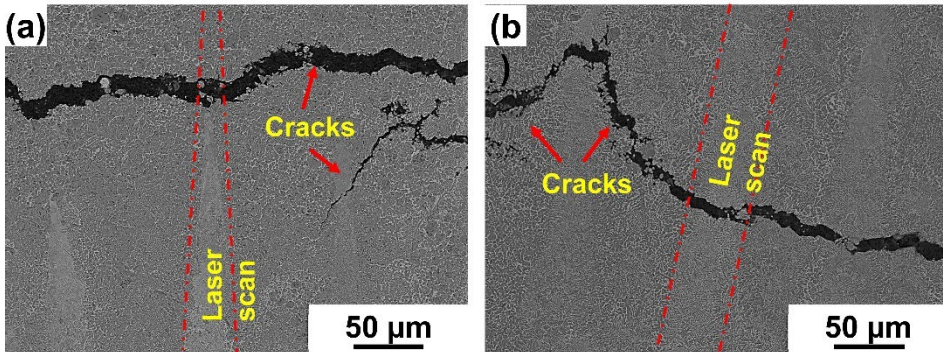


Figure 15. Scanning electron microscopy images of the TiC- 30vol.% Fe cermet parts fabricated via standard laser pulse with variation in laser melting peak power (a) SP-1 (60 Watt), (b) SP-2 (72 Watt). (Adapted from publication I)

### 3.1.2 Laser pulse shaping

Fabrication of the TiC-30 vol.% Fe cermet (CC1) via laser pulse shaping has been investigated in Publication I. Microstructural formation and mechanical properties were investigated under the influence of laser peak power variation during the laser pulse shaping. As part of the Laser pulse shaping process, five different laser events with varying laser peak power and exposure time have been adapted as shown in Fig. 14. Point scanning strategy has been adapted to expose the laser on the powder bed. The powder particles were melted and fused with the highest laser melting peak power (LMP) in Event 3. To study the effects of laser melting peak power on microstructural formation, only Event 3 laser peak power was varied. The other parameters of the event's process (Events 1,2,4,5) have been kept fixed.

Two distinct phases of TiC (fine dendritic and coarser) have been observed in all the microstructures of the as-built parts (Fig. 16). The dark phase corresponds to the TiC ceramic phase while the bright phase corresponds to the Pure Fe binder. Laser scan tracks are visible in both fabricated parts, which is a typical characteristic of SLM fabricated parts. The microstructural gradient could be related to Gaussian laser energy distribution (Z. Chen, 2018). This will affect the energy distribution on the powder bed and lead to a finer and coarser microstructure formation. Laser energy density is higher in the center of the laser scan than in the boundary region, resulting in a higher cooling rate in the center of the laser exposure, leading to the development of finer microstructures (Aramian, 2020b). In both cases (60 and 72W) similar gradient microstructure can be observed. However, samples with 60W laser power (CC1-1) have coarser microstructure as compared to 72-watt laser power (CC1-2) which could be attributed to the higher cooling rate of the melt pool and led to a fineness of the microstructure. In general, a higher cooling rate in the SLM process leads to a more finely-grained microstructure in the material.

The fineness of the microstructure of an SLM-processed part is determined by the solidification rate ( $R$ ), the thermal gradient ( $G$ ), and the cooling rate ( $T = G \times R$ ) (Casati, Hamidi Nasab, Coduri, Tirelli, & Vedani, 2018).  $G$  denotes the temperature gradient over a distance and is a function of time and place in the melt pool.  $R$  depends on the laser scanning speed and the angle between the laser scanning direction. The cooling rate ( $G \times R$ ) of a melt pool determines its microstructure fineness (Aramian, 2020c). Different Cermet compositions i.e. TiC with ferritic stainless steel binder (TiC-30 vol.% 430I FSS)

has also been fabricated adapting laser pulse shape techniques with variation in laser melting peak power (LMP with 38,48,60,72 and 84 Watt) (Maurya, 2021). Microstructure formation exhibited a similar trend as observed in CC1, with variations in laser melting peak power. Gradient microstructures have been observed with lower laser power and increasing the laser melting peak power led to finer microstructures and decreased gradient microstructures (coarse and fine TiC). An increase in cooling rate and change in melt pool width may be responsible for this variation in microstructural formation.

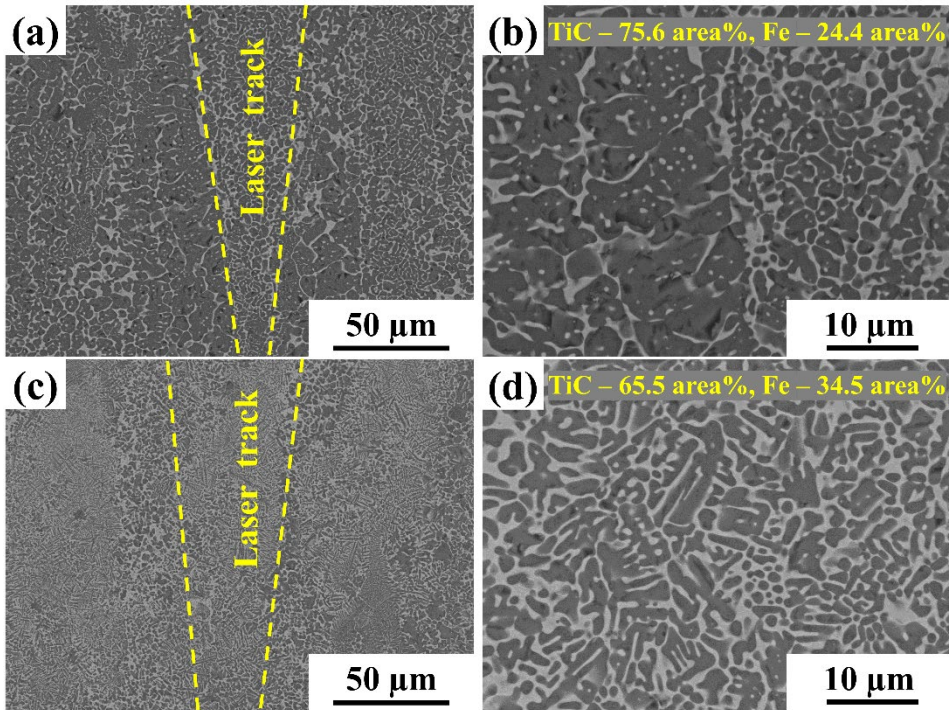


Figure 16. Scanning electron microscopy images of the TiC-30vol.% Fe cermets fabricated via laser pulse shaping with different laser melting peak power (a, b) CC1-1 (60 Watt), (c, d) CC1-2 (72 Watt) (Adapted from publication I).

To study the effect of pre-heating (Events 1 and 2) and cooling (Events 4 and 5) on the microstructural formation of the TiC-30 vol.% Fe cermet during laser pulse shaping, variation in process parameters of laser pulse shaping has been adapted and investigated in publication II. In this case, the laser peak power and exposure time of Event 3 have been kept constant while the process parameters of the other events (1,2,4, and 5) have been varied. Cermets sample with 72W Laser melting peak power (described in publication I) exhibits finer microstructures as compared to the sample with laser melting peak power (60 Watt). As a result, to study the effect of preheating and cooling through varying laser exposure times, sample PS1 (72-watt) has been considered as an optimal parameter to analyze the variation in microstructural formation. As can be seen in Fig. 17, changes in the exposure time of all the events in the laser pulse shaping led to variations in the microstructures and the defect formation such as porosity in the parts. Changing the exposure time led to a change in the scan speed and affected the overall

laser energy density of the exposed laser and the microstructural formation of the fabricated parts.

The laser energy density (LED) has been used to describe the energy density of each single laser pulse at each exposure time. In this study laser energy density (LED in  $J/mm^3$ ) affects the cermet forming and microstructure. The following formula can be used to calculate LED (Yu et al., 2021).

$$LED = \frac{P}{v \cdot h \cdot d} \dots\dots\dots (3)$$

where  $P$  (in watt) denotes the effective laser power,  $v$  (mm/s) represents the scan speed,  $h$  (mm) is the hatch distance, and  $d$  (mm) denotes the layer thickness of the powder bed.

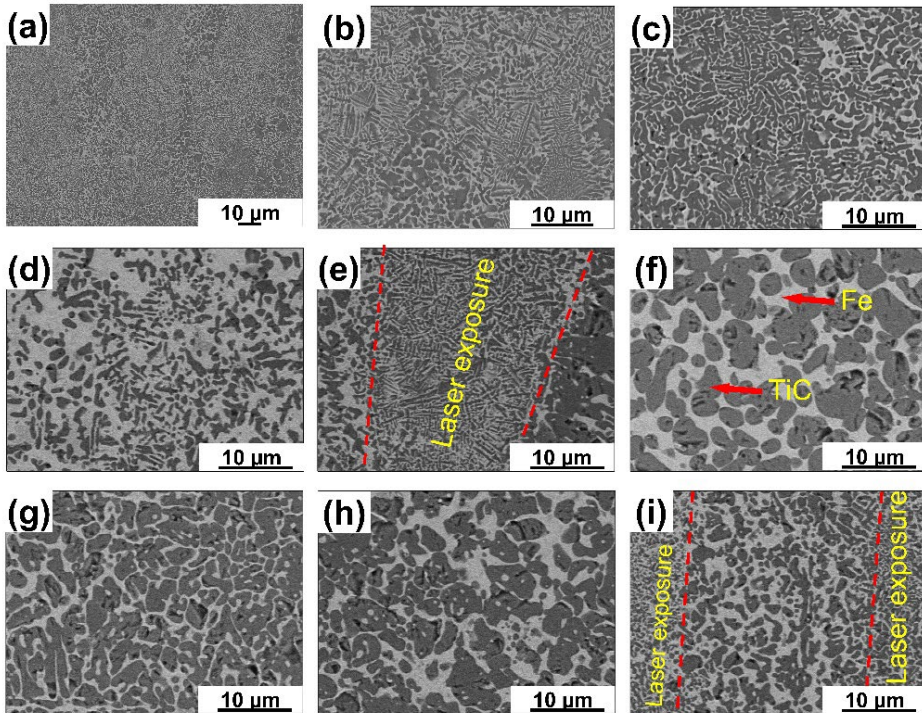


Figure 17. Scanning electron microscopy images of the TiC-30 vol.% Fe-based cermets fabricated with variation in laser process parameters (laser exposure time in  $\mu s$ ) via laser pulse shaping (Event 1-Event 2-Event 3-Event 4-Event 5) (a, b, c,) 100-200-200-500-200, (d) 100-250-200-250-200, (e) 100-250-200-50-200, (f) 100-200-200-250-200, (g) 100-200-200-0-0, (h) 100-250-200-500-200, (i) 100-50-200-500-200 (Adapted from publication II).

Pre-heating of the powder bed is imperative for the formation of such brittle materials during laser pulse shaping. The pre-heating pulse (Events 1 and 2) with low laser power and exposure time before the laser melting peak power, preheats the powder bed and prevents any sudden heat generation during the melting of the powder or high thermal gradients in the melt pool. Due to the controlled solidification/cooling of the melt pool, post-pulse laser peaks (Events 4 and 5) with lower laser power and wide exposure time, control the cooling of the powder bed and may lower the thermal residual stress during the fabrication of the parts resulting in lower process induced defects such as cracks (Kempen et al., 2014; Mertens et al., 2016; Park et al., 2021; Sadhu et al., 2020).

### 3.1.3 Multiple laser scanning

The development of the optimal laser process parameters to fabricate cermet parts with lower process defects and their effect on microstructural formation with multiple scan strategy techniques has been investigated in publication III. The SEM microstructure of the TiC-35 vol.% FSS cermet fabricated via Multiple laser scan technique has been depicted in Fig.18. Laser process parameter (i.e., scan speed and laser power) of both the preheating and melting scan plays a vital role in the microstructural formation (Bricin & Kriz, 2019; Karimi, Ma, Jia, & Prashanth, 2020; Uhlmann et al., 2015). High preheating scan speed with lower energy density and high melting scan speed with lower laser energy density seems to be optimal parameters to fabricate the parts with lower process defects (cracks and pores).

Modulating these laser process parameters (lowering the scan speed of both the preheating and melting scan) led to the increment of the laser energy density (according to eq. 3) and coarsened the microstructure (TiC phase) due to the lower cooling rate of the melt pool. Growth morphology and dispersion state of TiC phases are significantly affected by both the preheating and melting scan parameters. Typical SLM characteristic microstructure (coarser and finer TiC phase) can be observed in the fabricated parts with high laser scan speed (both preheating and melting scan) (Aramian, 2020b; Marchese et al., 2017; Sahoo, 2017).

At lower scan speeds (preheating and melting), less gradient in the microstructure can be observed due to a lower cooling rate and an adapted rotation scan strategy. Moreover, the scanning of the subsequent layer also leads to heat transfer to the previously solidified layer and causes the coarsening of the microstructure (Guan, Jiang, Zhang, & Chong, 2020; Karimi, Suryanarayana, Okulov, & Prashanth, 2020). As-built samples were found to be defect/crack-free after adapting multiple scanning techniques, thus supporting the idea that multiple scanning techniques can reduce thermal residual stress and facilitate the fabrication of cermets without cracks. However, fabricated cermets parts with multiple laser scanning exhibit porosity in the parts and samples with high preheating and melting scan speeds, maximum relative density was achieved (97.8%), while for samples with medium and low preheating and melting scan speeds, achieved relative density was 95.5% and 95.1% respectively.

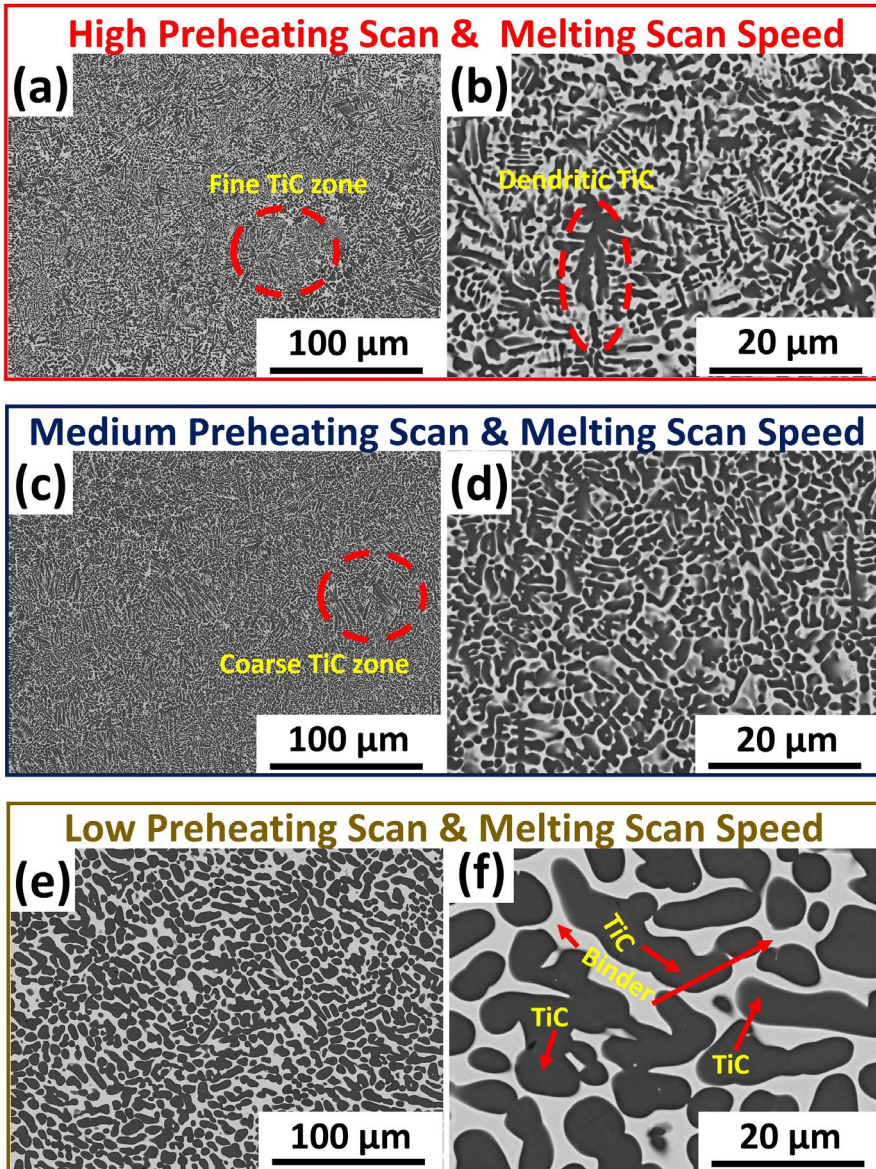


Figure 18. Scanning electron microscopy images of the TiC-35 vol.% 430L FSS-based cermet exhibiting variation in the microstructure with varying pre-heating (PHS) and melting scan (MS) energy densities. (a, b) CC2-1 (High PHS-MS), (c, d) CC2-2 (Medium PHS-MS), and (e, f) CC2-3 (Low PHS-MS) (**Adapted from publication III**).

### 3.2 Effect of adapted laser scan techniques on the microstructural formation

Microstructural formation of the TiC-Fe-based cermets with different laser scan techniques has been depicted in Fig. 19. In both the laser scan techniques, similar microstructural characteristics (coarser and finer dendritic TiC phase) have been observed. As explained before, this could be attributed to Gaussian laser energy distribution, high cooling rate, and the scan strategies adopted. In the case of the laser pulse shaping, laser scan zones are visible in the cross-section view of the fabricated parts due to the point scan strategy adopted without any rotation of the laser scanning (Fig. 19 (a, b)). In the case of Multiple laser scanning, there are no laser tracks visible in the SEM micrograph, which could be the result of the scanning rotation (60°) adapted after each layer of scanning, which could transfer heat energy to previously solidified layers, dissipating the laser scan area, and affecting the microstructure formation. Moreover, the MLS fabricated parts as compared to LPS exhibit finer microstructure and lower gradients in the coarse and fine zone that could be attributed to the introduction of the FeCr binder and scanning the powder twice with variations in laser energy density.

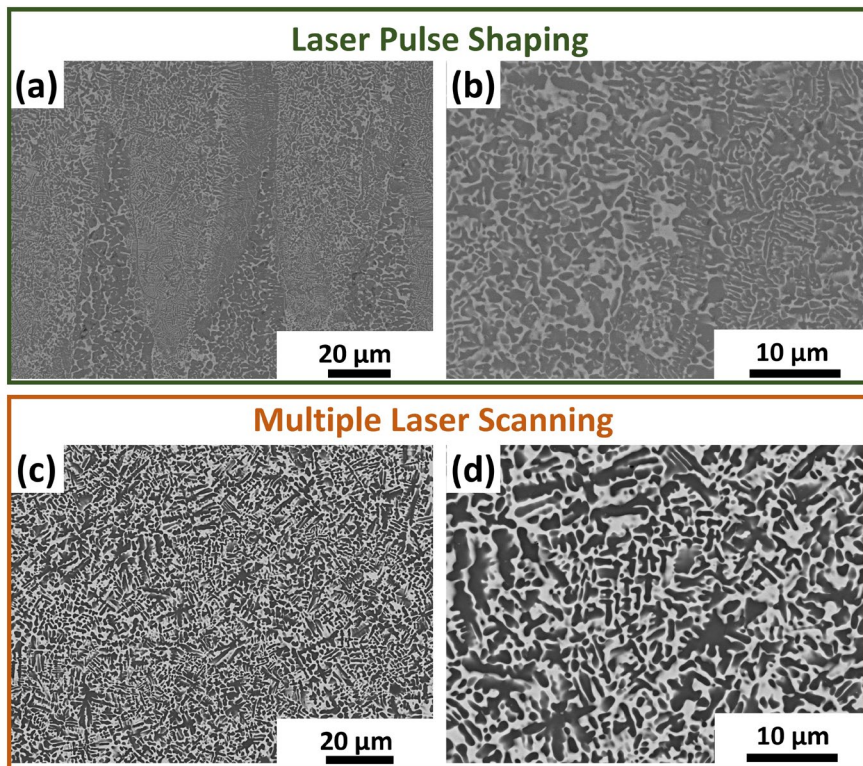


Figure 19. Microstructural formation of the TiC-Fe based cermets with different laser scanning techniques adapted (a, b) TiC-30 vol.% Fe by Laser pulse shaping (LPS), (b, c) TiC-35 vol.% 430L FSS by Multiple laser scanning (MLS) (Adapted from the publication I & II).

### 3.3 Effect of laser process parameters on the phase formation

The X-ray diffraction patterns of the SLM-built TiC-30 vol.% Fe based adapting laser pulse shaping technique with variation in laser peak power have been depicted in Fig. 20. According to the obtained XRD patterns, the SLM-processed cermetes exhibit prominent peaks corresponding to Titanium carbide (TiC) (simple cubic system with the space group Fm-3m (225) (line NaCl)), and  $\alpha$ -Fe (body-centered cubic system (bcc) with a space group Im-3m (229)). An XRD analysis in both cases (60- and 70-Watt laser peak power) shows some very low-intensity peaks or noise that may indicate the formation of some intermetallic carbide phases. However, due to their low volumetric percentage, they were not detected in the diffraction pattern of the as-built parts. Changing the laser melting peak power led to a change in the laser energy density and led to texture formation which can be attributed to the significant variation in XRD peak intensity. This is quite natural in the SLM process that the change in the energy density may change the preferential growth direction leading to texture in these cermetes.

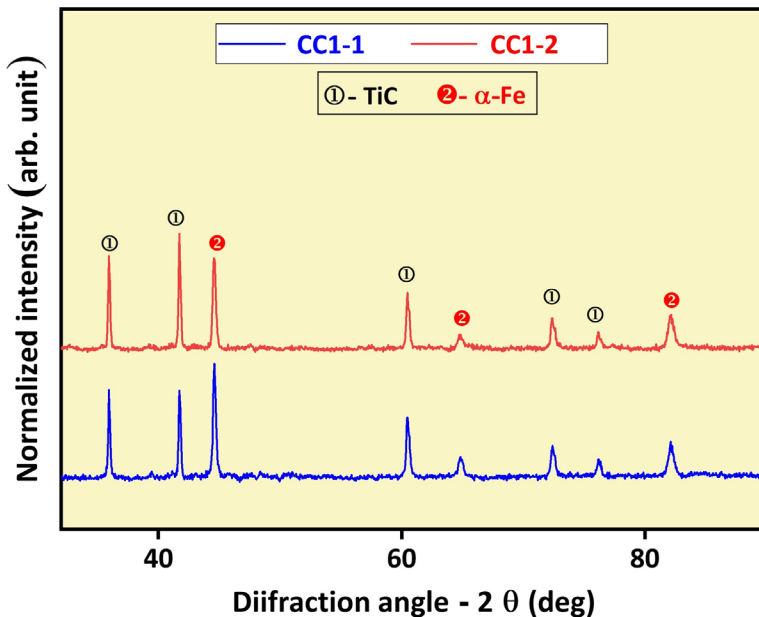


Figure 20. X-ray diffraction pattern of the TiC-30 vol.% Fe-based cermetes fabricated via laser pulse shaping with variation in laser melting peak power. (a) CC1-1 (60 Watt), (b) CC1-2 (72 Watt).

Fig. 21 exhibits the X-ray diffraction pattern of the TiC-35 vol.% 430L FSS cermet parts fabricated via multiple laser scanning techniques. Similar to LPS fabricated parts, XRD analysis of the MLS fabricated parts shows some lower intensity peaks or noise, which suggests that due to the higher affinity of Cr for carbide formation, there may be a lower volumetric percentage of additional carbide phases (such as iron carbide, chromium carbide, or complex metal carbides) (Kolnes et al., 2018). Moreover, some minor changes both in peak intensity and broadening of both phases (TiC and 430 L) can be observed. Variations in these peak intensities can be attributed to texture formation (preferred growth/orientation) in these samples as a function of preheating and melting energy densities. In the SLM process, changing the energy density may lead to changes in the

preferential growth direction resulting in a different texture. Changes in defect concentrations may lead to the broadening of the peaks (such as dislocations) and/or internal strain.

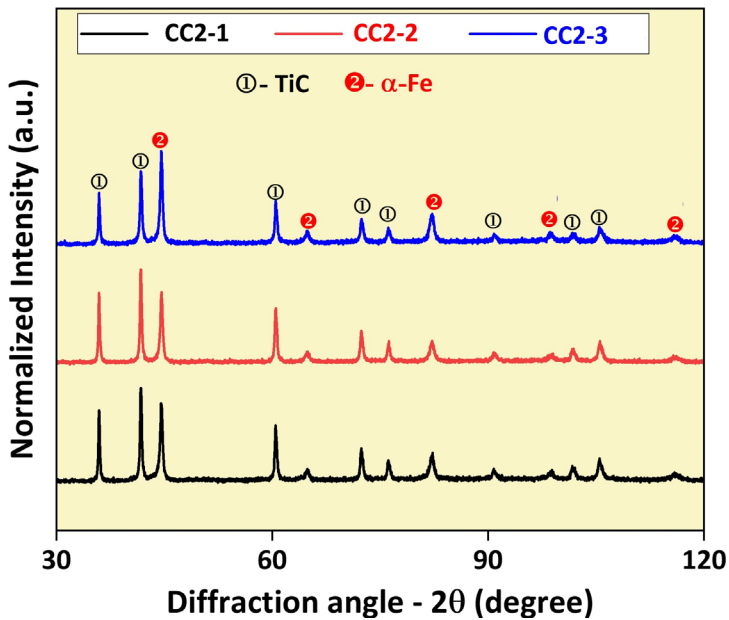


Figure 21. X-ray diffraction pattern of the TiC-35 vol.% 430L FSS-based cermets fabricated via Multiple laser scanning with variation in laser process parameters. (a) CC2-1 (High PHS-MS), (b) CC2-2 (Medium PHS-MS), and (c) CC2-3 (Low PHS-MS).

The elemental mapping distribution of the TiC-based cermets fabricated via multiple laser scanning has been depicted in Fig. 22. The elemental mapping revealed that Cr and Fe were evenly distributed in the binder phase. It is possible that no or only low volumes of intermetallic carbides are formed during the SLM process, which corroborates with the XRD data. However, processing such cermets via non-conventional techniques such as pressure less sintering could lead to the formation of intermetallic carbides. Kolnes et al. investigated the fabrication of TiC-30 wt.% FeCr based cermets via pressure less sintering (Kolnes et al., 2018). It was reported that the formation of complex intermetallic carbides ( $M_7C_3$ ,  $M_{23}C_6$ ,  $M_3C$ ,  $M_6C$ ) has been observed during the conventional sintering process. It can be attributed to the segregation of Cr from the binder during the processing due to the slow heating rate which allows for diffusion, resulting in the formation of metal carbides during the process. As a result of the formation of intermetallic complex carbides, the mechanical properties (toughness and strength) and corrosion resistance of the cermets were affected. The SLM process has the advantage of a high solidification/cooling rate, that may prevent the formation or lowering the unwanted formation of Fe-Cr- intermetallic carbide phases.

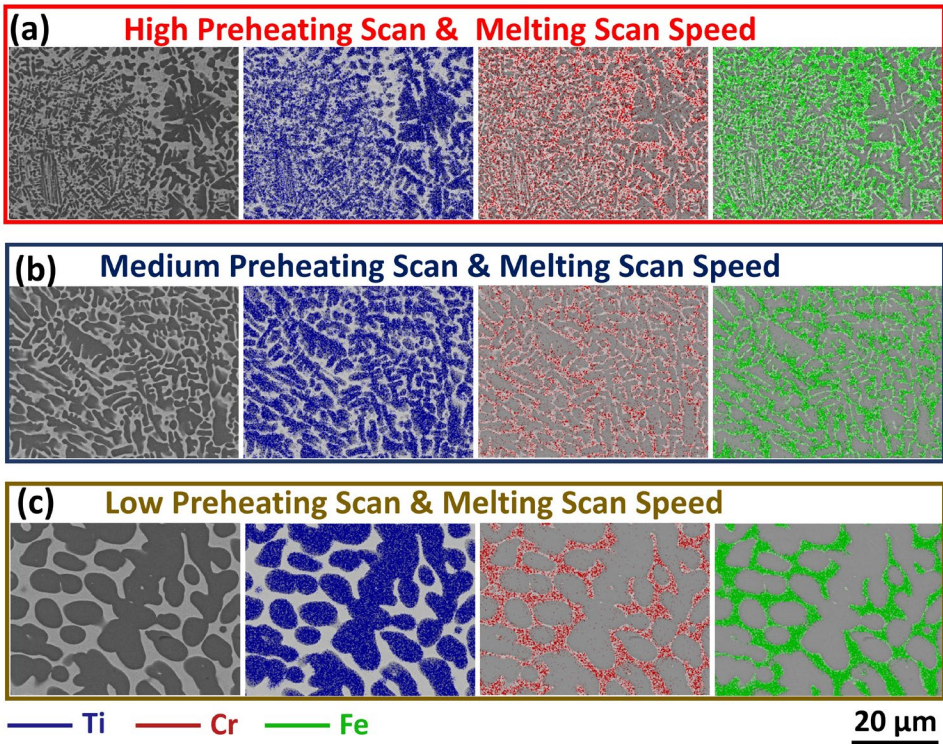


Figure 22. X-ray energy dispersive spectrum mapping of the TiC-35 vol.% 430L FSS based cermets via Multiple laser scanning techniques with variation in laser process parameters. (a) CC2-1 (High PHS-MS), (b) CC2-2 (Medium PHS-MS), and (c) CC2-3 (Low PHS-MS) (**Adapted from publication III**).

### 3.4 Process induced defects

Even though the SLM process can produce complex parts with a high material utilization rate, it is influenced by a variety of factors. SLM consists of complicated physics, such as absorbing and transmitting laser energy, melting and solidifying materials rapidly, evolving microstructures, and material evaporation from molten pools. Consequently, the process is affected by these factors to form defects such as porosities, incomplete fusion holes, cracks, and impurities as shown in Fig. 23. The mechanical and physical properties of fabricated parts are adversely affected by these defects, which restricts the application of SLM.

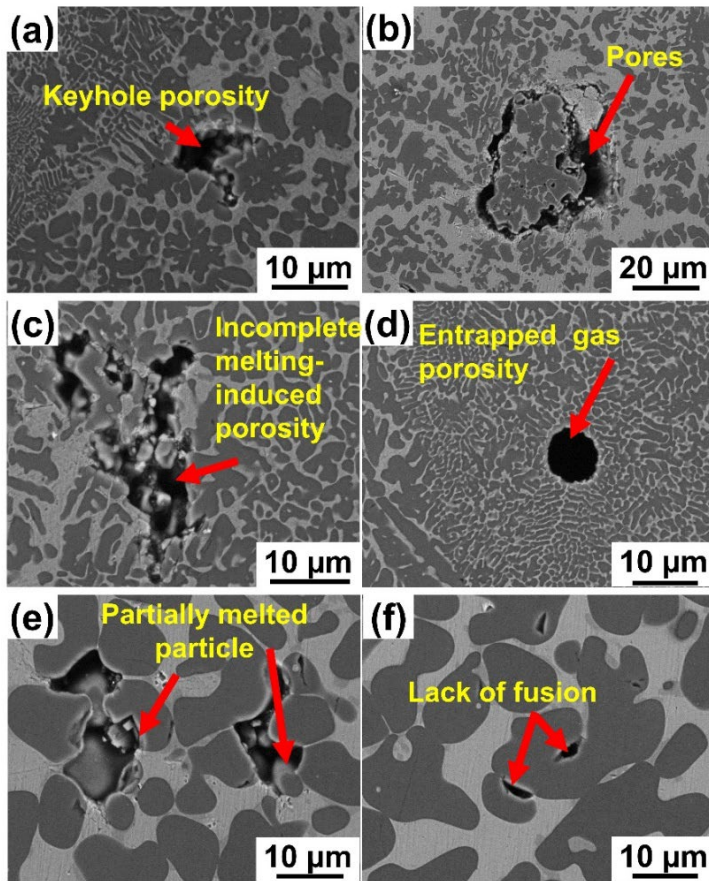


Figure 23. Characteristic process defects observed in the fabricated cermet parts (TiC-35 vol.% 430L FSS) as a function of varying process parameters. (a) Keyhole porosity, (b, c) Spattering effect, (d) Entrapped gas porosity, (e f) Low energy density (**Adapted from publication III**).

### 3.4.1 Keyhole effect

A keyhole feature may form in a melt pool as some elements evaporate during the fabrication process (Fig. 23 (a)). Process parameters such as laser energy density, temperature distribution in the melt pool, and cooling rate can affect keyhole depth, shape, and size (B. Liu, Fang, Lei, & Yan, 2022).

### 3.4.2 Spattering effect

In high laser energy density exposure, heat transfer can be inadequate between melt pool boundaries, causing overheating and evaporation of the material particles. As a result of vaporization, droplets or powder particles can be spattered (Fig. 23 (b)). When droplets are spattered from a molten pool, their volume decreases, which causes the formation of voids/pores after solidification (Aramian, 2020b). During the recoating of the next powder layer, these voids /pores are filled with powder particles, increasing the local layer thickness. This layer may not reach the previously solidified melt pool during the subsequent laser scanning, as the melt pool will be deeper in these zones. This deep melt pool can cause voids and the presence of partially melted or unmelted particles in the material after consolidation.

### 3.4.3 Entrapped gas

The formation of entrapped gas process defects could be caused by non-uniform feedstock power distribution, poor powder rheology (non-uniform morphology), or a wide particle size distribution (Fig. 23 (d)). Powder recoating causes trapped gases to be trapped between the powder particles, and the trapped gases can dissolve in the melting pool, but after solidification, they may remain as part of the solid because of the high cooling rate (Aramian, 2020b).

### 3.4.4 Low energy density

Typical defects of the SLM process are linear defects caused by a lack of melting. A lack of energy input during fabrication leads to these process defects (Fig. 23 (c, e, f)). As a result of low laser power, powder particles are not melted fully, resulting in gaps/pores forming during the melting of subsequent layers. During solidification, inadequate melt powder particles may cause poor bonding or unmelted metal powder may cause defects during fusion (Vilaro, 2011).

## 3.5 Mechanical properties

The mechanical properties of the SLM/LPBF fabricated parts via different laser processing techniques are a function of the laser process parameters. A change in the parameters of the laser process altered the laser energy density and affected the formation of the microstructure. The mechanical properties of both the cermets composition have been investigated in publications I and III.

### 3.5.1 Hardness

The microhardness graph of the SLM processed cermet compositions 1 and 2 via LPS and MLS respectively has been depicted in Fig. 24. It can be observed that there are wide deviations in hardness values in both cases (LPS and MLS). This may be related to the gradient microstructure (finer and coarser) of the TiC phase resulting from the complex thermal history of laser processing. Additionally, this wide variation can also be attributed to the area where the indenter is placed (Enneti & Prough, 2019b; Son, 2021). There is a wide range of microhardness values between the ceramic phase and the binder phase ( $TiC > 2000HV$  and  $Fe < 200HV$ ). As a result, if the indenter is placed in the TiC-rich phase, then the hardness value will be higher than in areas with Fe-based binder. According to this study, microhardness values are in agreement with those reported previously. Moreover, It was found that the microhardness value of cermets varied considerably depending on the fabrication method adopted, the type and amount of the binder phase, and the degree of defects present in the fabricated parts. Other researchers have reported hardness values ranging from 1300 to 1900 HV for TiC-based cermets using different metal binders and processing methods (Aramian, 2020b; Gaier et al., 2019; Heydari et al., 2021; Kolnes et al., 2018; Sahoo, 2017; Y. Xiong, 2010).

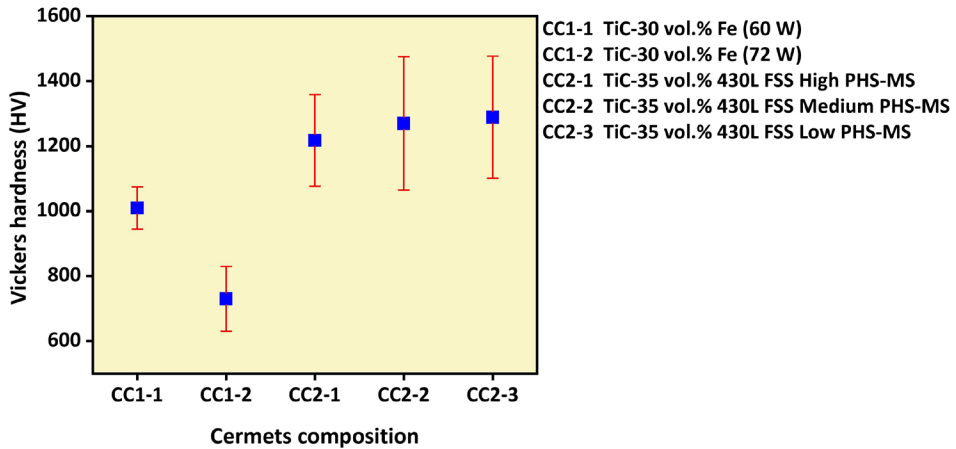


Figure 24. Hardness graph of the Cermet composition 1 and 2 fabricated via laser pulse shaping and multiple laser scanning techniques.

To study the variation in the microhardness value of the fabricated cermets parts, microhardness contour maps have been plotted and investigated in publication III. Fig. 25 illustrates the microhardness contour mapping along the longitudinal axis of the cermets fabricated via MLS. Comparatively to the binder phase, the TiC phase occupies a substantially larger volumetric percentage of some areas and vice versa. There is a possible explanation for the inhomogeneous distribution of binders and ceramic phases through variations in observed microhardness values (Son, 2021). As a result, microhardness fluctuation will differ if the indenter is placed on a ceramic (TiC), binder phase (Fe or FeCr), or an intermediate zone.

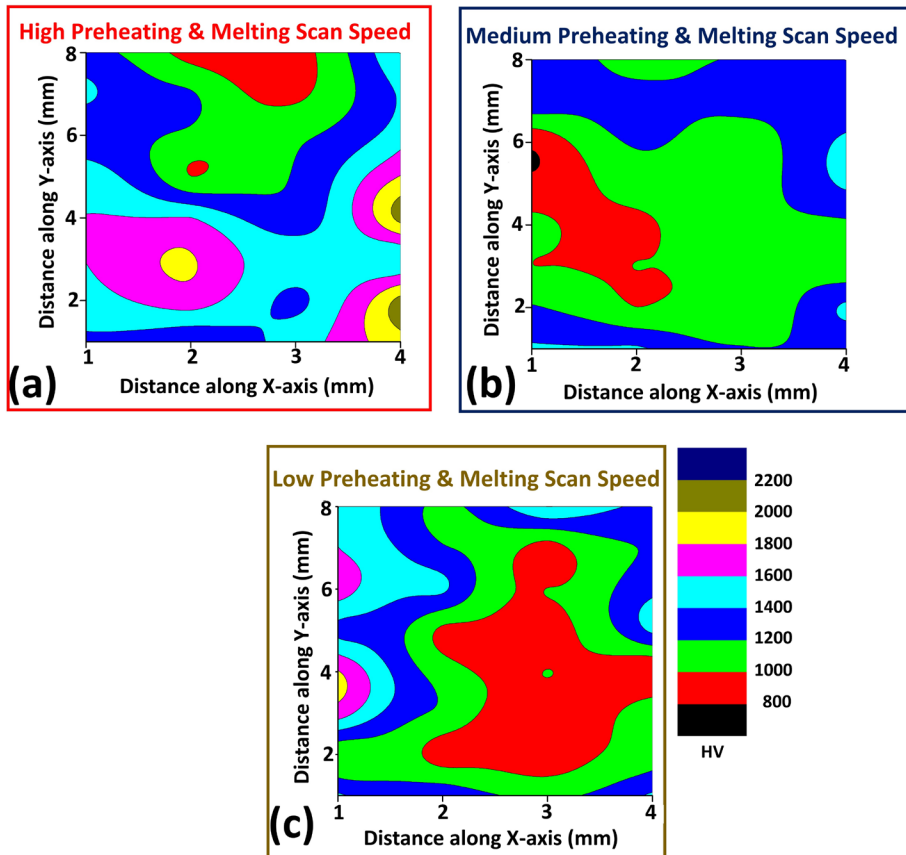


Figure 25. Microhardness contour mapping of the SLM processed cermet composition 2 (TiC-35 vol.% 430L FSS) fabricated via multiple laser scanning techniques. (a) CC2-1 (High PHS-MS), (b) CC2-2 (Medium PHS-MS), and (c) CC2-3 (Low PHS-MS) (Adapted from publication III).

As can be seen from Fig. 25, higher microhardness values in the edges of the samples can be observed as compared to the core region. Laser scan strategy and gradient of melt pool temperature could be responsible for such variation. At the beginning of laser exposure, the starting corner has a lower temperature, while the corner at the end of laser exposure has a higher temperature, as laser melting ends there, and this will be the last point to solidify. As a result, defects are observed along the corners, where there is melting pool instability.

### 3.5.2 Fracture toughness

A study on the fracture toughness of the SLM-processed cermet compositions 1 and 2 fabricated via LPS and MLS respectively has been reported in publications I and III. The fracture toughness value of both compositions has been depicted in Fig. 26. Cermet composition 2 exhibited a higher fracture toughness value as compared to cermet composition 1, owing to the presence of a FeCr-based binder that may refine the particle, improved wettability, and consequently improved fracture toughness.

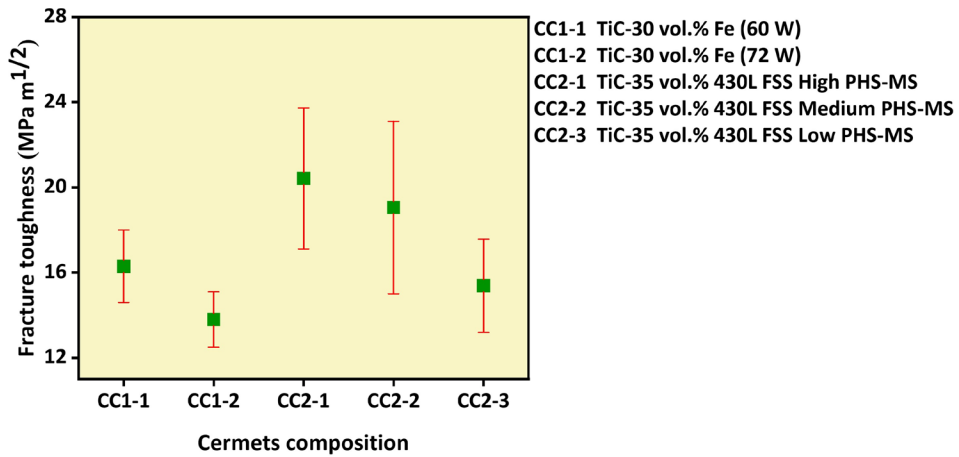


Figure 26. Fracture toughness micrograph of the cermet composition 1 and 2 via laser pulse shaping and multiple laser scanning techniques.

By analyzing the crack propagation behavior when the load is applied via the indenter, the toughness mechanisms in TiC-Fe-based cermets were investigated. A number of mechanisms were considered for toughening the TiC-Fe-based cermets, including grain bridging, grain fracture, crack deflection, and crack branching, which are commonly seen in brittle materials (Fig. 27). The fracture toughness of the SLM-processed as-built cermet is affected by the transgranular and intergranular fractures observed in its surface. Grains, particle distributions, TiC phase sizes, and variations in thermal expansion coefficients play an important role in toughness (Sergejev, Preis, Kübarsepp, & Antonov, 2008). Depending on the distribution and shape of the hard phases, crack propagation paths can be affected (Aramian, 2020a; Neumeister et al., 2013; Rodriguez-Suarez et al., 2009; Ullah et al., 2021).

Cermet parts with finer microstructures require more energy to propagate cracks, and crack deviation is more prone to these microstructures. With coarser TiC, crack initiation of the cracks consumes more energy, however, this is accompanied by easier crack propagation and less chance of crack deviation. A mismatch Thermal expansion coefficient between the TiC and binder phase results in residual compressive and tensile tensions within the matrix, resulting in microcracks and contributing to crack branching. As a result, more fracture energy was dissipated and crack extension was halted, resulting in improved toughness. This cermet was perceived to have greatly improved damage tolerance due to the gradient in TiC phases in its microstructure. Several defects, including porosity, can also reduce fracture toughness, as evidenced by samples with higher porosity.

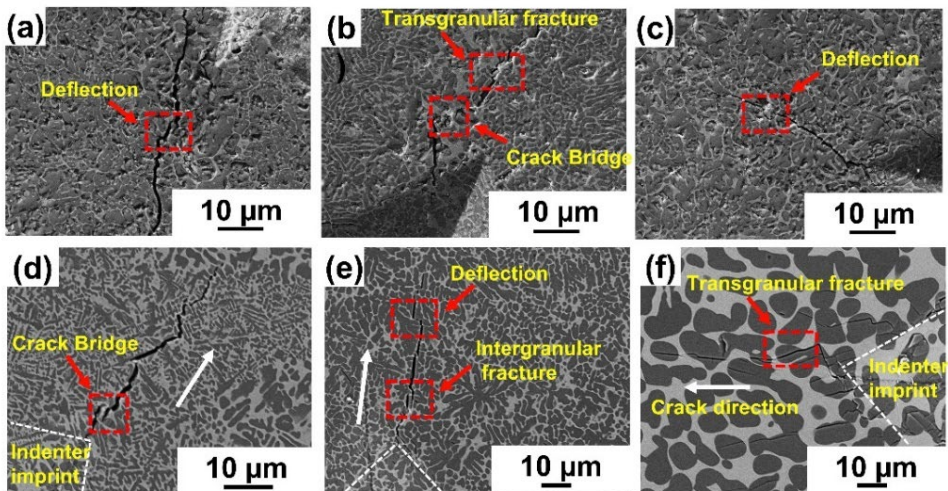


Figure 27. Crack propagation path observed in the SLM processed TiC-Fe based cermets fabricated via different laser scanning techniques (a, b, c) TiC-30 vol% Fe by Laser pulse shaping and (d, e, f) TiC-35 vol.% 430L FSS by Multiple laser scanning.

### 3.6 Tribological properties

The wear behavior of the additively manufactured Cermet composition 2 has been investigated in publication IV via scratch testing. Single- and multiple-pass scratch tests as a function of load have been conducted using a Rockwell indenter to study binder and matrix phase wear mechanisms. The SEM micrograph of the scratched area after the single pass of the indenter has been depicted in Fig. 28. It has been observed that at lower loads (10N), the TiC phases have remained intact or have suffered only minor fractures. Increasing the applied load, however, resulted in the smear out of the soft binder material and the fracture of the coarse TiC particles. Despite all applied loads (10, 30, and 50N), no fracture was observed in the finer TiC phase, indicating that its wear resistance is higher than that of the coarser TiC phase.

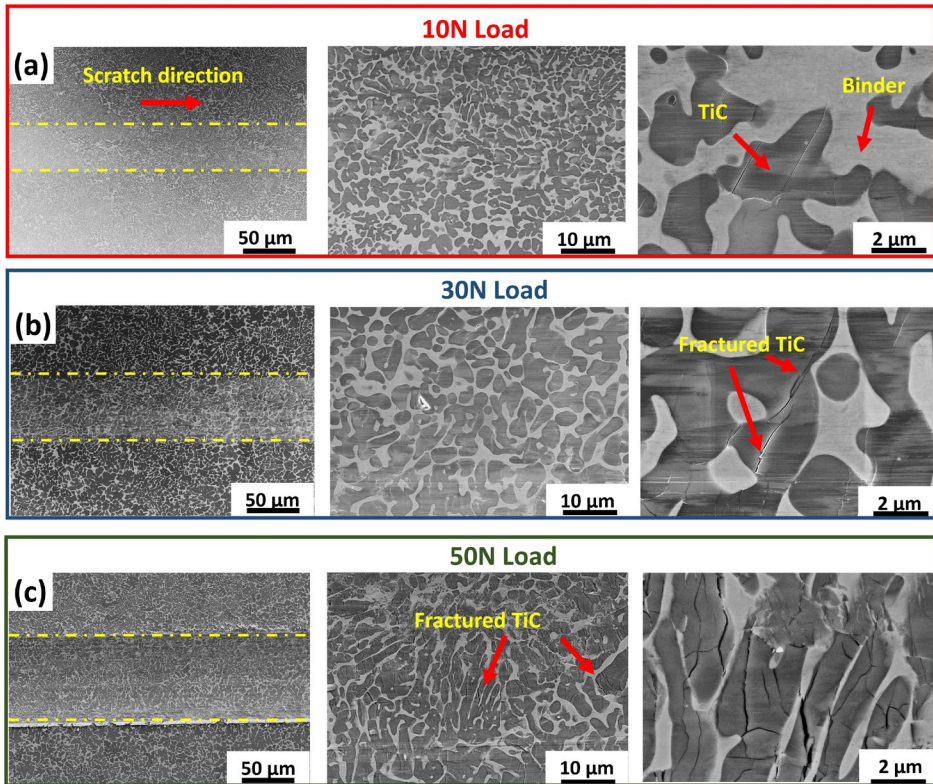


Figure 28. Scanning electron microscopy images of the scratched surface of the TiC-35 vol.% 430L FSS-based cermets (CC2-1) after a single pass of the indenter as a function of loads (a) 10N, (b) 30N, (c) 50N.

Fig. 29 exhibits the SEM micrograph of the scratched cermet parts after the multiple passes (5 times) with variation in applied loads. There is no significant variation in the scratched zone under lower load (10N) and it behaves similarly to a single-pass scratched test. However, scratched tracks undergo a complete microstructural change with an increase in load during multiple passes. The TiC and binder phases are not visible in the scratched region at higher loads (30N and 50N). Bypassing the indenter multiple times, the TiC phase was severely fragmented, smearing out the binder material and causing mechanical mixing between the two phases, causing the formation of the tribolayer. It appears that under higher loads, the dominant mechanism for severe wear is localized coarse TiC particle fragmentation accompanied by plastic deformation of the binder phase.

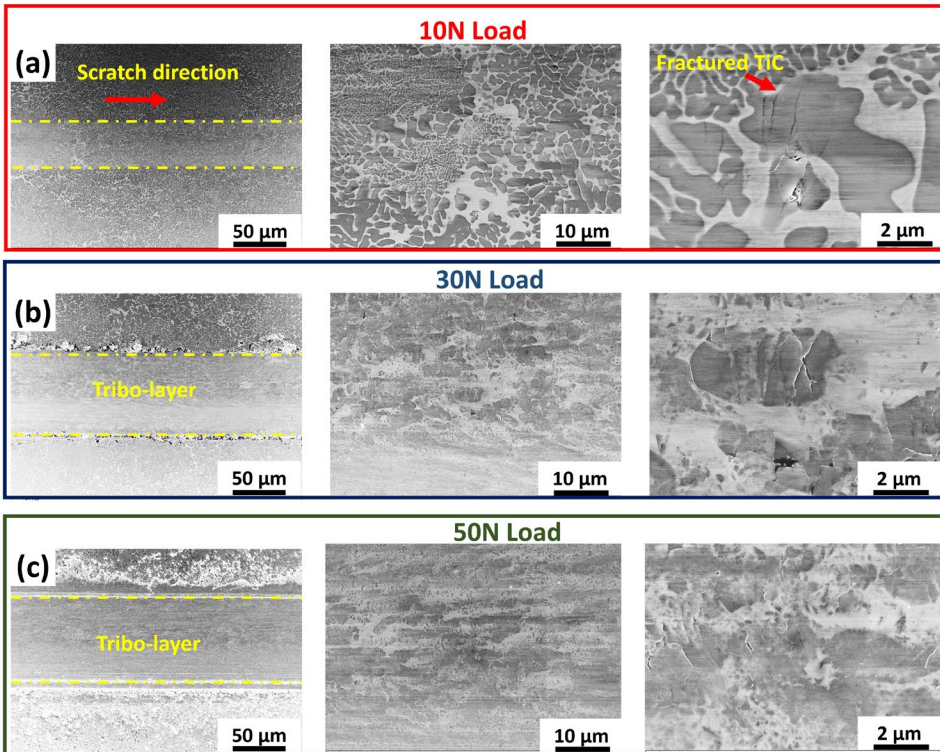


Figure 29. Scanning electron microscopy images of the scratched surface of TiC-35 vol.% 430L FSS-based cermets (CC2-1) after the multiple passes of the indenter as a function of loads (a) 10N, (b) 30N, (c) 50N.

Fig. 30 depicts the 3D optical surface profile of the scratch track with single and multiple passes as a function of load. As described earlier, lower wear has been observed at 10N load with single and multiple passes. Increasing the load with the single and multiple passes results in more smearing and pile-up of the plow material.

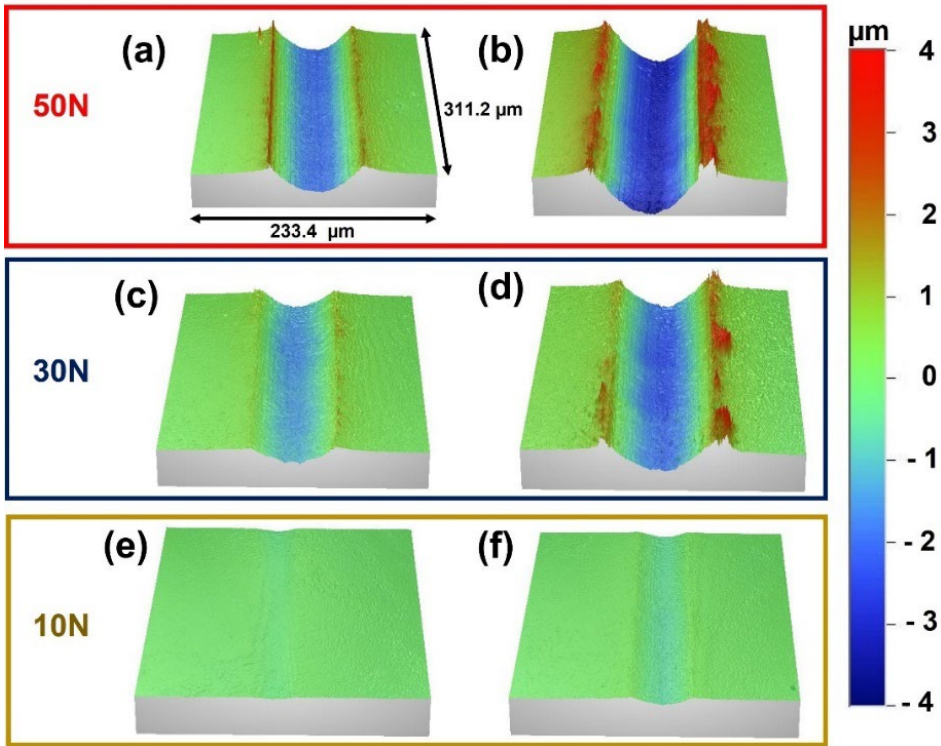


Figure 30. 3D optical surface profilometry images of the scratch track observed on the TiC-35 vol.% 430L FSS based cermets (CC2-1) as a function of loads (a, c, e) Single pass, (b, d, f) Multiple passes of the indenter (**Adapted from publication IV**).

Fig. 31. exhibits the Coefficient of Friction plot of the cermet's as a function of load and indenter passes. In the case of the smaller load, there is only a slight variation in the COF value, which can be supported by the SEM micrograph. It could be due to the fact that the COF is resistant to forming wear debris or the fact that it has stronger microstructural stability at 10N loads. The COF fluctuates strongly under conditions of single-pass or multiple-pass operations when the load is higher (30 and 50 N). As the stylus tip slides over the cermet surface, wear debris will accumulate in the crevices of its tip and act as a third body abrasive wear of the cermet's materials and lead to the fluctuation of the CoF value.

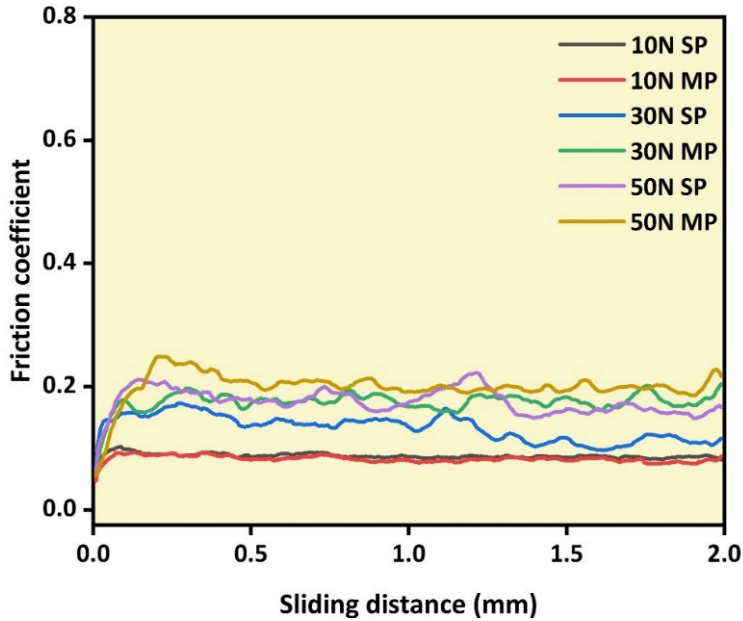


Figure 31. Coefficient of friction plot of the TiC-35 vol.% 430L FSS based cermets (CC2-1) under single pass and multiple pass conditions as a function of loads (Adapted from publication IV).

### 3.7 TiC -Fe-based cermets via Conventional sintering route

Various conventional powder metallurgy techniques such as Conventional Pressureless Sintering, Spark Plasma Sintering, Hot Isostatic Pressing, etc. have been extensively adapted by industries and researchers over the decades to fabricate cermets parts with different factors (for example temperature, pressure) impacting grain size and hence the material properties. In recent years, the ability to rapidly manufacture (3D print) cermets and hard metals is becoming a more attractive means of producing complex parts in one step. The literature related to the fabrication of cermets using AM techniques is limited; most of it relates to the production of conventional hard metals. The purpose of this chapter is to compare the characteristics of TiC-based cermets manufactured via conventional routes (CPS and SPS) and Additive manufacturing processes (SLM). There are advantages and disadvantages to each processing route on the fabricated cermet parts, which will be addressed in this section using the same cermet material (TiC-430L FSS).

Mart et al. investigated the fabrication of the TiC-based cermets with AISI 430L FSS as a binder material (TiC-30 wt.% 430L FSS) via a conventional sintering route. For the fabrication of the cermet parts, Liquid phase sintering has been adapted at different sintering temperatures to produce a dense cermet part (Kolnes et al., 2018). Maurya et al. also recently investigated the fabrication of the TiC-based cermets with steel as a binder material (TiC-35 vol.% 430L FSS) adapting Spark plasma sintering conventional route to compare the fabricated cermets parts with the Additive manufactured cermets part (Maurya et al., 2023). The following section discusses the influence of fabrication routes on the microstructural and mechanical properties of fabricated TiC-based cermets parts, as well as the advantages and disadvantages of each process.

### 3.7.1 Microstructural formation

Fig. 32 exhibits the SEM micrographs of the TiC-based cermets with AISI 430L FSS as a binder material via different processing routes obtained from the literature and the current thesis work. Across all processing routes, different microstructural formations (both in length scale, size, and distribution) can be observed, which may be related to solidification and cooling rates, feedstock powder morphology, and the adapted process parameters (temperature, heating rate, dwell time, etc) In all three cases (CPS, SPS, and SLM), the bright phase in the microstructure corresponds to the binder phase rich in Fe-Cr and the darker phase represents the TiC phase. An investigation was performed by Mart et al. on the fabrication of TiC-based cermets with 430L FSS as a binder at two different sintering temperatures. Fig. 32 (a) shows the powder feedstock used for fabricating the cermet parts after being milled for 72 hours in order to achieve homogeneity and reduce particle size. Cermet parts fabricated through LPS at higher sintering temperatures (1500 °C) exhibit a microstructure exhibiting nearly complete densification (Fig. 32 (c)). A globular shape TiC microstructure can be observed at such sintering temperatures, with a core-rim structure typical of such cermets (Zhou et al., 2023). The core and core rim structure comprise of TiC phase due to the dissolution-precipitation mechanism and the  $M_7C_3$  carbides bonded with the metallic binder phase (Fig. 32 (f)). Further, increasing the sintering temperature (1300–1500 °C) has been reported to produce a homogeneous microstructure due to the reduction of the wetting angle between carbide grains and binder.

As a result of SPS fabrication, inhomogeneous distributions of TiC particles are observed with wide variations in TiC particle shapes (elliptical and polygonal shapes). (Fig. 32 (d, g)). During the SPS process, particles are not completely melted, but rather diffused across particle boundaries, preserving their shapes. Furthermore, pressure deforms the particles, resulting in deformed powder particles (Namini, 2019; Tokita, 2021). The inhomogeneous distribution of the TiC particle could be related to wide feedstock particle size distribution (Fig. 32 (b)) and the slower cooling rate as compared to LPS fabricated parts (Tang, 2021; Xiong, 2009). It has been found that SPS fabricated cermets parts have a lower relative density (95%) due to the wide particle size distribution of the feedstock powder that can interfere with densification (Diouf & Molinari, 2012). The slow cooling rate has also been found to affect flowability/dynamic viscosity, causing pores in the fabricated parts (K. Xiong, 2022).

SLM fabricated cermets parts, however, exhibit distinct microstructures, which could be caused by laser energy distribution, High solidification/cooling rates of the process, feedstock powder morphology, and adapted laser process parameters and laser scan techniques that have been previously discussed in section 3.1.3. A general conclusion can be drawn that the cooling rate of the process changed the microstructural formation of the cermets. Compared to another conventional sintering route, SLM fabricated cermets parts have a finer microstructure.

Another significant aspect that needs to be addressed is the fact that in both the CPS and SPS fabricated parts, intermetallic carbides were formed and chromium was unevenly distributed, which could affect the mechanical properties (toughness and strength) of cermet parts (Kolnes et al., 2018).

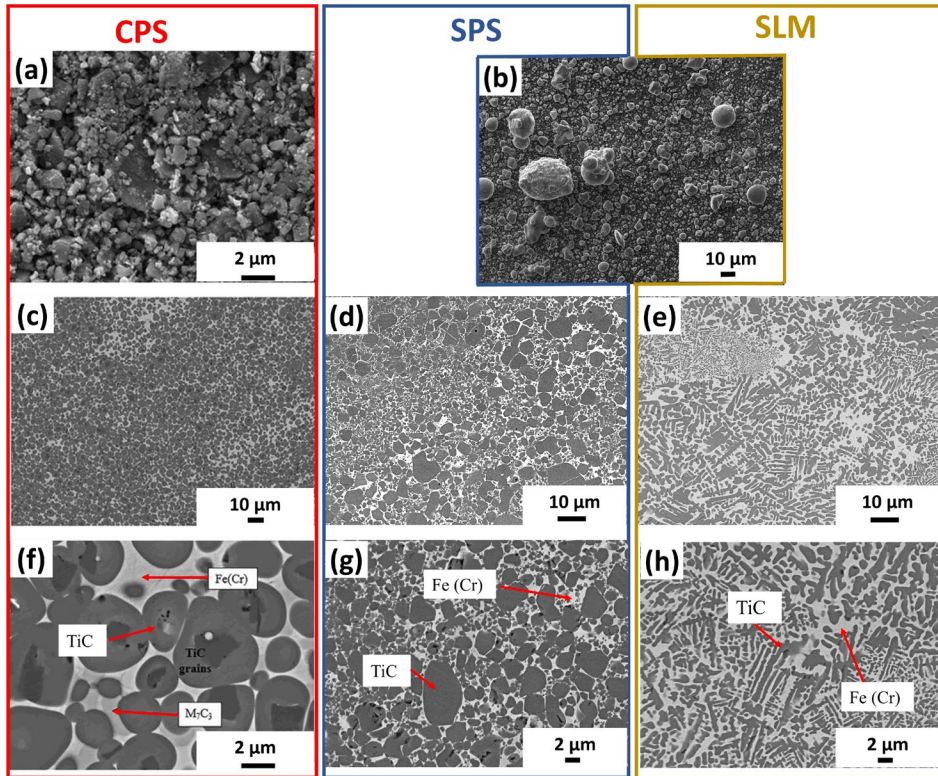


Figure 32. Scanning electron microscopy images of the TiC-based cermets fabricated by different processing routes. (a) TiC-22 vol.% 430L FSS by CPS (Kolnes et al., 2018), (b) TiC-35 vol.% 430L FSS by SPS (Maurya et al., 2023), (c) TiC-35 vol.% 430L FSS by SLM (Maurya, 2022).

Fig. 33. exhibits the elemental mapping of the TiC-430L FSS cermets parts fabricated via CPS, SPS, and SLM. It was reported that both the CPS and SPS cermets parts exhibit an uneven chromium distribution and the formation of the intermetallic carbides (Fe-Cr complex carbides) (Fig. 33 (a, b, d, e,)). Due to the slow heating rate of the fabrication process, Cr separates from the binder, allowing diffusion to occur during the process, resulting in the formation of metal carbides. In these Cr-rich zone regions, the Cr was partially substituted by the Cr-based carbides, resulting in the reduction of Cr from the metallic binder phase. In contrast, there has not been any evidence of the formation of such unwanted intermetallic carbides in large volumes in SLM fabricated parts (according to XRD analysis). In addition, Fe and Cr distribution in the binder phases was quite homogeneous as compared to cermets parts with similar composition fabricated via conventional sintering route (Fig. 33 (c, f)). These results could be attributed to the higher solidification/cooling rate involved in the SLM process (Kolnes et al., 2018; Zeisig et al., 2020).

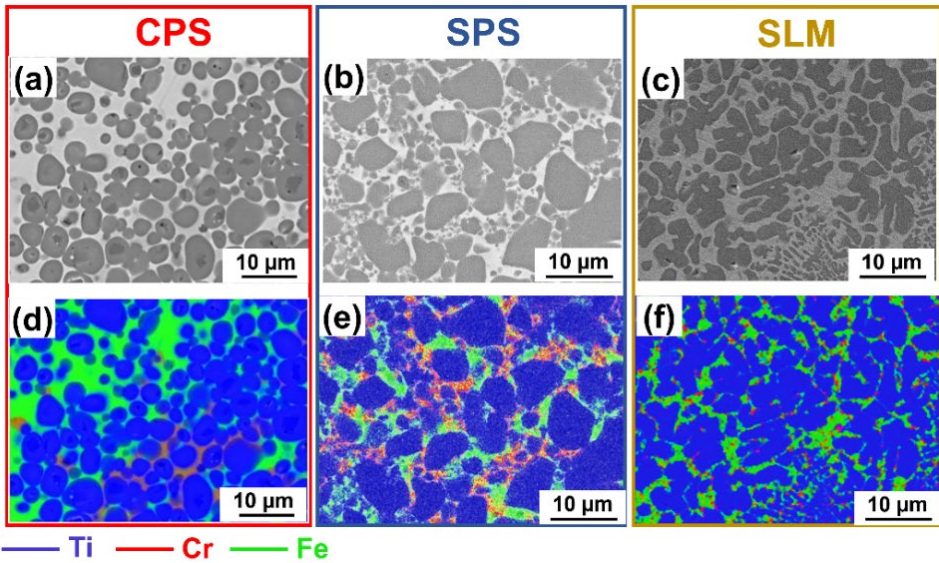


Figure 33. Elemental distribution mapping of the TiC-based cermets fabricated by different processing routes. (a, d) TiC-22 vol.% 430L FSS by CPS (Kolnes et al., 2018), (b) TiC-35 vol.% 430L FSS by SPS (Maurya et al., 2023), (c) TiC-35 vol.% 430L FSS by SLM (Maurya, 2022).

### 3.7.2 Mechanical properties

A comparison study of the mechanical characteristics of TiC-based cermets fabricated using conventional and additive manufacturing routes is shown in Fig. 34. A comparison of mechanical properties of the current thesis work was also made with literature data on WC-based hard metals and cermets fabricated conventionally and by AM route.

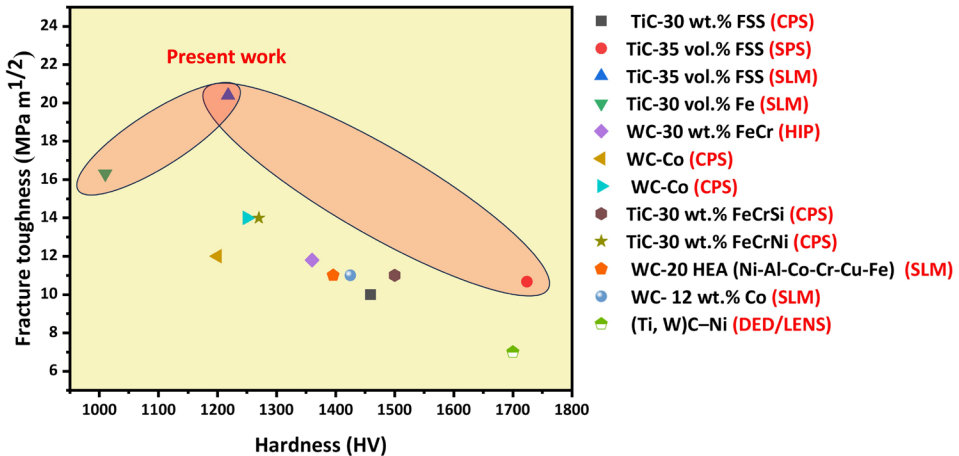


Figure 34. Hardness and Indentation fracture toughness of the TiC-430L FSS cermets compared with various TiC-Fe based cermets, WC-Co grades, and Cemented carbide fabricated via different fabrication routes.

Table 6. List of Cermets and Hardmetals fabricated via Conventional and Additive manufacturing routes (detail of Fig. 34)

Compositions	Fabrication route	Ref.
TiC-30 wt.% FSS	Conventional Pressureless Sintering	(Kolnes et al., 2018)
TiC-35 vol.% FSS	Spark Plasma Sintering	(Maurya et al., 2023)
TiC-35 vol.% FSS	Selective Laser Melting	(Publication III)
TiC-30 vol.% Fe	Selective Laser Melting	(Publication I)
WC-30 wt.% FeCr	Hot Isostatic Pressing	(Tarraste et al., 2018)
WC-Co	Conventional Pressureless Sintering	(Tarraste et al., 2018)
WC-Co	Conventional Pressureless Sintering	(Tarraste et al., 2018)
TiC-30 wt.% FeCrSi	Conventional Pressureless Sintering	(Kübarssepp et al., 1993)
TiC-30 wt.% FeCrNi	Conventional Pressureless Sintering	(Reshetnyak, 1994)
WC-20 HEA (Ni-Al-Co-Cr-Cu-Fe)	Selective Laser Melting	(C.-W. Li, 2019)
WC- 12 wt.% Co	Selective Laser Melting	(L. Zhang, 2022)
(Ti, W) C-Ni	Directed Energy Deposition	(Y. Xiong, 2010)

It has been observed that the microstructure of cermets influences the mechanical properties of fabricated parts. Compared to conventional-based TiC cermets, TiC-430L FSS-based AM cermets exhibit high fracture toughness. However, conventionally fabricated TiC-based cermets and WC-Co-based hard metals have higher hardness values. Improvement in the fracture toughness could be attributed to the finer microstructure that can affect the crack propagation (discussed in 3.5.2). It is, however, difficult to achieve full density through AM fabrication with adapted process parameters and feedstock powder rheology, which can affect the hardness of the fabricated cermets parts.

## 4 Conclusion

The development of TiC cermets with Fe-based binder may offer an alternative to conventional WC-Co cermets due to their low cost, non-toxicity, and superior high-temperature mechanical properties. Green technology such as Laser-based direct additive manufacturing (L-PBF/SLM) could be adapted to fabricate Cermet's parts with modulating microstructure and complex geometry parts at one step. As a whole, the present dissertation reaches the following conclusions.

1. When cermet parts are processed with regular laser pulse waves, cracks appear on the specimens. Therefore, for the first time, TiC-based cermets with different Fe-based binders have been fabricated by adapting a novel laser scan technique with variation in laser process parameters to distribute the laser energy with a single pulse for lowering the formation of the thermal residual stress and subsequently lowering the process defects such as cracks by controlling the melting pool/powder bed temperature.

2. The Laser pulse shaping (LPS) and Multiple laser scanning (MLS) techniques may be considered an optimal method to fabricate such brittle materials via laser-based processing to achieve lower process defects in the fabricated parts. The laser scanning techniques are influencing the melt pool melting and cooling rates or solidification, thus eliminating the cracks. Cermet parts exhibit mainly TiC and  $\alpha$ -Fe phases in the as-built condition, with no or a very low quantity of other phases (such as intermetallic complex carbides).

3. Fabricated cermet's parts exhibit a characteristic SLM microstructure with variations in finer dendritic and coarser TiC phases. Microstructure gradients can be attributed to SLM complex thermal history and Gaussian laser energy distribution.

4. To avoid sudden melting or wide thermal gradients of the melt pool/powder beds during pulse shaping, preheating the powder beds is quite imperative during the fabrication of these cermets. Similarly, laser pulse shaping can reduce the cooling rate and may reduce the thermal residual stresses in the parts by controlling the cooling rate or lowering the thermal gradient.

5. The mechanical properties (hardness and Indentation Fracture toughness) of the pulse-shaped TiC-Fe-based cermets depend on the microstructural characteristics of the fabricated parts. The maximum hardness and Indentation fracture toughness have been achieved for the sample with a laser peak power of 60 Watt ( $1010 \pm 65$  HV<sub>1</sub> and  $16.3 \pm 1.7$  MPa·m<sup>1/2</sup>) due to the presence of fine and coarse TiC phases and large gradient in the microstructure. A maximum density of 98% has been achieved with LPS with a laser peak power of 72 watts.

6. The mechanical properties (Microhardness and Indentation fracture toughness) of the Multiple laser scan samples depict better mechanical properties due to the dual morphology of the ceramic phase and the introduction of the Fe-Cr-based binder, The maximum hardness and Indentation fracture toughness has been achieved for the sample with high preheating scan speed and lower melting scan speed ( $1218 \pm 141$  HV<sub>1</sub> and  $20.42 \pm 3.3$  MPa·m<sup>1/2</sup>) resulting cermets parts with finer microstructure and lower process defects. The maximum density has been achieved for the fabricated parts with MLS is 97.8%.

7. The investigation of the wear behavior of the fabricated parts via scratch testing shows that gradient microstructure affects the wear resistance of the parts. For both single-pass conditions and multiple-pass conditions, better wear resistance was observed under low loads, and the plastic deformation of the soft binder material was found to be the dominant wear mechanism. Additionally, tribo-layers formed over multiple passes do not contribute to improved wear resistance due to the brittle nature of cermets.

8. SLM-built cermets (TiC-430L FSS) have relatively fine microstructures and a gradient morphology of the TiC phase as compared to conventionally manufactured cermets (Pressureless sintering and Spark plasma sintering). These results can be attributed to the high solidification/cooling rate and unique thermophysical phenomenon of the SLM process.

## 5 Kokkuvõte

Tulenevalt Fe-baasil sideainetega titaankarbiidsete kermiste madalast maksumusest, mittetoksilisusest ja suurepärasest mehaanilistest omadustest kõrgetel temperatuuridel võivad nad pakkuda alternatiivi WC-Co kõvasulamitele. "Rohelisi tehnoloogiaid", näiteks laseri-baasil otsene kihtlisandustehnoloogia (L-PBF/SLM), saab kasutada valmistamiseks moduleeritud mikrostruktuuri ja keerulise geomeetriaga kermisdetaile ühe tsükliga. Laseri-baasil konsolideerimistehnoloogiat kasutati esmakordselt Fe-baasil sideainega TiC-baasil kermiste valmistamiseks. Käesolevast dissertatsioonist saab välja tuua järgnevad järeldused:

1. Kermiste töötlemine korrapärase laserimpulsslainetega põhjustab pragude tekke katsekehades. Seetõttu võeti edukalt kasutusele uudne laseriga skaneerimistehnoloogia muutes lasertöötamise parameetreid jaotamiseks laseri energiat ühe impulsi kaupa, kontrollides sellega pulbri sulavanni temperatuuri, vähendamaks termilisi jääkpingeid ja seeläbi vähendades pragude teket.

2. Laserimpulss töötlemise (LPS) ja mitmekordse laseriga skaneerimise (MLS) tehnoloogiat võib käsitleda kui optimaalset meetodit tootmaks hapraid materjale kasutades laseri-baasil töötlemist vähendamaks valmistatud detailides protsessist tulenevaid defekte. Laseriga skannerimise tehnoloogiad mõjutavad sulavanni sulamis- ja jahtumiskiirusi või tahkumist, elimineerides sellega pragude teket. Nendel tingimustel valmistatud kermistes on peamiselt TiC ja  $\alpha$ -Fe faasid, kuid võib esineda ka väikesel määral muid faase.

3. Valmistatud kermiseid iseloomustab SLM kasutamisele omane mikrostruktuur, milles esinevad koos peened dendriitsed ning jämedad titaankarbiidi terad. Mikrostruktuuri gradientsust saab seletada SLM käigus toimuvate keerukate termiliste protsesside ja laseri energia Gaussi jaotusega.

4. Vältimaks ootamatut sulamist või suurt temperatuuri gradienti pulbrivannis laserimpulssiga töötlemise ajal, on hädavajalik pulbrivanni eelkuumutamine kermiste valmistamise korral. Laserimpulssiga töötlemine võimaldab vähendada jahtumiskiirust ja võib vähendada jääkpingete teket katsekehades kontrollides jahtumiskiirust või vähendades temperatuuri gradienti.

5. Laserimpulssiga töödeldud Fe-baasil sideainetega TiC-baasil kermiste mehaanilised omadused (kõvadus, purunemissitkus) sõltuvad valmistatud kermiste mikrostruktuurist. Kõrgeimad kõvaduse ja purunemissitkuse näitajad saavutati kasutades laseri tippvõimsust 60 W ( $1010 \pm 65 \text{ HV}_1$  ja  $16.3 \pm 1.7 \text{ MPa}\cdot\text{m}^{1/2}$ ) tulenevalt antud mikrostruktuuri suurest gradientsusest, kus peene- ja jämedateralised titaankarbiidi terad esinevad mikrostruktuuris samaaegselt. Laser impulss töötlemise (laser pulse shaping LPS) teel valmistatud detailide korral saavutati maksimaalne tihedus – 98%, kasutades laseri tippvõimsust 72 vatti.

6. Mitmekordselt laseriga skaneeritud (MLS) kermiseid iseloomustavad paremad mehaanilised omadused (mikrokõvadus, purunemissitkus ja survetugevus) tulenevalt antud kermistes kasutatud suuremast keraamilise faasi sisaldusest ja

FeCr-baasil sideainest. Maksimaalne kõvadus ja purunemissitkus ( $1218 \pm 141$  HV<sub>1</sub> ja  $20.42 \pm 3.3$  MPa·m<sup>1/2</sup>) saavutati kasutades suuremat eelkuumutava skaneerimise ja madalamat sulatava skaneerimise kiirust tulenevalt saavutatud peenemast mikrostruktuurist ja väiksemast defektide arvust. MLS teel valmistatud kermiste kõrgeim tihedus oli 97.8%.

7. Valmistatud kermiste kulumiskindlust uuriti kasutades kriipetesti. Kulutamiskatsed näitasid, et kermiste gradientstruktuur mõjutab nende kulumiskindlust. Nii ühe kui mitme läbimiga kriipetesti korral oli kulumiskindlus suurem madalamate koormuste korral, peamiseks kulumismehhanismiks oli pehme sideainefaasi plastne deformatsioon. Mitme läbimi kasutamise korral kulumisjäljele tekkinud tribo-kiht ei tõstnud kulumiskindlust tulenevalt kermiste haprusest.

8. Võrreldes tavatehnoloogiate (survevaba paagutus ja plasmaaktiveeritud paagutus (SPS)) teel valmistatud TiC-430L FSS kermistega iseloomustab selektiivse lasersulatuse (SLM) teel valmistatud TiC-430L FSS kermiseid suhteliselt peen terasuurus ja TiC faasi gradientsus. Seda saab seletada kiire tahkumise/jahtumisega selektiivse lasersulatuse (SLM) korral ja selektiivse lasersulatusega (SLM) kaasneva unikaalse termofüüsikalise käitumisega.

## 6 Future work

The current thesis works add to the broader understanding of the adapted novel laser scan techniques for the fabrication of brittle materials such as cermets by laser-based solidification process. To provide a more comprehensive understanding of the development of these cermets with improved microstructural and mechanical properties, the following further studies are recommended:

1. Through LPBF/SLM, it is possible to fabricate cermet parts with higher density and lower process defects by adapting feedstock powder with better rheology and morphology. There is a need for a detailed study on the fabrication of cermets parts with different feedstock morphologies.
2. Introducing binder elements that are not critical raw materials (CRM, as defined by EU) could be adapted to improve the wettability or mechanical properties of the fabricated parts.
3. A thermodynamic analysis or phase calculation of these materials can certainly give insights into the unavoidable phase formation and improvements in the mechanical properties of the materials when binders are introduced.
4. Studying the mechanical and tribological behavior of these fabricated parts at higher temperatures could lead to disclosing the wear behavior of these materials at such temperatures.
5. Fabrication of the TiC-based cermets with Fe-based binder via another direct Additive manufacturing process based on laser/electron-based solidification such as Directed energy deposition (DED), Electron beam melting (EBM), etc. needs to be addressed. This will provide a better understanding of the fabrication of cermet parts with fewer process defects and the advantages and disadvantages of the various processes.

## References

- Akinribide, O. J., Obadele, B. A., Akinwamide, S. O., Bilal, H., Ajibola, O. O., Ayeleru, O. O., ... Olubambi, P. A. (2019). Sintering of binderless TiN and TiCN-based cermet for toughness applications: Processing techniques and mechanical properties: A review. *Ceramics International*, 45(17), 21077–21090. <https://doi.org/10.1016/j.ceramint.2019.07.191>
- Aramian, A. (2020a). Effect of selective laser melting process parameters on microstructural and mechanical properties of TiC–NiCr cermet. *Ceramics International*, 46(18, Part A), 28749–28757. <https://doi.org/https://doi.org/10.1016/j.ceramint.2020.08.037>
- Aramian, A. (2020b). Effect of selective laser melting process parameters on microstructural and mechanical properties of TiC–NiCr cermet. *Ceramics International*, 46(18, Part A), 28749–28757. <https://doi.org/https://doi.org/10.1016/j.ceramint.2020.08.037>
- Aramian, A. (2020c). In situ fabrication of TiC–NiCr cermets by selective laser melting. *International Journal of Refractory Metals and Hard Materials*, 87(December 2019), 105171. <https://doi.org/10.1016/j.ijrmhm.2019.105171>
- Aramian, A. (2021). Room and High-Temperature Sliding Wear Behavior of In Situ TiC-Based Cermet Fabricated through Selective Laser Melting. *Journal of Materials Engineering and Performance*, 30(9), 6777–6787. <https://doi.org/10.1007/s11665-021-05995-8>
- Aramian, A., Razavi, S. M. J., Sadeghian, Z., & Berto, F. (2020). A review of additive manufacturing of cermets. *Additive Manufacturing*, 33(July 2019), 101130. <https://doi.org/10.1016/j.addma.2020.101130>
- Aramian, A., Sadeghian, Z., Narimani, M., Razavi, N., & Berto, F. (2023). A review on the microstructure and properties of TiC and Ti(C,N) based cermets. *International Journal of Refractory Metals and Hard Materials*, 115, 106320. <https://doi.org/https://doi.org/10.1016/j.ijrmhm.2023.106320>
- Aramian, A., Sadeghian, Z., Wan, D., Holovenko, Y., Razavi, S. M. J., & Berto, F. (2021). Microstructure and texture evolution during the manufacturing of in situ TiC–NiCr cermet through selective laser melting process. *Materials Characterization*, 178, 111289. <https://doi.org/https://doi.org/10.1016/j.matchar.2021.111289>
- Ardila, L. C., Garcíandia, F., González-Díaz, J. B., Álvarez, P., Echeverría, A., Petite, M. M., ... Ochoa, J. (2014). Effect of IN718 Recycled Powder Reuse on Properties of Parts Manufactured by Means of Selective Laser Melting. *Physics Procedia*, 56, 99–107. <https://doi.org/https://doi.org/10.1016/j.phpro.2014.08.152>
- Azam, F. I. (2018). An In-Depth Review on Direct Additive Manufacturing of Metals. *IOP Conference Series: Materials Science and Engineering*, 328(1), 12005. <https://doi.org/10.1088/1757-899X/328/1/012005>
- Berger. (2022). Binder-jetting of TiCN-based cermets. *Powder Metallurgy*, 65(5), 382–389. <https://doi.org/10.1080/00325899.2022.2099636>
- Berman, B. (2012). 3-D printing: The new industrial revolution. *Business Horizons*, 55(2), 155–162. <https://doi.org/https://doi.org/10.1016/j.bushor.2011.11.003>
- Bricín, D. (2020). Development of the structure of cemented carbides during their processing by slm and hip. *Metals*, 10(11), 1–17. <https://doi.org/10.3390/met10111477>

- Bricin, D., & Kriz, A. (2019). Processability of WC-CO powder mixtures using slm additive technology. *MM Science Journal*, 2019(June), 2939–2944. [https://doi.org/10.17973/MMSJ.2019\\_06\\_2018115](https://doi.org/10.17973/MMSJ.2019_06_2018115)
- Campanelli, S. L., Contuzzi, N., Posa, P., & Angelastro, A. (2019). Printability and Microstructure of Selective Laser Melting of WC/Co/Cr Powder. *Materials*, Vol. 12. <https://doi.org/10.3390/ma12152397>
- Casati, R., Hamidi Nasab, M., Coduri, M., Tirelli, V., & Vedani, M. (2018). Effects of Platform Pre-Heating and Thermal-Treatment Strategies on Properties of AlSi10Mg Alloy Processed by Selective Laser Melting. *Metals*, Vol. 8. <https://doi.org/10.3390/met8110954>
- Chang, S.-H., Chang, M.-H., & Huang, K.-T. (2015). Study on the sintered characteristics and properties of nanostructured WC–15 wt% (Fe–Ni–Co) and WC–15 wt% Co hard metal alloys. *Journal of Alloys and Compounds*, 649, 89–95. <https://doi.org/https://doi.org/10.1016/j.jallcom.2015.07.119>
- Chen, J., Huang, M., Fang, Z. Z., Koopman, M., Liu, W., Deng, X., ... Wang, Z. (2019). Microstructure analysis of high density WC-Co composite prepared by one step selective laser melting. *International Journal of Refractory Metals and Hard Materials*, 84(January), 104980. <https://doi.org/10.1016/j.ijrmhm.2019.104980>
- Chen, Z. (2018). Thermal dynamic behavior during selective laser melting of K418 superalloy: numerical simulation and experimental verification. *Applied Physics A: Materials Science and Processing*, 124(4), 1–16. <https://doi.org/10.1007/s00339-018-1737-8>
- D’Errico, G. E., Bugliosi, S., Cuppini, D., & Guglielmi, E. (1997). A study of cermets’ wear behaviour. *Wear*, 203–204(96), 242–246. [https://doi.org/10.1016/S0043-1648\(96\)07397-8](https://doi.org/10.1016/S0043-1648(96)07397-8)
- Davydova, A., Domashenkov, A., Sova, A., Movtchan, I., Bertrand, P., Desplanques, B., ... Iacob, C. (2016). Selective laser melting of boron carbide particles coated by a cobalt-based metal layer. *Journal of Materials Processing Technology*, 229, 361–366. <https://doi.org/10.1016/j.jmatprotec.2015.09.033>
- De Wild, M., Ghayor, C., Zimmermann, S., Rüegg, J., Nicholls, F., Schuler, F., ... Weber, F. E. (2019). Osteoconductive Lattice Microarchitecture for Optimized Bone Regeneration. *3D Printing and Additive Manufacturing*, 6(1), 40–49. <https://doi.org/10.1089/3dp.2017.0129>
- Diouf, S., & Molinari, A. (2012). Densification mechanisms in spark plasma sintering: Effect of particle size and pressure. *Powder Technology*, 221, 220–227. <https://doi.org/https://doi.org/10.1016/j.powtec.2012.01.005>
- Domashenkov, A., Borbély, A., & Smurov, I. (2017). Structural modifications of WC/Co nanophased and conventional powders processed by selective laser melting. *Materials and Manufacturing Processes*, 32(1), 93–100. <https://doi.org/10.1080/10426914.2016.1176195>
- Enneti, R. K., & Prough, K. C. (2019a). Effect of binder saturation and powder layer thickness on the green strength of the binder jet 3D printing (BJ3DP) WC-12%Co powders. *International Journal of Refractory Metals and Hard Materials*, 84, 104991. <https://doi.org/https://doi.org/10.1016/j.ijrmhm.2019.104991>
- Enneti, R. K., & Prough, K. C. (2019b). Wear properties of sintered WC-12%Co processed via Binder Jet 3D Printing (BJ3DP). *International Journal of Refractory Metals and Hard Materials*, 78(September 2018), 228–232. <https://doi.org/10.1016/j.ijrmhm.2018.10.003>

- Enneti, R. K., & Prough, K. C. (2019c). Wear properties of sintered WC-12%Co processed via Binder Jet 3D Printing (BJ3DP). *International Journal of Refractory Metals and Hard Materials*, 78(September 2018), 228–232. <https://doi.org/10.1016/j.ijrmhm.2018.10.003>
- Enneti, R. K., & Prough, K. C. (2019d). Wear properties of sintered WC-12%Co processed via Binder Jet 3D Printing (BJ3DP). *International Journal of Refractory Metals and Hard Materials*, 78, 228–232. <https://doi.org/https://doi.org/10.1016/j.ijrmhm.2018.10.003>
- Enneti, R. K., Prough, K. C., Trasorras, J. L., Klein, A., Studley, N., Useldinger, R., & Droschel, M. (2020). Dimensional capability of the binder jet 3D printing (BJ3DP) process applied to the manufacture of WC-12%Co parts. *Euro PM 2018 Congress and Exhibition*.
- Enneti, R. K., Prough, K. C., Wolfe, T. A., Klein, A., Studley, N., & Trasorras, J. L. (2018). Sintering of WC-12%Co processed by binder jet 3D printing (BJ3DP) technology. *International Journal of Refractory Metals and Hard Materials*, 71(July 2017), 28–35. <https://doi.org/10.1016/j.ijrmhm.2017.10.023>
- Ettmayer, P. (1989). Hardmetals and Cermets. *Annual Review of Materials Science*, 19(1), 145–164. <https://doi.org/10.1146/annurev.ms.19.080189.001045>
- Fortunato, A., Valli, G., Liverani, E., & Ascari, A. (2019). Additive Manufacturing of WC-Co Cutting Tools for Gear Production. *Lasers in Manufacturing and Materials Processing*, 6(3), 247–262. <https://doi.org/10.1007/s40516-019-00092-0>
- Fries, S., Genilke, S., Wilms, M. B., Seimann, M., Weisheit, A., Kaletsch, A., ... Broeckmann, C. (2020). Laser-Based Additive Manufacturing of WC-Co with High-Temperature Powder Bed Preheating. *Steel Research International*, 91(3), 1–7. <https://doi.org/10.1002/srin.201900511>
- Gaier, M., Todorova, T. Z., Russell, Z., Farhat, Z. N., Zwanziger, J. W., & Plucknett, K. P. (2019). The influence of intermetallic ordering on wear and indentation properties of TiC-Ni3Al cermets. *Wear*, 426–427, 390–400. <https://doi.org/https://doi.org/10.1016/j.wear.2018.12.034>
- Gibson, I., Rosen, D., & Stucker, B. (2015). *Directed Energy Deposition Processes BT - Additive Manufacturing Technologies: 3D Printing, Rapid Prototyping, and Direct Digital Manufacturing* (I. Gibson, D. Rosen, & B. Stucker, Eds.). New York, NY: Springer New York. [https://doi.org/10.1007/978-1-4939-2113-3\\_10](https://doi.org/10.1007/978-1-4939-2113-3_10)
- Gómez, B., Gordo, E., & Torralba, J. M. (2006). Influence of milling time on the processing of Fe-TiCN composites. *Materials Science and Engineering A*, 430(1–2), 59–63. <https://doi.org/10.1016/j.msea.2006.05.051>
- Grigoriev, S., Tarasova, T., Gusarov, A., Khmyrov, R., & Egorov, S. (2019). Possibilities of manufacturing products from cermet compositions using nanoscale powders by additive manufacturing methods. *Materials*, 12(20). <https://doi.org/10.3390/ma12203425>
- Gu, D., & Meiners, W. (2010). Microstructure characteristics and formation mechanisms of in situ WC cemented carbide based hardmetals prepared by Selective Laser Melting. *Materials Science and Engineering: A*, 527(29), 7585–7592. <https://doi.org/https://doi.org/10.1016/j.msea.2010.08.075>
- Guan, J., Jiang, Y., Zhang, X., & Chong, X. (2020). Microstructural evolution and EBSD analysis of AlSi10Mg alloy fabricated by selective laser remelting. *Materials Characterization*, 161(August 2019), 110079. <https://doi.org/10.1016/j.matchar.2019.110079>

- Guo, N., & Leu, M. C. (2013). Additive manufacturing: technology, applications and research needs. *Frontiers of Mechanical Engineering*, 8(3), 215–243. <https://doi.org/10.1007/s11465-013-0248-8>
- Hanzl, P. (2015). The Influence of Processing Parameters on the Mechanical Properties of SLM Parts. *Procedia Engineering*, 100, 1405–1413. <https://doi.org/https://doi.org/10.1016/j.proeng.2015.01.510>
- Heydari, L. (2021). Ti(C,n) and wc-based cermets: A review of synthesis, properties and applications in additive manufacturing. *Materials*, 14(22). <https://doi.org/10.3390/ma14226786>
- Heydari, L., Lietor, P. F., Corpas-Iglesias, F. A., & Laguna, O. H. (2021). Ti(C,n) and wc-based cermets: A review of synthesis, properties and applications in additive manufacturing. *Materials*, 14(22). <https://doi.org/10.3390/ma14226786>
- Hooper, P. A. (2018). Melt pool temperature and cooling rates in laser powder bed fusion. *Additive Manufacturing*, 22, 548–559. <https://doi.org/https://doi.org/10.1016/j.addma.2018.05.032>
- Hu, Y. (2018). A review on laser deposition-additive manufacturing of ceramics and ceramic reinforced metal matrix composites. *Ceramics International*, 44(17), 20599–20612. <https://doi.org/10.1016/j.ceramint.2018.08.083>
- Ibe, H. (2021). Controlling WC/Co two-phase microstructure of cemented carbides additive-manufactured by laser powder bed fusion: Effect of powder composition and post heat-treatment. *Materials & Design*, 210, 110034. <https://doi.org/https://doi.org/10.1016/j.matdes.2021.110034>
- Jin, C., Onuoha, C. C., Farhat, Z. N., Kipouros, G. J., & Plucknett, K. P. (2017). Microstructural damage following reciprocating wear of TiC-stainless steel cermets. *Tribology International*, 105(September 2016), 201–218. <https://doi.org/10.1016/j.triboint.2016.10.011>
- Jose, S. A. (2022). Cermet Systems: Synthesis, Properties, and Applications. *Ceramics*, Vol. 5, pp. 210–236. <https://doi.org/10.3390/ceramics5020018>
- Jung, H. Y., Choi, S. J., Prashanth, K. G., Stoica, M., Scudino, S., Yi, S., ... Eckert, J. (2015). Fabrication of Fe-based bulk metallic glass by selective laser melting: A parameter study. *Materials and Design*, 86, 703–708. <https://doi.org/10.1016/j.matdes.2015.07.145>
- Karimi, J., Ma, P., Jia, Y. D., & Prashanth, K. G. (2020). Linear patterning of high entropy alloy by additive manufacturing. *Manufacturing Letters*, 24, 9–13. <https://doi.org/10.1016/j.mfglet.2020.03.003>
- Karimi, J., Suryanarayana, C., Okulov, I., & Prashanth, K. G. (2020). Selective laser melting of Ti6Al4V: Effect of laser re-melting. *Materials Science and Engineering A*, 805, 140558. <https://doi.org/10.1016/j.msea.2020.140558>
- Kempen, K., Vrancken, B., Buls, S., Thijs, L., Van Humbeeck, J., & Kruth, J. P. (2014). Selective Laser Melting of Crack-Free High Density M2 High Speed Steel Parts by Baseplate Preheating. *Journal of Manufacturing Science and Engineering, Transactions of the ASME*, 136(6). <https://doi.org/10.1115/1.4028513>
- Kenneth J. A. Brookes. (1992). *Hardmetals and Other Hard Materials*. Retrieved from <https://www.epma.com/publications/all-other-publications/product/hardmetals-and-other-hard-materials>

- Kernan, B. D., Sachs, E. M., Oliveira, M. A., & Cima, M. J. (2007). Three-dimensional printing of tungsten carbide–10wt% cobalt using a cobalt oxide precursor. *International Journal of Refractory Metals and Hard Materials*, 25(1), 82–94. <https://doi.org/https://doi.org/10.1016/j.ijrmhm.2006.02.002>
- Khmyrov, R. S., Safronov, V. A., & Gusarov, A. V. (2017). Synthesis of Nanostructured WC-Co Hardmetal by Selective Laser Melting. *Procedia IUTAM*, 23, 114–119. <https://doi.org/10.1016/j.piutam.2017.06.011>
- Khmyrov, R S, Safronov, V. A., & Gusarov, A. V. (2017). Synthesis of Nanostructured WC-Co Hardmetal by Selective Laser Melting. *Procedia IUTAM*, 23, 114–119. <https://doi.org/10.1016/j.piutam.2017.06.011>
- Khmyrov, Roman S., Shevchukov, A. P., Gusarov, A. V., & Tarasova, T. V. (2017). Phase composition and microstructure of WC-Co alloys obtained by selective laser melting. *Mechanics and Industry*, 18(7). <https://doi.org/10.1051/meca/2017059>
- Kim, K. W. (2021). Direct energy deposition of ultrastrong WC-12Co cemented carbide: Fabrication, microstructure and compressive properties. *International Journal of Refractory Metals and Hard Materials*, 99(January), 105591. <https://doi.org/10.1016/j.ijrmhm.2021.105591>
- Kolnes, M., Mere, A., Kübarsepp, J., Viljus, M., Maaten, B., & Tarraste, M. (2018). Microstructure evolution of TiC cermets with ferritic AISI 430L steel binder. *Powder Metallurgy*, 61(3), 197–209. <https://doi.org/10.1080/00325899.2018.1447268>
- Konyashin, I. (2023). Approaching the 100th anniversary of the Hardmetal invention: From first WC-Co samples towards modern advanced Hardmetal grades. *International Journal of Refractory Metals and Hard Materials*, 111, 106113. <https://doi.org/https://doi.org/10.1016/j.ijrmhm.2023.106113>
- Kruth, J.-P. P. (2007). Consolidation phenomena in laser and powder-bed based layered manufacturing. *CIRP Annals*, 56(2), 730–759. <https://doi.org/https://doi.org/10.1016/j.cirp.2007.10.004>
- Ku, N., Pittari, J. J., Kilczewski, S., & Kudzal, A. (2019). Additive Manufacturing of Cemented Tungsten Carbide with a Cobalt-Free Alloy Binder by Selective Laser Melting for High-Hardness Applications. *Jom*, 71(4), 1535–1542. <https://doi.org/10.1007/s11837-019-03366-2>
- Kübarsepp, J., & Juhani, K. (2020, November). Cermets with Fe-alloy binder: A review. *International Journal of Refractory Metals and Hard Materials*, Vol. 92, p. 105290. Elsevier Ltd. <https://doi.org/10.1016/j.ijrmhm.2020.105290>
- Kübarsepp, J., Klaasen, H., & Pirso, J. (2001). Behaviour of TiC-base cermets in different wear conditions. *Wear*, 249(3), 229–234. [https://doi.org/https://doi.org/10.1016/S0043-1648\(01\)00569-5](https://doi.org/https://doi.org/10.1016/S0043-1648(01)00569-5)
- Kübarsepp, J., Reshetnyak, H., & Annuka, H. (1993). Characterization of the serviceability of steel-bonded hardmetals. *International Journal of Refractory Metals and Hard Materials*, 12(6), 341–348. [https://doi.org/https://doi.org/10.1016/0263-4368\(93\)90024-A](https://doi.org/https://doi.org/10.1016/0263-4368(93)90024-A)
- Kühnle, T., & Partes, K. (2012). In-Situ Formation of Titanium Boride and Titanium Carbide by Selective Laser Melting. *Physics Procedia*, 39, 432–438. <https://doi.org/https://doi.org/10.1016/j.phpro.2012.10.058>
- Kulu, P. (2001). *Metal studies and metal technology*. TTÜ kirjastus. Retrieved from [https://www.ester.ee/record=b1526274\\*est](https://www.ester.ee/record=b1526274*est)

- Lele, A. (2019). Additive manufacturing (AM). *Smart Innovation, Systems and Technologies*, 132, 101–109. [https://doi.org/10.1007/978-981-13-3384-2\\_5](https://doi.org/10.1007/978-981-13-3384-2_5)
- Lengauer, W., Duretek, I., Fürst, M., Schwarz, V., Gonzalez-Gutierrez, J., Schuschnigg, S., ... Morrison, V. (2019). Fabrication and properties of extrusion-based 3D-printed hardmetal and cermet components. *International Journal of Refractory Metals and Hard Materials*, 82, 141–149. <https://doi.org/https://doi.org/10.1016/j.ijrmhm.2019.04.011>
- Lengauer, W., Duretek, I., Schwarz, V., Kukla, C., Kitzmantel, M., Neubauer, E., ... Morrison, V. (2020). Preparation and properties of extrusion-based 3D-printed hardmetal and cermet parts. *Euro PM 2018 Congress and Exhibition*.
- Li, C.-W. (2019). On the microstructure and properties of an advanced cemented carbide system processed by selective laser melting. *Journal of Alloys and Compounds*, 782, 440–450. <https://doi.org/https://doi.org/10.1016/j.jallcom.2018.12.187>
- Li, C. W. (2018). Microstructure characterization of cemented carbide fabricated by selective laser melting process. *International Journal of Refractory Metals and Hard Materials*, 75(May), 225–233. <https://doi.org/10.1016/j.ijrmhm.2018.05.001>
- Li, C. W. (2019). On the microstructure and properties of an advanced cemented carbide system processed by selective laser melting. *Journal of Alloys and Compounds*, 782, 440–450. <https://doi.org/https://doi.org/10.1016/j.jallcom.2018.12.187>
- Li, X., Zhao, Y., Guo, Z., Liu, Y. Y., Wang, H., Zhang, J., ... Bai, P. (2022). Influence of different substrates on the microstructure and mechanical properties of WC-12Co cemented carbide fabricated via laser melting deposition. *International Journal of Refractory Metals and Hard Materials*, 104(January), 105787. <https://doi.org/10.1016/j.ijrmhm.2022.105787>
- Li, Y., Bai, P., Wang, Y., Hu, J., & Guo, Z. (2009). Effect of Ni contents on the microstructure and mechanical properties of TiC-Ni cermets obtained by direct laser fabrication. *International Journal of Refractory Metals and Hard Materials*, 27(3), 552–555. <https://doi.org/10.1016/j.ijrmhm.2008.07.006>
- Lim, J. S. (2021). Selection of effective manufacturing conditions for directed energy deposition process using machine learning methods. *Scientific Reports*, 11(1), 1–13. <https://doi.org/10.1038/s41598-021-03622-z>
- Liu, B., Fang, G., Lei, L., & Yan, X. (2022). Predicting the porosity defects in selective laser melting (SLM) by molten pool geometry. *International Journal of Mechanical Sciences*, 228, 107478. <https://doi.org/https://doi.org/10.1016/j.ijmecsci.2022.107478>
- Liu, D., Yue, W., Kang, J., & Wang, C. (2021). Effects of different substrates on the formability and densification behaviors of cemented carbide processed by laser powder bed fusion. *Materials*, 14(17). <https://doi.org/10.3390/ma14175027>
- Liu, D., Yue, W., Kang, J., & Wang, C. (2022). Effect of Laser Remelting Strategy on the Forming Ability of Cemented Carbide Fabricated by Laser Powder Bed Fusion (L-PBF). *Materials*, 15(7). <https://doi.org/10.3390/ma15072380>
- Liu, J., Chen, J., Zhou, L., Liu, B., Lu, Y., Wu, S., ... Qu, Z. (2021). Role of Co Content on Densification and Microstructure of WC-Co Cemented Carbides Prepared by Selective Laser Melting. *Acta Metallurgica Sinica (English Letters)*, 34(9), 1245–1254. <https://doi.org/10.1007/s40195-021-01195-4>
- Lofaj, F., & Kaganovskii, Y. S. (1995). Kinetics of WC-Co oxidation accompanied by swelling. *Journal of Materials Science*, 30(7), 1811–1817. <https://doi.org/10.1007/BF00351615>

- Marchese, G., Garmendia Colera, X., Calignano, F., Lorusso, M., Biamino, S., Minetola, P., & Manfredi, D. (2017). Characterization and Comparison of Inconel 625 Processed by Selective Laser Melting and Laser Metal Deposition. *Advanced Engineering Materials*, 19(3), 1600635. <https://doi.org/10.1002/adem.201600635>
- Maurya. (2021). Additive manufacturing of TiC-based cermet with stainless steel as a binder material. *Material Today: Proceeding*.
- Maurya, H. S. (2022). Effect of powder bed preheating on the crack formation and microstructure in ceramic matrix composites fabricated by laser powder-bed fusion process. *Additive Manufacturing*, 103013. <https://doi.org/https://doi.org/10.1016/j.addma.2022.103013>
- Maurya, H. S., Jayaraj, J., Vikram, R. J., Juhani, K., Sergejev, F., & Prashanth, K. G. (2023). Additive manufacturing of TiC-based cermets: A detailed comparison with spark plasma sintered samples. *Journal of Alloys and Compounds*, 960, 170436. <https://doi.org/https://doi.org/10.1016/j.jallcom.2023.170436>
- Mertens, R., Vrancken, B., Holmstock, N., Kinds, Y., Kruth, J. P., & Van Humbeeck, J. (2016). Influence of powder bed preheating on microstructure and mechanical properties of H13 tool steel SLM parts. *Physics Procedia*, 83, 882–890. <https://doi.org/10.1016/j.phpro.2016.08.092>
- Molobi, E., Sacks, N., & Theron, M. (2022). Crack mitigation in laser engineered net shaping of WC-10wt%FeCr cemented carbides. *Additive Manufacturing Letters*, 2(November 2021), 100028. <https://doi.org/10.1016/j.addlet.2022.100028>
- Mumtaz, K. A., & Hopkinson, N. (2010). Selective Laser Melting of thin wall parts using pulse shaping. *Journal of Materials Processing Technology*, 210(2), 279–287. <https://doi.org/10.1016/j.jmatprotec.2009.09.011>
- Mumtaz, K., & Hopkinson, N. (2010). Selective laser melting of Inconel 625 using pulse shaping. *Rapid Prototyping Journal*, 16(4), 248–257. <https://doi.org/10.1108/13552541011049261>
- Namini, S. (2019). Effect of TiB<sub>2</sub> addition on the elevated temperature tribological behavior of spark plasma sintered Ti matrix composite. *Composites Part B: Engineering*, 172(May), 271–280. <https://doi.org/10.1016/j.compositesb.2019.05.073>
- Neumeister, P., Jurisch, M., Jelitto, H., Engert, A. R., Schneider, G. A., & Balke, H. (2013). Effective permittivity of air-filled cracks in piezoelectric ceramics due to crack bridging. *Acta Materialia*, 61(4), 1061–1069. <https://doi.org/https://doi.org/10.1016/j.actamat.2012.10.006>
- Nickels, L. (2016). Additive manufacturing: A user's guide. *Metal Powder Report*, 71(2), 100–105. <https://doi.org/https://doi.org/10.1016/j.mprp.2016.02.045>
- Olakanmi, E. O., Cochrane, R. F., & Dalgarno, K. W. (2015). A review on selective laser sintering/melting (SLS/SLM) of aluminium alloy powders: Processing, microstructure, and properties. *Progress in Materials Science*, 74, 401–477. <https://doi.org/10.1016/j.pmatsci.2015.03.002>
- Oyesola, M. (2021). Optimization of selective laser melting process parameters for surface quality performance of the fabricated Ti6Al4V. *The International Journal of Advanced Manufacturing Technology*, 114(5), 1585–1599. <https://doi.org/10.1007/s00170-021-06953-3>
- Park, J. H., Bang, G. B., Lee, K. A., Son, Y., Kim, W. R., & Kim, H. G. (2021). Effect on microstructural and mechanical properties of Inconel 718 superalloy fabricated by selective laser melting with rescanning by low energy density. *Journal of Materials Research and Technology*, 10, 785–796. <https://doi.org/10.1016/j.jmrt.2020.12.053>

- Picas, J. A., Xiong, Y., Punset, M., Ajdelsztajn, L., Forn, A., & Schoenung, J. M. (2009a). Microstructure and wear resistance of WC-Co by three consolidation processing techniques. *International Journal of Refractory Metals and Hard Materials*, 27(2), 344–349. <https://doi.org/10.1016/j.ijrmhm.2008.07.002>
- Picas, J. A., Xiong, Y., Punset, M., Ajdelsztajn, L., Forn, A., & Schoenung, J. M. (2009b). Microstructure and wear resistance of WC-Co by three consolidation processing techniques. *International Journal of Refractory Metals and Hard Materials*, 27(2), 344–349. <https://doi.org/https://doi.org/10.1016/j.ijrmhm.2008.07.002>
- Pirso, J., Viljus, M., Letunovits, S., Juhani, K., & Joost, R. (2011). Three-body abrasive wear of cermets. *Wear*, 271(11), 2868–2878. <https://doi.org/https://doi.org/10.1016/j.wear.2011.06.005>
- Prashanth, K. G. (2017). Is the energy density a reliable parameter for materials synthesis by selective laser melting? *Materials Research Letters*, 5(6), 386–390. <https://doi.org/10.1080/21663831.2017.1299808>
- Rahmani, R., Antonov, M., Kollo, L., Holovenko, Y., & Prashanth, K. G. (2019). Mechanical behavior of Ti6Al4V scaffolds filled with CaSiO<sub>3</sub> for implant applications. *Applied Sciences (Switzerland)*, 9(18), 3844. <https://doi.org/10.3390/app9183844>
- Reshetnyak, H. (1994). Mechanical properties of hard metals and their erosive wear resistance. *Wear*, 177(2), 185–193. [https://doi.org/https://doi.org/10.1016/0043-1648\(94\)90244-5](https://doi.org/https://doi.org/10.1016/0043-1648(94)90244-5)
- Rodriguez-Suarez, T., Lopez-Esteban, S., Pecharromán, C., Moya, J. S., El Attaoui, H., Benaqqa, C., & Chevalier, J. (2009). Slow crack growth resistance and bridging stress determination in alumina-rich magnesium aluminate spinel/tungsten composites. *Acta Materialia*, 57(7), 2121–2127. <https://doi.org/https://doi.org/10.1016/j.actamat.2009.01.004>
- Sabatello, S., Frage, N., & Dariel, M. P. (2000). Graded TiC-based cermets. *Materials Science and Engineering A*, 288(1), 12–18. [https://doi.org/10.1016/S0921-5093\(00\)00889-3](https://doi.org/10.1016/S0921-5093(00)00889-3)
- Sadhu, A., Choudhary, A., Sarkar, S., Nair, A. M., Nayak, P., Pawar, S. D., ... Nath, A. K. (2020). A study on the influence of substrate pre-heating on mitigation of cracks in direct metal laser deposition of NiCrSiBC-60%WC ceramic coating on Inconel 718. *Surface and Coatings Technology*, 389, 125646. <https://doi.org/https://doi.org/10.1016/j.surfcoat.2020.125646>
- Sahoo, C. K. (2017). Microstructure and mechanical properties of TiC-Ni coating on AISI304 steel produced by TIG cladding process. *Journal of Materials Processing Technology*, 240, 126–137. <https://doi.org/https://doi.org/10.1016/j.jmatprotec.2016.09.018>
- Santos, E. C., Shiomi, M., Osakada, K., & Laoui, T. (2006). Rapid manufacturing of metal components by laser forming. *International Journal of Machine Tools and Manufacture*, 46(12–13), 1459–1468. <https://doi.org/10.1016/j.ijmachtools.2005.09.005>
- Scheithauer, U., Pötschke, J., Weingarten, S., Schwarzer, E., Vornberger, A., Moritz, T., & Michaelis, A. (2017). Droplet-based additive manufacturing of hard metal components by thermoplastic 3D Printing (T3DP). *Journal of Ceramic Science and Technology*, 8(1), 155–160. <https://doi.org/10.4416/JCST2016-00104>
- Sergejev, F., Preis, I., Kübarsepp, J., & Antonov, M. (2008). Correlation between surface fatigue and microstructural defects of cemented carbides. *Wear*, 264(9), 770–774. <https://doi.org/https://doi.org/10.1016/j.wear.2007.02.024>

- Sing, S. L., Yeong, W. Y., Wiria, F. E., Tay, B. Y., Zhao, Z., Zhao, L., ... Yang, S. (2017). Direct selective laser sintering and melting of ceramics: a review. *Rapid Prototyping Journal*, 23(3), 611–623. <https://doi.org/10.1108/RPJ-11-2015-0178>
- Son, S. (2021). Correlation between microstructural heterogeneity and mechanical properties of WC-Co composite additively manufactured by selective laser melting. *Materials Letters*, 293, 129683. <https://doi.org/https://doi.org/10.1016/j.matlet.2021.129683>
- Svetlizky, D., Das, M., Zheng, B., Vyatskikh, A. L., Bose, S., Bandyopadhyay, A., ... Eliaz, N. (2021). Directed energy deposition (DED) additive manufacturing: Physical characteristics, defects, challenges and applications. *Materials Today*, 49(October), 271–295. <https://doi.org/10.1016/j.mattod.2021.03.020>
- Tan, C., Hu, J., Shi, Q., Khanlari, K., Xie, H., & Liu, X. (2022). Enhanced hardness and toughness in WC/W2C-Ni-Cu composites fabricated by selective laser melting. *International Journal of Refractory Metals and Hard Materials*, 105(July 2021), 105805. <https://doi.org/10.1016/j.ijrmhm.2022.105805>
- Tang, M. (2021). Microstructural evolution, mechanical and tribological properties of TiC/Ti6Al4V composites with unique microstructure prepared by SLM. *Materials Science and Engineering: A*, 814, 141187. <https://doi.org/https://doi.org/10.1016/j.msea.2021.141187>
- Tarraste M.; Kolnes, M.; Kübarsepp, J.; Juhani, K.; Viljus, M.; Külaviir, J. (2020). Green WC-FeMn cemented carbides for industrial wear parts. In *Euro PM2020 Congress Proceedings*.
- Tarraste, M., Kübarsepp, J., Juhani, K., Mere, A., Kolnes, M., Viljus, M., & Maaten, B. (2018). Ferritic chromium steel as binder metal for WC cemented carbides. *International Journal of Refractory Metals and Hard Materials*, 73, 183–191. <https://doi.org/https://doi.org/10.1016/j.ijrmhm.2018.02.010>
- Tokita, M. (2021). Progress of Spark Plasma Sintering (SPS) Method, Systems,. *Ceramics*, 39, 160–198.
- Tonelli, L., Fortunato, A., & Ceschini, L. (2020). CoCr alloy processed by Selective Laser Melting (SLM): effect of Laser Energy Density on microstructure, surface morphology, and hardness. *Journal of Manufacturing Processes*, 52, 106–119. <https://doi.org/https://doi.org/10.1016/j.jmapro.2020.01.052>
- Uhlmann, E., Bergmann, A., & Bolz, R. (2018). Manufacturing of carbide tools by Selective Laser Melting. *Procedia Manufacturing*, 21, 765–773. <https://doi.org/10.1016/j.promfg.2018.02.182>
- Uhlmann, E., Bergmann, A., & Gridin, W. (2015). Investigation on Additive Manufacturing of Tungsten Carbide-cobalt by Selective Laser Melting. *Procedia CIRP*, 35, 8–15. <https://doi.org/10.1016/j.procir.2015.08.060>
- Ullah, R., Lu, J., Sang, L., Rizwan, M., Zhang, Y., & Zhang, Z. (2021). Investigating the microstructural evolution during deformation of laser additive manufactured Ti–6Al–4V at 400 °C using in-situ EBSD. *Materials Science and Engineering: A*, 823, 141761. <https://doi.org/https://doi.org/10.1016/j.msea.2021.141761>
- Vilaro, T. (2011). As-Fabricated and Heat-Treated Microstructures of the Ti-6Al-4V Alloy Processed by Selective Laser Melting. *Metallurgical and Materials Transactions A*, 42(10), 3190–3199. <https://doi.org/10.1007/s11661-011-0731-y>
- Voitovich, V. B., Sverdel, V. V., Voitovich, R. F., & Golovko, E. I. (1996). Oxidation of WC-Co, WC-Ni and WC-Co-Ni Hard Metals in the Temperature Range 500-800°C. *International Journal of Refractory Metals and Hard Materials*, 14(4), 289–295. [https://doi.org/10.1016/0263-4368\(96\)00009-1](https://doi.org/10.1016/0263-4368(96)00009-1)

- Wang, L., Liu, H., Huang, C., Zou, B., & Liu, X. (2014). Effects of sintering processes on mechanical properties and microstructure of Ti(C,N)–TiB<sub>2</sub>–Ni composite ceramic cutting tool material. *Ceramics International*, 40(10, Part B), 16513–16519. <https://doi.org/https://doi.org/10.1016/j.ceramint.2014.08.003>
- Wang, Y. (2023). Fabrication of diamond/AlSi10Mg composite using SLM: Effects of processing parameters and pre-/post-treatments. *Journal of Manufacturing Processes*, 95, 27–37. <https://doi.org/https://doi.org/10.1016/j.jmapro.2023.04.001>
- Wu, Y., Xiong, J., Guo, Z., Yang, M., Chen, J., Xiong, S., ... Luo, J. (2011). Microstructure and fracture toughness of Ti(CO.7N0.3)-WC-Ni cermets. *International Journal of Refractory Metals and Hard Materials*, 29(1), 85–89. <https://doi.org/https://doi.org/10.1016/j.ijrmhm.2010.08.004>
- Wysocki, B., Maj, P., Sitek, R., Buhagiar, J., Kurzydłowski, K. J., & Świąszkowski, W. (2017). Laser and Electron Beam Additive Manufacturing Methods of Fabricating Titanium Bone Implants. *Applied Sciences*, Vol. 7. <https://doi.org/10.3390/app7070657>
- Xing, M., Wang, H., Zhao, Z., Zhang, Y., Lou, H., Liu, C., ... Song, X. (2022). SLM printing of cermet powders: Inhomogeneity from atomic scale to microstructure. *Ceramics International*. <https://doi.org/https://doi.org/10.1016/j.ceramint.2022.06.254>
- Xiong. (2009). The influence of working distance on laser deposited WC-Co. *Journal of Materials Processing Technology*, 209(10), 4935–4941. <https://doi.org/10.1016/j.jmatprotec.2009.01.016>
- Xiong, K. (2022). Cooling-Rate Effect on Microstructure and Mechanical Properties of Al<sub>0.5</sub>CoCrFeNi High-Entropy Alloy. *Metals*, Vol. 12. <https://doi.org/10.3390/met12081254>
- Xiong, Y. (2010). (Ti,W)C-Ni cermets by laser engineered net shaping. *Powder Metallurgy*, 53(1), 41–46. <https://doi.org/10.1179/174329009X380581>
- Xiong, Y., Smugeresky, J. E., Lavernia, E. J., & Schoenung, J. M. (2008). Processing and microstructure of WC-CO cermets by laser engineered net shaping. *19th Annual International Solid Freeform Fabrication Symposium, SFF 2008*, 116–127.
- Yadroitsev, I., & Yadroitsava, I. (2015). Evaluation of residual stress in stainless steel 316L and Ti6Al4V samples produced by selective laser melting. *Virtual and Physical Prototyping*, 10(2), 67–76. <https://doi.org/10.1080/17452759.2015.1026045>
- Yang, Y., Zhang, C., Wang, D., Nie, L., Wellmann, D., & Tian, Y. (2020). Additive manufacturing of WC-Co hardmetals : a review. *International Journal of Advanced Manufacturing Technology*, 108(5–6), 1653–1673. <https://doi.org/10.1007/s00170-020-05389-5>
- Yu, Z. (2022). Analysis of microstructure, mechanical properties, wear characteristics and corrosion behavior of SLM-NiTi under different process parameters. *Journal of Manufacturing Processes*, 75, 637–650. <https://doi.org/https://doi.org/10.1016/j.jmapro.2022.01.010>
- Yu, Z., Xu, Z., Guo, Y., Xin, R., Liu, R., Jiang, C., ... Ren, L. (2021). Study on properties of SLM-NiTi shape memory alloy under the same energy density. *Journal of Materials Research and Technology*, 13, 241–250. <https://doi.org/https://doi.org/10.1016/j.jmrt.2021.04.058>
- Zeisig, J., Schädlich, N., Hufenbach, J., Wendrock, H., Kimme, J., & Kühn, U. (2020). Effect of cooling rate on precipitation behaviour and transformation characteristics of a novel FeCrVC cast alloy. *Journal of Alloys and Compounds*, 816, 152544. <https://doi.org/https://doi.org/10.1016/j.jallcom.2019.152544>

- Zhang, L. (2022). Laser powder bed fusion of cemented carbides by developing a new type of Co coated WC composite powder. *Additive Manufacturing*, 55, 102820. <https://doi.org/https://doi.org/10.1016/j.addma.2022.102820>
- Zhang, X., Guo, Z., Chen, C., & Yang, W. (2018). Additive manufacturing of WC-20Co components by 3D gel-printing. *International Journal of Refractory Metals and Hard Materials*, 70, 215–223. <https://doi.org/https://doi.org/10.1016/j.ijrmhm.2017.10.005>
- Zheng, B., Haley, J. C., Yang, N., Yee, J., Terrassa, K. W., Zhou, Y., ... Schoenung, J. M. (2019). On the evolution of microstructure and defect control in 316L SS components fabricated via directed energy deposition. *Materials Science and Engineering: A*, 764, 138243. <https://doi.org/https://doi.org/10.1016/j.msea.2019.138243>
- Zheng, T., Pan, S., Murali, N., Li, B., & Li, X. (2022). Selective laser melting of novel 7075 aluminum powders with internally dispersed TiC nanoparticles. *Materials Letters*, 319, 132268. <https://doi.org/https://doi.org/10.1016/j.matlet.2022.132268>
- Zhou, Q., Huang, D., Xu, K., Lou, M., Lv, J., Wang, F., ... Chang, K. (2023). Effect of La<sub>2</sub>O<sub>3</sub> addition on microstructure and mechanical properties of TiC-based cermets. *Ceramics International*, 49(11, Part B), 18125–18133. <https://doi.org/https://doi.org/10.1016/j.ceramint.2023.02.181>
- Zhuang, Q., Lin, N., He, Y., & Kang, X. (2017). Influence of temperature on sintering behavior and properties of TiC-Fe-Co-Ni-Cr-Mo cermets. *Ceramics International*, 43(17), 15992–15998. <https://doi.org/10.1016/j.ceramint.2017.08.186>

## List of other publications

- V. **H.S. Maurya**, J. Jayaraj, R.J. Vikram, K. Juhani, F. Sergejev, K.G. Prashanth (2023), Additive manufacturing of TiC-based cermets: A detailed comparison with spark plasma sintered samples, *Journal of Alloys and Compounds*, 960, 170436.
- VI. **H.S. Maurya**, R.J. Vikram, K. Kosiba, K. Juhani, F. Sergejev, S. Suwas, K.G. Prashanth (2023), Additive manufacturing of CMCs with bimodal microstructure, *Journal of Alloys and Compounds*, 938, 168416.
- VII. **H.S. Maurya**, L. Kollo, M. Tarraste, Prashanth K. G. (2022), Effect of the Laser Processing Parameters on the Selective Laser Melting of TiC–Fe-Based Cermets, *Journal of Manufacturing and Materials Processing*, 6(2), 35.
- VIII. **H.S. Maurya**, L. Kollo, M. Tarraste, K. Juhani, F. Sergejev, K.G. Prashanth (2023), Selective Laser Melting of TiC-Based Cermet: HIP Studies, *Transactions of the Indian Institute of Metals*, 76, 565–570.
- IX. **H.S. Maurya**, K. Juhani, F. Sergejev, K.G. Prashanth (2022), Additive manufacturing of TiC-based cermet with stainless steel as a binder material, *Materials Today: Proceedings*, 57, 824–828.
- X. S. Mohanty, **H.S. Maurya**, K.G. Prashanth (2023), Selective laser melting of Inconel 718: Effect of thermal treatment on mechanical properties, *Material Today: Proceedings*.

## Acknowledgments

Taking on this Ph.D. journey has been an incredibly life-changing experience for me, and I couldn't have accomplished it without the support and guidance I received from many people. To begin with, I would like to thank my esteemed supervisors Professor and Dean of the Faculty of Engineering, Fjodor Seregjev, and my co-supervisor, Dr. Kristjan Juhani, for his invaluable support, supervision, and tutelage during my PhD degree course. My sincerest gratitude goes to Professor Prashanth Konda Gokuldoss, Head of the Additive Manufacturing lab, for his valuable and enormous guidance and for helping me gain a deeper understanding of additive manufacturing processes. A special thanks to Prof. Jakob Kübarsepp for sharing his in-depth knowledge of hard metals and cermets during my research work and for guiding me. The completion of this Ph.D. would not have been possible without their guidance and constant feedback.

I gratefully acknowledge the funding received towards my Ph.D. from Estonia Research Council (Project No. PRG1145, 2021-2025) under the scope of development of composites “ceramics – Fe alloy” for a wide range of application conditions”. Additionally, I would like to thank Kerli Roosimaa and Program Director Dr. Rocio Estefania Rojas Hernandez, for helping me receive funding from the Fundamental Science and Technology Program of the European Union- Dora Plus grants and Erasmus Plus mobility grants for attending insight and knowledgeable conferences, seminars, summer schools, and short-term research stays.

I also would like to thank Professor Jayaraj Jayamani at Dalarna University, Sweden for accepting my invitation for the short-term research visit. The support and contributions he provided to my research work in the fields of tribology and electrochemistry are greatly appreciated. I would also like to thank Dr. Konrad Kosiba from the Erich Schmid Institute of Materials Science, Austria for his contribution to the part of the research work. In addition, special thanks to R.J Vikram from the Indian Institute of Science, India for his contribution to EBSD analysis.

The academic staff and experimental officers deserve a big thank you for their support and assistance Dr. Lauri Kollo, Dr. Marek Tarraste, Dr. Maksim Antonov Dr. Rainer Traksmaa, Dr. Mart Viljus, Endel Esinurm, Mrs. Laivi Väljaots, Dr. Le Liu, Hans Vallner, Dr. Mart Saarna, and Dr. Märt Kolnes. Their hard-earned experience and expertise were generously imparted in the metallography preparation of the samples, mechanical testing, optical and electron microscopy, XRD, and so on. Special thanks to my friends and lab mates Shangavi, Javad, and Mayank for their warm support. It would not have been possible to complete the work without their assistance. Thanks go out to the Department of Mechanical and Industrial Engineering, and Taltech as a whole, for making my transition to a Ph.D. smooth. Thanks, from the bottom of my heart to some incredible people who visited Taltech for a research visit from different universities and created some memories that will last a lifetime. Among them, Shalini, Dinesh, Jayashree, Lokesh, and Viraj deserve special mention.

Lastly, to my family, I would like to thank them for encouraging me in all of my endeavours and for providing me with the inspiration to pursue my dreams. Their belief in me has kept my spirits and motivation high during this process. I would also like to thank my friends for all the entertainment and emotional support.

Himanshu Singh Maurya  
October 2023, Tallinn

## Abstract

### Additive Manufacturing of TiC-based cermets with Fe based Binders using Novel Laser Scan Techniques

Cermets or ceramic matrix composites belong to the special class of materials that combine both ceramic and metallic phases to reap the properties of both ceramics and metallic phases together. Contrary to conventional WC-based hard metals, TiC-based ceramics exhibit better oxidation resistance, thermal stability, high red hardness, and wear resistance at elevated temperatures.

Cermets are primarily used in tool applications and parts requiring high wear resistance. It is possible to improve the properties of the Hardmetals and Cermets by combining the right binder material or proportion of the ceramic and binder phase (carbides, nitrides vs. binder), which allows engineers to explore a wide range of possibilities. Moreover, in terms of health and economics, W, Co, and Ni have been declared carcinogens and incorporated into the list of critical raw materials by the European Union. Due to this, recent developments have focused on the development of TiC-based cermets with low cost and superior wear resistance.

Cermets and Hardmetals are generally prepared using the classical powder metallurgical route – press and sinter. Moreover, fabrication of such materials via a conventional sintering route involves restrictions such as geometrical complexity and size, excessive equipment requirements for the processes such as powder injection molding, time- and cost-consuming post-processing, and extensive machining operation.

Novel additive manufacturing (AM) processes may be used to fabricate the parts from the cermets to broaden their applications and fabricate intricate parts with added functionalities. AM-based technologies such as “laser-based processing” use a laser as a power source to melt and fuse powder components. As the AM process involves layer-by-layer fabrication, cermets can yield parts with intricate shapes without boundary restriction. The laser powder-bed fusion process (L-PBF) commonly known as selective laser melting (SLM) can be used to fabricate the parts from the cermets using the laser solidification route. The advantage of solidification-based AM is that it allows for the production of near-dense and neat-net-shaped components without the need for further post-processing.

The current thesis focuses on the development of TiC-based cermets with different Fe-based binders by direct Additive manufacturing technology based on laser powder bed fusion (LPBF) such as Selective Laser Melting (SLM). Novel laser scanning techniques, Laser Pulse Shaping, and Multiple laser Scanning have been adapted to consolidate such brittle materials by controlling the melt pool/powder bed temperature during the fabrication of parts. The application of such laser scan strategies to the cermets parts allows for modulation of the microstructure and process defects. Moreover, the influence of the laser process parameters of both laser scan techniques on the fabrication of the cermets parts has been investigated; the optimal parameters to fabricate such cermets parts via the Additive manufacturing route have been developed.

The microstructure of the TiC-based cermets with different Fe-based binders exhibits gradient microstructure due to SLM’s complex thermal history. Variations in microstructure resulted from the adaptation of different laser scanning techniques and laser process parameters. Moreover, SLM-fabricated cermets parts exhibit a finer microstructure compared to conventionally produced TiC-based cermets.

Mechanical properties such as microhardness, fracture toughness, and compressive strength of the fabricated parts from the cermets have been discussed extensively. The wear behavior of the additively manufactured cermets parts has been investigated by scratch testing as a function of load. The effect of SLM characteristic microstructures on the wear mechanism has been investigated in detail.

**Keywords:** Cermets, Titanium carbide-based cermets, Selective Laser Melting, Steel binder, Laser Pulse shaping, Rescanning

## Lühikokkuvõte

### Titaankarbiidsete Fe-baasil sideainega kermiste valmistamine uudse laserskaneeriva kihtlisandustehnoloogia teel

Kermised ehk keraamilis-metalsed komposiidid on keraamilise ja metalse faasi baasil komposiitmaterjalid, milles on ühendatud keraamika kõvadus metalse faasi plastisusega kombineerides sellega mõlema omadusi. Erinevalt klassikalistest volframkarbiidi baasil kõvasulamitest iseloomustab titaankarbiidi baasil kermiseid parem oksüdeerumiskindlus, termiline stabiilsus ning suur kõvadus ja kulumiskindlus kõrgematel temperatuuridel.

Kermiste peamisteks kasutusvaldkondadeks on metallide töötlemise tööriistad ja masinaosad, kus on nõutav kõrge kulumiskindlus. Kombineerides kõvasulamite ja kermiste keraamilise ja metalse faasi suhet (karbiid, nitriid vs sideaine) või kasutades erinevaid sideaine kombinatsioone on võimalik valmistada komposiite mis sobivad kasutamiseks laias kasutustingimuste vahemikus ja laiendavad tunduvalt inseneride võimalusi seadmete projekteerimisel. Samas, arvestades tervishoiu ja keskkonnakaitse ning kättesaadavuse aspekte on W-baasil kõvasulamites kasutatavad W ja Co ning Ti-baasil kermistes laialt kasutatav Ni tunnistanud kantserogeenseteks ning lisatud ka Euroopa Liidu kriitiliste toorainete (Critical Raw Materials – CRM) nimekirja. Seetõttu on viimasel ajal kermistealane uurimistöö fokuseerunud W-, Co- ja Ni-vabade kõrgendatud kulumiskindlusega titaankarbiidi baasil kermiste arendamisele.

Kermiseid valmistatakse kasutades traditsioonilist pulbermetallurgia tootmistehnoloogiat – pressimine ja paagutamine. Traditsioonilise tehnoloogia kasutamise puuduseks on tehnoloogia olemusest tulenevad piirangud toote geomeetria ja mõõtmetele, samuti kasutatavate seadmete (näites pulbersurvevalu masinate) kõrge maksumus, aega- ja ressursi nõudev järeltöötlus.

Uudsete kihtlisandustehnoloogiate (AM) kasutamine kermiste valmistamiseks võimaldab laiendada nende kasutusvaldkondi ja toota keeruka kujuga ja täiendatud funkionaalsusega detaile. Kihtlisandustehnoloogiad, näiteks “laseri-baasil töötlemine” kasutab laserit energiaallikana pulbriosakeste sulatamiseks. Kuna kihtlisandustehnoloogia korral valmistatakse detail kiht-kihi haaval on võimalik valmistada keeruka geomeetriaga kujupiiranguteta kermisest detaile. Laseriga pulbrivannis materjali sulatamise protsessi (L-PBF), laiemalt tuntud kui selektiivne laser sulatus (SLM), on võimalik kasutada kermiste valmistamiseks laser-tahkumine meetodil. Sellise meetodi eeliseks on, et ta võimaldab valmistada teoreetilise lähedase tiheduse ja kõrge täpsusega detaile, mis välistab vajaduse järeltöötamiseks.

Käesolev doktoritöö keskendub Fe-baasil sideainetega titaankarbiidsete kermiste valmistamisele, kasutades otsest laseriga pulbrivannis materjali sulatamise protsessi (L-PBF) kihtlisandustehnoloogiat (AM) selektiivne laser sulatus (SLM). Uudsed laseriga skaneerimise meetodid, laserimpulss töötlemine (laser pulse shaping) ja mitmekordne laseriga skaneerimine kohandati habraste materjalide valmistamiseks kontrollides pulbrivanni temperatuuri valmistamise käigus. Uuritud laseri kasutamisstrateegia kermiste valmistamiseks võimaldas moduleerida kermiste mikrostruktuuri ja protsessi defekte. Uuriti protsessi parameetrite mõju kermistele mõlema laseriga skaneerimise meetodi korral; töötati välja optimaalsed protsessiparameetrid titaankarbiidsete kermiste valmistamiseks kasutades kihtlisandustehnoloogiat.

Kihltisandustehnoloogia teel valmistatud Fe-baasil sideainega titaankarbiidseid kermiseid iseloomustav gradientne mikrostruktuur on põhjustatud selektiivse lasersulatuse (SLM) käigus toimunud keerukatest termilistest protsessidest. Erinevused mikrostruktuurides tulenevad erinevate laseriga skaneerimise meetodite kasutamisest ja kasutatud protsessi parameetritest. Selektiivse lasersulatuse (SLM) teel valmistatud titaankarbiidsed kermised on peeneteralisema struktuuriga võrreldes traditsioonilise tehnoloogia teel valmistatutega.

Uuriti kihltisandustehnoloogia teel valmistatud Fe-baasil sideaine titaankarbiidsete kermiste mehaanilisi omadusi (mikrokõvadus, purunemissitkus ja survetugevus) ja kulumiskindlust kasutades kriipetesti erinevate koormustega, selgitati välja kulumismehhanismi sõltuvus mikrostruktuurist.

**Märksõnad:** kermised, titaankarbiidsed kermised, selektiivne lasersulatus, terassideaine, pulseeriv laser, üleskaneerimine

## Appendix

### **Publication I**

Himanshu Singh Maurya, Lauri Kollo, Marek Tarraste, Kristjan Juhani, Fjodor Sergejev, Konda Gokuldoss Prashanth, Selective Laser Melting of TiC-Fe via Laser Pulse Shaping: Microstructure and Mechanical Properties. 3D Printing and Additive Manufacturing (2022).





ORIGINAL ARTICLE

# Selective Laser Melting of TiC-Fe via Laser Pulse Shaping: Microstructure and Mechanical Properties

Himanshu Singh Maurya,<sup>1</sup> Lauri Kollo,<sup>1</sup> Marek Tarraste,<sup>1</sup> Kristjan Juhani,<sup>1</sup> Fjodor Sergejev,<sup>1</sup> and Konda Gokuldoss Prashanth<sup>1-3</sup>

## Abstract

In the present study, TiC-Fe cermets were fabricated through selective laser melting (SLM) for the first time employing pulse wave using a pulse shaping technique and regular laser pulse wave. Two samples were fabricated each with adapting pulse shaping technique and regular laser pulse wave with varied laser peak power and exposure time to obtain an optimized parameter. The pulse shaping technique proves to be an optimal method for fabrication of the TiC-Fe-based cermet. The effect of the laser peak power and pulse shaping on the microstructure development was investigated through scanning electron microscopy and X-ray diffraction analysis. Two-phased microstructures revealed the distribution of TiC and Fe. A maximum hardness and fracture toughness of  $1010 \pm 65$  MPa and  $16.3 \pm 1.7$  MPa m<sup>1/2</sup>, respectively, were observed for the pulsed-shaped samples illustrating that pulse shaping can be an effective way to avoid cracking in brittle materials processed by SLM.

**Keywords:** pulse shaping, cermets, additive manufacturing, carbides

## Introduction

CERMETS ARE USEFUL in applications that demand high hardness and wear resistance combined with a high toughness.<sup>1-5</sup> Some of their applications include high-speed metal cutting and high temperature erosive and corrosive environments.<sup>6,7</sup> TiC-based cermets have received renewed interest in recent years, especially bonded with iron-based alloys, where environmentally harmful and scarce metals such as W, Co, and Ni are excluded. Due to its high hardness, wear resistance, chemical, and high temperature stability, TiC proves to be a most promising alternative for conventional tungsten carbide (WC)-based cermets.<sup>8-11</sup>

Fe-based binders are considered an alternative solution as they are abundantly available, cost-effective, and nontoxic and offer to strengthen by heat treatment. Selective laser melting (SLM) or laser-based powder bed fusion is an additive manufacturing technique based on powder bed fusion (PBF) technology that fabricates parts layer by layer by scanning the powder bed se-

lectively and melting and fusing the subsequent layer of fine metal powder to deposit on the substrate.<sup>12-14</sup> The formation of melt pool during laser scan and the subsequent rapid solidification offers a wide range of advantages including refined microstructures compared with their conventional counterparts.<sup>15-19</sup>

There is increasing demand to fabricate parts using additive manufacturing especially for rapid tooling applications due to its high density, high temperature wear resistance, hardness, and homogeneity in the microstructure.<sup>20-22</sup> Even though laser power has a significant influence on the processing of parts,<sup>23</sup> laser beam emission type (i.e., continuous or pulsed wave) plays a significant role. Laser beam may act as the heat source for melting the single powder layer, and the temporal distribution of laser power plays a vital role in achieving the density and evolution of unique microstructure in the processed parts.<sup>24-26</sup>

Due to strong metallurgical bonding between layers and small heat-affected regions, pulsed wave lasers (PWs) have

<sup>1</sup>Department of Mechanical and Industrial Engineering, Tallinn University of Technology, Tallinn, Estonia.

<sup>2</sup>Erich Schmid Institute of Materials Science, Austrian Academy of Sciences, Leoben, Austria.

<sup>3</sup>CBCMT, School of Mechanical Engineering, Vellore Institute of Technology, Vellore, India.

been found to be more suitable for SLM manufactured parts than continuous-wave lasers.<sup>26–28</sup> The process parameters influence the fabrication process and generate thermal stress and temperature gradient in the parts, and the parameters should be carefully optimized to produce parts without defects such as cracks, porosities, warpage, and delamination.<sup>29–31</sup> There are only a few studies on cermets fabricated using SLM, and the majority of these studies focus on the classical WC-Co-based cermets.<sup>7,32–34</sup>

*In situ* TiC processing, where TiC is used as a reinforcement particle in the metal matrix, has been documented by several researchers.<sup>35–37</sup> However, the authors are not aware of any literature dealing with the processing of TiC-based cermets and yielding crack-free specimens. Most of these cermets are anticipated to induce cracks during the SLM process because of their inherent brittleness, which limits the processing of these materials by solidification-based additive manufacturing processes.

In this work, the pulse shaping technique is adapted as it temporarily distributes the energy within a single layer of the pulse. Pulse shaping help to control the laser material exposure by delivering controlled energy.<sup>38</sup> In particular, pulse shape and duration regulate the release of the energy onto the processed material.<sup>38–40</sup> By tuning the pulse with different peak powers, exposure times allow gradual heating and/or prolonged cooling effect within the powder bed that helps controlling the melt pool properties and subsequently the formation of the final part.

The thermal history of the laser emission is considerably linked with the heating and cooling rates, which influence both the microstructure and in turn their mechanical properties. The difference in the laser scanning strategy plays a vital role in the melt pool formation due to the nonuniform heating and cooling effect in the melt pool and eventually inducing differences in the microstructure.<sup>31</sup> Accordingly, for the first time, this article deals with the fabrication of TiC-based cermets with Fe as binder through an additive manufacturing process by adapting a point exposure and in the *y*-direction, scanning strategy with different pulse shaping to avoid possible cracking in the cermet during solidification.

## Experimental Details

### Powder preparation

The details of both TiC and Fe powder used in the present work are furnished in Table 1. Feedstock powder (200 g) for SLM with 60 wt.% TiC and 40 wt.% Fe was prepared by mechanical mixing with the help of zirconia balls (five in number with the following dimensions: 2 mm in diameter and five in number) for 24 h at 10 rpm. Stainless steel vial with a

volume of 500 mL, dimensions of 80 mm in diameter and 130 mm in height was used.<sup>41</sup>

Figure 1 shows the scanning electron microscopy (SEM) images of the initial and the mixed powders. It can be observed from Figure 1a that the Fe particles are spherical in shape with quite significant distribution in size. However, the TiC particles are irregular in shape with a narrow size distribution (Fig. 1b). The cermet powder after mechanical mixing shows the presence of both spherical and irregularly shaped powder particles with a very wider distribution in their size (Fig. 1c). However, they are <45  $\mu$ m in size. The X-ray diffraction (XRD) pattern of the mixed cermet shows the presence of the peaks of both TiC and Fe phases (Fig. 1d). No other additional phases are observed indicating that the mechanical milling process does not form any new phases.

### Selective laser melting

The pulsed laser was used for the fabrication of TiC-Fe-based cermets using Realizer 50 SLM system equipped with Nd:YAG laser with a maximum power of 100 W. Samples with both standard and shaped pulse laser were used for fabrication. A schematic diagram showing the scanning strategy adapted for a single pulse to fabricate the samples with both types of pulses is shown in Figure 2. The focal diameter of the laser beam spot on the work piece surface is fixed at 0.0134 mm. Stainless steel substrate was used to build the samples in an argon atmosphere to protect the melt pool from oxidation. With the standard pulse laser, the scan direction was along the *y*-axis with a hatch distance of 0.5  $\mu$ m and an exposure time of 200  $\mu$ s.

Samples A and B were printed with the same exposure time and with different laser powers (60 and 72 W, respectively, Fig. 2c). However, for the samples, C and D pulse shaping technique was adapted with different peak laser powers with the employment of pulse to fabricate the cermets, as shown in Figure 2d. With the employment of pulsing, the laser exposure was targeted to an exposure point and the same pulse is repeated to each laser exposure point. The samples were built in the vertical direction with a layer thickness of 0.035 mm and a point distance of 0.5  $\mu$ m. Table 2 represents the SLM process parameter adapted for the fabrication of cermets.

### Phase identification and microstructure observation

The printed cermets were ground and polished for the microstructural characterization. The longitudinal section of the cermets was examined by SEM Zeiss EVO MA15 equipped with the X-ray spectroscopy (EDS) system INCA for microstructural and elemental composition analysis, respectively. The structural characterization (in terms of phase identification) was carried out by the Rigaku SmartLab X-Ray Diffractometer.

Thermo-Calc<sup>®</sup> software with TCFE9 database was used to study the possible phase formation during the SLM process (Fig. 3a). Since Ti, C, and Fe are the elements involved, the following observations are made using Thermo-Calc: TiC phase is stable over a wide range of compositions. No new intermetallic phase can be observed. Iron titanium solid solution can be seen along with graphite formation at lower temperatures. The volume of the phases present and particle size were measured from the SEM images using the ImageJ software.

TABLE 1. THE SIZE, PURITY, AND SOURCE OF THE POWDERS USED IN THIS STUDY

Material	Average particle size ( $\mu$ m)	Purity (%)	Source
TiC	2–3	99.9	Pacific Particulate Materials Ltd.
Fe	45	99.8	TLS Technik GmbH

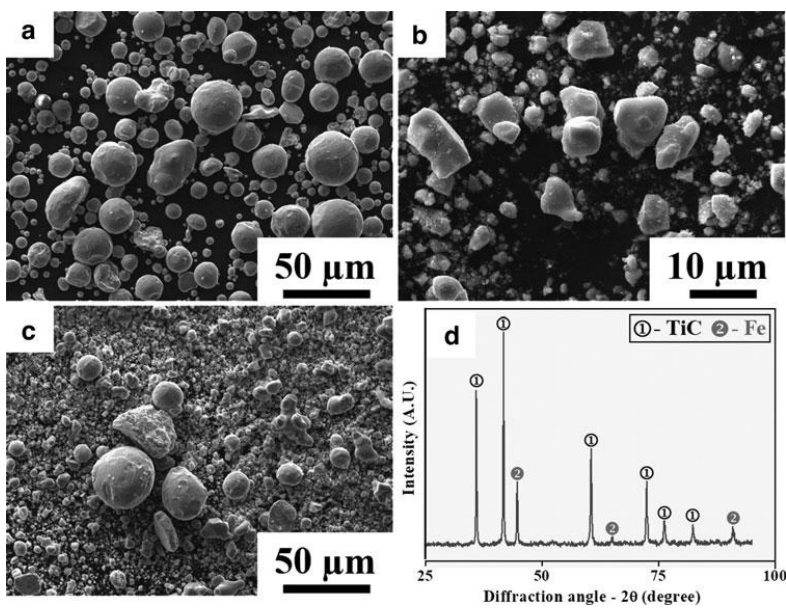


FIG. 1. SEM images of the starting powders: (a) Fe and (b) TiC and mechanically mixed cermet (c) TiC-Fe mixture. (d) The X-ray diffraction pattern of the mixed cermet TiC-Fe powder. SEM, scanning electron microscopy.

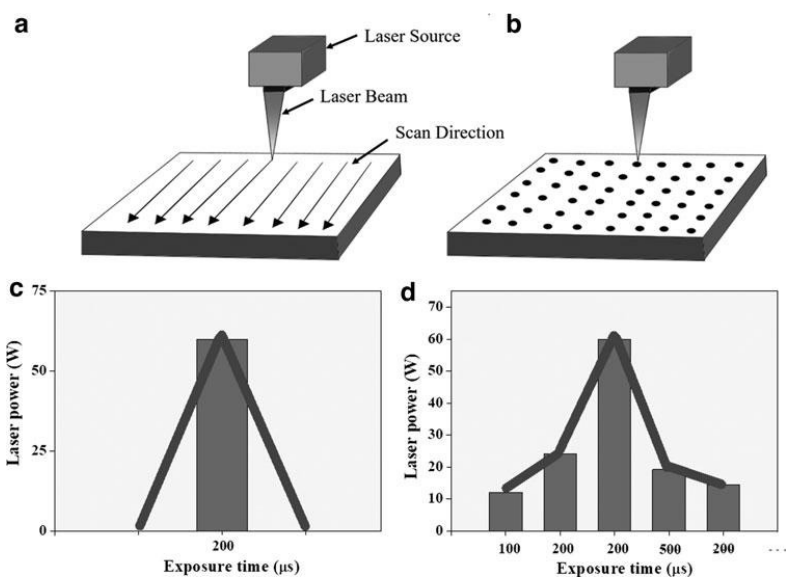


FIG. 2. Schematics illustrating the different pulse shaping used in the present study: (a) hatching along the y-axis (conventional hatching) and (b) laser point exposure. Plots showing the two different pulsing strategies used to produce the TiC-Fe cermets (c) regular pulse (used to fabricate samples A and B) and (d) pulse shaping (used to fabricate samples C and D).

TABLE 2. THE SELECTIVE LASER MELTING PROCESS PARAMETERS USED IN THIS STUDY TO BUILD THE TiC-Fe CERMETS

Sample designation	Pulse type	Laser power (W)	Exposure time ( $\mu$ s)
A	Standard pulse	60	200
B	Standard pulse	72	200
C	Pulse shaping	12-24-60-19.2-14.4	100-200-200-500-200
D	Pulse shaping	12-24-72-19.2-14.4	100-200-200-500-200

**Mechanical characterization**

Cuboidal shaped TiC-Fe samples with near theoretical density were fabricated through SLM with different pulse shaping parameters. Vickers Hardness tests (longitudinal section) were performed using a microhardness testing machine Indentec 5030KV (Indentec Hardness Testing Machines Limited, West Midlands, UK) with a 30 kg load and dwell time of 10 s. The fracture toughness values of the samples were measured through the indentation method with the same load as used for the hardness test. The following equation<sup>42</sup> was used to calculate the fracture toughness.

$$K_{IC} = 0.15 \sqrt{\frac{HV_{30}}{\sum l}} \tag{1}$$

where  $K_{IC}$  is the fracture toughness,  $\sum l$  is the sum of crack lengths of each indentation in mm, and  $HV$  is the hardness value in  $N \cdot mm^{-2}$ . All the reported mechanical testing results are an average of three samples.

**Results and Discussion**

**Phase identification**

Figure 3b shows the XRD results obtained from the longitudinal section of the SLM fabricated cermets. The patterns reveal the presence of high intense sharp peaks corresponding to the following phases: TiC and  $\alpha$ -Fe, where TiC belongs to a simple cubic system with the space group Fm-3m (225) (line NaCl) and  $\alpha$ -Fe belongs to body-centered cubic system (bcc)

with a space group Im-3m (229). No intermetallic and carbide phases appear in the diffraction peak. It may be safe to say that laser pulsing did not have a significant influence on phase formation.

**Microstructure**

Figure 4 shows the surface morphologies of the SLM processed samples through (regular) conventional pulse mode without shaping but as a function of energy density. It shows the presence of the typical laser scan tracks existing on the surface of the sample. Two distinct zones with different TiC phases can be observed in the microstructure (Fig. 4b).

The presence of unmelted TiC particles in the melt pool due to the inhomogeneous powder distribution in the feed-stock powder and its poor flowability can be found as near-spherical particles with light gray areas. The dark gray area represents TiC dendritic phase after melting/dissolution. However, the bright areas correspond to the bcc  $\alpha$ -Fe phase (Fig. 4b, c). The scan speed for samples A and B was kept constant at  $250 \text{ mm} \cdot \text{s}^{-1}$ . However, the change in the laser power varies their energy density. The equation used to calculate the volumetric energy density is as follows<sup>43</sup>:

$$E_v = \frac{P \cdot ET}{PD \cdot HS \cdot h} \tag{2}$$

where  $P$  represents the laser power in Watt,  $ET$  represents exposure time in  $\text{mm} \cdot \text{s}^{-1}$ ,  $PD$  represents point distance in mm,  $HS$  represents hatch space in mm, and  $h$  represents layer thickness in mm. The energy density for samples A and B was found to be 137 and  $165 \text{ J} \cdot \text{mm}^{-3}$ , respectively. In the melt pool, the dendritic TiC phase can be found due to melting and subsequent solidification. With increasing energy density, relatively finer dendritic TiC is observed (Fig. 4d-f).

Coarser TiC phase can be observed along the metal pool boundaries, where minimum temperature gradient ( $G$ ) is observed due to the Gaussian distribution of laser energy (where the maximum temperature gradient is observed at the center of the melt pool and minimum value at its boundaries). The change in the grain size from the melt pool to the

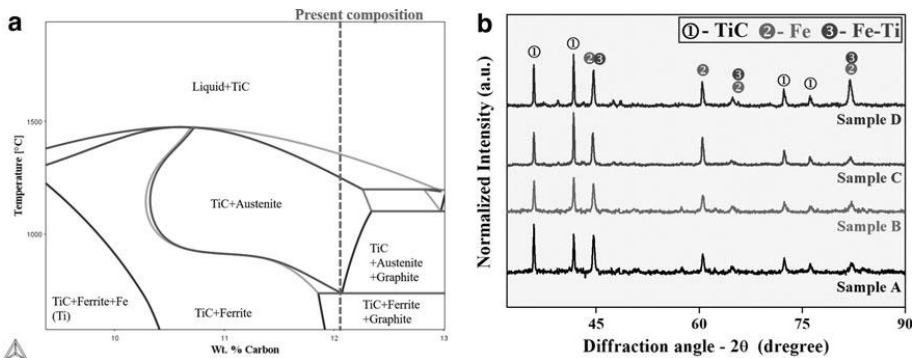


FIG. 3. (a) Ti-C-Fe phase diagram calculated using Thermo-Calc<sup>®</sup> software and TCFE9 database. (b) The XRD patterns of the SLM fabricated cermets fabricated as function of laser pulsing. SLM, selective laser melting; XRD, X-ray diffraction.

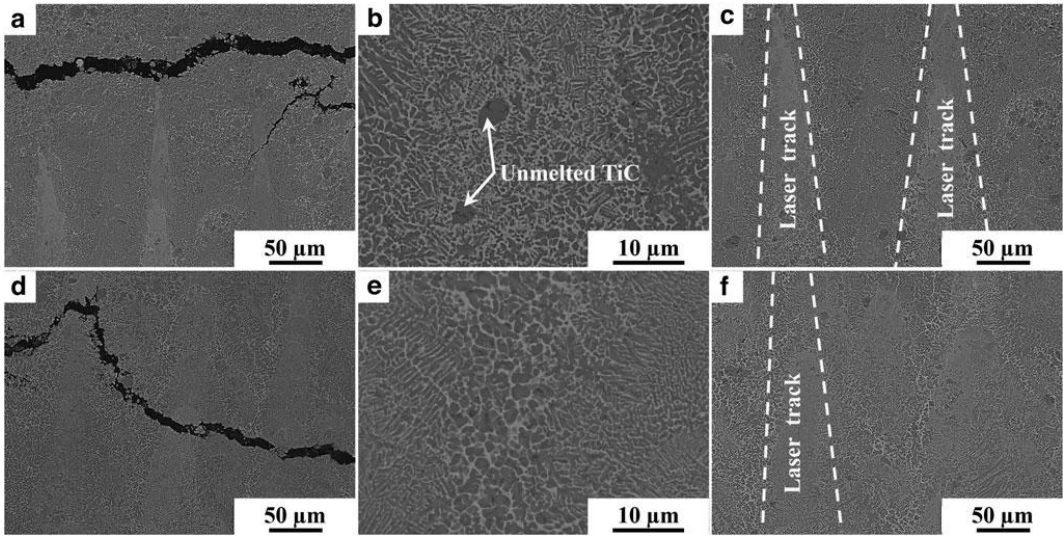


FIG. 4. SEM images (longitudinal section) of the as-built cermet through regular pulsing but with varying energy densities: (a–c) sample A,  $E_v$   $137 \text{ J} \cdot \text{mm}^{-3}$ ; (d–f) sample B,  $E_v$   $165 \text{ J} \cdot \text{mm}^{-3}$ .

boundary can be explained using a thermal gradient ( $G$ ), solidification rate ( $R$ ), and cooling rate ( $T$ ) by fineness factor ( $T = G \times R$ ) and shape factor ( $G/R$ ).<sup>40–47</sup> The maximum temperature in the melt pool for the Gaussian distributed laser source is proportional to the  $P/\sqrt{\nu}$  ratio.<sup>48</sup>

$$T_{\max} \propto \frac{P}{\sqrt{\nu}}, \quad (3)$$

where  $P$  is the laser power in Watt and  $\nu$  is the scanning speed in  $\text{mm} \cdot \text{s}^{-1}$ . In the present study, the scanning speed is kept constant; however, an increase in the laser power increases the temperature of the melt pool, which means higher  $G$ , and apparently higher  $G/R$  ratio resulting in a finer microstructure. However, surrounding the melt pool boundaries, these  $G/R$  ratios will be low due to the Gaussian distribution of laser energy, and hence, coarser equiaxed grains were formed.

On the surface of as-built samples, cracks can be observed perpendicular to the direction of the melt pool/laser tracks. The large thermal residual stress, which is inherent to SLM samples in the as-built condition due to rapid melting and cooling rates under a high-intensity laser input, leads to crack formation.<sup>29,49–51</sup> The length and number of cracks increase with the increase in the cooling rate and increasing cooling rate increase the degree of residual stresses.<sup>52–54</sup> These multidirectional cracks initiated from the sample's edge and spread across its entire surface.

Due to surface and internal defects in as-built samples, the fabrication of TiC-based cermet using regular pulsing without shaping was not considered optimal. The exhibition of cracks hampers the mechanical performance of the samples and shortens the lifetime during constant or cyclic loadings and leads to premature failure of the as-built cermet parts. Consequently, it is very important to suppress these cracks

and produce dense parts for real-time applications. Therefore, for the first time, pulse-shaping technology is adapted for the fabrication of TiC-Fe-based cermets to control the energy distribution of the laser power during fabrication, and significantly, these distributions in energy affect the melting and cooling rate of the process.

Figure 5 shows the characteristic morphology of the TiC and Fe phase fabricated with the application of pulse shaping using SLM. It can be noticed that changes in the laser power significantly influence the morphology of the TiC phase, similar to the counterpart without laser shaping. Using a laser power of 60 W (Fig. 5a, b), columnar dendritic microstructure can be observed near the zone of laser exposure surrounded by coarse TiC phase. There exists a gradient microstructure in terms of TiC size as we move from the core of the melt pool toward the overlapping boundaries, which may be attributed to the laser shape (pulse shaping).

However, increasing the laser power to 72 W, a high cooling/solidification rate will be observed, leading to finer microstructure similar to the ones observed for the samples A and B fabricated without pulse shaping. Samples produced with 72 W laser power shows more uniform finer dendrites along with the core of the melt pool and even in the overlapping regions; coarse TiC particles (significantly reduced in size compared with the samples fabricated with 60 W laser power) are observed. A gradient in the size of the TiC dendrites is observed moving from the center of the melt pool toward the overlapping regions due to the inherent laser beam geometry (Fig. 5). This might also be attributed to the difference in the solidification rates observed along the different sides of the melt pool.<sup>55–57</sup>

The most interesting aspect to be noticed is that with the introduction of pulse shaping, the SLM fabricated cermets do not show signs of cracking, and in fact, no visible cracks are

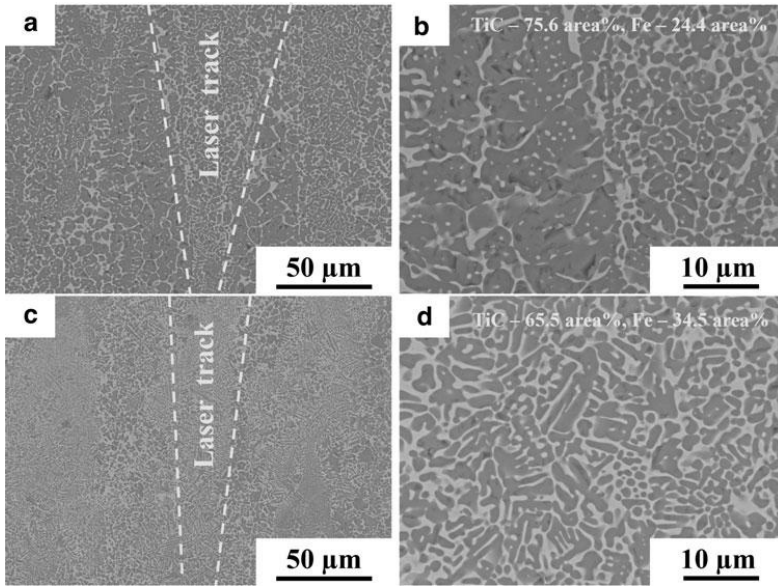


FIG. 5. SEM images (longitudinal section) of the as-built cermets with pulse shaping showing different morphologies at different laser powers: (a, b) sample C, 60 W laser power; (c, d) sample D, 72 W laser power.

observed in these microstructures (Fig. 4). In addition, no unmelted TiC particles are present suggesting a complete melting of the initial powder particles. The results suggest that the fabrication of cermets through the pulse shaping technique can eliminate the formation of cracks and may be considered an optimal way to fabricate TiC-Fe-based cermets.

Figure 6 shows the EDS elemental maps of the longitudinal section of the printed sample, where the elemental distribution of Ti, C, and Fe can be observed. It may be observed from Figure 6 that the SLM samples show the

nonuniform distribution of phases in terms of their sizes, where the presence of both fine and coarse features are observed, typical for SLM samples.<sup>12</sup>

*Mechanical properties*

The mechanical properties of the pulse-shaped as-built SLM samples were investigated via hardness and fracture toughness measurements. Since the samples fabricated without laser pulse shaping do show the presence of cracks all over their

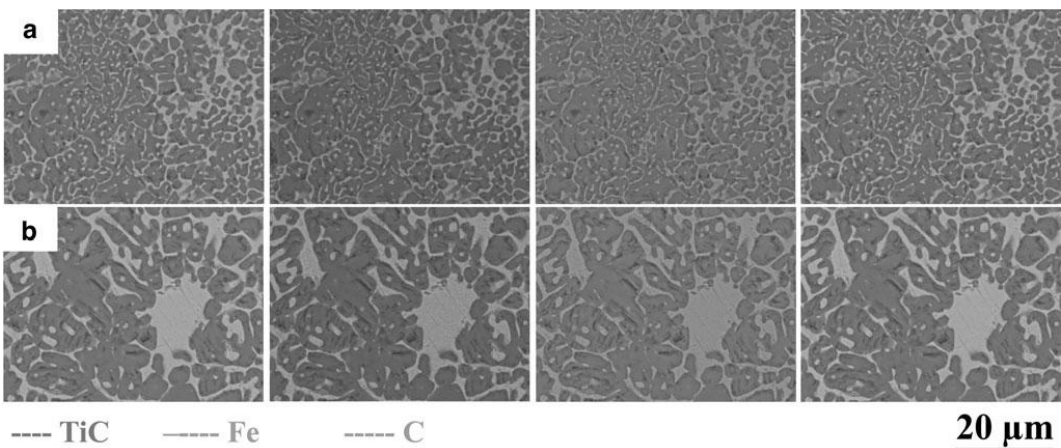


FIG. 6. Energy-dispersive spectroscopy mapping of the cermet samples fabricated through pulse shaping: (a) sample C, (b) sample D.

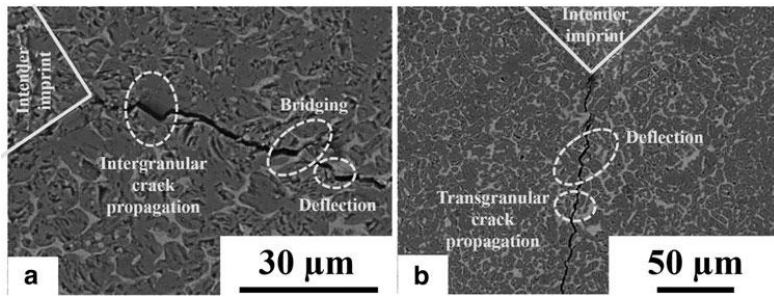


FIG. 7. Scanning electron micrographs showing the crack propagation in the SLM prepared: (a) sample C, (b) sample D.

surface, the SLM samples produced without pulse-shaping was not utilized for any hardness and toughness measurements. The fluctuation in the hardness values (large error bars) can be observed due to the significant difference in the hardness values of TiC (>2000 HV) and Fe (<200 HV).

Hence, the hardness fluctuation depends on where the indenter is placed as in on the TiC phase or on the Fe phase or intermediate to these two phases. Both samples C and D show a reduction in their hardness values with the increase in laser power from  $1010 \pm 65$  to  $730 \pm 100$  HV, respectively. The gradual decrease in the hardness by increasing the laser peak power is attributed to the decreased formation of the gradient TiC phase, and thus, a reduction in the volume fraction of TiC and at the expense of an increase in the volume of the  $\alpha$ -Fe phase (Fig. 5).

First, the fracture toughness values observed for these SLM processed TiC-Fe-based cermets are in the range of other TiC-based cermets, suggesting that the SLM processed samples are sound without any appreciable defects present within them.<sup>58–60</sup> Fracture toughness for samples C and D is

$16.3 \pm 1.7$  and  $13.8 \pm 1.3$   $\text{MPa} \cdot \text{m}^{1/2}$ , respectively. The results show that depending on the laser peak strength, the fracture toughness value varies significantly. To better understand the fracture toughness, the crack propagation mechanism was investigated. Figure 7 shows the crack propagation in the pulsed shaped samples. The propagation of the crack follows a zigzag path corroborating crack deflection during propagation.

Due to different mechanical features and interfacial mismatches, a strain field is observed at the interface of TiC and  $\alpha$ -Fe. When the crack tip reaches this interface, the accumulation of stress concentration occurs due to which the propagation of the crack tends to lower the fracture energy at the interface and causes a transgranular fracture. The total length of the crack increases due to deflection, which consumes the fracture energy and reduces the driving grains providing a restraining force for the crack growth due to which intergranular fracture occur and it consumed fracture energy sharply during crack propagation and improves the toughness of the material.<sup>61–63</sup>

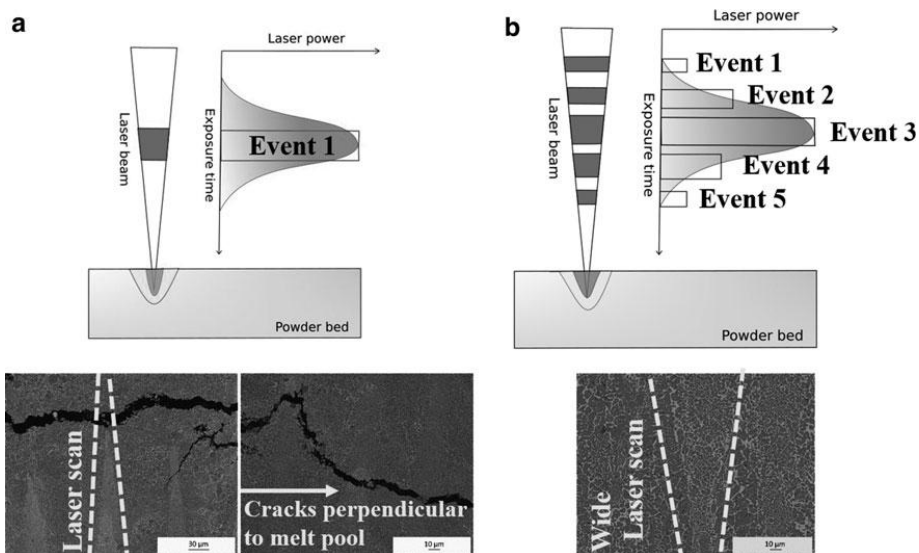


FIG. 8. Schematics illustrating the difference between laser pulsing (a) without and (b) with shaping.

Moreover, grain refinement reduces the crack propagation length and improves the strength and toughness of the material. Therefore, higher fracture toughness of the sample C was ascribed by these fracture energies consuming mechanisms.

#### *Pulse shaping mechanism*

This article aims to investigate the effect of the laser emission regimen on the formation of TiC-based cermets. The temporal profile of laser power given to the material has a significant effect on the thermal process of SLM. A PW produces bursts of energy having a specific amount of energy for a predetermined length of time (Fig. 8a). It can also be characterized as a change in laser power that alters the form of the output pulse and, as a result, the heat distribution within the pulse. The laser temporal emission mode effect on temperature fields of the melt pool influences the size, stability, and densification behavior in the melt pool. A pulse wave emission has been proved to have a beneficial effect in minimizing thermal distortions and increasing process resolution.<sup>64</sup>

However, pulse shaping is a technique for distributing energy temporally within a single laser pulse. Figure 8 reveals the schematic diagram illustrating the working of pulse shaping versus a regular pulse mode. In the case of the regular pulse, contour and hatching scanning modes were used (Fig. 8a), and the hatch distance was predefined by the CAD design. The direction of the laser scan is along the *y*-axis; therefore, the melt pool/laser scan area is defined and narrow compared with the pulse shaping melt/scan area. The direction of the crack generation and propagation of the thermal residual stresses will be perpendicular to the laser scan direction.

However, in the case of the pulse shaping, point scanning strategies were adapted, and for each exposure point, a number of pulse raster's on the one single exposure point is defined as an event here (Fig. 8b). Each event has a varied power and exposure time, which aids in controlling the laser energy distribution. Events (1,2) and (4,5) in a series of pulse shaping have modest laser power and varying exposure times. However, event 3 has a high laser power, the peak power. Event (1,2) can be considered a pre-pulsing event that helps to preheat the feedstock powder with low laser energy density, whereas event (4,5) is a post-pulsing event with varying laser energy densities.

Due to the low laser intensity and prolonged laser exposure duration, post-pulsing serves as a controlled cooling of the melt pool. This energy distribution, together with a controlled heating/cooling rate, aids in the reduction of thermal residual stress and the eradication of cracks. The pre-pulsing events (events 1 and 2) work similar to the raster heating event adopted in the electron beam melting process, which is used to heat the powder bed.<sup>65,66</sup> Because of the high power and regulated laser exposure time, a larger melt pool area is observed, and thus, the melt pool area is strongly reliant on the parameters of the predefined laser exposure parameters.

So in general, the laser shaping leads to preheating of the powder bed (events 1 and 2), actual melting of the powder bed (event 3), and controlled solidification/post-processing of the powder bed (events 4 and 5). The preheating event leads to the elimination of cracks that form due to sudden expansion/contraction in the cermets and the post-processing events lead to partial annealing of the thermal residual stresses, avoids the formation of solidification cracks.

Hence, the present work for the first time demonstrates the effective fabrication of W- and Ni-free TiC-Fe-based cermets without any cracks using the laser pulse shaping technique. The pulsed shaping offers the combined advantage of preheating, melting, and controlled solidification/postheating events that may be suitable for processing brittle materials using the SLM, additive manufacturing process.

#### **Conclusions**

In this study, the TiC-Fe cermet was fabricated successfully for the first time through SLM, by adapting pulse-shaping technology. The samples show the presence of TiC and Fe phases without the formation of new additional phases in the as-built condition. The samples processed through regular pulse waves lead to specimens with cracks. However, the pulse shaping technique helps in eliminating the crack by controlled the energy distribution of laser pulse, which controls the melting and cooling rate in the melt pool. The as-built cermets show a maximum hardness of  $1010 \pm 65$  MPa and a fracture toughness of  $\sim 16.3$  MPa m<sup>1/2</sup>.

Mixed events involving intergranular, transgranular, crack deflection, and crack bridging control the crack propagation and in turn the fracture toughness mechanisms. The results illustrate that effective employment of laser pulse shaping can have a controlled heat input, melting, and dissipation effect on the powder bed, leading to crack-free cermets.

#### **Authors' Contributions**

Conceptualization: H.S.M., L.K., and M.T. Methodology: H.S.M., L.K., and M.T. Validation: H.S.M., K.J., F.S., and K.G.P. Formal analysis: H.S.M., L.K., and M.T. Investigation: H.S.M., L.K., and M.T. Resources: K.J., F.S., and K.G.P. Writing—original draft preparation: H.S.M. Writing—reviewing and editing: H.S.M., L.K., and K.G.P. Funding acquisition: M.T. and K.G.P. All authors have read and agreed to the published version of the article.

#### **Acknowledgment**

The authors would like to express their gratitude to Hans Vallner for the technical assistance.

#### **Author Disclosure Statement**

No competing financial interests exist.

#### **Funding Information**

This work was supported by Estonian Research Council grants PRG1145 and European Regional Development grant ASTRA6-6.

#### **References**

1. Ettmayer P. Hardmetals and cermets. *Annu Rev Mater Sci* 1989;19:145–164.
2. Das K, Bandyopadhyay TK, Das S. A Review on the various synthesis routes of TiC reinforced ferrous based composites. *J Mater Sci* 2002;37:3881–3892.

3. Aramian A, Sadeghian Z, Prashanth KG, *et al.* *In situ* fabrication of TiC-NiCr cermets by selective laser melting. *Int J Refract Met Hard Mater* 2020;87:105171.
4. Yi D, Yu P, Hu B, *et al.* Preparation of nickel-coated titanium carbide particulates and their use in the production of reinforced iron matrix composites. *Mater Des* 2013;52:572–579.
5. Oh NR, Lee SK, Hwang KC, *et al.* Characterization of microstructure and tensile fracture behavior in a novel infiltrated TiC-steel composite. *Scr Mater* 2016;112:123–127.
6. Kübarsepp J, Juhani K. Cermets with Fe-alloy binder: A review. *Int J Refract Metals Hard Mater* 2020;92:105290.
7. Aramian A, Razavi SMJ, Sadeghian Z, *et al.* A review of additive manufacturing of cermets. *Addit Manuf* 2020;33:101130.
8. Sabahi Namini A, Dilawary SAA, Motalebzadeh A, *et al.* Effect of TiB<sub>2</sub> addition on the elevated temperature tribological behavior of spark plasma sintered Ti matrix composite. *Compos Part B Eng* 2019;172:271–280.
9. Klaasen H, Kollo L, Kübarsepp J. Mechanical properties and wear performance of compression sintered TiC based cermets. *Powder Metall* 2007;50:132–136.
10. Klaasen H, Kübarsepp J, Sergejev F. Strength and failure of TiC based cermets. *Powder Metall* 2009;52:111–115.
11. Santos EC, Osakada K, Shiomi M, *et al.* Microstructure and mechanical properties of pure titanium models fabricated by selective laser melting. *Proc Inst Mech Eng Part C J Mech Eng Sci* 2004;218:711–719.
12. Prashanth KG, Scudino S, Klauss HJ, *et al.* Microstructure and mechanical properties of Al-12Si produced by selective laser melting: Effect of heat treatment. *Mater Sci Eng A* 2014;590:153–160.
13. Singh A, Basha DA, Matsushita Y, *et al.* Domain structure and lattice effects in a severely plastically deformed CoCrFeMnNi high entropy alloy. *J Alloys Compd* 2020;812:152028.
14. DebRoy T, Wei HL, Zuback JS, *et al.* Additive manufacturing of metallic components—Process, structure and properties. *Prog Mater Sci* 2018;92:112–224.
15. Zhao C, Wang Z, Li D, *et al.* Selective laser melting of Cu–Ni–Sn: A comprehensive study on the microstructure, mechanical properties, and deformation behavior. *Int J Plast* 2021;138:102926.
16. Wang Z, Xie M, Li Y, *et al.* Premature failure of an additively manufactured material. *NPG Asia Mater* 2020;12:1–10.
17. Suryawanshi J, Prashanth KG, Scudino S, *et al.* Simultaneous enhancements of strength and toughness in an Al-12Si alloy synthesized using selective laser melting. *Acta Mater* 2016;115:285–294.
18. Xi LX, Zhang H, Wang P, *et al.* Comparative investigation of microstructure, mechanical properties and strengthening mechanisms of Al-12Si/TiB<sub>2</sub> fabricated by selective laser melting and hot pressing. *Ceram Int* 2018;44:17635–17642.
19. Salman OO, Brenne F, Niendorf T, *et al.* Impact of the scanning strategy on the mechanical behavior of 316L steel synthesized by selective laser melting. *J Manuf Process* 2019;45:255–261.
20. Marchese G, Garmendia Colera X, Calignano F, *et al.* Characterization and comparison of inconel 625 processed by selective laser melting and laser metal deposition. *Adv Eng Mater* 2017;19:1600635.
21. Wang Z, Tang SY, Scudino S, *et al.* Additive manufacturing of a martensitic Co–Cr–Mo alloy: Towards circumventing the strength–ductility trade-off. *Addit Manuf* 2021;37:101725.
22. Suryawanshi J, Prashanth KG, Ramamurty U. Tensile, fracture, and fatigue crack growth properties of a 3D printed maraging steel through selective laser melting. *J Alloys Compd* 2017;725:355–364.
23. Prashanth KG, Scudino S, Maity T, *et al.* Is the energy density a reliable parameter for materials synthesis by selective laser melting? *Mater Res Lett* 2017;5:386–390.
24. Karami K, Blok A, Weber L, *et al.* Continuous and pulsed selective laser melting of Ti6Al4V lattice structures: Effect of post-processing on microstructural anisotropy and fatigue behaviour. *Addit Manuf* 2020;36:101433.
25. Demir AG, Colombo P, Previtali B. From pulsed to continuous wave emission in SLM with contemporary fiber laser sources: Effect of temporal and spatial pulse overlap in part quality. *Int J Adv Manuf Technol* 2017;91:2701–2714.
26. Olakanmi EO, Cochrane RF, Dalgarno KW. A review on selective laser sintering/melting (SLS/SLM) of aluminium alloy powders: Processing, microstructure, and properties. *Prog Mater Sci* 2015;74:401–477.
27. Dalgarno KW, Wright CS. Approaches to processing metals and ceramics through the laser scanning of powder beds—A review. *Powder Metal Prog* 2001;1:70–79.
28. Santos EC, Shiomi M, Osakada K, *et al.* Rapid manufacturing of metal components by laser forming. *Int J Mach Tools Manuf* 2006;46:1459–1468.
29. Prashanth KG, Shakur Shahabi H, Attar H, *et al.* Production of high strength Al 85 Nd 8 Ni 5 Co 2 alloy by selective laser melting. *Addit Manuf* 2015;6:1–5.
30. Schwab H, Prashanth KG, Löber L, *et al.* Selective laser melting of Ti-45Nb alloy. *Metals (Basel)* 2015;5:686–694.
31. Prashanth KG, Scudino S, Eckert J. Defining the tensile properties of Al-12Si parts produced by selective laser melting. *Acta Mater* 2017;126:25–35.
32. Khmyrov RS, Safronov VA, Gusarov AV. Obtaining crack-free WC-Co alloys by selective laser melting. *Phys Proc* 2016;83:874–881.
33. Khmyrov RS, Safronov VA, Gusarov AV. Synthesis of nanostructured WC-Co hardmetal by selective laser melting. In: *Procedia IUTAM*. The Author(s), 2017; pp. 114–119.
34. Copley SM, Todd JA, Yankova M, *et al.* Solidification of AgCu alloys at high growth rates produced by continuous laser melt quenching. *Laser Process Surf Treat Film Depos* 1996;307:93–119.
35. Gu D, Wang Z, Shen Y, *et al.* *In-situ* TiC particle reinforced Ti-Al matrix composites: Powder preparation by mechanical alloying and selective laser melting behavior. *Appl Surf Sci* 2009;255:9230–9240.
36. Lu L, Fuh JYH, Chen ZD, *et al.* *In situ* formation of TiC composite using selective laser melting. *Mater Res Bull* 2000;35:1555–1561.
37. AlMangour B, Grzesiak D, Yang JM. *In-situ* formation of novel TiC-particle-reinforced 316L stainless steel bulk-form composites by selective laser melting. *J Alloys Compd* 2017;706:409–418.
38. Mumtaz K, Hopkinson N. Selective laser melting of Inconel 625 using pulse shaping. *Rapid Prototyp J* 2010;16:248–257.
39. Demir AG, Pangovski K, O’Neill W, *et al.* Investigation of pulse shape characteristics on the laser ablation dynamics of TiN coatings in the ns regime. *J Phys D Appl Phys* 48:235202.
40. Mumtaz KA, Hopkinson N. Selective laser melting of thin wall parts using pulse shaping. *J Mater Process Technol* 2010;210:279–287.

41. Prashanth KG, Scudino S, Chaubey AK, *et al.* Processing of Al-12Si-TNM composites by selective laser melting and evaluation of compressive and wear properties. *J Mater Res* 2016;31:55–65.
42. Sheikh S, M'Saoubi R, Flasar P, *et al.* Fracture toughness of cemented carbides: Testing method and microstructural effects. *Int J Refract Met Hard Mater* 2015;49:153–160.
43. Gu D, Hagedorn YC, Meiners W, *et al.* Nanocrystalline TiC reinforced Ti matrix bulk-form nanocomposites by Selective Laser Melting (SLM): Densification, growth mechanism and wear behavior. *Compos Sci Technol* 2011;71:1612–1620.
44. Li W, Li S, Liu J, *et al.* Effect of heat treatment on Al-Si10Mg alloy fabricated by selective laser melting: Microstructure evolution, mechanical properties and fracture mechanism. *Mater Sci Eng A* 2016;663:116–125.
45. Thijs L, Kempen K, Kruth JP, *et al.* Fine-structured aluminium products with controllable texture by selective laser melting of pre-alloyed AlSi10Mg powder. *Acta Mater* 2013;61:1809–1819.
46. Trevisan F, Calignano F, Lorusso M, *et al.* On the selective laser melting (SLM) of the AlSi10Mg alloy: Process, microstructure, and mechanical properties. *Materials (Basel)* 2017;10:76.
47. Yan C, Hao L, Hussein A, *et al.* Microstructure and mechanical properties of aluminium alloy cellular lattice structures manufactured by direct metal laser sintering. *Mater Sci Eng A* 2015;628:238–246.
48. Cao S, Chen Z, Lim CVS, *et al.* Defect, microstructure, and mechanical property of Ti-6Al-4V alloy fabricated by high-power selective laser melting. *JOM* 2017;69:2684–2692.
49. Gu D, Hagedorn YC, Meiners W, *et al.* Densification behavior, microstructure evolution, and wear performance of selective laser melting processed commercially pure titanium. *Acta Mater* 2012;60:3849–3860.
50. Singh N, Hameed P, Ummethala R, *et al.* Selective laser manufacturing of Ti-based alloys and composites: Impact of process parameters, application trends, and future prospects. *Mater Today Adv* 2020;8:100097.
51. Wang Z, Ummethala R, Singh N, *et al.* Selective laser melting of aluminum and its alloys. *Materials (Basel)* 2020;13:1–67.
52. Martin JH, Yahata BD, Hundley JM, *et al.* 3D printing of high-strength aluminium alloys. *Nature* 2017;549:365–369.
53. Qi T, Zhu H, Zhang H, *et al.* Selective laser melting of Al7050 powder: Melting mode transition and comparison of the characteristics between the keyhole and conduction mode. *Mater Des* 2017;135:257–266.
54. Kempen K, Vrancken B, Buls S, *et al.* Selective laser melting of crack-free high density M2 high speed steel parts by baseplate preheating. *J Manuf Sci Eng Trans ASME* 2014;136:061026.
55. Zhao C, Wang Z, Li D, *et al.* Cu-Ni-Sn alloy fabricated by melt spinning and selective laser melting: A comparative study on the microstructure and formation kinetics. *J Mater Res Technol* 2020;9:13097–13105.
56. Maity T, Chawake N, Kim JT, *et al.* Anisotropy in local microstructure—Does it affect the tensile properties of the SLM samples? *Manuf Lett* 2018;15:33–37.
57. Prashanth K, Scudino S, Chatterjee R, *et al.* Additive manufacturing: Reproducibility of metallic parts. *Technologies* 2017;5:8.
58. Liu N, Han CL, Ying WH, *et al.* Microstructure, hardness and fracture toughness of TiC based cermets with nano TiN powders addition. *Powder Metall* 2007;50:142–147.
59. Zhang X, Liu N, Rong C. Microstructure and fracture toughness of TiC-ZrC-WC-Mo-Ni cermets. *Int J Refract Met Hard Mater* 2008;26:346–356.
60. Zheng Y, Zhou Y, Li R, *et al.* Preparation and mechanical properties of TiC-Fe cermets and TiC-Fe/Fe bilayer composites. *J Mater Eng Perform* 2017;26:4933–4939.
61. Zhao G, Huang C, Liu H, *et al.* A study on *in-situ* synthesis of TiB<sub>2</sub>-SiC ceramic composites by reactive hot pressing. *Ceram Int* 2014;40:2305–2313.
62. Wang L, Liu H, Huang C, *et al.* Effects of sintering processes on mechanical properties and microstructure of Ti(C,N)-TiB<sub>2</sub>-Ni composite ceramic cutting tool material. *Ceram Int* 2014;40:16513–16519.
63. Hu W, Huang Z, Cai L, *et al.* Microstructural characterization and mechanical properties of a novel TiC-based cermet bonded with Ni<sub>3</sub>(Al,Ti) and NiAl duplexalloy. *Mater Charact* 2018;135:295–302.
64. Mumtaz K, Hopkinson N. Top surface and side roughness of Inconel 625 parts processed using selective laser melting. *Rapid Prototyp J* 2009;15:96–103.
65. Karimi J, Suryanarayana C, Okulov I, *et al.* Selective laser melting of Ti6Al4V: Effect of laser re-melting. *Mater Sci Eng A* 2020;805:140558.
66. Tang H, Wang J, Lu S, *et al.* Research progress in selective electron beam melting. *Mater China* 2015;34:225–235.

Address correspondence to:

Himanshu Singh Maurya

Department of Mechanical and Industrial Engineering

Tallinn University of Technology

Ehitajate Tee 5

Tallinn 19086

Estonia

E-mail: himaur@taltech.ee

Konda Gokuldoss Prashanth

Department of Mechanical and Industrial Engineering

Tallinn University of Technology

Ehitajate Tee 5

Tallinn 19086

Estonia

E-mail: kgprashanth@gmail.com

**Publication II**

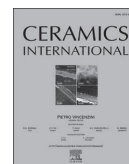
H.S. Maurya, L. Kollo, K. Juhani, F. Sergejev, K.G. Prashanth, Effect of preheating and cooling of the powder bed by laser pulse shaping on the microstructure of the TiC based cermets. *Ceramics International* 48 (2022) 20612–20618.





Contents lists available at ScienceDirect

Ceramics International

journal homepage: [www.elsevier.com/locate/ceramint](http://www.elsevier.com/locate/ceramint)

# Effect of preheating and cooling of the powder bed by laser pulse shaping on the microstructure of the TiC based cermets

H.S. Maurya<sup>a,\*</sup>, L. Kollo<sup>a</sup>, K. Juhani<sup>a</sup>, F. Sergejev<sup>a</sup>, K.G. Prashanth<sup>a,b,c</sup>

<sup>a</sup> Department of Mechanical and Industrial Engineering, Tallinn University of Technology, Ehitajate Tee 5, 19086, Tallinn, Estonia

<sup>b</sup> Erich Schmid Institute of Materials Science, Austrian Academy of Sciences, Jahnstrasse 12, 8700, Leoben, Austria

<sup>c</sup> CBCMT, School of Mechanical Engineering, Vellore Institute of Technology, Vellore, 630014, Tamil Nadu, India

## ARTICLE INFO

### Keywords:

Laser pulsing  
Microstructure  
Cermets  
Selective laser melting

## ABSTRACT

For the fabrication of brittle materials like cermets through Selective Laser Melting (SLM), the pulse shaping technique has proven to be an effective and optimal way to produce cermet with no cracks. The purpose of this work is to investigate the effect of laser peak in pulse shaping as a preheating and cooling approach for the melt pool of TiC – Fe based cermet using the pulse shaping technique. Several samples were fabricated with variations in laser power and exposure time refereed as pre-pulse and post-pulse before and after the laser peak power (LPP). Microstructural and phase analyses were performed on the fabricated SLM sample using SEM and XRD to study the effect of pulse shaping with variation in exposure time and therefore energy density. Mechanical properties like microhardness were calculated and hence the effect of hardness and energy density were studied. Results indicated that preheating and cooling through laser pulse during pulse shaping has a beneficial effect on the fabrication of the crack-free brittle cermet.

## 1. Introduction

TiC based cermet are mostly used for wear-resistant cutting tools and are ideal for high-temperature applications due to their high melting point, high hardness, and good thermal stability in the air [1–5]. Cermets are widely used in machining, mining, oil and gas industries, aerospace, and automotive sectors [3,6]. Despite the toughness and hardness of cermets based on WC-Co at high temperatures, these materials are poor at oxidation resistance and plastic deformation, which makes them unsuitable for high-temperature application [6–10]. As a result, TiC-based cermets have gained an increasing amount of attention due to their unique features. In comparison to W, Co, Cr, and Ni, Fe-based binder uses a greater proportion of Fe, resulting in lowered costs and health benefits to the environment [3–6,11–14]. The REACH program has classified Co as very toxic for human health in Europe. The US.NTP (National Toxicology Program) states that WC-Co is toxic, and it can increase the cancer risk in both the powder and sintered form [12]. These factors, combined with increasing raw material costs and supply, have led researchers to investigate ways to replace Co as a binder, either completely or partially [15]. Ni has been the most promising metal for replacing Co in hard metals (cemented carbides), but both Co and Ni are deemed carcinogenic by the US National Toxicology Program and EU

REACH programs. Efficiencies in resource use, the substitution of critical raw materials (CRM), and waste recycling will be crucial in the future manufacturing chain [16]. Developing new hard materials with alternative metallic binders (beyond Co) and carbides (beyond WC) has become a key objective in the hard metals and diamond tool industries [15].

In recent decades, additive manufacturing processes such as selective laser melting (SLM) of laser-based powder-bed fusion process (LBPF) has emerged as a promising method for producing complex, near-net-shaped samples [17–20]. SLM is a rapid prototyping technology based on the powder bed fusion process with high heating and cooling rates (ranging between  $10^4$ – $10^6$  K/s) [21–23] that enables the creation of complicated parts and assemblies directly from computer-aided design (CAD) models [24–27]. The SLM machine heats the powder bed selectively to form a melt pool that is rapidly solidified to form a single layer, as dictated by CAD model [28–31]. The parameters of the SLM processes such as laser power, layer thickness, point distance, and scan speed, as well as the powder properties, play a key role in determining the metallurgical properties of the molten pool and subsequent microstructural and mechanical properties of the fabricated final product [22,32–34]. Several advances have been made in recent years to expand the types of materials that are used in additive manufacturing like SLM, including

\* Corresponding author.

E-mail address: [himaaur@taltech.ee](mailto:himaaur@taltech.ee) (H.S. Maurya).

<https://doi.org/10.1016/j.ceramint.2022.04.029>

Received 6 February 2022; Received in revised form 3 April 2022; Accepted 4 April 2022

Available online 11 April 2022

0272-8842/© 2022 Elsevier Ltd and Techna Group S.r.l. All rights reserved.

polymers, metals, ceramics, and their combinations, such as cermet materials [35–40].

Due to rapid heating and cooling of the melt pool during the SLM process, brittle materials such as cermets may lead to process defects like pores, delamination, cracks, etc., Ceramic particles have a higher thermal expansion coefficient than metal particles leading to weak points along with the interface of brittle and ductile phases. Consequently, thermal residual stress from SLM processing causes as-built samples to crack and delaminate [41–44]. There are few reports currently available that discuss the fabrication of cermets using SLM, and most of these reports focus on the production of WC-Co cermets [45–50]. Pulse shaping of the laser appears to be the most efficient method of removing such process defects especially crack, as it helps in precise control of the melting and solidification of the melt pool because of which the cracks can be eliminated [51–53]. By dividing the laser pulse into multiple laser peaks using pulse shaping technology, the temperature gradient in the melt pool can be controlled by the laser power and exposure time during each of the cycles (of laser pulse) [54]. Hence, the pulse shaping of the laser can be effectively utilized to control the melting/solidification behavior of the material during the SLM process.

Accordingly, in this study, various laser peak shape during pulse shaping has been adapted to study the effect of the laser pulse peak during the formation of the samples fabricated through SLM. Microstructural evolution of the SLM-processed under different laser processing conditions was studied and the microstructure formation mechanisms during laser processing were interpreted. Mechanical properties like the microhardness of the SLM processed samples were studied to correlate the microstructure-property relation [55].

## 2. Experimental

### 2.1. Materials

The feedstock powder materials contain commercially available TiC powder (99.9% purity, Pacific particulate materials Ltd.) and Fe particles (99.8% purity, TLS Technik GmbH) in the stoichiometric ratio of 70 vol% TiC - 30 vol% Fe. The morphologies of the initial feedstock powder are depicted in Fig. 1. It can be seen from Fig. 1(a) that the Fe powders show a spherical or near-spherical morphology with a particle size dimension (PSD) ranging from 10 to 45  $\mu\text{m}$ . On the other hand, the TiC

particles show an irregular shape morphology with a particle size distribution below 10  $\mu\text{m}$ , as shown in Fig. 1(b). To achieve a homogeneous distribution, both the powders were mechanically mixed in a plastic vial for 24 h at the speed of 10 rpm. Zirconia balls (of 10 mm diameter and 8 in number) were used to aid the mixing and provide attrition during mixing. Fig. 1(c) shows the SEM micrographs of the mechanically mixed feedstock cermet powder, which shows a nearly homogeneous distribution of the TiC and Fe powder particle. Fig. 1(d–f) shows the elemental distribution of the mixed feedstock powder used for the fabrication of the TiC–Fe-based cermet.

### 2.2. SLM processing

An SLM device Realizer 50 equipped with an Nd: YAG fiber laser with a maximum laser power of 100 W developed by Realizer GmbH (Germany) was used to fabricate cermet samples in this study. The laser focal diameter was fixed at 0.0134 mm. The laser processing parameters include laser power range from 12 to 72 W, point distance 0.05 mm, and layer thickness 0.035 mm. A point scanning strategy for laser exposure is applied. Pulse lasers are used in this study, and the lasers are exposed to powder beds at the exposure point. A pulse-shaped laser is exposed to a single exposure point and the same pulse laser is repeated for each exposure point. A pulse-shaped laser contains several short laser peak powers during a single laser pulse, which causes the controlled melting/solidification of the melt pool, referred to as “pulse shaping”. Laser pulse shaping contains the number of laser pulses at each exposure point, which varies significantly with exposure time and laser power. Laser peak power during pulse shaping was kept constant i.e. 72 W for all the samples. Fig. 2. (a) Illustrates the schematics of the laser pulse shaping technique and Fig. 2(b) shows the point scanning strategy and direction of the scan adapted for the pulse shaping in this study. A time gap of 0.08 ms was kept between each laser exposure within a single laser pulse. To prevent oxidation and contamination of the feedstock powder during fusion, the working chamber was filled with argon gas and an oxygen concentration below 40 ppm was maintained throughout the process. Stainless steel substrate was used as a building platform. The laser parameter used for the fabrication of the sample were depicted in Table 1. The total exposure time and energy density for each laser exposure point of a single laser pulse are also calculated using the volumetric energy density formula [56]. The volumetric energy density

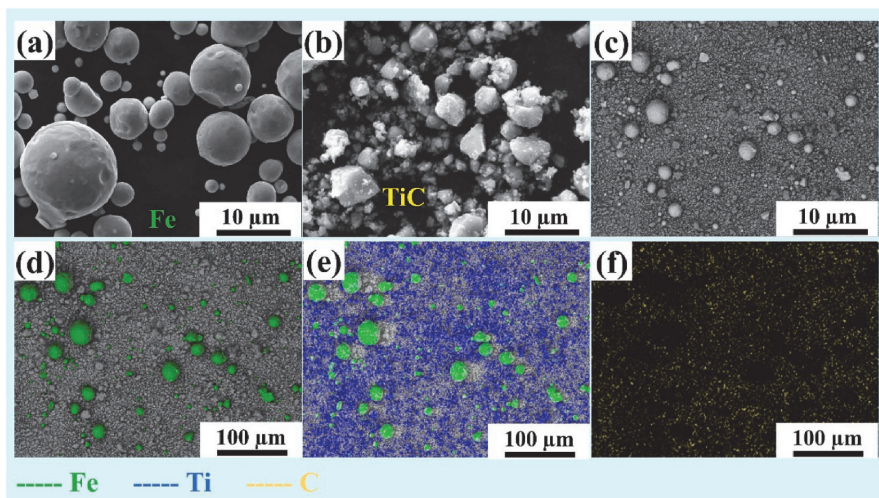


Fig. 1. Scanning electron microscopy images of the starting (a) Fe, (b) TiC powders (c) Homogeneously mixed TiC–Fe powder, and (d–f) its energy-dispersive scanning mapping.

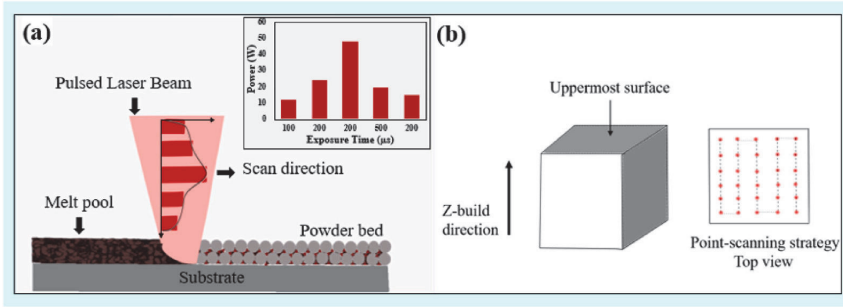


Fig. 2. Schematics illustrating the (a) single-pulse parameter adapted for the fabrication of the cermet samples, and (b) point scanning strategy of the SLM process through pulse shaping.

**Table 1**  
SLM pulse shaping parameters of a single pulse adapted to fabricated TiC–Fe based cermets.

Sample Designation	Laser Power (W)	Exposure Time (μs)	Total Exposure Time (μs)	Energy Density (J/mm <sup>3</sup> )	Total Energy Density (J/mm <sup>3</sup> )
PS1	12-24-	100-200-	1200	13.7-	376
	72-	200-500-		54.8-	
	19.2-	200		164.5-	
	14.4			109.7-	
PS2	12-24-	100-250-	1000	13.7-	334
	72-	200-250-		68.5-	
	19.2-	200		164.5-	
	14.4			54.8-32.9	
PS3	12-24-	100-250-	800	13.7-	291
	72-	200-50-		68.5-	
	19.2-	200		164.5-	
	14.4			10.9-32.9	
PS4	12-24-	100-200-	950	13.7-	321
	72-	200-250-		54.8-	
	19.2-	200		164.5-	
	14.4			54.8-32.9	
PS5	12-24-	100-200-	500	13.7-	233
	72-	200-0-0		54.8-	
				164.5-0-0	
PS6	12-24-	100-250-	1250	13.7-	376
	72-	200-500-		68.5-	
	19.2-	200		164.5-	
	14.4			109.7-	
PS7	12-24-	100-50-	1050	13.7-	335
	72-	200-500-		13.7-	
	19.2-	200		164.5-	
	14.4			109.7-	
PS8	0-0-72-	0-0-200-	900	0-0-	307
	19.2-	500-200		164.5-	
				109.7-	
				32.9	

(VED) is used to describe the volumetric energy density of each single laser pulse energy density and total energy density of a single pulse at each exposure time. In this study energy density (VED) affects the cermet formation and its microstructure. The volumetric energy density (VED) can be calculated using the following formula [57].

$$ED = \frac{P}{v \cdot h \cdot t} \tag{1}$$

where  $P$  (Watt) is the effective laser power,  $v$  (mm/s) is the scan speed,  $h$  (mm) is the hatch distance, and  $t$  (mm) is the layer thickness of the powder bed. This gives an energy input per unit volume of powder bed

in J/mm<sup>3</sup>. A range of laser parameters and pulse shaping techniques were employed to construct the cuboidal-shaped samples.

2.3. Microstructural and mechanical characterization

To prepare samples for metallographic examination, they were ground and polished according to standard metallographic procedures. Morphology and microstructure of the as-built samples and the initial feedstock powder were examined using scanning electron microscopy Zeiss EVO MA15 equipped with the X-ray spectroscopy (EDS) system INCA. X-ray diffraction (XRD) measurements were performed to identify the phases present in the printed samples using a Rigaku Ultima IV diffractometer with monochromatic Cu K $\alpha$  radiation ( $\lambda = 1.5406 \text{ \AA}$ ). All the XRD patterns were scanned in the  $2\theta$  range of  $30^\circ\text{--}90^\circ$  with the scan step of 0.02 deg. The porosity of the SLM samples were measured using the Archimedes principle. The microhardness measurements of the SLMed cuboidal samples were carried out using a Buehler Micromet on a longitudinal section of the fabricated samples at a normal load of 1000 g using a dwell time of 10 s. The reported microhardness represents the average of at least 3 measurements for each sample.

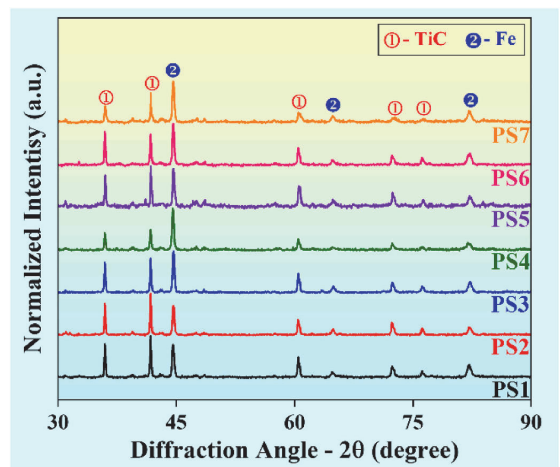


Fig. 3. X-ray diffraction patterns of the different pulse-shaped samples processed through SLM showing the presence of Fe and TiC phases.

### 3. Results and discussion

#### 3.1. Phases identification

Fig. 3 shows the X-ray diffraction patterns (XRD) of TiC–Fe cermets with varying pulse shaping parameters as built by SLM. Each sample designated as PS (1–8) has been fabricated with different pulse shaping (PS) using pulsed laser resulting from the variation in laser power and exposure time. In all the samples fabricated with different laser pulse shaping parameters, the diffraction peaks corresponding to TiC (simple cubic system with the space group Fm-3m (225) (line NaCl)) and  $\alpha$ -Fe (body-centered cubic system (bcc) with a space group Im-3m (229)) phases are observed. The results suggest that the powder mixture does not lead to the formation of any new phase after SLM fabrication. A variation in the exposure times and laser power before and after laser peak power (LPP) pulse results in a change in the peak intensity of both the phases TiC and Fe. This significant variation in the intensity of TiC and  $\alpha$ -Fe peaks can be attributed to the formation of texture due to laser pulsing. The diffraction peak corroborates the absence of any intermetallic or carbide phases.

#### 3.2. Microstructure and mechanical properties

Fig. 4 shows the SEM surface morphologies (taken along the longitudinal section) of the TiC–Fe based cermet fabricated as a function of varying SLM process parameters through pulse shaping technique. All the SEM micrographs in general show the presence of two different phases with two different contrasts. The dark phase in the microstructure corresponds to the TiC phase while the brighter phase corresponds binder phase, Fe. The influence of the pulse on the microstructure and formation of the cermet before and after the LPP is referred to as pre-pulse and post-pulse effects, respectively, during the pulse shaping. Since exposure time is proportional to energy density, it affects the overall energy density by altering the exposure time of the pre-pulse and post-pulse [57]. Among the samples with maximum energy density, PS1 shows a uniform microstructure with homogeneous distributions of coarser TiC dendritic phases all over the surface (Fig. 4(a)). In addition, PS1 shows a maximum relative density of  $\sim$ 98.0%, when compared to the other counterparts. The relative density of the SLM fabricated cermets are shown in Table 2.

The homogeneous distribution of TiC phases observed in the sample PS1 by the effect of preheating through pre-pulse and cooling via post pulse can be explained as follows: after the LPP exposure, the post-pulse exposure time was kept relatively long, resulting in a slow scan speed (increasing energy density) as compared to other samples to control the cooling/solidification of the melt pool at a lower temperature. In this

**Table 2**

The relative density of the SLM fabricated TiC–Fe cermets using adoptive pulse shaping technique.

Sample Designation	Relative density (%)
PS1	98.0
PS2	96.4
PS3	94.5
PS4	92.1
PS5	93.3
PS6	93.5
PS7	97.2

way, the residual thermal stress was reduced, resulting in the TiC phases forming with a relatively homogeneous shape. Sample PS1 with higher energy density and optimal exposure time has been used as an optimal and standard parameter for the fabrication of TiC–Fe based cermets; changes to exposure time have been done using the same pulse shaping for the other samples to study the effects of pre and post pulses on the microstructure. The exposure time has been varied in sample PS2 by increasing the pre-pulse time, lowering the LPP and post pulse exposure times. Changing the exposure time changes the scan rate of the laser and reduced the total energy density, and this, in turn, resulted in fine and irregular TiC dendritic phases microstructures, and relatively inhomogeneous distributions (Fig. 4(b)). As a result of the higher scan speed at LPP (250 mm/s), melt pools and laser tracks are not visible. Additionally, the high heating rate and cooling rate of the TiC particles permit relatively fine TiC particle size distribution.

In the case of PS3, pulse shaping was patterned in the same manner as sample PS2, with the exception that the exposure time in the post pulse was reduced (50  $\mu$ s) and the exposure time at LPP was increased (200  $\mu$ s). Due to the Gaussian distribution of laser energy, increasing the exposure period of the laser at LPP increases the energy density of the melt pool, there is a temperature gradient (G) in the laser scan area with a maximum value at the center of the melt pool and minimum value at its boundaries and thus the variation in the TiC phase at the melt pool and surrounding can be noticed (Fig. 4(c)) [49,50,58]. In the center of the melt pool, fine TiC dendritic phases can be observed while coarser dendritic TiC phases can be observed near the laser exposed area. Reduced post-pulse exposure time causes an increase in cooling rate, resulting in this gradient in TiC phases. The thermal gradient (G), solidification rate (R), and cooling rate ( $T = G \cdot R$ ) can all be used to calculate the fineness of TiC phases [59]. The microstructure of the melt pool will become finer as the cooling rate of the melt pool increases.

The PS4 pulse shaping parameters were adapted in the same way as sample PS1, except for a change in the exposure time of the post pulse (250  $\mu$ s). Overall exposure time has been reduced for the sample due to

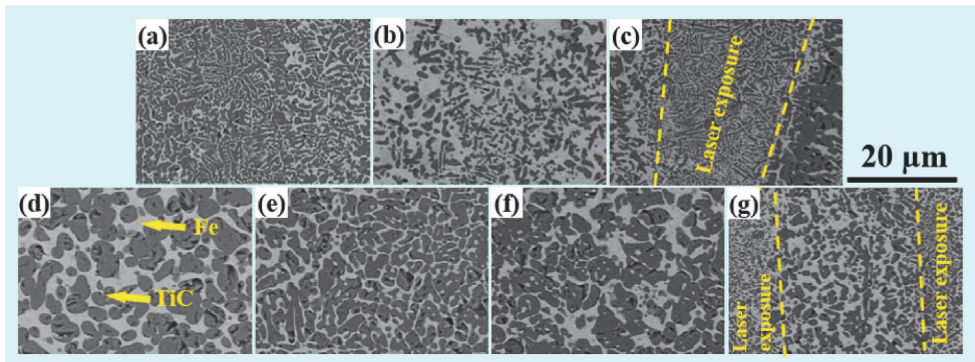


**Fig. 4.** Scanning electron microscopy images of the SLM fabricated as-built cermet samples with variation in laser power and exposure time. Sample (a) PS1 (376 J/mm<sup>3</sup>), (b) PS2 (334 J/mm<sup>3</sup>), (c) PS3 (291 J/mm<sup>3</sup>), (d) PS4 (321 J/mm<sup>3</sup>), (e) PS5 (233 J/mm<sup>3</sup>), (f) PS6 (376 J/mm<sup>3</sup>), and (g) PS7 (335 J/mm<sup>3</sup>).

which during post-pulse these changes in exposure time influence energy density in post pulse after the LPP with less cooling exposure time and hence this change in the energy density with low post pulse exposure time causes the formation of the irregular coarser TiC phases (Fig. 4 (d)). This coarsening of the TiC phases could be the result of a high-energy laser beam and variations in the reduced cooling rate due to the short post-pulse exposure time. No post-pulse laser peaks were considered for Sample PS5. The sample was pre-heated as a pre-pulse before being exposed to LPP. Due to the lack of a post-pulse, no controlled cooling as post pulse was performed, resulting in a low overall total energy density, but a high LPP and pre-pulse energy density. The high energy density of the laser at LPP and the lack of a post pulse, affect the temperature of the melt pool. As a result, the coarser TiC dendritic phases with porosity form. (Fig. 4(e)).

The effects of pre-pulse on the samples PS6 to PS8 have been investigated. The exposure time and laser power were kept the same as in sample PS1, except for a change in the pre-pulse exposure time. For the sample PS6, the pre-pulse exposure time was increased, increasing overall density and maximum exposure time relative to other samples, leading the melt pool temperature to rise due to lower scan speed ( $200 \text{ mm s}^{-1}$ ), resulting in TiC coarser phases with many cracks and inhomogeneous distribution of TiC phases with irregular form. (Fig. 4(f)). However, for the sample PS7, the pre-pulse exposure time was reduced to  $50 \mu\text{s}$ , resulting in a reduction in total exposure time (increased scan rate to  $1000 \text{ mm s}^{-1}$ ) and energy density. Due to which it causes lower preheating temperature and sudden increment in the temperature of the melt pool. As a result, the gradient TiC phases can be seen on the SEM images (Fig. 4. (g)). Finer particles in the melt pool's center and coarser TiC phases around the laser scan region have been observed, like the microstructure of the sample PS3 which is similar to most of the SLM-based microstructure. However, for the sample PS3, the TiC dendritic phases sizes were finer as compared to Sample PS7. This can be explained by the high energy density and total exposure time affecting the microstructure of the melt pool. A higher cooling rate causes the finer microstructure for the PS3 sample however for the PS7 the cooling rate decreases due to increases in the post pulse exposure time leading to the growth of the TiC phases [60]. For sample PS8, no pre-pulse laser peaks were adapted for the study of the importance of pre-pulse on the formation of cermet through pulse shaping, because of which the sample started deteriorating like a layered chip after each layer of laser scan due to higher thermal residual stress generated by higher heating and cooling rates. As a result, it can be stated that pre-heating the powder by pre-pulse plays a critical role in the formation of cermet during the pulse shaping technique.

### 3.3. Mechanical properties

Fig. 5 represents the correlation among microhardness and total energy density of the as-built TiC–Fe based cermet obtained through variation in laser peak through pulse shaping technology. The microstructure, formation, and mechanical properties of the samples are affected by variations in pre-pulse and post-pulse exposure time. However, from the graph, no relation between total energy density and hardness has been seen as here the effect of post pulsing and pre-pulsing plays a characteristic role of the hardness value, not the total energy density. This suggests that the VED equation is just an empirical one as already reported by Prashanth et al. Illustrating using Al–12Si alloy [56, 61,62]. The results suggest that the fabrication of a sample through pulse shaping melting/solidification plays an important role. The hardness value varies due to variations in the TiC and binder phase distributions, as well as the indenter placed on the hard phase or binder phase. Hardness values of  $990 \text{ HV}_1$  have been achieved for sample PS1 with higher energy density. However, the minimum value is achieved for the sample PS2 which is  $608 \text{ HV}_1$ . The sample with finer microstructure in the melt pool and gradient TiC phases at the boundary of the laser scan area has a lower hardness value (PS2, PS4, and PS7).

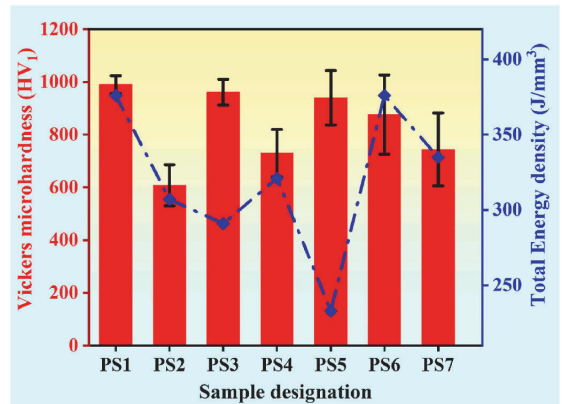


Fig. 5. Hardness vs total energy density micrograph of the TiC–Fe based cermets fabricated by selective laser melting.

However, the sample with coarser TiC phases has a hardness in the range of  $876\text{--}990 \text{ HV}_1$ . TiC phases with less variation in size have larger volumes of hard phase region, which leads to a higher value of total hardness. With the controlled heating and solidification rate, pre-heating and post-heating laser peaks provide the optimal amount of time for melt pools to form homogeneous microstructures. Furthermore, laser peak power also plays a crucial role in dictating both the mechanical properties and the subsequent microstructural formation.

## 4. Conclusion

TiC-30 vol% Fe cermets are successfully fabricated via pulse shaping technique using the selective laser melting (SLM) process. The pulse shaping technique proves to be optimal and beneficial in the fabrication of the crack-free cermet. Several samples were fabricated with variations in laser peak power and exposure time. This study concludes that pulse shaping including pre-pulsing and post pulsing plays a vital role during the formation of the cermet. Variation in pre/post pulsing laser changes the microstructure and the mechanical property of the cermet. Pre-heating is quite important during the formation of the cermet during pulse shaping. Using the pre-heating pulse before the laser peak power allows the melt pool to be preheated and controls the thermal gradient of the melt pool and any sudden heat generated from melting powder during the laser exposure. Due to the controlled cooling and solidification of the melt pool, the post-pulse effect contributes to the control of thermal residual stress, ultimately affecting the sample formation. Sample PS1 shows a higher hardness value and can be considered as the optimal parameter for the fabrication of TiC cermet through the pulse shaping technique.

### Author's disclosure statement

The authors state there is no conflict of interest.

### Data availability

The present data forms a part of the ongoing study, and the results may be shared upon reasonable request from the corresponding author (s).

### Declaration of competing interest

The authors declare that they have no known competing financial interests or personal relationships that could have appeared to influence

the work reported in this paper.

## Acknowledgments

This work was supported by Estonian Research Council grants PRG1145 and European Regional Development Grant ASTRA6-6.

## References

- [1] J. Kübarssepp, H. Klaasen, J. Pirso, Behavior of TiC-base cermets in different wear conditions, *Wear* 249 (2001) 229–234, [https://doi.org/10.1016/S0043-1648\(01\)00569-5](https://doi.org/10.1016/S0043-1648(01)00569-5).
- [2] W.D. Kaplan, D. Rittel, M. Lieberthal, N. Frage, M.P. Dariel, Static and dynamic mechanical damage mechanisms in TiC-1080 steel cermets, *Scripta Mater.* 51 (2004) 37–41, <https://doi.org/10.1016/j.scriptamat.2004.03.021>.
- [3] C. Jin, C.C. Onuoha, Z.N. Farhat, G.J. Kipouros, K.P. Plucknett, Reciprocating wear behaviour of TiC-stainless steel cermets, *Tribol. Int.* 105 (2017) 250–263, <https://doi.org/10.1016/j.triboint.2016.10.012>.
- [4] C. Jin, K.P. Plucknett, Microstructure instability in TiC-316L stainless steel cermets, *Int. J. Refract. Metals Hard Mater.* 58 (2016) 74–83, <https://doi.org/10.1016/j.jrmhm.2016.03.012>.
- [5] J. Wang, Y. Liu, J. Ye, S. Ma, J. Pang, The fabrication of multi-core structure cermets based on (Ti,W,Ta)CN and TiCN solid-solution powders, *Int. J. Refract. Metals Hard Mater.* 64 (2017) 294–300, <https://doi.org/10.1016/j.jrmhm.2016.09.011>.
- [6] C. Jin, C.C. Onuoha, Z.N. Farhat, G.J. Kipouros, K.P. Plucknett, Microstructural damage following reciprocating wear of TiC-stainless steel cermets, *Tribol. Int.* 105 (2017) 201–218, <https://doi.org/10.1016/j.triboint.2016.10.011>.
- [7] K. Aigner, W. Lengauer, P. Ettmayer, Interactions in iron-based cermet systems, *J. Alloys Compd.* 262–263 (1997) 486–491, [https://doi.org/10.1016/S0925-8388\(97\)00360-5](https://doi.org/10.1016/S0925-8388(97)00360-5).
- [8] J. Kübarssepp, K. Juhani, Cermets with Fe-alloy binder: a review, *Int. J. Refract. Metals Hard Mater.* (2020) 92, <https://doi.org/10.1016/j.jrmhm.2020.105290>.
- [9] B. Casas, X. Ramis, M. Anglada, J.M. Salla, L. Llanes, Oxidation-induced strength degradation of WC-Co hardmetals, *Int. J. Refract. Metals Hard Mater.* 19 (2001) 303–309, [https://doi.org/10.1016/S0263-4368\(01\)00033-6](https://doi.org/10.1016/S0263-4368(01)00033-6).
- [10] F. Lofaj, Y.S. Kaganovskii, Kinetics of WC-Co oxidation accompanied by swelling, *J. Mater. Sci.* 30 (1995) 1811–1817, <https://doi.org/10.1007/BF00351615>.
- [11] V.B. Voitovich, V.V. Sverdel, R.F. Voitovich, E.I. Golovko, Oxidation of WC-Co, WC-Ni and WC-Co-Ni hard metals in the temperature range 500–800°C, *Int. J. Refract. Metals Hard Mater.* 14 (1996) 289–295, [https://doi.org/10.1016/0263-4368\(96\)00009-1](https://doi.org/10.1016/0263-4368(96)00009-1).
- [12] X. Shi, H. Yang, G. Shao, X. Duan, S. Wang, Oxidation of ultrafine-cemented carbide prepared from nanocrystalline WC-10Co composite powder, *Ceram. Int.* 34 (2008) 2043–2049, <https://doi.org/10.1016/j.ceramint.2007.07.029>.
- [13] C. Jin, K. Plucknett, The effects of microstructure on Vickers indentation damage in TiC-316L stainless steel cermets, *Int. J. Refract. Metals Hard Mater.* 61 (2016) 151–161, <https://doi.org/10.1016/j.jrmhm.2016.09.006>.
- [14] C.C. Onuoha, G.J. Kipouros, Z.N. Farhat, K.P. Plucknett, The reciprocating wear behaviour of TiC-304L stainless steel composites prepared by melt infiltration, *Wear* 303 (2013) 321–333, <https://doi.org/10.1016/j.wear.2013.03.040>.
- [15] L. He, Q. Liu, Y. Gao, Y. Li, Z. Liu, W. Zhai, C. Zhou, W. Yuan, W. Chen, W. Yan, Abnormal oxidation behavior of Fe in Ti(C,N)-304ss cermet during early oxidation stage, *J. Alloys Compd.* 790 (2019) 20–26, <https://doi.org/10.1016/j.jallcom.2019.03.008>.
- [16] B. Rooks, Rapid tooling for casting prototypes, *Assemb. Autom.* 22 (2002) 40–45, <https://doi.org/10.1108/01445150210416664>.
- [17] K.G. Prashanth, S. Scudino, J. Eckert, Defining the tensile properties of Al-12Si parts produced by selective laser melting, *Acta Mater.* 126 (2017) 25–35, <https://doi.org/10.1016/j.actamat.2016.12.044>.
- [18] N. Singh, P. Hameed, R. Ummethala, G. Manivasagam, K.G. Prashanth, J. Eckert, Selective laser manufacturing of Ti-based alloys and composites: impact of process parameters, application trends, and future prospects, *Materials Today Advances* 8 (2020), 100097, <https://doi.org/10.1016/j.mtdadv.2020.100097>.
- [19] P. Wang, J. Eckert, K.G. Prashanth, M. wei Wu, I. Kaban, L. Xi, S. Scudino, A review of particulate-reinforced aluminum matrix composites fabricated by selective laser melting, *Trans. Nonferrous Metals Soc. China* 30 (2020) 2001–2034, [https://doi.org/10.1016/S1003-6326\(20\)65357-2](https://doi.org/10.1016/S1003-6326(20)65357-2).
- [20] K. Prashanth, L. Löber, H.-J. Klaus, U. Kühn, J. Eckert, Characterization of 316L steel cellular dodecahedron structures produced by selective laser melting, *Technologies* 4 (2016) 34, <https://doi.org/10.3390/technologies4040034>.
- [21] H.Y. Jung, S.J. Choi, K.G. Prashanth, M. Stoica, S. Scudino, S. Yi, U. Kühn, D. H. Kim, K.B. Kim, J. Eckert, Fabrication of Fe-based bulk metallic glass by selective laser melting: a parameter study, *Mater. Des.* 86 (2015) 703–708, <https://doi.org/10.1016/j.matdes.2015.07.145>.
- [22] Z. Wang, M. Xie, Y. Li, W. Zhang, C. Yang, L. Kollo, J. Eckert, K.G. Prashanth, Premature failure of an additively manufactured material, *NPG Asia Mater.* 12 (2020) 1–10, <https://doi.org/10.1038/s41427-020-0212-0>.
- [23] C. Zhao, Z. Wang, D. Li, L. Kollo, Z. Luo, W. Zhang, K.G. Prashanth, Cu-Ni-Sn alloy fabricated by melt spinning and selective laser melting: a comparative study on the microstructure and formation kinetics, *J. Mater. Res. Technol.* 9 (2020) 13097–13105, <https://doi.org/10.1016/j.jmrt.2020.09.047>.
- [24] P.K. Gokuldoss, S. Kolla, J. Eckert, Additive manufacturing processes: selective laser melting, electron beam melting and binder jetting-selection guidelines, *Materials* 10 (2017) 1–11, <https://doi.org/10.3390/ma10060672>.
- [25] K.G. Prashanth, S. Scudino, H.J. Klaus, K.B. Surreddi, L. Löber, Z. Wang, A. K. Chaubey, U. Kühn, J. Eckert, Microstructure and mechanical properties of Al-12Si produced by selective laser melting: effect of heat treatment, *Mater. Sci. Eng.* 590 (2014) 153–160, <https://doi.org/10.1016/j.msea.2013.10.023>.
- [26] A. Singh, D.A. Basha, Y. Matsushita, K. Tsuchiya, Z. Lu, T.G. Nieh, T. Mukai, Domain structure and lattice effects in a severely plastically deformed CoCrFeMnNi high entropy alloy, *J. Alloys Compd.* 812 (2020), 152028, <https://doi.org/10.1016/j.jallcom.2019.152028>.
- [27] T. DebRoy, H.L. Wei, J.S. Zuback, T. Mukherjee, J.W. Elmer, J.O. Milewski, A. M. Beese, A. Wilson-Heid, A. De, W. Zhang, Additive manufacturing of metallic components – process, structure and properties, *Prog. Mater. Sci.* 92 (2018) 112–224, <https://doi.org/10.1016/j.pmatsci.2017.10.001>.
- [28] D. Herzog, V. Seyda, E. Wycisk, C. Emmelmann, Additive manufacturing of metals, *Acta Mater.* 117 (2016) 371–392, <https://doi.org/10.1016/j.actamat.2016.07.019>.
- [29] J. Karimi, P. Ma, Y.D. Jia, K.G. Prashanth, Linear patterning of high entropy alloy by additive manufacturing, *Manuf. Lett.* 24 (2020) 9–13, <https://doi.org/10.1016/j.mfglet.2020.03.003>.
- [30] J. Karimi, C. Suryanarayana, I. Okulov, K.G. Prashanth, Selective laser melting of Ti6Al4V: effect of laser re-melting, *Mater. Sci. Eng.* 805 (2020), 140558, <https://doi.org/10.1016/j.msea.2020.140558>.
- [31] J. Karimi, M.S. Xie, Z. Wang, K.G. Prashanth, Influence of substructures on the selective laser melted Ti-6Al-4V alloy as a function of laser re-melting, *J. Manuf. Process.* 68 (2021) 1387–1394, <https://doi.org/10.1016/j.jmapro.2021.06.059>.
- [32] C. Zhao, Z. Wang, D. Li, L. Kollo, Z. Luo, W. Zhang, K. Gokuldoss, K.G. Prashanth, Selective laser melting of Cu – Ni – Sn : a comprehensive study on the microstructure , mechanical properties , and deformation behavior, *Int. J. Plast.* 138 (2021), 102926, <https://doi.org/10.1016/j.ijplas.2021.102926>.
- [33] C. Zhao, Z. Wang, D. Li, M. Xie, L. Kollo, Z. Luo, W. Zhang, K.G. Prashanth, Comparison of additively manufacturing samples fabricated from pre-alloyed and mechanically mixed powders, *J. Alloys Compd.* (2020) 830, <https://doi.org/10.1016/j.jallcom.2020.154603>.
- [34] Z. Wang, S.Y. Tang, S. Scudino, Y.P. Ivanov, R.T. Qu, D. Wang, C. Yang, W. Zhang, A.L. Greer, J. Eckert, K.G. Prashanth, Additive manufacturing of a martensitic Co–Cr–Mo alloy: towards circumventing the strength–ductility trade-off, *Addit. Manuf.* 37 (2021), 101725, <https://doi.org/10.1016/j.addma.2020.101725>.
- [35] A. Arianian, Z. Sadeghian, K.G. Prashanth, F. Berto, In situ fabrication of TiC-NiCr cermets by selective laser melting, *Int. J. Refract. Metals Hard Mater.* 87 (2020), 105171, <https://doi.org/10.1016/j.jrmhm.2019.105171>.
- [36] A. Arianian, Z. Sadeghian, S.M.J. Razavi, K.G. Prashanth, F. Berto, Effect of selective laser melting process parameters on microstructural and mechanical properties of TiC–NiCr cermet, *Ceram. Int.* 46 (2020) 28749–28757, <https://doi.org/10.1016/j.ceramint.2020.08.037>.
- [37] Y. Holovenko, L. Kollo, M. Saarna, R. Rahmani, T. Soloviova, M. Antonov, K. G. Prashanth, S. Cygan, R. Veinthal, Effect of lattice surface treatment on performance of hardmetal - titanium interpenetrating phase composites, *Int. J. Refract. Metals Hard Mater.* 86 (2020), 105087, <https://doi.org/10.1016/j.jrmhm.2019.105087>.
- [38] R. Rahmani, M. Antonov, L. Kollo, Y. Holovenko, K.G. Prashanth, Mechanical behavior of Ti6Al4V scaffolds filled with CaSiO3 for implant applications, *Appl. Sci.* 9 (2019) 3844, <https://doi.org/10.3390/app9183844>.
- [39] R. Rahmani, M. Brojan, M. Antonov, K.G.K.G. Prashanth, Perspectives of metal-diamond composites additive manufacturing using SLM-SPS and other techniques for increased wear-impact resistance, *Int. J. Refract. Metals Hard Mater.* 88 (2020), 105192, <https://doi.org/10.1016/j.jrmhm.2020.105192>.
- [40] N. Kamboj, M.A. Rodríguez, R. Rahmani, K.G. Prashanth, I. Hussainova, Bioceramic scaffolds by additive manufacturing for controlled delivery of the antibiotic vancomycin, *Proc. Est. Acad. Sci.* 68 (2019) 185–190, <https://doi.org/10.3176/proc.2019.2.10>.
- [41] K.G. Prashanth, H. Shakur Shahabi, H. Attar, V.C. Srivastava, N. Ellenid, V. Uhlenwinkel, J. Eckert, S. Scudino, Production of high strength Al 85 Nd 8 Ni 5 Co 2 alloy by selective laser melting, *Addit. Manuf.* 6 (2015) 1–5, <https://doi.org/10.1016/j.addma.2015.01.001>.
- [42] K.G. Prashanth, S. Scudino, A.K. Chaubey, L. Löber, P. Wang, H. Attar, F. P. Schimansky, F. Pyczak, J. Eckert, Processing of Al-12Si-TNM composites by selective laser melting and evaluation of compressive and wear properties, *J. Mater. Res.* 31 (2016) 55–65, <https://doi.org/10.1557/jmr.2015.326>.
- [43] K. Kempen, B. Vrancken, S. Buls, L. Thijs, J. Van Humbeeck, J.P. Kruth, Selective laser melting of crack-free high density M2 high speed steel parts by baseplate preheating, *J. Manuf. Sci. Eng. Trans. ASME* 136 (2014), <https://doi.org/10.1115/1.4028513>.
- [44] Y. Zhou, Y.-S. Che, C. Wang, R. Liu, S.-F. Wen, Selective laser melting high-performance ZrC-reinforced tungsten composites with tailored microstructure and suppressed cracking susceptibility, *Tungsten* 3 (2021) 72–88, <https://doi.org/10.1007/s42864-021-00076-8>.
- [45] A. Domashenko, A. Borbély, I. Smurov, Structural modifications of WC/Co nanophased and conventional powders processed by selective laser melting, *Mater. Manuf. Process.* 32 (2017) 93–100, <https://doi.org/10.1080/10426914.2016.1176195>.
- [46] R.S. Khmyrov, V.A. Srafnonov, A.V. Gusarov, Obtaining crack-free WC-Co alloys by selective laser melting, *Phys. Procedia* 83 (2016) 874–881, <https://doi.org/10.1016/j.phpro.2016.08.091>.

- [47] R.S. Khmyrov, V.A. Safronov, A.V. Gusarov, Synthesis of nanostructured WC-Co hardmetal by selective laser melting, *Procedia IUTAM* 23 (2017) 114–119, <https://doi.org/10.1016/j.piutam.2017.06.011>.
- [48] L. Lu, J.Y.H. Fuh, Z.D. Chen, C.C. Leong, Y.S. Wong, In situ formation of TiC composite using selective laser melting, *Mater. Res. Bull.* 35 (2000) 1555–1561, [https://doi.org/10.1016/S0025-5408\(00\)00339-1](https://doi.org/10.1016/S0025-5408(00)00339-1).
- [49] D. Gu, Z. Wang, Y. Shen, Q. Li, Y. Li, In-situ TiC particle reinforced Ti-Al matrix composites: powder preparation by mechanical alloying and Selective Laser Melting behavior, *Appl. Surf. Sci.* 255 (2009) 9230–9240, <https://doi.org/10.1016/j.apsusc.2009.07.008>.
- [50] K.A. Mumtaz, N. Hopkinson, Selective Laser Melting of thin wall parts using pulse shaping, *J. Mater. Process. Technol.* 210 (2010) 279–287, <https://doi.org/10.1016/j.jmatprotec.2009.09.011>.
- [51] Y. Zheng, Y. Zhou, R. Li, J. Wang, L. Chen, S. Li, Preparation and mechanical properties of TiC-Fe cermets and TiC-Fe/Fe bilayer composites, *J. Mater. Eng. Perform.* 26 (2017) 4933–4939, <https://doi.org/10.1007/s11665-017-2914-1>.
- [52] N. Liu, C.L. Han, W.H. Ying, X.M. Huang, Microstructure, hardness and fracture toughness of TiC based cermets with nano TiN powders addition, *Powder Metall.* 50 (2007) 142–147, <https://doi.org/10.1179/174329007X186534>.
- [53] H.S. Maurya, L. Kollo, M. Tarraste, K. Juhani, F. Sergejev, K.G. Prashanth, Selective laser melting of TiC-Fe via laser pulse shaping: microstructure and mechanical properties, *3D Print. Addit. Manuf.* (2021), <https://doi.org/10.1089/3dp.2021.0221>.
- [54] H.S. Maurya, K. Juhani, F. Sergejev, K.G. Prashanth, Additive manufacturing of TiC-based cermet with stainless steel as a binder material, *Mater. Today Proc.* (2022), <https://doi.org/10.1016/J.MATPR.2022.02.428>.
- [55] H.S. Maurya, L. Kollo, M. Tarraste, K. Juhani, F. Sergejev, K. Gokuldoss Prashanth, Effect of the laser processing parameters on the selective laser melting of TiC-Fe-based cermets, *J. Manuf. Mater. Process.* 6 (2022) 35, <https://doi.org/10.3390/JMMP6020035>. Page 35. 6, 2022.
- [56] K.G. Prashanth, S. Scudino, T. Maity, J. Das, J. Eckert, Is the energy density a reliable parameter for materials synthesis by selective laser melting? *Mater. Res. Lett.* 5 (2017) 386–390, <https://doi.org/10.1080/21663831.2017.1299808>.
- [57] C. Yan, L. Hao, A. Hussein, P. Young, J. Huang, W. Zhu, Microstructure and mechanical properties of aluminium alloy cellular lattice structures manufactured by direct metal laser sintering, *Mater. Sci. Eng.* 628 (2015) 238–246, <https://doi.org/10.1016/j.msea.2015.01.063>.
- [58] K.G. Prashanth, J. Eckert, Formation of metastable cellular microstructures in selective laser melted alloys, *J. Alloys Compd.* 707 (2017) 27–34, <https://doi.org/10.1016/j.jallcom.2016.12.209>.
- [59] F. Trevisan, F. Calignano, M. Lorusso, J. Pakkanen, A. Aversa, E.P. Ambrosio, M. Lombardi, P. Fino, D. Manfredi, On the selective laser melting (SLM) of the AISi10Mg alloy: process, microstructure, and mechanical properties, *Materials* 10 (2017), <https://doi.org/10.3390/ma10010076>.
- [60] W. Li, J. Liu, Y. Zhou, S. Wen, Q. Wei, C. Yan, Y. Shi, Effect of substrate preheating on the texture, phase and nanohardness of a Ti-45Al-2Cr-5Nb alloy processed by selective laser melting, *Scripta Mater.* 118 (2016) 13–18, <https://doi.org/10.1016/j.scriptamat.2016.02.022>.
- [61] T. Maity, N. Chawake, J.T. Kim, J. Eckert, K.G. Prashanth, Anisotropy in local microstructure – does it affect the tensile properties of the SLM samples? *Manufact. Lett.* 15 (2018) 33–37, <https://doi.org/10.1016/j.mfglet.2018.02.012>.
- [62] Z. Wang, S. Scudino, J. Eckert, K.G. Prashanth, Selective laser melting of nanostructured Al-Y-Ni-Co alloy, *Manufact. Lett.* 25 (2020) 21–25, <https://doi.org/10.1016/j.mfglet.2020.06.005>.



**Publication III**

H.S. Maurya, K. Kosiba, K. Juhani, F. Sergejev, K.G. Prashanth, Effect of powder bed preheating on the crack formation and microstructure in ceramic matrix composites fabricated by laser powder-bed fusion process. Additive Manufacturing 58(2022)103013.





Contents lists available at ScienceDirect

## Additive Manufacturing

journal homepage: [www.elsevier.com/locate/addma](http://www.elsevier.com/locate/addma)

# Effect of powder bed preheating on the crack formation and microstructure in ceramic matrix composites fabricated by laser powder-bed fusion process

H.S. Maurya<sup>a,\*</sup>, K. Kosiba<sup>b</sup>, K. Juhani<sup>a</sup>, F. Sergejev<sup>a</sup>, K.G. Prashanth<sup>a,c,d,\*\*</sup>

<sup>a</sup> Department of Mechanical and Industrial Engineering, Tallinn University of Technology, Ehitajate tee 5, 19086 Tallinn, Estonia

<sup>b</sup> Department of Alloy Design and Processing, Institute for Complex Materials, IFW Dresden e.V., Helmholtzstraße 20, D-01069 Dresden, Germany

<sup>c</sup> Erich Schmid Institute of Materials Science, Austrian Academy of Sciences, Jahnstrasse 12, 8700 Leoben, Austria

<sup>d</sup> CBCMT, School of Mechanical Engineering, Vellore Institute of Technology, Vellore 630014 Tamil Nadu, India

## ARTICLE INFO

## Keywords:

Titanium carbide-based cermets  
Rescanning  
Selective laser melting  
Steel binder

## ABSTRACT

Ceramic matrix composites like cermets are difficult candidates to be fabricated by additive manufacturing (AM). Green cermets like the TiC-430 L AISI ferritic stainless steel (430 L-FSS) have been fabricated using the AM process like laser powder-bed fusion (LPBF) process or also known as selective laser melting (SLM). Multiple laser scanning was employed as a tool to preheat and melt the powder bed with different laser scanning parameters for each (two laser scans namely pre-heating scan and melting scan) scan to fabricate crack-free cermets. As a part of the preheating scanning (PHS) and melting scans (MS), different laser energy parameters are used to study the microstructure evolution and to study their densification process and mechanical properties. Lowering the preheating and melting scan speed results in prolonged laser exposure and higher temperature in the powder bed and melt pool, which led to the refinement of the microstructure due to higher cooling rate and generation of the cracks in the as-built parts caused by thermal gradient in the melt pool. Scanning electron microscopy and X-ray diffraction were performed to study the microstructure and phase analysis of the fabricated sample. Mechanical properties like density, hardness, fracture toughness, and compression tests were performed and discussed in detail. The results suggest that the laser PHS can effectively eliminate the presence of cracks. On the other hand, increasing the energy density of both PHS and MS results in a coarser microstructure with porosity, which also hampers the fracture toughness of these SLM fabricated cermets.

## 1. Introduction

A ceramic matrix composite (CMC) is a material that contains ceramic as a matrix and is added with a reinforcement that generally has a metallic component. CMCs are generally used to have high hardness, wear resistance, and oxidation resistance [1–4]. CMCs find their applications as wear parts in several industries, including mining, machining, petrochemicals, and aerospace applications [4,5]. Additionally, the CMCs are a potential choice of materials for high-temperature applications due to their excellent chemical and mechanical properties. Cermets are a class of CMCs and WC-Co (cemented carbide) is one of the most widely used cermets in the industrial realm, which offers improved toughness, hardness, and wear resistance [4,6–8]. The high-temperature oxidation is poor for the cemented carbides as WC and binder phases such as cobalt are oxidized into WO<sub>3</sub> and CoWO<sub>4</sub> [9]. This oxidation will

lead to part deformation and mass gain in the WC-based cermets and hence severely deteriorates their mechanical properties, which severely restricts its application range at high temperatures. TiC-based cermets are widely used in the new-generation cermets compared to conventional WC-based cermets because of their high hardness and low density. Cermets made with TiC and steel binders are promising as structural materials. These materials exhibit good wear resistance and corrosion resistance at elevated temperatures [10,11]. Typically, the transition group metals (like Fe, Co, Ni, Mo) are used as binder phase due to their better wettability, favor densification, and improved mechanical properties [12].

As a part of the REACH program in 2019, the European Commission has listed critical raw materials that have supply risk due to their availability and at the same time have high economic importance for the European Union. Elements like tungsten, cobalt, etc. are included in the

\* Corresponding author.

\*\* Corresponding author at: Department of Mechanical and Industrial Engineering, Tallinn University of Technology, Ehitajate tee 5, 19086 Tallinn, Estonia.  
E-mail addresses: [himaurya@taltech.ee](mailto:himaurya@taltech.ee) (H.S. Maurya), [kgprashanth@gmail.com](mailto:kgprashanth@gmail.com) (K.G. Prashanth).

list [5,13]. In addition, the recent surge in worldwide demand for such elements as Ni, Mo, W, Co, etc. has also driven the price of these metals. Moreover, Ni and WC-Co were both declared to be carcinogens by the US NTP (National Toxicity Program) and were considered hazardous to human health, both as powder and in the sintered form [14–16]. Consequently, finding a suitable alternative hard and binder phase is of interest as it can replace critical materials either completely or partially, thereby reducing the reliance on these strategic materials in the future. Fe, which is abundant in nature, low in cost, and not harmful to human health, has been regarded as the most popular alternative to Ni- and Co-free cemented carbides [5]. A wide variety of TiC-based cermets have demonstrated high-quality performance when used in wear parts and semi-finished or finished cutting tools. As a binder system for cermets, Fe and Fe-based alloys have also shown satisfactory mechanical, corrosion, and wear performances [5]. Such cermets are generally fabricated using powder metallurgical processes involving sintering and/or hot isostatic pressing [4]. However, using such a powder metallurgical process fabrication of complex/intricate shapes is rather limited. Hence, there is an urge to find suitable fabrication techniques to produce cermets with complex shapes.

The LPBF process is also known as Selective Laser Melting (SLM) offers the possibility to fabricate parts with complex geometrical features with high density and can process a wide spectrum of materials including cermets while achieving features that would not be possible with other conventional processes [17–19]. The SLM process involves the stacking of metal powder layer-by-layer and is fused with the help of a laser. Laser beams work in conjunction with thin powder beds to create desired patterns as dictated by the CAD data. The process is repeated until the final 3D geometry is fabricated [13,20]. SLM has several advantages, such as the ability to produce intricate shapes with minimal material loss, and the ease of process planning makes it a popular green technology in a wide range of industries. By optimizing the parameters of the SLM process, dense parts can be made with good/improved mechanical properties. Otherwise, processing defects such as porosities, cracks, delamination, and unmelted powder particles might be present in the SLM fabricated parts [19]. Various process parameters such as laser power, scan speed, powder rheology, etc. play a crucial role in the fabrication of the parts and these process parameters can affect the microstructure and severely influences the mechanical behavior of the as-built components [10,16,21]. Thus, process parameter optimization is essential for avoiding defects in the SLM fabricated parts. The presence of large residual stresses in the SLM fabricated parts may lead to cracking and at times failure of the component, which occurs due to the rapid melting and solidification in each layer [13,16].

To the best of the authors' knowledge, there have been only a few studies focused on the fabrication of TiC-based cermets via AM processes such as LPBF/SLM, and most of them have been concentrated on WC-Co cermets [17,22–24]. TiC-based materials have received very little attention with most of the research focused on the use of TiC as reinforcement [25–27]. Although few studies have focused on the TiC-based cermets, however, cracks and porosity were prevalent in the final as-built parts [28–30]. Ceramics (including CMCs) are brittle in nature and hence make it difficult to be processed by solidification-based processes like laser-based powder-bed fusion process (LPBF) [4,16]. Accordingly, this study aimed to reduce the process defects such as cracks in the LPBF/SLM processed parts by employing a laser multi-scanning strategy in each layer that serves as preheating and melting of the powder bed. During laser rescanning, the laser scans each sliced layer twice before spreading the next layer of powder. This procedure can be easily carried out for each sliced layer during the SLM process and is referred to as selective laser rescanning. Using this scanning strategy, the first laser scan with a lower energy density acts as a preheating scan (PHS) for the powder bed, followed by the next laser scan with a higher energy density considered as the melting scan (MS) to melt and fuse the powder bed. The formation of defects in TiC-Fe based cermet has been studied using different laser energy density parameters

(such as preheating and melting parameters). The PHS is usually accompanied by a low energy density mainly employed to pre-heat the powder bed, which can avoid the sudden level of temperature increases. Such reduction in the sudden level of temperature rise can reduce the thermal residual stresses in the fabricated materials and thus help in producing crack-free components [14]. The preheating and controlled cooling of the powder bed during laser exposure affect the cermet formation as well as the process defects that have been discussed in detail previously [13,14]. This study deals with the fabrication of TiC-based cermets using AISI 430 L ferritic stainless steel (430 L-FSS) as a binder material by adapting laser multi-scanning techniques via the SLM process. The aim is to fabricate such brittle CMCs/cermets without process defects, such as cracks with near theoretical density. The effect of pre-heating on mechanical properties such as hardness, fracture toughness, and compression tests were conducted and discussed in detail.

## 2. Experimental details

### 2.1. Powder preparation

In this study, TiC powder supplied by Pacific Particulate Materials Ltd. and 430 L-FSS powder supplied by Sandvik Osprey Ltd. were used to fabricate TiC-430 L-FSS-based cermets with the TiC content of ~65 vol %. Table 1 shows the elemental composition of the initial feedstock powder. A mechanical mixer was used to mix the powder homogeneously for 24 h at a speed of 10 rpm using Ytria Stabilized Zirconia (YSZ) balls as a mixing medium (ball diameter: 8 mm) [31]. TiC powder particles are irregular in shape with a mean particle size in the range of 1–3  $\mu\text{m}$ , as shown in Fig. 1(a). A near-spherical powder of 430 L-FSS was observed (Fig. 1(b)), with a size distribution in the range of 10–45  $\mu\text{m}$ . Fig. 1(c) shows the SEM image of the homogeneously mixed feedstock powder. The TiC and 430 L-FSS binder exhibit a wide range of variations in their powder particle size. A substantial amount of TiC particles sticks to the ductile surface of the 430 L-FSS particles. Fig. 1(d) shows the XRD pattern of the initially mixed feedstock powder. It shows a high-intensity peak corresponding to the TiC and binder ( $\alpha$ -ferritic phase), indicating that no new phases were formed during mixing.

### 2.2. LPBF/SLM fabrication

Cermet fabrication was performed using a ReaLizer SLM 50 (ReaLizer GmbH, Borchon, Germany) equipped with a 100 W laser made of Nd: YAG fiber. A set of working parameters was optimized during the fabrication of the cermet samples to achieve dense and crack-free cermets. Table 2 furnishes the optimized processing parameters employed during the SLM of TiC-430 L-FSS cermets. The layer thickness and hatch distance were maintained constant at 0.025 mm and 0.045 mm, respectively. The sample designation used through the study (DS1, DS2, and DS3) is stated in Table 2. Bulk cuboids with dimensions of 4 mm  $\times$  4 mm  $\times$  8 mm were fabricated via the SLM process. Eight number of samples were printed in each build job and several build jobs were fabricated to ascertain the reproducibility of the build parts [32]. A comparison of single scanning (SS) with multiple scanning (DS1) was made using the same melting scan parameters used in DS1 to study the effect of preheating the powder bed with multiple scanning. All the parameters involved in the present study are shown in Table 2.

The selective laser pre-heating scanning process will be referred to as "PHS" and the melting scan as "MS" throughout this paper. Both the PHS

**Table 1**  
Chemical composition of the initial feedstock powder in wt%.

Material	Ti	C	Cr	Mn	Si	Fe	Others
TiC	Bal	19.1	–	–	–	–	0.32
AISI 430 L	–	0.03	17.0	0.7	0.7	Bal	0.04

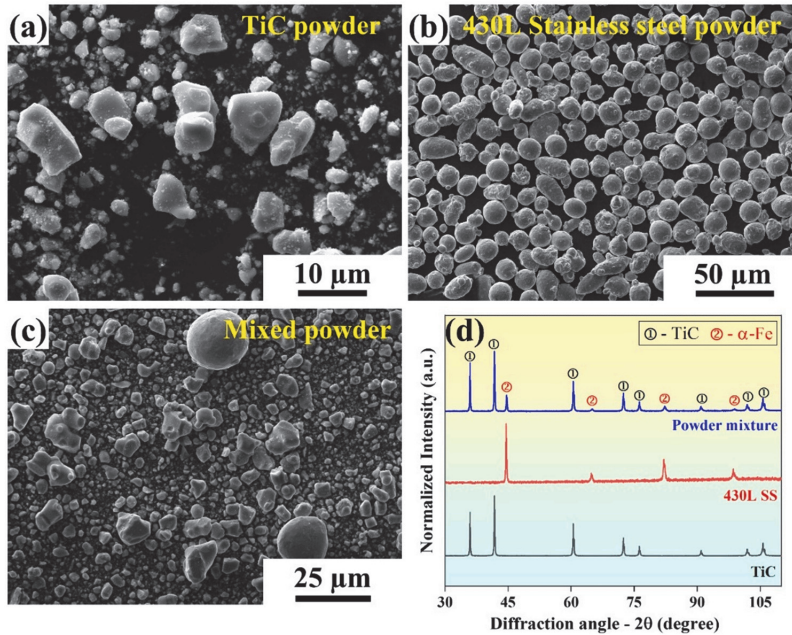


Fig. 1. Scanning electron microscopy images of the initial powder particles (a) TiC, (b) Fe, and (c) mixed feedstock powder. (d) The X-ray diffraction pattern of the starting and mixed feedstock powders.

Table 2

The process parameter includes the laser scan speed and energy density employed for both pre-heating scan and melting scan during the selective laser melting of cermets.

Sample	Pre-heating scan (PHS)			Melting scan (MS)		
	Laser power (W)	Scan speed (mm/s)	Energy Density ( $J/mm^3$ )	Laser power (W)	Scan speed (mm/s)	Energy Density ( $J/mm^3$ )
SS1	–	–	–	94	99	844.7
DS1	44.2	488	80.4	94	99	844.7
DS2	19.2	203	84.5	87.4	81	958.7
DS3	19.2	176	97	71	56	1127.6

and MS were conducted with the same laser scanning direction. However, a scan rotation of  $60^\circ$  was employed between two consecutive powder layers. First, laser scanning was employed to scan the powder layer with low energy density and high scanning speed. Due to the low laser exposure power and high scanning speed, there will be no melting of the powder bed. Therefore, high-speed scanning is used only to pre-heat the powder prior to high energy density laser exposure. In the same powder layer, laser exposure with high laser energy density and low scan speed is used to melt and fuse the powder during the MS. A schematic of the laser scan strategy with both scans PHS and MS is shown in Fig. 2. To reduce oxygen contamination during the SLM processes, the building chamber was under an argon pressure, which contains  $< 20$  ppm of oxygen. A stainless-steel substrate was used, and the samples were oriented vertically to the building direction. The longitudinal samples were orientated parallel to the laser beam direction (X-Z plane). Cuboidal samples with a dimension of  $4 \text{ mm} \times 4 \text{ mm} \times 8 \text{ mm}$  were fabricated by SLM via PHS and MS scanning strategy. The scan speed  $-v$  ( $\text{mm} \cdot \text{s}^{-1}$ ), laser power  $-P$  (Watt), hatch distance  $-h$  (mm), and layer thickness of the powder  $-t$  (mm) are the four parameters that affect the fabrication of the sample and are considered when calculating the volumetric energy density  $-VED$  ( $J/mm^3$ ), or the volumetric energy

delivered per unit volume of the laser, which is obtained from the following equation [33,34].

$$VED = \frac{P}{v * h * t} \quad (1)$$

### 2.3. Structural, microstructural, and surface characterization

Samples fabricated using SLM were ground and polished for microstructural and phase analysis. The microstructure and elemental distribution of the as-built parts were observed by SEM (Zeiss EVO MA15) coupled with the EDS system INCA. An analysis of phase constitution of the SLM fabricated parts (longitudinal section) were carried out by the Rigaku Smart lab X-Ray Diffractometer (XRD) equipped with Cu-K $\alpha$  radiation ( $\lambda = 0.1542 \text{ nm}$ ) at room temperature with a scan range of  $30\text{--}120^\circ$  ( $2\theta$ ) with a step size of  $0.04^\circ$ . Samples with a geometry of about  $1.5 \text{ mm} \times 1.5 \text{ mm} \times 6 \text{ mm}$  were extracted using a Struers cutting device (Accutom 50) for  $\mu$ -X-ray computed tomography ( $\mu$ CT - Phoenix nanotom, General Electric).  $\mu$ CT was carried out at 120 kV and 100 mA with a voxel size of  $2.75 \mu\text{m}$  to illustrate present cracks and/or pores.

### 2.4. Mechanical testing

Analytical balance (Mettler Toledo ME204) was used to measure the density of the SLM-processed bulk samples at room temperature according to Archimedes' principle. Calculation of the theoretical density was performed using the rule of mixtures. Vickers microhardness of the SLM processed samples (across longitudinal and cross-sectional) was determined at room temperature using a microhardness testing machine (Buehler Micromet) using a 1000 g load with a dwell time of 10 s. The mean value was reported for each sample from 10 indentation measurements. Using the method of fracture by indentation using a loading of 30 kgf with a dwell time of 10 s, the fracture toughness ( $K_{IC}$ ) of the SLM fabricated parts was determined with the most common empirical equations for brittle materials [35]:

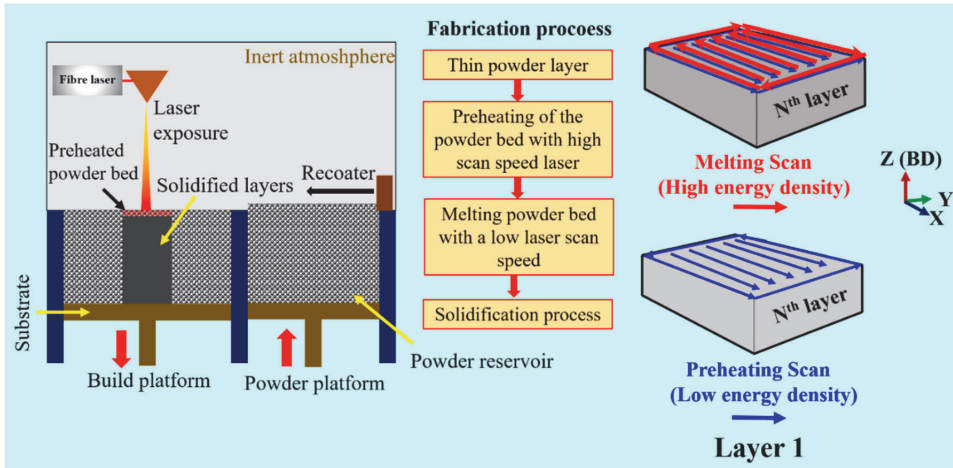


Fig. 2. Schematics illustrating the selective laser melting process and the two laser scans (pre-heating scan and melting scan) employed during the selective laser melting process.

$$K_{IC} = 0.15 \sqrt{\frac{HV}{\sum l}} \quad (1)$$

where  $K_{IC}$  ( $\text{MPa}\cdot\text{m}^{1/2}$ ) is the fracture toughness,  $\sum l$  (mm) is the sum lengths of the cracks tip from the indent, and  $HV$  ( $\text{N}/\text{mm}^2$ ) is the Vickers microhardness. Indentation values from three samples were reported as the mean value. Room-temperature compression tests were carried out on a servo-hydraulic testing machine (Instron 8516) at a strain rate of 0.6 mm/min with a capacity of 100 kN.

### 3. Results and discussion

#### 3.1. Phase analysis

The XRD patterns of the TiC-430 L cermet fabricated by SLM with different energy densities are presented in Fig. 3. According to the XRD patterns, the SLM processed cermet shows peaks corresponding to titanium carbide (TiC), and  $\alpha$ -Fe solid solution. No new phase formation is observed as a result of the fabrication process indicating that no reaction

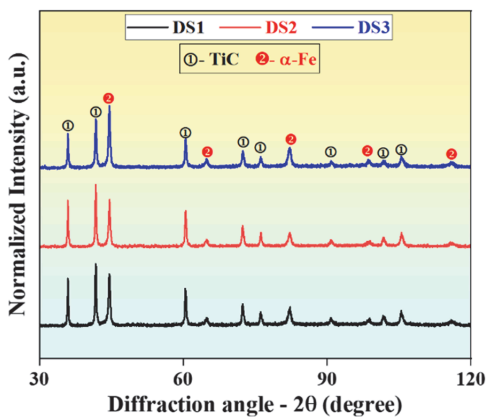


Fig. 3. The X-ray diffraction patterns of the TiC-430 L cermet fabricated by selective laser melting as a function of varying energy densities.

between the ceramic matrix and the metallic reinforcement has taken place during the SLM process. It is important to register that no inter-metallic carbide phase other than TiC is observed/formed (like iron carbide/chromium carbide). In addition, no changes in the phase composition can be observed with the change in energy density of both PHS and MS. However, some minor changes in both the intensity and broadening of the peaks may be observed for both phases (TiC and 430 L). The variation in the peak intensities may be attributed to the formation of texture (preferred orientation/growth) in these samples as a function of PHS and MS energy densities. This is quite natural in the SLM process that the change in the energy density may change the preferential growth direction leading to texture in these cermet [36–38]. The changes in the broadening of the peaks are due to the changes in the defect concentration (internal defects like dislocations) and/or internal strain [39,40]. It has been observed that all three cermet show a dislocation density in the order of  $4 \pm 0.3 \times 10^{14} \text{ m}^{-2}$  [41–43]. A high dislocation density, which is a characteristic of the SLM process has been confirmed in the present study as well. However, the difference in the dislocation density between the three samples is minimal. Hence the changes in the broadening of the peaks should be attributed to the changes in the internal strain due to varying energy densities. Since the feed stock powder mixture and all the samples with double scanning did not show any change in the phase excepting the shape and intensity of the peaks, XRD scan for the single scan strategy sample (SS1) has not been conducted assuming the single scanned specimen will also have no phase changes. In addition, due to the complexity of fabricated parts, caused by cracks in the as-built parts, which leads to the failure of the parts, XRD measurement was difficult to be carried out for the single scan specimens.

#### 3.2. Microstructural characterization

Fig. 4 depicts the microstructure of the samples fabricated via single scanning strategy (SS1) with high laser power. Cracks were evident in all the images shown in Fig. 4. These cracks generate due to high degree of internal stresses present in these parts. Due to the existence of cracks in the as-built parts, the parts gradually weaken from the base, and the material crumbles out after some layers of printing. Adapting single laser scanning causes a wide thermal gradient in the melt pool and this causes a high thermal residual stress in the parts during the fabrication and led to the failure of the parts during the printing. The effect of the single

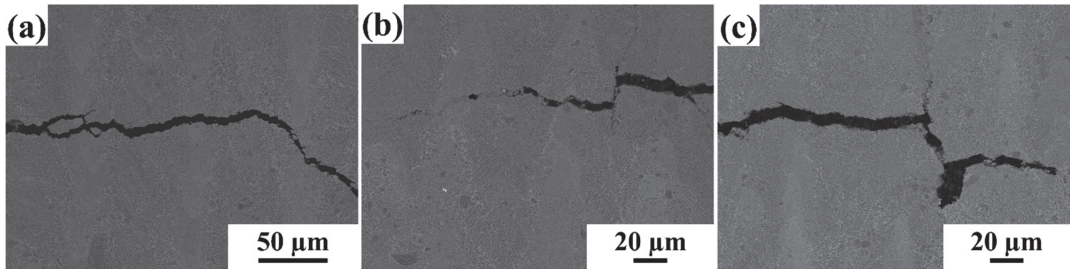


Fig. 4. Scanning electron microscopy images of the TiC- SS based cermets showing the formation of cracks in the as-built parts during the single scan melting strategy.

scanning with different laser parameters has been explained in the previous work [13,14].

Fig. 5 shows the typical microstructure of SLM processed TiC-430 L cermets with different laser processed parameters. It may be noted that a higher scanning speed is used for the PHS compared to the MS. Such higher speeds employed during PHS lead to just heating of the powder bed and avoids melting them due to the supply of a lower energy density. The scan speed was kept very low for the second laser exposure to the powder bed (keeping the energy density relatively high). As a result of this increase in the energy density during MS, the powder particles will fuse as the powder bed melts. The PHS through high scan laser exposure

influences the melting and solidification rates of the melt pool, which will ultimately influence the microstructure of these fabricated cermets. When the powder bed is preheated using a low energy density scan, the temperature of the powder bed increases, preventing the sudden heating and cooling of the melt pool during the high energy density laser exposure during MS, which will reduce the thermal residual stress generated during the fabrication process. The reduced cooling rates and the reduction in the residual thermal stresses result in eliminating the formation of cracks during the fabrication process. It may be observed from Fig. 5 that irrespective of the changes in the energy densities of the PHS and MS, there are no minor cracks observed in these

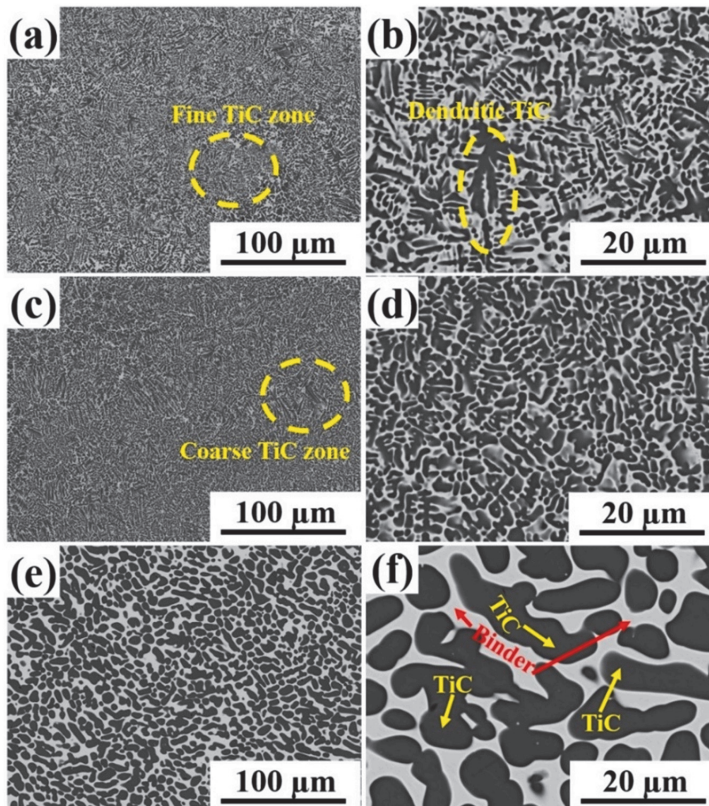


Fig. 5. Scanning electron microscopy images of the TiC-based cermet showing the difference in the distribution of the TiC phases with varying pre-heating scan (PHS) and melting scan (MS) energy densities. (a,b) DS1, (c,d) DS2, and (e,f) DS3.

microstructures. It may be concluded that the PHS can have a significant effect on the thermal gradient of the melt pool which ultimately leads to the reduction of crack formation by lowering the thermal residual stresses/gradient [44]. The microstructure of the as-built part shows the impact of the energy densities employed during PHS and MS. The PHS and MS process parameters significantly affect the growth morphology and dispersion state of the TiC phases. Two distinct phases of TiC (dendritic and coarser) are observed in all the microstructures. The dark phase corresponds to the TiC ceramic phase while the bright phase corresponds to the 430 L ferritic stainless-steel binder. For the sample DS1 where the scanning speed is relatively high for the PHS (488 mm/s) (leading to a low energy density  $\sim 80 \text{ J/mm}^3$ ) and the energy density is relatively low for the MS (845  $\text{J/mm}^3$ ), the TiC phase exhibit a dendritic morphology with a non-uniform distribution in size and shape (Fig. 5 (a)). Such non-uniform variation in the size and shape of the TiC phase may be attributed to the laser beam with gaussian distribution of energy. As the laser energy is concentrated more towards the center of the laser exposure area, the melting of the powder is accelerated in the center, resulting in a temperature gradient at the laser exposed zone and at the laser scan boundary, which directly influences phase shape and fineness [45,46]. It has been observed that laser beam profile also has influence on the microstructure and mechanical properties of the as built component. Changing laser beam profiles affects the melt pool shape and size; in addition, different laser exposure profiles introduce process defects. [47–49].

By increasing the laser energy density of both PHS (laser energy density  $\sim 85 \text{ J/mm}^3$  – laser scan speed  $\sim 203 \text{ mm/s}$ ) and MS (laser energy density  $\sim 959 \text{ J/mm}^3$ ), a relatively coarser microstructure for the DS2 sample is observed (Fig. 5(b)). A higher magnification image revealed that TiC phases typically show two different morphologies. The first type features a slender dendritic structure with a refined dendritic arm length and the second type features accumulated coarser TiC phases

with irregular shapes. When the MS energy density ( $1128 \text{ J/mm}^3$ ) is increased further, the DS3 microstructure does not reflect the finer dendritic structure, but rather coarser TiC phase (Fig. 5(c)). The lower scan speed during PHS (176 mm/s) can be attributed to this modification of the TiC morphology. This lower scan speed allows enough time to raise the temperatures of the laser-exposed powder bed and, consequently, the melt pool temperature increases during the MS laser scan reducing the cooling rate drastically. Such reduced cooling rates allow the microstructure to grow during solidification without hindrance and hence a coarser microstructure (for both TiC and 430 L – ferritic phase) is observed.

The fineness of the microstructure of the SLM-processed part is influenced by their solidification rate ( $R$ ), thermal gradient ( $G$ ), and cooling rate of the melt pool ( $T = G \times R$ ) [50].  $G$  is the difference in temperature over a distance and changes according to time and place in the melt pool.  $R$  depends on the laser scan speed and angle between the laser moving direction. A microstructure's fineness is determined by its cooling rate ( $G \times R$ ). In general, the higher the cooling rate, the finer is the microstructure of the material. The SLM process exhibits high cooling rates in the order of  $10^3$  and  $10^{11} \text{ K/s}$  [51–53], which can result in fine microstructures in the SLM-processed parts with a higher scan speed during PHS. However, the MS with a lower scan speed has an adverse effect on the cooling rate because it raises the powder bed's temperature. At the same time, increased PHS temperatures result in reduced cooling rates, thus coarsening of the phases. In conclusion, these microstructures of the as-built parts are highly dependent on both the PHS and MS, and thus, a change in these parameters may significantly influence the microstructural formation and in turn, their mechanical properties of the SLM fabricated samples. Through multiple scanning, there were no cracks observed in the microstructure of the as-built samples, thus proving that multiple scanning including PHS, and MS reduces the thermal residual stress and facilitates the formation of

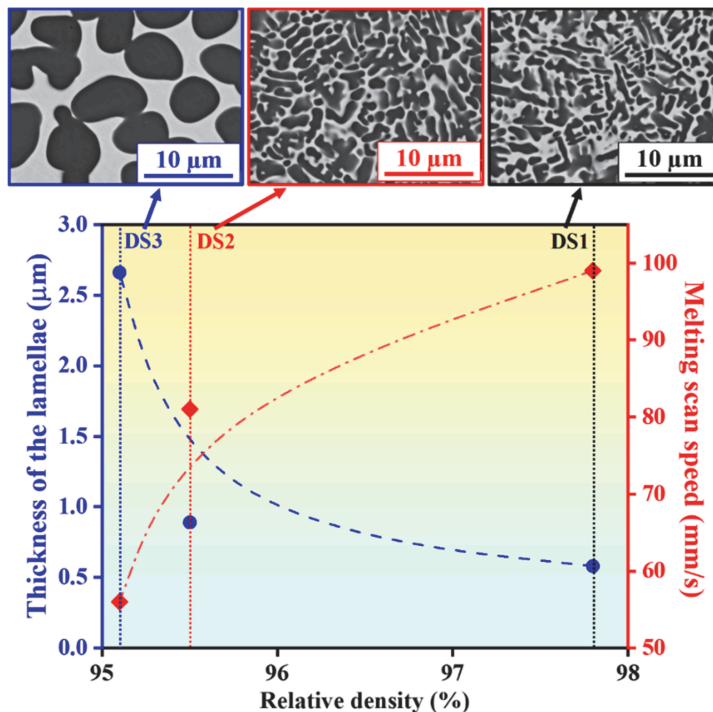


Fig. 6. Relative Density and thickness of the TiC phase in the microstructure as a function of melting scan speed.

the defect-free/crack-free cermets.

Fig. 6 illustrates the effect of MS laser scan on the microstructural formation and the density of the as-built components. A high laser scan speed employed during MS results in a finer microstructure. On the other hand, a lower scan speed during MS resulted in a coarser microstructure. It can be observed from Fig. 6 that an increase in the laser scan speed during the MS increases the density of the sample and at the same time, the average thickness of the TiC lamellae decreases. For instance, the TiC lamellae thickness is observed to be lowest when the employed scan speed is highest (99 mm/s). This is because when the scan speed increases the cooling rate increase (an increase in the energy density) and hence a finer microstructure is observed and vice versa. A similar effect is observed for PHS as well. Fig. 7 shows the elemental mapping of the as-built cermets fabricated through multiple scanning strategies with different energy densities. The distribution of Ti, Fe, and Cr in the microstructure of the as-built parts represent the distribution of ceramic and binder particles in the different samples fabricated via multiple laser scanning. The present results corroborate with the SEM results, where the dark regions correspond to the TiC ceramic phase and the bright phase corresponds to the 430 L ferritic stainless steel.

### 3.3. Porosity and density

Table 3 represents the measured density and porosity of the as-built cermets with different laser energy densities employed for both PHS and MS. Based on the preheating and melting scans of the as-built cermet, it can be observed that the density of the as-built samples is subject to its energy density and the scan speed of the laser [54–56]. The density of the sample can be affected by increasing the laser energy density of the MS [57–59]. A maximum density of 97.8% is achieved for the DS1 sample by employing a high scan speed during PHS (low energy density) and low energy density during MS scan (845 J/mm<sup>3</sup>). Changes in the laser energy density of both the PHS and MS affect the formation of

**Table 3**

Density and porosity values were obtained for the SLM fabricated cermets using Archimedes' principle.

Sample Designation	Porosity (vol%)	Relative density (%)
DS1	2.2	97.8
DS2	4.5	95.5
DS3	4.9	95.1

microstructures and can lead to the formation of process defects, hence resulting in a variation in relative density of the as-built SLM processed parts [60]. The DS3 sample, however, was found to have the lowest density due to the lower scan speed of the PHS scanning (176 mm/s). Using a lower laser scan speed during PHS gives enough time to fuse or partially melt the powder particles and increase the melting pool temperature, which will ultimately affect thermal residual stress and generate process defects. The relatively prolonged exposure time (compared to the other two counterparts) may lead to gas pickups that may end up as porosity in these samples [61].

Micro-computed tomography images of the as-built samples have been shown in Fig. 8. All defects indicated with red color in the reconstructions are observed inside the specimen while the darker grey defects are on the surface of the scanned specimens. In comparison with other samples, sample DS1 has a lower porosity. As illustrated in Fig. 8, porosity is not distributed evenly throughout the samples, which is probably due to poor powder rheology, as TiC powder particles are irregularly shaped, while stainless steel powder is spherical, which affects powder flowability during subsequent recoating powder layers. As a result of the laser scanning strategy and melt pool temperature variance, most of the pores/process defects are located along with the corners of the sample. Laser scanning starts from one corner, and the scan move towards the other end, increasing melt pool temperature, but there is a slight variation in melting pool temperature at the other corner/end.

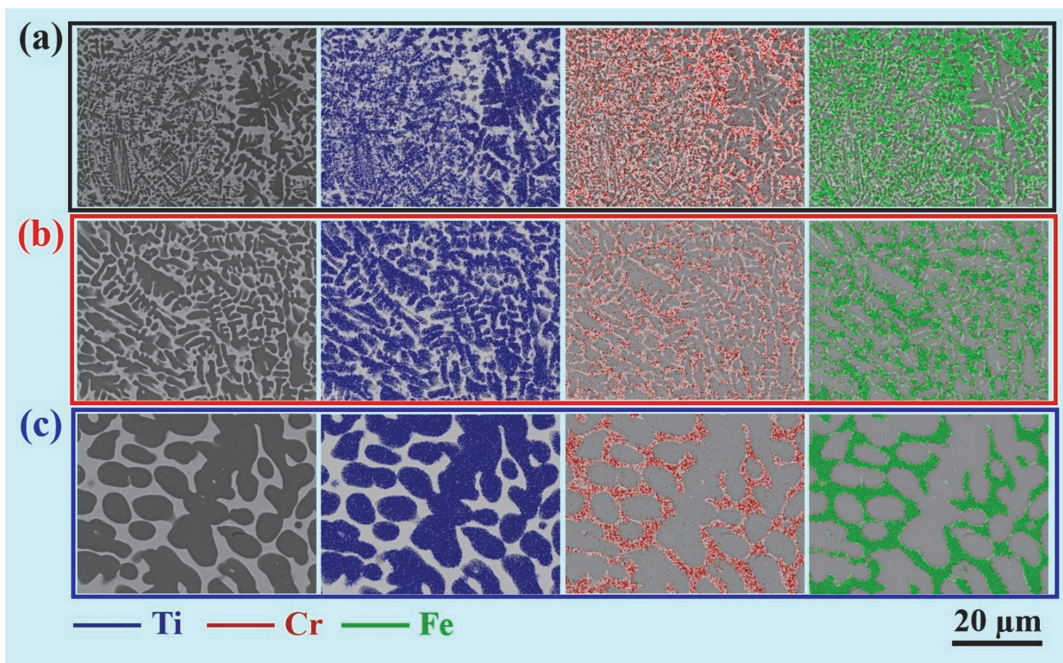


Fig. 7. X-ray energy dispersive spectrum mapping for the selective laser melted cermets with different preheating and melting scan parameters. (a) DS1, (b) DS2, and (c) DS3.

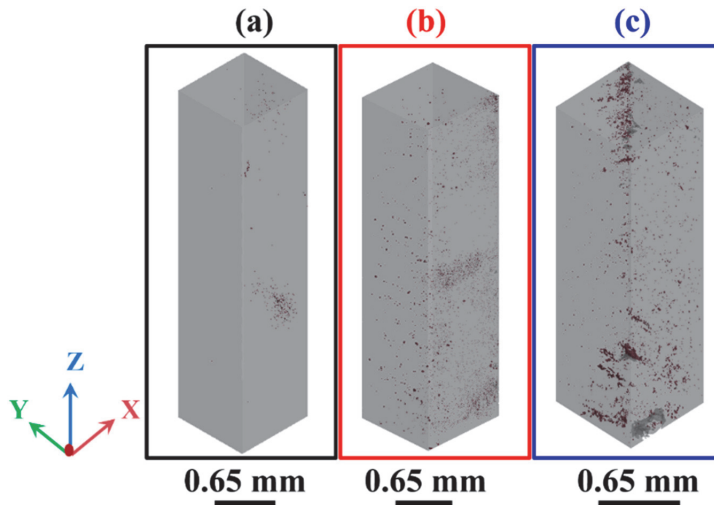


Fig. 8. X-ray micro-computed tomography image of the samples fabricated through multiple scanning by selective laser melting. (a) DS1, (b) DS2, and (c) DS3.

In the other corner, a higher temperature is observed than the starting corner, resulting in defects mostly present in corners of the as-built cermet. Laser power, scanning speed, layer thickness, powder materials rheology, and chamber environment are among the variables that affect SLM as-built parts. An incorrect selection of any of these parameters will introduce defects. SLM defects will negatively impact the fabrication process on-site and the mechanical performance of the samples. There are several mechanisms responsible for the as-built process defect during the AM of the cermet. The possibility of defect formation has been reported as powder defects, insufficient laser energy, entrapped gas, balling effect, and keyhole defect [62].

The SEM images along the longitudinal sections show the different types of defects formed during the solidification process (Fig. 9). As a part of the LPBF/SLM build processes, the heat source has a relatively Gaussian distribution and is focused on the powder bed with a gradient in laser energy distribution. A melting zone is characterized by a variety of physical phenomena, including interactions between solid, liquid, and gas phases. A lack of uniform power distribution, poor powder rheology, and wide particle size distribution could be responsible for the formation of entrapped gas defects [63]. As a result of the gas present between the powder particles during powder recoating, gases are trapped and may dissolve in the melting pool but may stay in the solid after solidification owing to the high cooling rate. Linear defects, which occur as a result of lack of melting, are very typical of the SLM process defects. They are mainly caused by insufficient energy input during fabrication [64–66]. When the laser power is low, powder particles are not fully melted and during the melting of the subsequent layer, it results in the formation of a gap/pore. Insufficient melt powder particles during solidification may result in poor bonding, or unmelted metal powder during solidification may contribute to fusion defects [67,68].

### 3.4. Hardness

Fig. 10 shows the hardness contour mapping of the longitudinal section of the as-built cermets. The variation in the observed hardness values possibly explains the inhomogeneous phase distribution of the binder and ceramic phases. A large volumetric percentage of the TiC phase resides in some areas compared to the binder phase and vice versa. Thus, the hardness fluctuation depends on whether the indenter is placed on the TiC phase, Fe phase, or an intermediate area between these two phases. The hardness values of the TiC and  $\alpha$ -Fe phases are in

the range of  $> 2000$  HV, and Fe  $< 200$  HV, respectively. The edges of the samples show higher hardness compared to the core. There is a possibility that it's due to the laser scan strategy and the gradient in melt pool temperature. The starting corner has a lower temperature when laser exposure begins, while the other corner ends with a higher temperature as the laser melting ends there and this will be the last point to solidify. Hence, the defects are observed along the starting corner where there exists instability in the melt pool. This also explains the presence of porosity in the sample near the edge, as shown in Fig. 8. The hardness values reported by other researchers range from 1300 to 1900 HV for TiC based cermets with different metals binders and using different processing routes [69,70].

Fig. 11 shows the microhardness values of the cermets (along the longitudinal section) fabricated by SLM using different PHS and MS. The microhardness of the parts is affected by the changes in the energy densities of both PHS and MS. Lower MS energy density has a lower hardness value for the DS1 sample ( $1217 \pm 141$  HV). The maximum hardness value was achieved for the sample DS3 ( $1289 \pm 188$  HV) with a relatively high MS energy density and lower MS scan speed. The maximum hardness for sample DS3 could be the result of a higher pre-heating temperature and high MS energy density that could have resulted in a coarser microstructure. However, irrespective of the huge variation in the microstructure (including the morphology of the phases) the variation in the hardness observed between the samples DS1, DS2, and DS3 is minimal (with a difference of only 100 HV).

### 3.5. Fracture toughness

Fig. 11 shows the mean fracture toughness ( $K_{IC}$ ) values of the as-built TiC based cermets. As can be seen in the graph, a maximum fracture toughness value has been maximum for the DS1 sample, which could explain the lower porosity and gradient in TiC dendritic phases. A gradient in the TiC phase helps in improving the toughness of the cermet. However, the DS3 sample shows the least fracture toughness value due to the presence of a relatively high volume of porosities and the presence of a coarser TiC phase.

Fig. 12 shows the SEM micrographs of the crack propagation in the as-built cermets fabricated via SLM. It can be seen that the indentation is regular, and it does not have any crushed edges, as well as the visible cracks are on the corner, showing that it has been deformed through plastic deformation. As illustrated in Fig. 12, the toughening

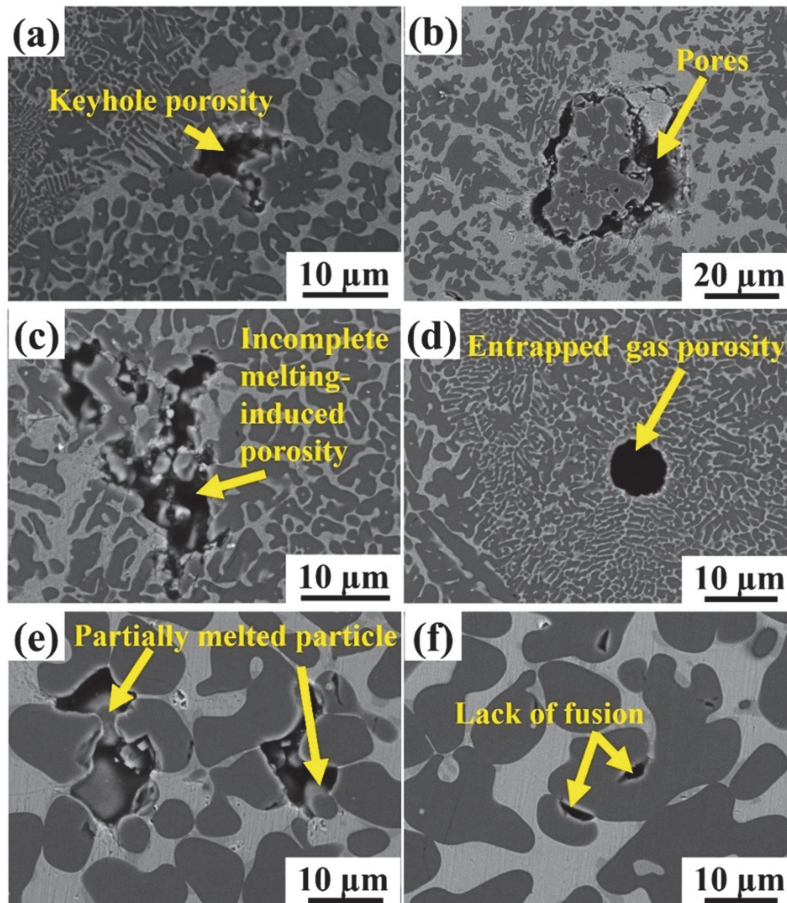


Fig. 9. Characteristic defects were observed in the selective laser melted parts fabricated as a function of varying process parameters. (a,b) DS1, (c,d) DS2, and (e, f) DS3.

mechanisms of the TiC-Fe based cermets were considered as grain bridging, crack branching, crack deflection, and fracture of grains which usually occurs in brittle materials [71,72]. Both the transgranular and intergranular fractures can be observed in the cermet surface, which affects the fracture toughness of the SLM processed as-built cermet. The grain shape, distribution of the particle, size of the TiC phases, variation in the thermal expansion coefficient of the ceramic and binder material plays an important role in the toughness mechanism. Crack propagation paths are affected by the shape and distribution of hard phases. With finer microstructures (DS1), the crack propagation requires more energy to initiate and crack deviation is more likely to occur. However, as the TiC phase becomes coarser, the crack initiation process becomes more energy intensive, but in this case the crack propagation may be much easier, and the deviation of the crack is less probable as can be seen from (Fig. 12). The grain matrix interface debonding on the crack's front usually occurs when it encounters a TiC particle, and the crack propagates through a more tortuous path as a result [73,74]. TiC and Fe-based cermets have thermal expansion coefficient mismatches, which resulted in residual tensile and compressive tensions within the matrix, resulting in microcracks and contributing to the branching of the crack when the main crack propagated due to which more fracture energy was dissipated and the crack extension was impeded, thus leading to improved

toughness [75,76]. The crack bridging effect is shown in Fig. 12(a) by a TiC particle, which provides a restraining force for the crack growth. The TiC particle fractures after consuming energy sharply during the crack propagation process, which hinders the crack propagation and resulted in improved toughness (Fig. 12(c)). It could be seen that gradient in the TiC phase with finer and coarser dendritic TiC forms a kind of interlocking and hinders the crack propagation path [77–79]. The gradient in TiC phases in the microstructure was considered to greatly improve the damage tolerance of these cermets [80]. Defects like porosity also degrade the toughness and samples with higher porosity have exhibited a lower fracture toughness value.

### 3.6. Compressive strength

Especially for cermets and CMCs, brittle fracture dominates the failure of the tool. When the minimum principle tensile stress reaches a critical value, materials fail by brittle fracture. Fig. 13 shows the compressive strength data for the SLM processed samples with multiple scanning strategies. It can be observed that the porosity doesn't affect the compressive properties of the sample while the hardness effect can be seen on the compressive test. This is because the porosities may undergo closure during the compression test and may not have a significant

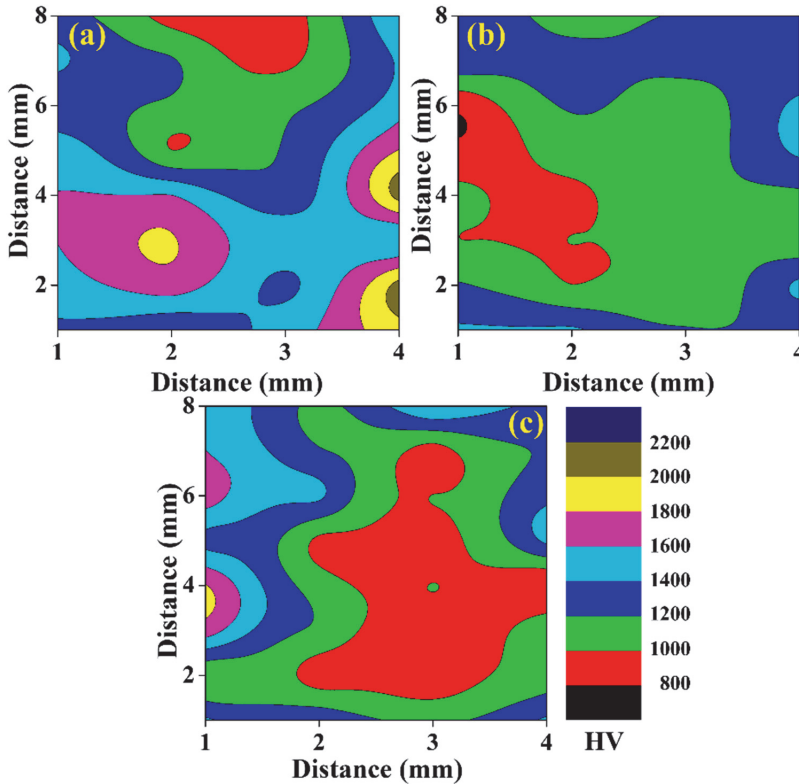


Fig. 10. Contour map showing the hardness distribution in the selective laser melted cermet fabricated with pre-heat and melting scans. (a) DS1, (b) DS2, and (c) DS3.

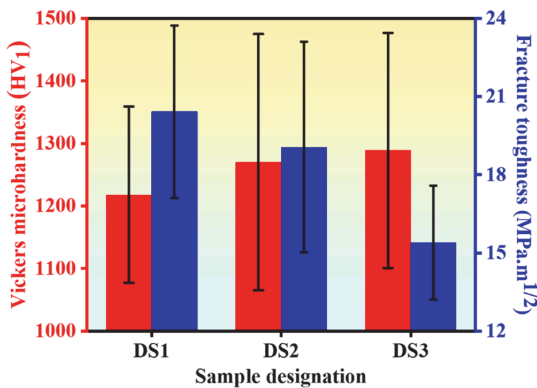


Fig. 11. Microhardness and fracture toughness data of the TiC-430 L cermet fabricated by the selective laser melting process different energy densities employed during the pre-heat scan and melting scan.

influence [81–83]. The compressive strength of all three samples does not show a significant variation, considering the error values. There is a marginal difference in the compression values that may be due to the difference in the microstructural features and the porosity distribution.

The DS3 sample shows a coarse microstructure with the highest porosity and hence relatively lower compressive strength. On the other

hand, the microstructure of the samples DS1 and DS2 are similar excepting the porosity levels. Since the porosity does not influence the compressive properties significantly both the samples DS1 and DS2 have very similar compressive properties within experimental errors. Hence, the higher preheating scan and lower melting scan led to a finer microstructure, and these finer microstructures enhanced the mechanical properties of the as-built cermet fabricated via SLM. Compression strength of the cermet is also affected by the binder composition and their volume percentage [84]. It was reported that addition of elements like Mo, Cr. etc. improves the mechanical properties of the parts by improving the wettability and refining the microstructure [85]. (Table 4).

#### 4. Conclusion

Crack formation in the fabrication of brittle material such as cermet through the SLM process is a critical problem and therefore in this study multi-scanning techniques have been employed as PHS and MS for the fabrication of crack-free cermet. A TiC-430 L binder-based cermet was successfully fabricated without any cracks using the SLM process. As-built samples were assessed for microstructural evolution, density, porosity, hardness, compressive strength, and fracture toughness. This study summarizes the following conclusions:

1. Based on the results of the microstructural studies, the laser parameters used during PHS, and MS determine the TiC phase morphology. Decreasing energy density during both PHS and MS lead to the formation of finer TiC phases. On the other hand,

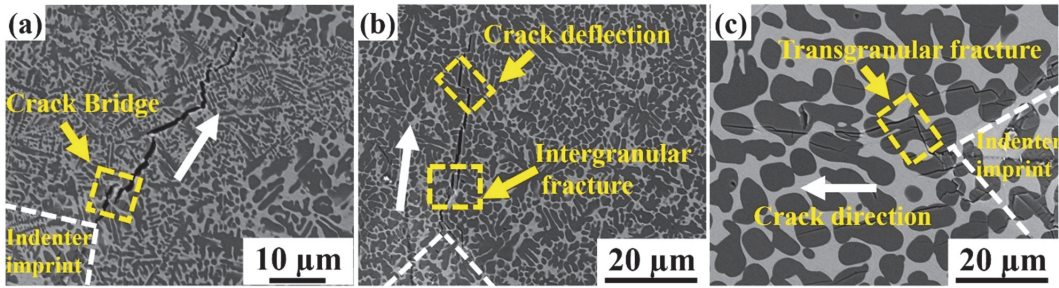


Fig. 12. Crack propagation path and toughness mechanisms observed in the TiC-430 L based cermets fabricated using selective laser melting. (a) DS1, (b) DS2, and (c) DS3.

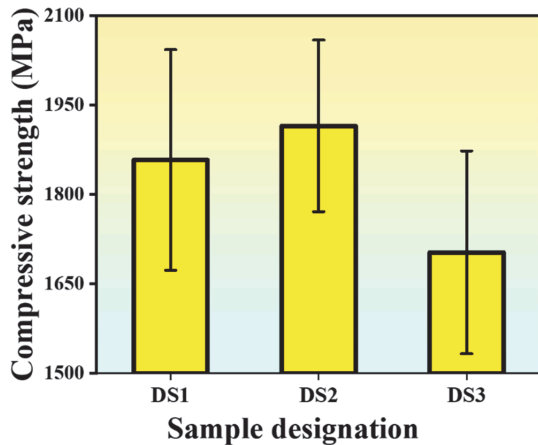


Fig. 13. Compressive strength of the TiC-430 L cermets produced by the selective laser melting process.

Table 4

Mechanical properties of the as-built cermets fabricated through selective laser melting with different energy densities were employed during the laser-pre scan and melting scan.

Sample Designation	Relative Density (%)	Hardness (HV <sub>1</sub> )	Fracture toughness (MPa.m <sup>1/2</sup> )	Compressive strength (Mpa)
DS1	97.8	1218 ± 141	20.42 ± 3.3	1858 ± 185
DS2	95.5	1270 ± 205	19.06 ± 4.0	1915 ± 144
DS3	95.1	1289 ± 188	15.39 ± 2.1	1703 ± 170

increasing the energy density during both PHS (lowering scan speed) and MS results in increasing the overall temperature of the melting pool, resulting in coarser TiC phases with less gradient.

- Microstructure and defects are influenced greatly by the scan speed during the PHS of the powder bed. As a result of the lower scan speed (high energy density), the preheated powder bed temperature increased, and this had a negative effect on the thermal residual stress, thus resulting in more defects such as cracks in parts with higher preheating temperatures.
- The SLM processed as-built parts with finer microstructure and lower porosity achieved the best combination of hardness (1218 ± 141 HV, DS1) and fracture toughness (20.4 ± 3.3 MPa.m<sup>1/2</sup>, DS1). Crack deflection, crack branching, grain bridging, and grain fracture were

considered toughening mechanisms of the TiC- stainless steel binder cermet.

Thus, it is concluded that preheating the powder bed does play an important role in fabricating crack-free cermets since it lowers the thermal residual stress, which results in as-built cermets parts of good mechanical properties. Although some defects, such as pores, cannot be completely eliminated from the process, however, the overall density and mechanical properties of the as-built parts seem to be improved in the future.

#### CRediT authorship contribution statement

**H.S. Maurya:** Conceptualization, Methodology, Data curation, Validation, Formal analysis, Investigation, Writing – original draft preparation. **K. Kosiba:** Data curation, Formal analysis, Investigation. **K. Juhani:** Validation, Writing – review & editing, Resources, Supervision, Funding acquisition. **F. Sergejev:** Validation, Writing – review & editing, Resources, Supervision, Funding acquisition. **K.G. Prashanth:** Validation, Writing – original draft preparation, Writing – review & editing, Resources, Supervision, Funding acquisition.

#### Declaration of Competing Interest

The authors declare that they have no known competing financial interests or personal relationships that could have appeared to influence the work reported in this paper.

#### Data availability

Data will be made available on request.

#### Acknowledgments

This work was supported by Estonian Research Council grants PRG1145 and European Regional Development Grant ASTRA6–6. Financial support from the Guangdong Natural Science Foundation - China (2020A1515011242), the High-end Foreign Experts Recruitment Program - China (G2021163004L), and the Guangdong International Science and Technology Cooperation Program - China (2021A0505050002), are appreciated.

#### Author's Disclosure Statement

The authors state there is no conflict of interest.

#### Data availability

The present data forms a part of the ongoing study, and the results

may be shared upon reasonable request from the corresponding author (s).

## References

- [1] C. Zhang, Y. Du, S. Zhou, Y. Peng, J. Wang, Grain growth and hardness of TiC-based cermets: Experimental investigation and thermodynamic calculations, *Ceram. Int.* 42 (2016) 19289–19295, <https://doi.org/10.1016/j.ceramint.2016.09.096>.
- [2] S. Kang, *Cermets* (2014), <https://doi.org/10.1016/B978-0-08-096527-7.00005-2>.
- [3] P. Ettmayer, *Hardmetals and cermets*, *Annu. Rev. Mater. Sci.* 19 (1989) 145–164, <https://doi.org/10.1146/annurev.ms.19.080189.001045>.
- [4] A. Aramian, S.M.J. Razavi, Z. Sadeghian, F. Berto, A review of additive manufacturing of cermets, *Addit. Manuf.* 33 (2020), 101130, <https://doi.org/10.1016/j.addma.2020.101130>.
- [5] J. Kübarsepp, K. Juhani, Cermets with Fe-alloy binder: a review, *Int. J. Refract. Met. Hard Mater.* 92 (2020), <https://doi.org/10.1016/j.jirmhm.2020.105290>.
- [6] J. Kübarsepp, K. Juhani, Cermets with Fe-alloy binder: A review, *Int. J. Refract. Met. Hard Mater.* 92 (2020), 105290, <https://doi.org/10.1016/j.jirmhm.2020.105290>.
- [7] J. Kübarsepp, H. Klaasen, J. Pirso, Behaviour of TiC-base cermets in different wear conditions, *Wear* 249 (2001) 229–234, [https://doi.org/10.1016/S0043-1648\(01\)00569-5](https://doi.org/10.1016/S0043-1648(01)00569-5).
- [8] A. Aramian, Z. Sadeghian, S.M.J. Razavi, F. Berto, Room and high-temperature sliding wear behavior of in situ TiC-based cermet fabricated through selective laser melting, *J. Mater. Eng. Perform.* 30 (2021) 6777–6787, <https://doi.org/10.1007/s11665-021-05995-8>.
- [9] D.-Q. L.H.-Q. L. M. W. S. C.J. Xu, Effect of high temperature oxidation on cemented carbide during brazing, *Cailiao Rechuli Xuebao/Trans. Mater. Heat. Treat.* 36 (2015) 75–79.
- [10] A. Aramian, Z. Sadeghian, S.M.J. Razavi, K.G. Prashanth, F. Berto, Effect of selective laser melting process parameters on microstructural and mechanical properties of TiC–NiCr cermet, *Ceram. Int.* 46 (2020) 28749–28757, <https://doi.org/10.1016/j.ceramint.2020.08.037>.
- [11] A. Aramian, Z. Sadeghian, K.G. Prashanth, F. Berto, In situ fabrication of TiC–NiCr cermets by selective laser melting, *Int. J. Refract. Met. Hard Mater.* 87 (2020), 105171, <https://doi.org/10.1016/j.jirmhm.2019.105171>.
- [12] A. Rajabi, M.J. Ghazali, J. Syarif, A.R. Daud, Development and application of tool wear: A review of the characterization of TiC-based cermets with different binders, *Chem. Eng. J.* 255 (2014) 445–452, <https://doi.org/10.1016/j.cej.2014.06.078>.
- [13] H.S. Maurya, L. Kollo, M. Tarraste, K. Juhani, F. Sergejev, K.G. Prashanth, Selective laser melting of TiC-Fe via laser pulse shaping: microstructure and mechanical properties, *3D Print. Addit. Manuf.* (2021), <https://doi.org/10.1089/3dp.2021.0221>.
- [14] H.S. Maurya, L. Kollo, K. Juhani, F. Sergejev, K.G. Prashanth, Effect of preheating and cooling of the powder bed by laser pulse shaping on the microstructure of the TiC based cermets, *Ceram. Int.* (2022), <https://doi.org/10.1016/j.ceramint.2022.04.029>.
- [15] H.S. Maurya, K. Juhani, F. Sergejev, K.G. Prashanth, Additive manufacturing of TiC-based cermet with stainless steel as a binder material, *Mater. Today: Proc.* 57 (2022) 824–828, <https://doi.org/10.1016/j.matpr.2022.02.428>.
- [16] H.S. Maurya, L. Kollo, M. Tarraste, K. Juhani, F. Sergejev, K.G. Prashanth, Effect of the Laser Processing Parameters on the Selective Laser Melting of TiC–Fe-Based Cermets, *J. Manuf. Mater. Process.* 6 (2022), <https://doi.org/10.3390/jmmp6020035>.
- [17] D. Bricin, A. Kriz, Processability of WC–CO powder mixtures using slm additive technology, *MM Sci. J.* 2019 (2019) 2939–2944, <https://doi.org/10.17973/MMSJ.2019.06.2018115>.
- [18] N.B. K. V. K. A.K. Tigga, S. Barad, A.K. S, Influence of post-processing techniques on residual stresses of SLM processed HPNGV, *J. Manuf. Process.* 66 (2021) 189–197, <https://doi.org/10.1016/j.jmapro.2021.04.020>.
- [19] Z. Zhao, C. Dong, D. Kong, L. Wang, X. Ni, L. Zhang, W. Wu, L. Zhu, X. Li, Influence of pore defects on the mechanical property and corrosion behavior of SLM 18Ni300 maraging steel, *Mater. Charact.* 182 (2021), 111514, <https://doi.org/10.1016/j.matchar.2021.111514>.
- [20] J. Karimi, C. Suryanarayana, I. Okulov, K.G. Prashanth, Selective laser melting of Ti6Al4V: Effect of laser re-melting, *Mater. Sci. Eng. A.* 805 (2020), 140558, <https://doi.org/10.1016/j.msea.2020.140558>.
- [21] N. Singh, P. Hameed, R. Ummethala, G. Manivasagam, K.G. Prashanth, J. Eckert, Selective laser manufacturing of Ti-based alloys and composites: impact of process parameters, application trends, and future prospects, *Mater. Today Adv.* 8 (2020), 100097, <https://doi.org/10.1016/j.mtaadv.2020.100097>.
- [22] Y. Yang, C. Zhang, D. Wang, L. Nie, D. Wellmann, Y. Tian, Additive manufacturing of WC-Co hardmetals: a review, *Int. J. Adv. Manuf. Technol.* 108 (2020) 1653–1673, <https://doi.org/10.1007/s00170-020-05389-5>.
- [23] H. Ibe, Y. Kato, J. Yamada, M. Kato, A. Suzuki, N. Takata, M. Kobashi, Controlling WC/Co two-phase microstructure of cemented carbides additive-manufactured by laser powder bed fusion: Effect of powder composition and post heat-treatment, *Mater. Des.* 210 (2021), 110034, <https://doi.org/10.1016/j.matdes.2021.110034>.
- [24] N. Ku, J.J. Pittari, S. Kilczewski, A. Kudzal, Additive manufacturing of cemented tungsten carbide with a cobalt-free alloy binder by selective laser melting for high-hardness applications, *Jom* 71 (2019) 1535–1542, <https://doi.org/10.1007/s11837-019-03366-2>.
- [25] M. Tang, L. Zhang, N. Zhang, Microstructural evolution, mechanical and tribological properties of TiC/Ti6Al4V composites with unique microstructure prepared by SLM, *Mater. Sci. Eng. A.* 814 (2021), <https://doi.org/10.1016/j.msea.2021.141187>.
- [26] V. Mandal, P. Tripathi, A. Kumar, S.S. Singh, J. Ramkumar, A study on selective laser melting (SLM) of TiC and B4C reinforced IN718 metal matrix composites (MMCs), *J. Alloy. Compd.* 901 (2022), <https://doi.org/10.1016/j.jallcom.2021.163527>.
- [27] D. Gu, Y.C. Hagedorn, W. Meiners, K. Wissenbach, R. Poprawe, Nanocrystalline TiC reinforced Ti matrix bulk-form nanocomposites by Selective Laser Melting (SLM): Densification, growth mechanism and wear behavior, *Compos. Sci. Technol.* 71 (2011) 1612–1620, <https://doi.org/10.1016/j.compscitech.2011.07.010>.
- [28] X. Li, Y. Zhao, Z. Guo, Y. Liu, H. Wang, J. Zhang, D. Yi, Y. Cao, X. Yang, B. Liu, Y. Liu, P. Bai, Influence of different substrates on the microstructure and mechanical properties of WC–2Co cemented carbide fabricated via laser melting deposition, *Int. J. Refract. Met. Hard Mater.* 104 (2022), 105787, <https://doi.org/10.1016/j.jirmhm.2022.105787>.
- [29] S. Grigoriev, T. Tarasova, A. Gusarov, R. Khmyrov, S. Egorov, Possibilities of manufacturing products from cermet compositions using nanoscale powders by additive manufacturing methods, *Materials* 12 (2019), <https://doi.org/10.3390/ma12203425>.
- [30] S. Fries, S. Genilke, M.B. Wilms, M. Seimann, A. Weisheit, A. Kaletsch, T. Bergs, J. H. Schleifenbaum, C. Broeckmann, Laser-Based Additive Manufacturing of WC–Co with High-Temperature Powder Bed Preheating, *Steel Res. Int.* 91 (2020) 1–7, <https://doi.org/10.1002/srin.201900511>.
- [31] Z. Wang, K.G. Prashanth, A.K. Chaubey, L. Löber, F.P. Schimansky, F. Pyczak, W. W. Zhang, S. Scudino, J. Eckert, Tensile properties of Al–12Si matrix composites reinforced with Ti–Al-based particles, *J. Alloy. Compd.* 630 (2015) 256–259, <https://doi.org/10.1016/j.jallcom.2014.12.254>.
- [32] K. Prashanth, S. Scudino, R. Chatterjee, O. Salman, J. Eckert, Additive manufacturing: reproducibility of metallic parts, *Technol. (Basel)*. 5 (2017) 8, <https://doi.org/10.3390/technologies5010008>.
- [33] Z. Yu, Z. Xu, Y. Guo, R. Xin, R. Liu, C. Jiang, L. Li, Z. Zhang, L. Ren, Study on properties of SLM–NiTi shape memory alloy under the same energy density, *J. Mater. Res. Technol.* 13 (2021) 241–250, <https://doi.org/10.1016/j.jmrt.2021.04.058>.
- [34] K.G. Prashanth, S. Scudino, T. Maity, J. Das, J. Eckert, Is the energy density a reliable parameter for materials synthesis by selective laser melting? *Mater. Res. Lett.* 5 (2017) 386–390, <https://doi.org/10.1080/21663831.2017.1299808>.
- [35] W.D. Schubert, H. Neumeister, G. Kinger, B. Lux, Hardness to toughness relationship of fine-grained WC–Co hardmetals, *Int. J. Refract. Met. Hard Mater.* 16 (1998) 133–142, [https://doi.org/10.1016/S0263-4368\(98\)00028-6](https://doi.org/10.1016/S0263-4368(98)00028-6).
- [36] K.G. Prashanth, S. Scudino, H.J. Klaus, K.B. Surreddi, L. Löber, Z. Wang, A. K. Chaubey, U. Kühn, J. Eckert, Microstructure and mechanical properties of Al–12Si produced by selective laser melting: Effect of heat treatment, *Mater. Sci. Eng. A* 590 (2014) 153–160, <https://doi.org/10.1016/j.msea.2013.10.023>.
- [37] M. Ghayoor, K. Lee, Y. He, C. hung Chang, B.K. Paul, S. Pasebani, Selective laser melting of 304L stainless steel: Role of volumetric energy density on the microstructure, texture and mechanical properties, *Addit. Manuf.* 32 (2020), 101011, <https://doi.org/10.1016/j.addma.2019.101011>.
- [38] P. Ma, K. Prashanth, S. Scudino, Y. Jia, H. Wang, C. Zou, Z. Wei, J. Eckert, Influence of Annealing on Mechanical Properties of Al–20Si Processed by Selective Laser Melting, *Met. (Basel)*. 4 (2014) 28–36, <https://doi.org/10.3390/met4010028>.
- [39] R. Yogamalar, R. Srinivasan, A. Vinu, K. Ariga, A.C. Bose, X-ray peak broadening analysis in ZnO nanoparticles, *Solid State Commun.* 149 (2009) 1919–1923, <https://doi.org/10.1016/j.ssc.2009.07.043>.
- [40] T. Ungár, Microstructural parameters from X-ray diffraction peak broadening, *Scr. Mater.* 51 (2004) 777–781, <https://doi.org/10.1016/j.scriptamat.2004.05.007>.
- [41] C. Zhao, Z. Wang, D. Li, L. Kollo, Z. Luo, W. Zhang, K.G. Prashanth, Cu–Ni–Sn alloy fabricated by melt spinning and selective laser melting: a comparative study on the microstructure and formation kinetics, *J. Mater. Res. Technol.* 9 (2020) 13097–13105, <https://doi.org/10.1016/j.jmrt.2020.09.047>.
- [42] C. Zhao, Z. Wang, D. Li, L. Kollo, Z. Luo, W. Zhang, K. Gokuldoss, K.G. Prashanth, Selective laser melting of Cu – Ni – Sn: A comprehensive study on the microstructure, mechanical properties, and deformation behavior, *Int. J. Plast.* 138 (2021), 102926, <https://doi.org/10.1016/j.iplas.2021.102926>.
- [43] Z. Wang, M. Xie, Y. Li, W. Zhang, C. Yang, L. Kollo, J. Eckert, K.G. Prashanth, Premature failure of an additively manufactured material, *NPG Asia Mater.* 12 (2020) 1–10, <https://doi.org/10.1038/s41427-020-0212-0>.
- [44] K.G. Prashanth, H. Shakur Shahabi, H. Attar, V.C. Srivastava, N. Ellendt, V. Uhlenwinkel, J. Eckert, S. Scudino, Production of high strength Al 85 Nd 8 Ni 5 Co 2 alloy by selective laser melting, *Addit. Manuf.* 6 (2015) 1–5, <https://doi.org/10.1016/j.addma.2015.01.001>.
- [45] L. Thijs, K. Kempen, J.P. Kruth, J. Van Humbeeck, Fine-structured aluminium products with controllable texture by selective laser melting of pre-alloyed AlSi10Mg powder, *Acta Mater.* 61 (2013) 1809–1819, <https://doi.org/10.1016/j.actamat.2012.11.052>.
- [46] S. Van Bael, G. Kerckhofs, M. Moesen, G. Pyka, J. Schrooten, J.P. Kruth, Micro-CT-based improvement of geometrical and mechanical controllability of selective laser melted Ti6Al4V porous structures, *Mater. Sci. Eng. A.* 528 (2011) 7423–7431, <https://doi.org/10.1016/j.msea.2011.06.045>.
- [47] J. Wu, S. Ren, Y. Zhang, Y. Cao, D. Zhang, C. Yin, Influence of spatial laser beam profiles on thermal-fluid transport during laser-based directed energy deposition, *Virtual Phys. Prototyp.* 16 (2021) 444–459, <https://doi.org/10.1080/17452759.2021.1960734>.

- [48] T.M. Wischeropp, H. Tarhini, C. Emmelmann, Influence of laser beam profile on the selective laser melting process of AlSi10Mg, *J. Laser Appl.* 32 (2020), 022059, <https://doi.org/10.2351/7.0000100>.
- [49] S. Huang, R. Lakshmi Narayan, J.H.K. Tan, S.L. Singh, W.Y. Yoeng, Resolving the porosity-unmelted inclusion dilemma during in-situ alloying of Ti34Nb via laser powder bed fusion, *Acta Mater* 204 (2021), 116522, <https://doi.org/10.1016/j.actamat.2020.116522>.
- [50] R. Casati, M. Hamidi Nasab, M. Coduri, V. Tirelli, M. Vedani, Effects of platform pre-heating and thermal-treatment strategies on properties of AlSi10Mg alloy processed by selective laser melting, *Metals* 8 (2018), <https://doi.org/10.3390/met8110954>.
- [51] H.Y. Jung, S.J. Choi, K.G. Prashanth, M. Stoica, S. Scudino, S. Yi, U. Kühn, D. H. Kim, K.B. Kim, J. Eckert, Fabrication of Fe-based bulk metallic glass by selective laser melting: A parameter study, *Mater. Des.* 86 (2015) 703–708, <https://doi.org/10.1016/j.matdes.2015.07.145>.
- [52] P.A. Hooper, Melt pool temperature and cooling rates in laser powder bed fusion, *Addit. Manuf.* 22 (2018) 548–559, <https://doi.org/10.1016/j.addma.2018.05.032>.
- [53] S. Pauly, P. Wang, U. Kühn, K. Kosiba, Experimental determination of cooling rates in selectively laser-melted eutectic Al-33Cu, *Addit. Manuf.* 22 (2018) 753–757, <https://doi.org/10.1016/j.addma.2018.05.034>.
- [54] A.H. Maamoun, Y.F. Xue, M.A. Elbestawi, S.C. Veldhuis, Effect of selective laser melting process parameters on the quality of Al alloy parts: Powder characterization, density, surface roughness, and dimensional accuracy, *Materials* 11 (2018) 2343, <https://doi.org/10.3390/ma11122343>.
- [55] A. Suzuki, R. Nishida, N. Takata, M. Kobashi, M. Kato, Design of laser parameters for selectively laser melted maraging steel based on deposited energy density, *Addit. Manuf.* 28 (2019) 160–168, <https://doi.org/10.1016/j.addma.2019.04.018>.
- [56] T. de Terris, O. Andreau, P. Peyre, F. Adamski, I. Koutiri, C. Gorny, C. Dupuy, Optimization and comparison of porosity rate measurement methods of Selective Laser Melted metallic parts, *Addit. Manuf.* 28 (2019) 802–813, <https://doi.org/10.1016/j.addma.2019.05.035>.
- [57] Z. Wu, M. Asherloo, R. Jiang, M.H. Delpazir, N. Sivakumar, M. Paliwal, J. Capone, B. Gould, A. Rollert, A. Mostafaei, Study of printability and porosity formation in laser powder bed fusion built hydride-dehydride (HDH) Ti-6Al-4V, *Addit. Manuf.* 47 (2021), 102323, <https://doi.org/10.1016/j.addma.2021.102323>.
- [58] G. Vastola, Q.X. Pei, Y.W. Zhang, Predictive model for porosity in powder-bed fusion additive manufacturing at high beam energy regime, *Addit. Manuf.* 22 (2018) 817–822, <https://doi.org/10.1016/j.addma.2018.05.042>.
- [59] E.W. Jost, J.C. Miers, A. Robbins, D.G. Moore, C. Saldana, Effects of spatial energy distribution-induced porosity on mechanical properties of laser powder bed fusion 316L stainless steel, *Addit. Manuf.* 39 (2021), 101875, <https://doi.org/10.1016/j.addma.2021.101875>.
- [60] Z.E. Tan, J.H.L. Pang, J. Kaminski, H. Pepin, Characterisation of porosity, density, and microstructure of directed energy deposited stainless steel AISI 316L, *Addit. Manuf.* 25 (2019) 286–296, <https://doi.org/10.1016/j.addma.2018.11.014>.
- [61] P. Fathi-Hafshejani, A. Soltani-Tehrani, N. Shamsaei, M. Mahjouri-Samani, Laser incidence angle influence on energy density variations, surface roughness, and porosity of additively manufactured parts, *Addit. Manuf.* 50 (2022), 102572, <https://doi.org/10.1016/j.addma.2021.102572>.
- [62] B. Zhang, Y. Li, Q. Bai, Defect formation mechanisms in selective laser melting: a review, *Chin. J. Mech. Eng. (Engl. Ed.)* 30 (2017) 515–527, <https://doi.org/10.1007/s10033-017-0121-5>.
- [63] Z. Zhao, C. Dong, D. Kong, L. Wang, X. Ni, L. Zhang, W. Wu, L. Zhu, X. Li, Influence of pore defects on the mechanical property and corrosion behavior of SLM 18Ni300 maraging steel, *Mater. Charact.* 182 (2021), 111514, <https://doi.org/10.1016/j.matchar.2021.111514>.
- [64] I. Echeta, B. Dutton, R.K. Leach, S. Piano, Finite element modelling of defects in additively manufactured strut-based lattice structures, *Addit. Manuf.* 47 (2021), 102301, <https://doi.org/10.1016/j.addma.2021.102301>.
- [65] X. Luo, D.D. Li, C. Yang, A. Gebert, H.Z. Lu, T. Song, H.W. Ma, L.M. Kang, Y. Long, Y.Y. Li, Circumventing the strength-ductility trade-off of  $\beta$ -type titanium alloys by defect engineering during laser powder bed fusion, *Addit. Manuf.* 51 (2022), 102640, <https://doi.org/10.1016/j.addma.2022.102640>.
- [66] T.P. Moran, D.H. Warner, A. Soltani-Tehrani, N. Shamsaei, N. Phan, Spatial inhomogeneity of build defects across the build plate in laser powder bed fusion, *Addit. Manuf.* 47 (2021), 102333, <https://doi.org/10.1016/j.addma.2021.102333>.
- [67] A. du Plessis, E. Macdonald, Hot isostatic pressing in metal additive manufacturing: X-ray tomography reveals details of pore closure, *Addit. Manuf.* 34 (2020), 101191, <https://doi.org/10.1016/j.addma.2020.101191>.
- [68] C. Wei, L. Liu, Y. Gu, Y. Huang, Q. Chen, Z. Li, L. Li, Multi-material additive-manufacturing of tungsten-copper alloy bimetallic structure with a stainless-steel interlayer and associated bonding mechanisms, *Addit. Manuf.* 50 (2022), 102574, <https://doi.org/10.1016/j.addma.2021.102574>.
- [69] M. Gaier, T.Z. Todorova, Z. Russell, Z.N. Farhat, J.W. Zwanziger, K.P. Plucknett, The influence of intermetallic ordering on wear and indentation properties of TiC-Ni3Al cermets, *Wear* 426–427 (2019) 390–400, <https://doi.org/10.1016/j.wear.2018.12.034>.
- [70] C.K. Sahoo, M. Masanta, Microstructure and mechanical properties of TiC-Ni coating on AISI304 steel produced by TiG cladding process, *J. Mater. Process. Technol.* 240 (2017) 126–137, <https://doi.org/10.1016/j.jmatprotec.2016.09.018>.
- [71] W. Hu, Z. Huang, L. Cai, C. Lei, W. Yu, H. Zhai, S. Wo, X. Li, Y. Zhou, Microstructural characterization and mechanical properties of a novel TiC-based cermet bonded with Ni3(Al,Ti) and NiAl duplexalloy, *Mater. Charact.* 135 (2018) 295–302, <https://doi.org/10.1016/j.matchar.2017.11.003>.
- [72] L. Wang, H. Liu, C. Huang, B. Zou, X. Liu, Effects of sintering processes on mechanical properties and microstructure of Ti(C,N)-TiB2-Ni composite ceramic cutting tool material, *Ceram. Int.* 40 (2014) 16513–16519, <https://doi.org/10.1016/j.ceramint.2014.08.003>.
- [73] T. Rodriguez-Suarez, S. Lopez-Esteban, C. Pecharróman, J.S. Moya, H. el Attaoui, C. Benaqqa, J. Chevalier, Slow crack growth resistance and bridging stress determination in alumina-rich magnesium aluminate spinel/tungsten composites, *Acta Mater.* 57 (2009) 2121–2127, <https://doi.org/10.1016/j.actamat.2009.01.004>.
- [74] P. Neumeister, M. Jurisch, H. Jelitto, A.R. Engert, G.A. Schneider, H. Balke, Effective permittivity of air-filled cracks in piezoelectric ceramics due to crack bridging, *Acta Mater.* 61 (2013) 1061–1069, <https://doi.org/10.1016/j.actamat.2012.10.006>.
- [75] S. Gallots, T. Fett, J.W. Ager, J.J. Kruczic, Fatigue threshold R-curves predict small crack fatigue behavior of bridging toughened materials, *Acta Mater.* 59 (2011) 7654–7661, <https://doi.org/10.1016/j.actamat.2011.08.038>.
- [76] S.W. Kim, X. Li, H. Gao, S. Kumar, In situ observations of crack arrest and bridging by nanoscale twins in copper thin films, *Acta Mater.* 60 (2012) 2959–2972, <https://doi.org/10.1016/j.actamat.2012.02.002>.
- [77] Z. Suo, C.F. Shih, A.G. Varias, A theory for cleavage cracking in the presence of plastic flow, *Acta Metall.* 41 (1993) 1551–1557, [https://doi.org/10.1016/0956-7151\(93\)90263-R](https://doi.org/10.1016/0956-7151(93)90263-R).
- [78] R. Subramanian, J.H. Schneibel, The ductile-brittle size transition of iron aluminide ligaments in an FeAl/TiC composite, *Acta Mater.* 46 (1998) 4733–4741, [https://doi.org/10.1016/S1359-6454\(98\)00130-X](https://doi.org/10.1016/S1359-6454(98)00130-X).
- [79] J.C. Han, B.L. Wang, Thermal shock resistance enhancement of functionally graded materials by multiple cracking, *Acta Mater.* 54 (2006) 963–973, <https://doi.org/10.1016/j.actamat.2005.10.036>.
- [80] Y.C. Her, P.C. Wang, J.M. Yang, Fatigue crack initiation and multiplication of unnotched titanium matrix composites, *Acta Mater.* 46 (1998) 6645–6659, [https://doi.org/10.1016/S1359-6454\(98\)00249-3](https://doi.org/10.1016/S1359-6454(98)00249-3).
- [81] T. Duan, J. Wei, Q. Yan, A. Zhang, Z. Peng, Investigations on crack propagation and meshing characteristics of planetary gear train considering crack closure effect, *Eng. Fail. Anal.* 134 (2022), 106064, <https://doi.org/10.1016/j.engfailanal.2022.106064>.
- [82] J. Loureiro-Homs, P. Almqvist, F. Palmert, D. Gustafsson, K. Simonsson, R. Eriksson, D. Leidermark, Accounting for crack closure effects in out-of-phase TMF crack growth with extended hold times, *Int. J. Fatigue* 158 (2022), 106740, <https://doi.org/10.1016/j.ijfatigue.2022.106740>.
- [83] U. Schleinkofer, H.G. Sockel, P. Schlund, K. Görtling, W. Heinrich, Behaviour of hard metals and cermets under cyclic mechanical loads, *Mater. Sci. Eng.: A* 194 (1995) 1–8, [https://doi.org/10.1016/0921-5093\(94\)09660-0](https://doi.org/10.1016/0921-5093(94)09660-0).
- [84] J. Takagi, M.C. Shaw, Evaluation of Fracture Strength of Brittle Tools, 1981.
- [85] J. Gong, X. Pan, H. Miao, Z. Zhao, Effect of metallic binder content on the microhardness of TiCN-based cermets, *Mater. Sci. Eng. A* 359 (2003) 391–395, [https://doi.org/10.1016/S0921-5093\(03\)00396-4](https://doi.org/10.1016/S0921-5093(03)00396-4).



**Publication IV**

Investigation of the tribological behavior of the additively manufactured TiC-based cermets by scratch test. **H.S. Maurya**, J. Jayaraj, Z. Wang, K. Juhani, F. Sergejev, K.G. Prashanth. Journal of Alloy and Compound 959 (2023) 170496.





Contents lists available at ScienceDirect

## Journal of Alloys and Compounds

journal homepage: [www.elsevier.com/locate/jalcom](http://www.elsevier.com/locate/jalcom)

## Investigation of the tribological behavior of the additively manufactured TiC-based cermets by scratch testing

H.S. Maurya<sup>a,\*</sup>, J. Jayaraj<sup>b</sup>, Z. Wang<sup>c</sup>, K. Juhani<sup>a</sup>, F. Sergejev<sup>a</sup>, K.G. Prashanth<sup>a,d,e,\*\*</sup><sup>a</sup> Department of Mechanical and Industrial Engineering, Tallinn University of Technology, Ehitajate tee 5, 19086 Tallinn, Estonia<sup>b</sup> Materials Technology, School of Information and Engineering, Dalarna University, SE-79188 Falun, Sweden<sup>c</sup> School of Mechanical and Automotive Engineering, South China University of Technology, Guangzhou 510640, China<sup>d</sup> Erich Schmid Institute of Materials Science, Austrian Academy of Sciences, Jahnstrasse 12, 8700 Leoben, Austria<sup>e</sup> CBCMT, School of Mechanical Engineering, Vellore Institute of Technology, Vellore 630014 Tamil Nadu, India

## ARTICLE INFO

## Article history:

Received 7 April 2023

Received in revised form 28 April 2023

Accepted 7 May 2023

Available online 8 May 2023

## Keywords:

TiC-based cermets

Selective laser melting

Wear

Tribo-layer

Coefficient of friction

## ABSTRACT

This study deals with the tribological behavior of the TiC-430 L SS cermets fabricated via an additive manufacturing process such as laser powder bed fusion/selective laser melting. A gradient microstructure (finer and coarser morphology) can be observed in the fabricated parts due to SLM's complex thermal history. Using Rockwell indenter, single and multiple passes scratch tests have been performed as a function of applied load to study the wear mechanism of the binder and matrix phase. A surface 3D profilometer was used to analyze the scratch track variation in terms of scratch width and depth. Scanning Electron microscopy (SEM) analysis was performed on the scratched cermet parts to study the wear mechanism and microstructural analysis. It has been observed that the scratch hardness increases with increasing load and the same decreases with increasing the number of passes. Similarly, the coefficient of friction increases with increasing load. Cermets with complex microstructural features exhibit high wear resistance under low loads and for higher loads, multiple passes can lead to tribolayer formation.

© 2023 Elsevier B.V. All rights reserved.

## 1. Introduction

TiC and TiCN-based cermets have been extensively used as cutting tools for wear-resistant applications due to their excellent mechanical and tribological properties [1–4]. Cermets based on the WC-Co/Ni-based have been used in industries over the decades due to their properties like mechanical and tribological properties [5–7]. W, Co, and Ni have been declared as critical raw materials in Europe according to the REACH (Registration, Evaluation, Authorization, and Restriction of Chemical Substances) program and an increase in the price of the Co is also a major concern [8–10]. Moreover, W and Co prove to be a carcinogen to human health in both powder and sintered form according to US NTP (National Toxicology Program) [11]. Therefore, research on cermets should focus on low-cost and green cermets with better mechanical and tribological properties to replace these conventional cermets either partially or completely

[12,13]. TiC-based cermets prove to be an alternative solution to WC-based cermets due to their better mechanical properties, lower density, and excellent chemical, thermal, and dimensional stability at higher temperatures [14–16]. Fe-based binders are easily available at a lower price (as compared to Co) acts as a promising candidate to replace these Co/Ni-based binders [17].

Fabrication of cermets with conventional powder metallurgy routes such as spark plasma sintering (SPS), melt infiltration, pressure-less vacuum sintering, etc. has some limitations in terms of structural complexity, post-processing steps, etc., which can be overcome by the additive manufacturing (AM) processes such as selective laser melting (SLM) [18–21]. SLM is laser-based powder bed fusion technology that uses a laser as the energy source to selectively melt the feedstock powder bed and creates a 3D part layer-by-layer by using CAD data [22–24]. In addition, SLM offers the possibility to tune the mechanical properties of the as-built parts by modulating the process parameters and the laser source [25–28]. Moreover, SLM offers the fabrication of near-net-shaped parts without or with minimal post-processing in a single step making this a green technology. [23,29–31]. However, fabrication of these brittle materials such as cermets with laser-based processing methods is difficult due to the high solidification rates ( $10^9$ – $10^{11}$  K/s),

\* Corresponding author.

\*\* Corresponding author at: Department of Mechanical and Industrial Engineering, Tallinn University of Technology, Ehitajate tee 5, 19086 Tallinn, Estonia.

E-mail addresses: [himaurl@taltech.ee](mailto:himaurl@taltech.ee) (H.S. Maurya),[kgprashanth@gmail.com](mailto:kgprashanth@gmail.com) (K.G. Prashanth).

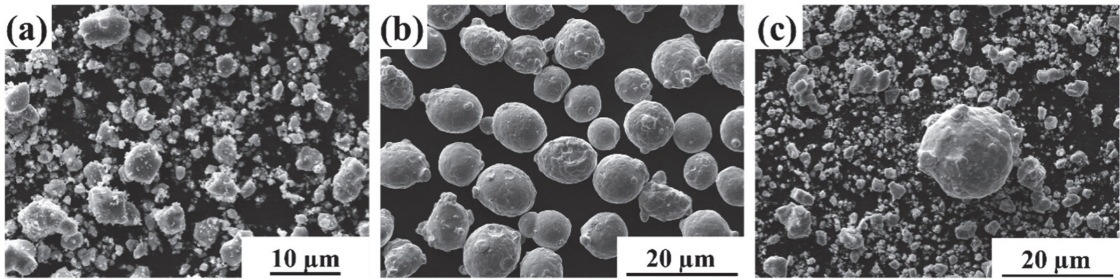


Fig. 1. Scanning electron microscopy images of the initial (a) TiC, (b) 430 L SS, and (c) mixed feedstock powder.

which leads to a high degree of internal stresses [9,32–34]. In addition, the thermal gradient leads to a high degree of residual stresses, which in turn leads to internal cracking of the fabricated parts [35–37]. Accordingly, in this work, a unique powder bed preheating technique has been adapted to control the temperature of the powder bed and to further control the melt pool temperature during the SLM fabrication, which allows for minimizing thermal gradient in the parts and reduces the process defects such as cracks [38].

The cermets fabricated via SLM show a distinct microstructure as compared to the conventionally manufactured cermet counterparts, like any other material produced by SLM [39–43]. Therefore wear behavior of the additively manufactured cermets need attention to understand the wear mechanism, especially with inhomogeneity in the microstructure [44–46]. Several studies have been performed on the wear behavior of the conventionally and additively manufactured WC-based cermets by a scratch test suggesting scratch test could be a simple and reliable way of investigating the wear mechanisms [47–51]. However, there is a paucity in the study of the wear behavior of additively manufactured TiC-based cermets. To the best of the authors' knowledge, only one dry sliding wear study has been reported for TiC-NiCr-based cermet [29]. In this work, the first-time wear behavior of the additively manufactured TiC-based "green" cermets has been studied by scratch testing as a function of the applied load.

## 2. Materials and method

### 2.1. Powder preparation

Initial feedstock powder consists of TiC and AISI 430 L stainless steel with a ratio of 65:35 in volume. For the preparation of the feedstock powder, the initial powder was mixed in a mechanical mixer for 24 h with a revolution speed of 20 rpm. Yttria stabilized zirconia balls were added as a mixing media to provide attrition during the mixing and powder to ball ratio was kept low to avoid mechanical milling during the preparation of the feedstock powder. Initial TiC powder was supplied by PPM particulate material Ltd. with an average particle size of 2–3 μm while the AISI 430 L powder was supplied by Sandvik Osprey Ltd. with an average particle size of

10–40 μm (Fig. 1(a, b)). Due to variation in the initial powder particle size, mixed powder exhibits a wide variation in the particle size maintaining the spherical shape of the stainless-steel powder with homogeneously distributed small TiC particles (Fig. 1(c)).

### 2.2. SLM fabrication

Fabrication of the TiC-430 L stainless steel cermet was carried out by the Realizer SLM 50 equipped with an Nd: YAG laser with a spot diameter of 80 μm and a maximum power of 100 W. Stainless steel substrate of 70 mm diameter has been used to fabricate these cermets (20 mm diameter). A unique laser scan strategy has been adopted by exposing a laser on the powder bed twice for controlling the melt pool temperature by scanning the powder with lower and high laser power, respectively. The preheating scan is used to heat the powder bed to reduce the cooling rate of the process (this strategy is commonly used during the electron beam melting process). Hence moderate laser power is used. Accordingly, during scan 1 a lower laser power with high scan speed is used to preheat the powder bed without melting. However, the second laser scan consists of high laser power with lower scan speed to selectively melt and fuse the feedstock powder. A scan rotation of 60° was employed during the fabrication of cermets. Argon gas has been used to provide an inert atmosphere and to avoid the oxidation of the melt pool during the printing process. The laser process parameters used for the fabrication of the cermets have been depicted in Table 1.

### 2.3. Microstructural characterization

SLM fabricated cermets have been prepared for microstructural investigation according to the standard metallographic procedure for hard metals. Scanning electron microscopy (SEM) and energy dispersive spectroscopy (EDS) analysis have been performed to investigate the microstructural and composition analysis. As reported in the previous work, a sample exhibiting better mechanical properties and lower porosity has been used to study the wear behavior of fabricated cermets parts and has a hardness, fracture toughness, and compressive strength of  $1218 \pm 141 \text{ HV}_1$ ,  $20 \pm 4 \text{ MPa}\cdot\text{m}^{1/2}$ , and  $1858 \pm 185 \text{ MPa}$  respectively [38].

Table 1  
SLM laser process parameters adapted for the fabrication of the TiC-based cermets.

Hatch distance (mm)	Layer thickness (mm)	Scan 1 (Preheating)		Scan 2 (Melting)	
0.045	0.025	Laser power (W)	Scan speed (mm/s)	Laser power (W)	Scan speed (mm/s)
		44	488	94	99

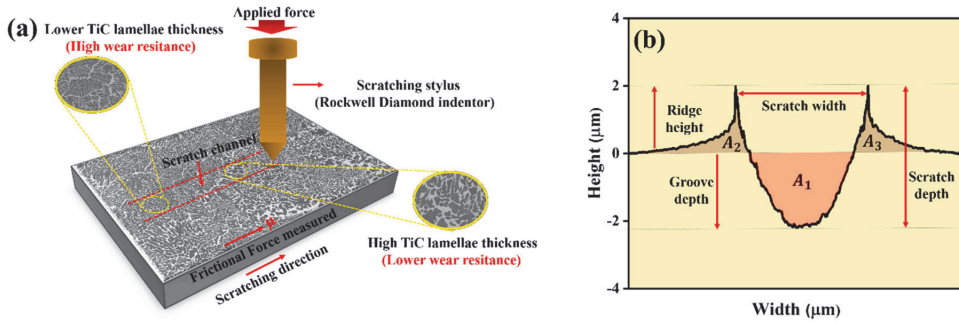


Fig. 2. (a) Schematics of the scratch testing performed on the selectively laser melted TiC-based cermets, and (b) 2D profile of the cermets scratch test.

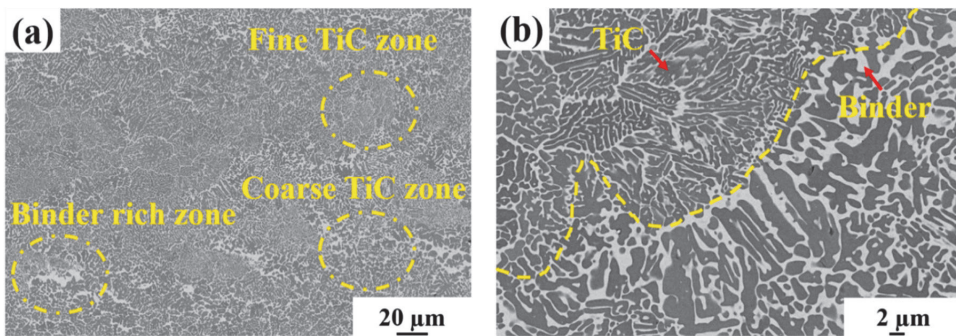


Fig. 3. Scanning electron micrographs of the TiC-based cermets fabricated via selective laser melting process displayed at both (a) lower and (b) higher magnifications.

#### 2.4. Scratch test

A scratch test has been performed on the polished cermets by pressing and sliding a tip of the indenter using CSM Revetest. Rockwell C diamond indenter of a radius of  $200\ \mu\text{m}$  with a  $120^\circ$  cone angle has been used for scratch testing. For all scratches, a variation in the normal load of 10, 30, and 50 N with a scratch length of 2 mm at a scratching speed of 10 mm/min is used. The schematic of the scratch test has been represented in Fig. 2(a). Single and multiple passes (5 passes) scratch tests have been performed in the polished cermets to study the effect of the load on their wear behavior. For the multi-pass scratch test, the scratching direction was not reversed i.e., unloading the load at the final position, and then applying the load from the initial position of the first pass for the next pass. All the tests were performed three times to evaluate their reproducibility.

### 3. Results and discussion

#### 3.1. Microstructure of the fabricated cermet parts

Fig. 3 exhibits the SEM microstructure of the TiC-430 L SS-based cermet fabricated via SLM with multiple laser scanning techniques. Typical SLM microstructure with finer and coarser TiC particles can be observed in the SLM built-parts [5,52]. Multiple laser scanning with variations in laser process parameters helps to control the melt pool temperature by preheating and avoiding instantaneous heating, which can lower the thermal residual stress generated. This can help in fabricating crack-free cermet parts. The XRD patterns confirm the

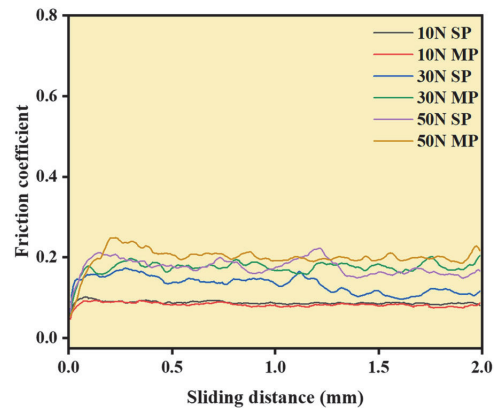


Fig. 4. Coefficient of friction observed from the scratch test as a function of different loads under single pass and multiple pass conditions.

formation of no new phase (except the presence of TiC and  $\alpha\text{-Fe}$ ) in the SLM-built part, suggesting no intermetallic phase has formed during the SLM process [38]. From the SEM microstructure, it can be ascertained that the dark phase corresponds to the TiC phase while the brighter phase represents the binder phase comprised of Fe-based material. The microstructure of the cermets shows the presence of both fine as well as coarse TiC phases. Such a variation in

the microstructure is attributed to the SLM's complex thermal history and laser process parameters adapted during the fabrication of the cermets [53]. The gradient in TiC phases was caused by the Gaussian distribution of laser energy, and higher solidification rates

[54–56]. Due to Gaussian laser energy distribution, the maximum laser energy density is exposed at the center of the laser focus as compared to the laser scan boundary. This leads to a thermal gradient in the melt pool. The higher temperature in the center of the melt pool refers to the higher cooling rate and hence results in a finer microstructure [30,57].

The laser scan boundary or hatch overlap is not visible in the microstructure due to scan rotation adapted for the fabrication of the parts. After each layer, a scan rotation of 60° has been employed, which could affect the solidified layer(s) below and can be led to partial remelting of the solidified region leading to the formation of a coarser TiC with binder-rich zones. The variation in the microstructure of the SLM fabricated parts depends on the adapted scan strategy. In addition, the laser beam profile also has some influence on the microstructural formation [58,59].

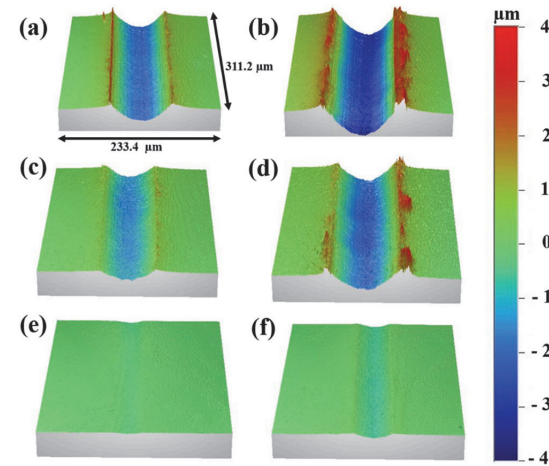
**Table 2**  
Scratch characteristics of the TiC-430L SS cermets observed as a function of load under both single and multi-pass conditions.

	Load (N)	Scratch hardness (kg/mm <sup>2</sup> )	Friction coefficient (μ)
Single pass	10	1112 ± 96	0.08 ± 0.002
	30	1346 ± 71	0.14 ± 0.003
	50	1611 ± 55	0.17 ± 0.004
Multiple passes	10	1079 ± 54	0.08 ± 0.006
	30	982 ± 59	0.17 ± 0.010
	50	1289 ± 87	0.20 ± 0.006

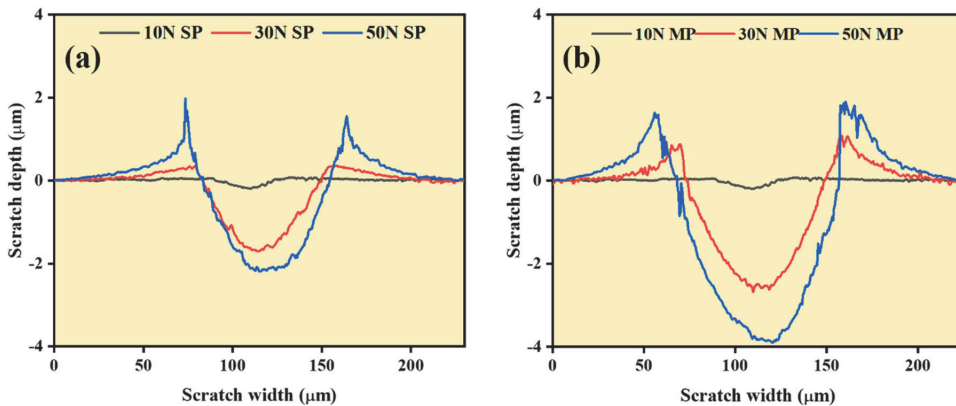
3.2. Scratch behavior

Fig. 4 represents the friction coefficient (COF) of the single and multi-pass scratch(s) with variations in the normal load. In the case of higher loads (30 and 50 N), the fluctuation of the COF is high for both the single-pass and multiple-pass conditions. The average COF value (shown in Table 2) is higher for higher loads (50 N than 30 N). Also, the average COF increases for the 5th pass during the multi-pass scratch test. Due to the higher load, the diamond stylus shall plow through the TiC-FeCr surface and shall produce wear debris from the relatively softer binder part of the cermet. During sliding, the wear debris shall be deposited in the crevices of the stylus tip and on the scratched surface of the cermet. The produced wear debris shall promote third-body abrasive wear condition and thus the increment and fluctuation in the COF values are observed for both 30 and 50 N loading conditions. The formation of wear debris at higher loads could be attributed to the lack of microstructural stability, which will be discussed later in Section 3.3. On the other hand, for the lower loads, 10 N (single and multiple passes), a lower COF, with lower fluctuation in the COF (i.e., stable value, see Fig. 4) was observed. Such behavior of COF at lower loads could be attributed to the resistance to the formation of wear debris (i.e., better microstructural stability at 10 N load) or the formation of a favorable tribo-layer.

Fig. 5 exhibits the 3D optical surface profilometry images of the scratch-tested (single and multiple passes) TiC- 430L SS cermets as a function of the applied load. For the higher loading conditions (50 and 30 N) and multiple passes, the scratch characteristics such as scratch width, scratch depth, and ridge height are pronounced as compared to the



**Fig. 5.** 3D optical surface profilometry images of the scratch track observed on the TiC-430L SS cermets under different loads (a) 50 N single pass, (b) 50 N multiple passed, (c) 30 N single pass, (d) 30 N multiple passes, (e) 10 N single pass, and (f) 10 N multiple passes.



**Fig. 6.** The scratch depth and scratch width observed for the TiC-based cermets during the scratch test as a function of load under (a) single pass, and (b) multiple pass conditions.

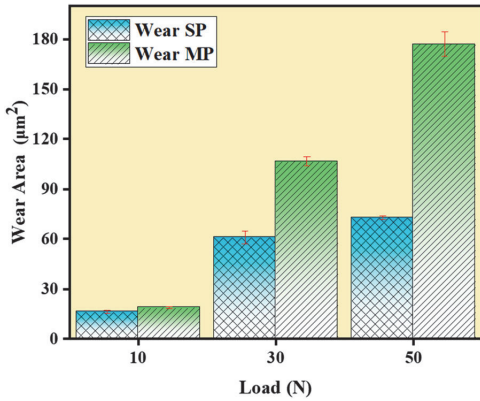


Fig. 7. Plot representing mean wear area during the scratch test as a function of different applied loads during single and multiple pass conditions.

single pass condition, see Fig. 5. The cross sections of the scratch tracks are quite rounded in profile, indicating that the material has a high concentration of soft binder content that permits significant plastic deformation. Further, the variation in the scratch depth (SD) and scratch width (SW) as a function of the applied load has been depicted in Fig. 6 as 2D surface profiles of the scratches. At high normal loads (50 and 30 N) a significant plastic deformation is observed and hence the values of SD, SW, and ridge height are pronounced. Further, these scratch characteristics are significantly pronounced for multi-pass conditions at both 50 and 30 N loads, respectively. Only minor variations in both SD and SW are observed for the low load condition (10 N) during both single and multiple pass conditions and it could be related to the scratch hardness behavior of the material.

The scratch hardness ( $H_s$ ) for the TiC-430 L SS cermet was calculated using the following equation [58],

$$H_s = \frac{8L}{\pi d^2} \quad (1)$$

where  $d$  corresponds to scratch width and  $L$  is the applied normal load and the values are given in Table 2. For the multi-pass conditions, the  $H_s$  value decreases significantly, especially at higher loads, 50 and 30 N. Whereas, for the low load (10 N) the change in  $H_s$  value is not high as compared to the other loading conditions.

The wear or material loss during the scratch test has been calculated using the following equation [51],

$$A_w = [A_1 - (A_2 + A_3)] \quad (2)$$

where  $A_w$  corresponds to the cross-sectional wear area,  $A_1$  denotes the groove area and  $(A_2 + A_3)$  represents the sum of the ridge area due to the pile-up of the plowing material (Figs. 2(b) and 6). The wear area of the scratch test under single and multiple passes has been represented in Fig. 7. A nominally linear trend has been observed for the wear area with increasing applied load for both SP and MP conditions. However, it can be noted that for the single and multiple pass conditions at lower loads (10 N), no or minor variation has been observed in the wear area suggesting better wear resistance observed in these cermets (especially at lower loads). The wear area increases dramatically with an increase in the number of passes and for higher loads, especially for the 50 N load, suggesting a third-body abrasive wear mechanism.

### 3.3. Microstructural analysis of the scratched parts

Fig. 8 represents the SEM microstructure of the TiC-based cermets demonstrating the extent of the damage induced after scratch testing under a multiple pass indenter with a higher normal load (50 and 30 N). The SEM microstructures reveal complex interaction of several factors including the bulk material microstructure, formation of the tribo-layer (mechanical mixer of binder and matrix phase) on the surface of the bulk material, fragmentation of the TiC particle, and formation of the wear debris along the scratch, etc. The higher magnification SEM images after 5 passes show the presence of

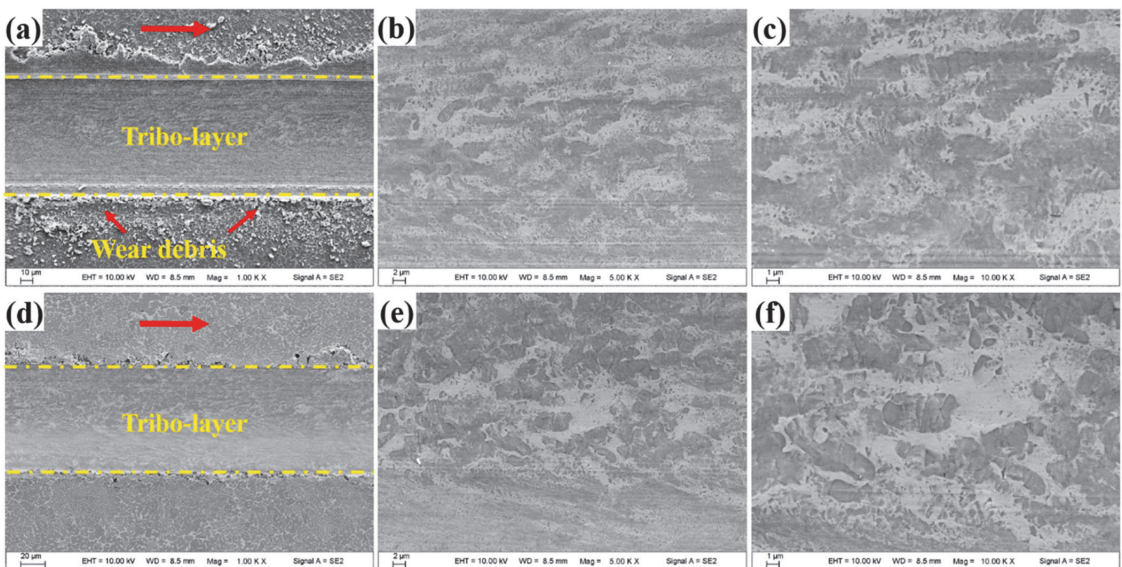
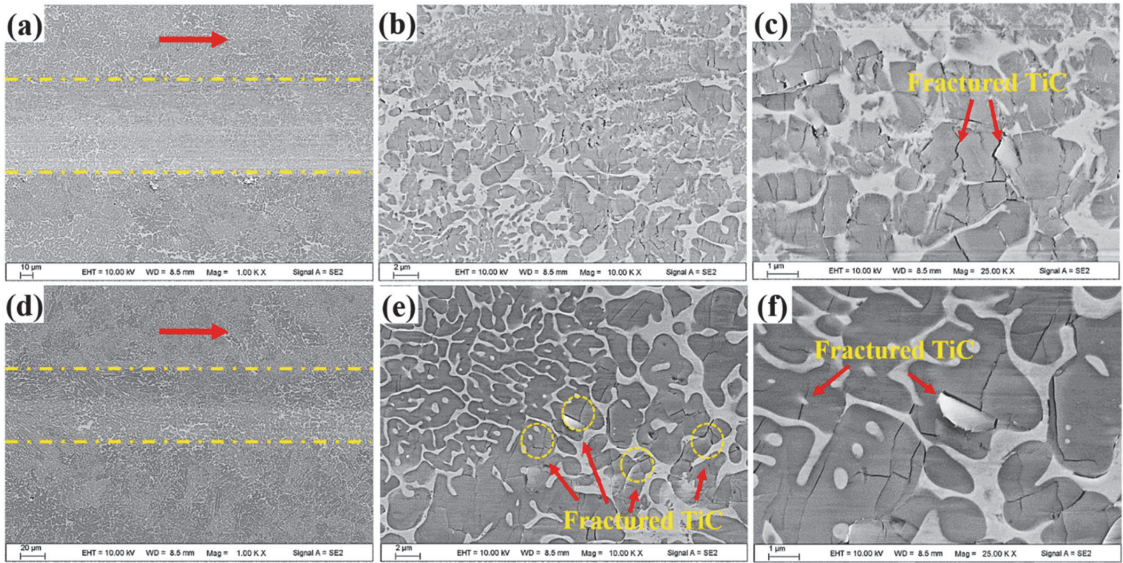


Fig. 8. Scanning electron micrographs of the scratched surface observed in the TiC- 430 L SS cermets as a function of applied load under multiple pass conditions at a load of (a-c) 50 N, and (d-f) 30 N, respectively.



**Fig. 9.** Scanning electron microscopy images of the scratched TiC-430 L SS cermets as a function of applied loads under single pass scratch tests under different loads: (a-c) 50 N, (d-f) 30 N.

fractured TiC grain mechanically mixed with the binder referred to as tribo-layer. TiC grain fragments dispersed in redeposited Fe-based binder matrix were found in the debris accumulated near the scratch track and on the pile-up region (Fig. 8(a, d)). It can be observed that a kind of mechanical mixing of the worn TiC and binder during the multiple pass condition (Fig. 8(b, e)). Passing the indenter multiple times on the same surface has led to the fracture of the TiC and pulling out of the TiC particle leading to a third body abrasive wear mechanism. This severe fracture of the binder and the TiC phases led to pulling out from the material surface. The brittle fracture and grooving could be considered as the main wear mechanism for the TiC-430 L SS cermets fabricated via SLM. For all the higher loading conditions the formation of the tribo-layer on the surface of the scratched track has been observed under multiple pass conditions. Tribo-layer formation becomes more prevalent under multiple passes due to the involvement of the fractured TiC in the scratch track and does not improve the overall wear resistance of the material under such high loads.

Fig. 9 depicts the SEM micrograph of the single pass scratch in the TiC-based cermets with the variation in the normal load (50 and 30 N). At higher loads, fracture of the TiC particle with little smearing of the soft binder material can be observed. From the SEM images, it is evident that even under higher loads the hard TiC particles maintain their shape and fracture occurs due to tearing out of the binder material (Fig. 9(b,e)). Under higher load conditions, no third-body abrasive wear can be observed. The microstructural complexity of SLM-processed cermets (fine and coarser TiC and binder-rich zones) leads to fluctuation in the COF value under high loads (Fig. 4). During mechanical loading at higher loads, it can be concluded that the fracture of the coarser TiC phase is more prominent as compared to the finer TiC phases (Fig. 9(b,e)). Several studies have reported that indenter stresses are concentrated on the circumference of the circular contact, so maximum damage is expected to occur on the scratched area [51,59]. More brittle fracture has been observed in the cermets at a higher applied load from the

SEM microstructure (Fig. 9(c,f)). The fracture of the coarse TiC phase tended to increase with the increase in the normal load (circled in Fig. 9(e)). No or very little fracture has been observed in the fine zone indicating a strong interfacial bond existing between the TiC particle and steel binder as compared to the coarse TiC zone. It may be concluded that the finer TiC zone seems to be a more wear-resistant zone as compared to the coarser zone.

A higher magnification SEM image at the considered highest load (50 N) confirms that the plastic deformation of the binder phase is the dominant mechanism with the localized coarser TiC particle fragmentation Fig. 9(c). The smearing of the softer binder material increases with an increase in the applied load. The higher wear resistance of the as-built cermet part could be attributed due to the combination of hardness ( $1218 \pm 141$  HV) and fracture toughness ( $20 \pm 4$  MPa.m<sup>1/2</sup>) of the as-printed cermets [38,60]. Fig. 10 depicts the SEM micrograph of the single and multiple pass scratches in the cermets under a lower load (10 N). For the lower applied loads (10 N) with single pass scratch condition, the microstructure of the cermets in the scratch track/channel appears quite stable without any evidence of wear debris formation (Fig. 10(a-c)). However, under multiple passes and at lower loads (10 N), very few cracks and/or minor fractures can be observed on the brittle TiC particle (Fig. 10(e, f)). During lower load conditions, wear may be caused by plastic deformation of the soft binder phases, which are higher in volume percentage, without or with minor fracture of the hard TiC phase. For the lower load (10 N), no major variation in the scratch track has been observed after multiple passes as compared to the single-pass scratch track microstructure, which justifies the lower fluctuation in the COF value and low wear rate (Figs. 4 and 7). It can be also noted that after the multiple passes and at lower loads, the material has not deformed anymore or not lost its stability and maintain the as-prepared microstructural characteristic suggesting that cermet parts exhibit a good wear resistance at lower loading conditions, (10 N) and are suitable for the sliding-contact based applications at such loading conditions.

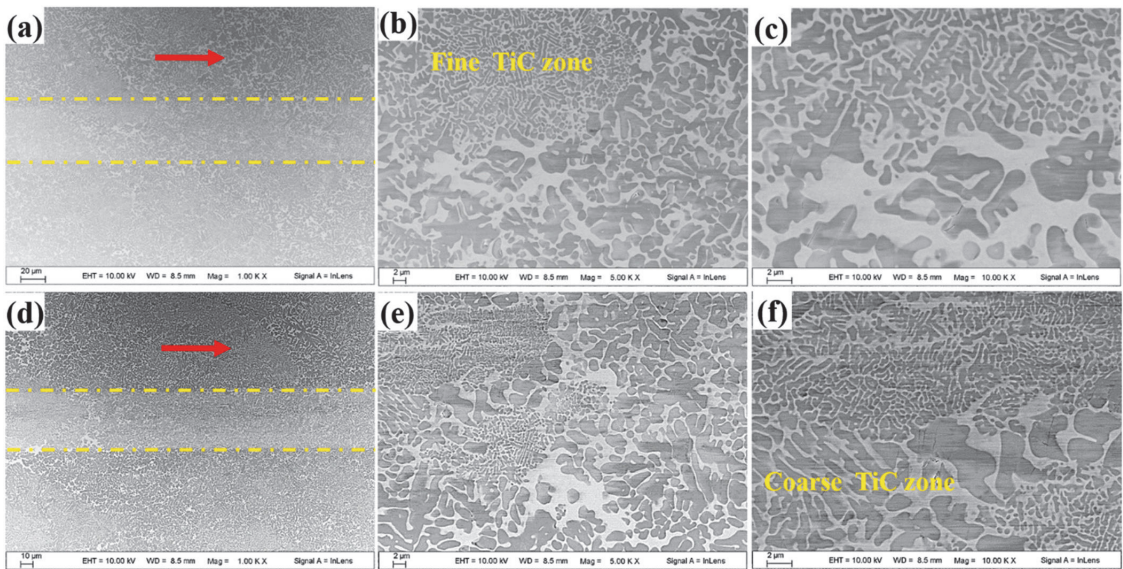


Fig. 10. Scanning electron microscopy image of the scratched TiC-430 L SS cermet at an applied load of 10 N under (a-c) single pass, and (d-f) multiple pass conditions.

#### 4. Conclusion

Scratch wear behavior of the additively manufactured TiC-430 L SS cermets has been investigated successfully. A gradient TiC phase (both finer and coarser morphology) has been observed in the fabricated cermets due to the complex thermal history observed during the SLM process. This has improved the material's toughness, hardness, and resistance to mechanical loading. Better wear resistance has been observed under low loads for both single and multiple-pass conditions and the plastic deformation of the soft binder material was observed to be the dominant wear mechanism along with the fracture of the TiC particle. For the single-pass condition, no wear debris has been observed, and the wear behavior under single and multiple-pass scratch tests shows a nominally linear trend as a function of the applied load. An increment in the load led to wearing out the material by fracturing the TiC particle and smearing out the soft binder material. A high wear-worn area has been observed for the cermets especially at higher mechanical loads (50 N) and under multiple pass conditions due to third-body abrasive wear along with TiC pull-out. The scratch hardness increases with increasing load and the same decreases with increasing the number of passes. As a result of better hardness and toughness of the materials, there is less fluctuation in COF at lower loads. The COF fluctuates more as the load increases (30 N and 50 N) under both single and multiple passes due to the presence of gradient microstructure. This will lead to TiC grains pulling out, causing particles to contact the indenter tip, causing an abrasive wear mechanism during the multiple passes as well as the formation of the tribo-layer. The coefficient of friction increases with increasing load. Furthermore, the formation of tribo-layers during multiple passes does not contribute to improved wear resistance due to the brittle nature of the cermets.

#### CRedit authorship contribution statement

Conceptualization: HSM, JJ, KJ, FS, and KGP Methodology: HSM, ZW, KJ, and KGP Validation: HSM, JJ, ZW, KK, and KGP Formal analysis: HSM, JJ, ZW, KK, SS, and KGP Investigation: HSM, JJ, and KGP

Writing original draft: HSM, ZW, KK Writing reviewing and editing: JJ, KJ, FS, and KGP Resources: JJ, KJ, FS, and KGP Project Administration: KJ, FS, and KGP Funding Acquisition: KJ, SS, and KGP.

#### Data Availability

Data will be made available on request.

#### Declaration of Competing Interest

The authors declare that they have no known competing financial interests or personal relationships that could have appeared to influence the work reported in this paper.

#### Acknowledgments

This work was supported by Estonian Research Council grants PRG1145 and European Regional Development Grant ASTRA6-6.

#### Author's disclosure statement

The authors declare that they have no known competing financial interests or personal relationships that could have appeared to influence the work reported in this paper.

#### References

- [1] J. Gong, X. Pan, H. Miao, Z. Zhao, Effect of metallic binder content on the microhardness of TiCN-based cermets, *Mater. Sci. Eng. A* 359 (2003) 391–395, [https://doi.org/10.1016/S0921-5093\(03\)00396-4](https://doi.org/10.1016/S0921-5093(03)00396-4)
- [2] M. Saha, M. Mallik, Additive manufacturing of ceramics and cermets: present status and future perspectives, *Sadhana* 46 (2021) 162, <https://doi.org/10.1007/s12046-021-01685-2>
- [3] L. Heydari, P.F. Lieten, F.A. Corpas-Iglesias, O.H. Laguna, Ti(C,N) and wc-based cermets: A review of synthesis, properties and applications in additive manufacturing, *Materials* 14 (2021), <https://doi.org/10.3390/ma14226786>
- [4] S. Kang, Cermets, 2014. <https://doi.org/10.1016/B978-0-08-096527-7.00005-2>.
- [5] D. Gu, W. Meiners, Microstructure characteristics and formation mechanisms of in situ WC cemented carbide based hardmetals prepared by Selective Laser Melting, *Mater. Sci. Eng.: A* 527 (2010) 7585–7592, <https://doi.org/10.1016/j.msea.2010.08.075>

- [6] K.W. Kim, G.S. Ham, S.H. Park, J.W. Cho, K.A. Lee, Direct energy deposition of ultrastrong WC-12Co cemented carbide: Fabrication, microstructure and compressive properties, *Int J. Refract. Met. Hard Mater.* 99 (2021) 105591, <https://doi.org/10.1016/j.jrmhm.2021.105591>
- [7] J.A. Picas, Y. Xiong, M. Punset, L. Ajdelsztajn, A. Forn, J.M. Schoenung, Microstructure and wear resistance of WC-Co by three consolidation processing techniques, *Int J. Refract. Met. Hard Mater.* 27 (2009) 344–349, <https://doi.org/10.1016/j.jrmhm.2008.07.002>
- [8] H.S. Maurya, L. Kollo, M. Tarraste, K. Juhani, F. Sergejev, K.G. Prashanth, Effect of the laser processing parameters on the selective laser melting of TiC-Fe-based cermets, *J. Manuf. Mater. Process.* 6 (2022), <https://doi.org/10.3390/jmmp6020035>
- [9] H.S.S. Maurya, L. Kollo, K. Juhani, F. Sergejev, K.G.G. Prashanth, Effect of pre-heating and cooling of the powder bed by laser pulse shaping on the microstructure of the TiC based cermets, *Ceram. Int* (2022), <https://doi.org/10.1016/j.ceramint.2022.04.029>
- [10] H.S. Maurya, K. Juhani, F. Sergejev, K.G. Prashanth, Additive manufacturing of TiC-based cermet with stainless steel as a binder material, *Material Today: Proceeding*, (2021).
- [11] J. Kūbarsepp, K. Juhani, Cermets with Fe-alloy binder: A review, *Int J. Refract. Met. Hard Mater.* 92 (2020) 105290, <https://doi.org/10.1016/j.jrmhm.2020.105290>
- [12] M. Kolnes, A. Mere, E. Kūbarsepp, M. Viljus, B. Maaten, M. Tarraste, Microstructure evolution of TiC cermets with ferritic AISI 430L steel binder, *Powder Metall.* 61 (2018) 197–209, <https://doi.org/10.1080/00325899.2018.1447268>
- [13] H.S. Maurya, L. Kollo, M. Tarraste, K. Juhani, F. Sergejev, K.G. Prashanth, Selective laser melting of TiC-Fe via laser pulse shaping: Microstructure and mechanical properties, *3D Print. Addit. Manuf.* (2021), <https://doi.org/10.1089/3dp.2021.0221>
- [14] A. Rajabi, M.J. Ghazali, A.R. Daud, Chemical composition, microstructure and sintering temperature modifications on mechanical properties of TiC-based cermet – A review, *Mater. Des.* 67 (2015) 95–106, <https://doi.org/10.1016/j.matdes.2014.10.081>
- [15] J. Jung, S. Kang, Effect of ultra-fine powders on the microstructure of Ti (CN)-xWC-Ni cermets, *Acta Mater.* 52 (2004) 1379–1386, <https://doi.org/10.1016/j.actamat.2003.11.021>
- [16] P. Alvaredo, D. Mari, E. Gordo, High temperature transformations in a steel-TiCN cermet, *Int J. Refract. Met. Hard Mater.* 41 (2013) 115–120, <https://doi.org/10.1016/j.jrmhm.2013.02.012>
- [17] M. Tarraste, J. Kūbarsepp, K. Juhani, A. Mere, M. Kolnes, M. Viljus, B. Maaten, Ferritic chromium steel as binder metal for WC cemented carbides, *Int J. Refract. Met. Hard Mater.* 73 (2018) 183–191, <https://doi.org/10.1016/j.jrmhm.2018.02.010>
- [18] A. Aramian, S.M.J. Razavi, Z. Sadeghian, F. Berto, A review of additive manufacturing of cermets, *Addit. Manuf.* 33 (2020) 101130, <https://doi.org/10.1016/j.addma.2020.101130>
- [19] D. Svetlizky, M. Das, B. Zheng, A.L. Vyatskikh, S. Bose, A. Bandyopadhyay, J.M. Schoenung, E.J. Lavernia, N. Eliaz, Directed energy deposition (DED) additive manufacturing: Physical characteristics, defects, challenges and applications, *Mater. Today* 49 (2021) 271–295, <https://doi.org/10.1016/j.mat.2021.03.020>
- [20] H.S. Maurya, L. Kollo, M. Tarraste, K. Juhani, F. Sergejev, K.G. Prashanth, Selective laser melting of TiC-based cermet: HIP studies, *Trans. Indian Inst. Met.* (2022), <https://doi.org/10.1007/s12666-022-02684-5>
- [21] A. Aramian, Z. Sadeghian, K.G. Prashanth, F. Berto, In situ fabrication of TiC-NiCr cermets by selective laser melting, *Int J. Refract. Met. Hard Mater.* 87 (2020) 105171, <https://doi.org/10.1016/j.jrmhm.2019.105171>
- [22] M. Xing, H. Wang, Z. Zhao, Y. Zhang, H. Lou, C. Liu, M. Wang, X. Song, SLM printing of cermet powders: Inhomogeneity from atomic scale to microstructure, *Ceram. Int* (2022), <https://doi.org/10.1016/j.ceramint.2022.06.254>
- [23] P.K. Gokuloss, S. Kolla, J. Eckert, Additive manufacturing processes: Selective laser melting, electron beam melting and binder jetting-selection guidelines, *Materials* 10 (2017) 672, <https://doi.org/10.3390/ma10060672>
- [24] Z. Zhang, P. Ma, Y. Fang, Z. Yang, N. Zhang, K.G. Prashanth, Y. Jia, Effect of NiCoFeAlTi high entropy intermetallic reinforcement particle size on the microstructure and mechanical properties of CoCrFeMnNi high-entropy alloy composites fabricated by selective laser melting, *J. Alloy. Compd.* 947 (2023) 169417, <https://doi.org/10.1016/j.jallcom.2023.169417>
- [25] K.G. Prashanth, S. Scudino, J. Eckert, Defining the tensile properties of Al-12Si parts produced by selective laser melting, *Acta Mater.* 126 (2017) 25–35, <https://doi.org/10.1016/j.actamat.2016.12.044>
- [26] J. Karimi, M. Antonov, L. Kollo, K.G. Prashanth, Role of laser remelting and heat treatment in mechanical and tribological properties of selective laser melted Ti6Al4V alloy, *J. Alloy. Compd.* 897 (2022) 163207, <https://doi.org/10.1016/j.jallcom.2021.163207>
- [27] J. Karimi, C. Suryanarayana, I. Okulov, K.G. Prashanth, Selective laser melting of Ti6Al4V: Effect of laser re-melting, *Mater. Sci. Eng. A* 805 (2020) 140558, <https://doi.org/10.1016/j.msea.2020.140558>
- [28] J. Karimi, M.S. Xie, Z. Wang, K.G. Prashanth, Influence of substrates on the selective laser melted Ti-6Al-4V alloy as a function of laser re-melting, *J. Manuf. Process* 68 (2021) 1387–1394, <https://doi.org/10.1016/j.jmpt.2021.06.059>
- [29] A. Aramian, Z. Sadeghian, S.M.J. Razavi, F. Berto, Room and high-temperature sliding wear behavior of in situ TiC-based cermet fabricated through selective laser melting, *J. Mater. Eng. Perform.* 30 (2021) 6777–6787, <https://doi.org/10.1007/s11665-021-05995-8>
- [30] A. Aramian, Z. Sadeghian, S.M.J. Razavi, K.G. Prashanth, F. Berto, Effect of selective laser melting process parameters on microstructural and mechanical properties of TiC-NiCr cermet, *Ceram. Int* 46 (2020) 28749–28757, <https://doi.org/10.1016/j.ceramint.2020.08.037>
- [31] Z. Lai, T. Guo, S. Zhang, L. Kollo, H. Attar, Z. Wang, K.G. Prashanth, Selective laser melting of commercially pure silicon, *J. Wuhan. Univ. Technol. Mater. Sci. Ed.* 37 (2022) 1155–1165, <https://doi.org/10.1007/S11595-022-2647-3>
- [32] P.A. Hooper, Melt pool temperature and cooling rates in laser powder bed fusion, *Addit. Manuf.* 22 (2018) 548–559, <https://doi.org/10.1016/j.addma.2018.05.032>
- [33] C. Yan, L. Hao, A. Hussein, P. Young, J. Huang, W. Zhu, Microstructure and mechanical properties of aluminium alloy cellular lattice structures manufactured by direct metal laser sintering, *Mater. Sci. Eng. A* 628 (2015) 238–246, <https://doi.org/10.1016/j.msea.2015.01.063>
- [34] H.Y. Jung, S.J. Choi, K.G. Prashanth, M. Stoica, S. Scudino, S. Yi, U. Kühn, D.H. Kim, K.B. Kim, J. Eckert, Fabrication of Fe-based bulk metallic glass by selective laser melting: A parameter study, *Mater. Des.* 86 (2015) 703–708, <https://doi.org/10.1016/j.matdes.2015.07.145>
- [35] F. Liu, X. Lin, G. Yang, M. Song, J. Chen, W. Huang, Microstructure and residual stress of laser rapid formed Inconel 718 nickel-base superalloy, *Opt. Laser Technol.* 43 (2011) 208–213, <https://doi.org/10.1016/j.optlastec.2010.06.015>
- [36] P. Bian, J. Shi, Y. Liu, Y. Xie, Influence of laser power and scanning strategy on residual stress distribution in additively manufactured 316L steel, *Opt. Laser Technol.* 132 (2020) 106477, <https://doi.org/10.1016/j.optlastec.2020.106477>
- [37] S. Waqar, K. Guo, J. Sun, Evolution of residual stress behavior in selective laser melting (SLM) of 316L stainless steel through preheating and in-situ re-scanning techniques, *Opt. Laser Technol.* 149 (2022) 107806, <https://doi.org/10.1016/j.optlastec.2021.107806>
- [38] H.S. Maurya, K. Kosiba, K. Juhani, F. Sergejev, K.G. Prashanth, Effect of powder bed preheating on the crack formation and microstructure in ceramic matrix composites fabricated by laser powder-bed fusion process, *Addit. Manuf.* (2022) 103013, <https://doi.org/10.1016/j.addma.2022.103013>
- [39] K.G. Prashanth, S. Scudino, H.J. Klaus, K.B. Surreddi, L. Löber, Z. Wang, A.K. Chaubey, U. Kühn, J. Eckert, Microstructure and mechanical properties of Al-12Si produced by selective laser melting: Effect of heat treatment, *Mater. Sci. Eng. A* 590 (2014) 153–160, <https://doi.org/10.1016/j.msea.2013.10.023>
- [40] S. Scudino, C. Unterdörfer, K.G. Prashanth, H. Attar, N. Ellenet, V. Uhlenwinkel, J. Eckert, Additive manufacturing of Cu-10Sn bronze, *Mater. Lett.* 156 (2015) 202–204, <https://doi.org/10.1016/j.matlet.2015.05.076>
- [41] D. Kumar, G. Shankar, K.G. Prashanth, S. Suwas, Texture dependent strain hardening in additively manufactured stainless steel 316L, *Mater. Sci. Eng. A* 820 (2021) 141483, <https://doi.org/10.1016/j.msea.2021.141483>
- [42] D. Kumar, S. Jhavar, A. Arya, K.G. Prashanth, S. Suwas, Mechanisms controlling fracture toughness of additively manufactured stainless steel 316L, *Int J. Fract.* 235 (2021) 61–78, <https://doi.org/10.1007/S10704-021-00574-3/FIGURES/10>
- [43] O.O. Salman, F. Brenne, T. Niendorf, J. Eckert, K.G. Prashanth, T. He, S. Scudino, Impact of the scanning strategy on the mechanical behavior of 316L steel synthesized by selective laser melting, *J. Manuf. Process* 45 (2019) 255–261, <https://doi.org/10.1016/j.jmpt.2019.07.010>
- [44] J. Suryawanshi, K.G. Prashanth, S. Scudino, J. Eckert, O. Prakash, U. Ramamurty, Simultaneous enhancements of strength and toughness in an Al-12Si alloy synthesized using selective laser melting, *Acta Mater.* 115 (2016) 285–294, <https://doi.org/10.1016/j.actamat.2016.06.009>
- [45] P. Ma, P. Ji, Y. Jia, X. Shi, Z. Yu, K.G. Prashanth, Effect of substrate plate heating on the microstructure and properties of selective laser melted Al-20Si-5Fe-3Cu-1Mg alloy, *Materials* 14 (2021) 330, <https://doi.org/10.3390/ma14020330>
- [46] H. Attar, K.G. Prashanth, A.K. Chaubey, M. Calin, L.C. Zhang, S. Scudino, J. Eckert, Comparison of wear properties of commercially pure titanium prepared by selective laser melting and casting processes, *Mater. Lett.* 142 (2015) 38–41, <https://doi.org/10.1016/j.matlet.2014.11.156>
- [47] M.G. Gee, Low load multiple scratch tests of ceramics and hard metals, *Wear* 250 (2001) 264–281, [https://doi.org/10.1016/S0043-1648\(01\)00591-9](https://doi.org/10.1016/S0043-1648(01)00591-9)
- [48] A.J. Gant, M.G. Gee, Abrasion of tungsten carbide hardmetals using hard counterfaces, *Int J. Refract. Met. Hard Mater.* 24 (2006) 189–198, <https://doi.org/10.1016/j.jrmhm.2005.05.007>
- [49] S. Ndlovu, K. Durst, M. Göken, Investigation of the sliding contact properties of WC-Co hard metals using nanoscratch testing, *Wear* 263 (2007) 1602–1609, <https://doi.org/10.1016/j.wear.2006.11.044>
- [50] M.G. Gee, L. Nimishakavi, Model single point abrasion experiments on WC/Co hardmetals, *Int. J. Refract. Met. Hard Mater.* 29 (2011) 1–9, <https://doi.org/10.1016/j.jrmhm.2010.04.009>
- [51] J.C.P. Zuñega, M.G. Gee, R.J.K. Wood, J. Walker, Scratch testing of WC/Co hardmetals, *Tribol. Int* 54 (2012) 77–86, <https://doi.org/10.1016/j.triboint.2012.02.027>
- [52] R.S. Khmyrov, A.P. Shevchukov, A.V. Gusarov, T.V. Tarasova, Phase composition and microstructure of WC-Co alloys obtained by selective laser melting, *Mech. Ind.* 18 (2017), <https://doi.org/10.1051/mecc/2017059>
- [53] C. Zhao, Z. Wang, D. Li, L. Kollo, Z. Luo, W. Zhang, K.G. Prashanth, Cu-Ni-Sn alloy fabricated by melt spinning and selective laser melting: a comparative study on the microstructure and formation kinetics, *J. Mater. Res. Technol.* 9 (2020) 13097–13105, <https://doi.org/10.1016/j.jmrt.2020.09.047>
- [54] P. Wang, L. Deng, K.G. Prashanth, S. Pauly, J. Eckert, S. Scudino, Microstructure and mechanical properties of Al-Cu alloys fabricated by selective laser melting of

- powder mixtures, *J. Alloy. Compd.* 735 (2018) 2263–2266, <https://doi.org/10.1016/j.jallcom.2017.10.168>
- [55] P.A. Hooper, Melt pool temperature and cooling rates in laser powder bed fusion, *Addit. Manuf.* 22 (2018) 548–559, <https://doi.org/10.1016/j.addma.2018.05.032>
- [56] S. Pauly, P. Wang, U. Kühn, K. Kosiba, Experimental determination of cooling rates in selectively laser-melted eutectic Al-33Cu, *Addit. Manuf.* 22 (2018) 753–757, <https://doi.org/10.1016/j.addma.2018.05.034>
- [57] L. Thijs, K. Kempen, J.P. Kruth, J. Van Humbeeck, Fine-structured aluminium products with controllable texture by selective laser melting of pre-alloyed AlSi10Mg powder, *Acta Mater.* 61 (2013) 1809–1819, <https://doi.org/10.1016/j.actamat.2012.11.052>
- [58] J. Jayaraj, M. Olsson, Effect of tribo-layer on the corrosion behavior of WC-Co and WC-Ni cemented carbides in synthetic mine water, *Int. J. Refract. Met. Hard Mater.* 100 (2021) 105621, <https://doi.org/10.1016/j.ijrmhm.2021.105621>
- [59] G.M. Hamilton, L.E. Goodman, The stress field created by a circular sliding contact, *J. Appl. Mech.* 33 (1966) 371–376, <https://doi.org/10.1115/1.3625051>
- [60] M. Gaier, H.-T. Lin, Z.N. Farhat, K.P. Plucknett, Precipitation hardenable TiC-Steel cermets, *Wear* 477 (2021) 203804, <https://doi.org/10.1016/j.wear.2021.203804>



# Curriculum vitae

## Personal data

Name: Himanshu Singh Maurya  
Date of birth: 17.01.1994  
Place of birth: Allahabad, India  
Citizenship: Indian

## Contact data

E-mail: himanshu.maurya@taltech.ee; himanshudes@gmail.com

## Education

2019–2023 Tallinn University of Technology, Estonia – PhD  
2016–2019 Politecnico Di Milano, Italy – MSc  
2011–2015 Annamalai University, India – BSC

## Language competence

Hindi Native  
English Fluent  
Italian Basic

## Professional employment

2015–2016 Research trainee, Indian Institute of Technology, Roorkee, India  
2019–2020 Manufacturing Engineer, Athanacy Engineering Private Limited, India

## Research visit

Sep. 2022 Department of Materials Engineering, Dalarna University, Falun, Sweden  
Feb.–July 2023 Department of Materials Engineering, Krakow Institute of Technology, Poland

## Conferences and Seminars

2023 3rd Korea-Tribology International Symposium 2023, Busan, Korea,  
2022 12th International Advances in Applied Physics & Materials Science Congress & Exhibition (APMAS2022) Fethiye-Mugla, Turkey  
2022 20th PLANSEE seminar, Reutte, Austria  
2022 Blended Intensive Programme “Materials Technology and Processes” Esslingen-University of Applied Sciences, Germany.  
2022 EPMA’s 20th Powder Metallurgy Summer School, University of Castilla la Mancha, Ciudad Real, Spain,  
2022 3rd International Conference on Aspects of Materials Science and Engineering (ICAMSE2022), Punjab, India

2022  
2021

TMS 2022 Annual Meeting & Exhibition California, USA.  
14th International Conference on Advanced Computational  
Engineering and Experimenting(ACEX2021), Malta

**Honors and Awards**

2023

**Excellence Poster Award**

3rd Korea-Tribology International Symposium (K-TRIB2023),  
Busan, South Korea.

2022

**Best Research Paper Award**

3rd International Conference on Aspects of Materials Science  
and Engineering, India

## Elulookirjeldus

### Isikuandmed

Nimi: Himanshu Singh Maurya  
Sünniaeg: 17.01.1994  
Sünnikoht: Allahabad, India  
Kodakondsus: India

### Kontaktandmed

E-post: himanshu.maurya@taltech.ee; himanshudes@gmail.com

### Hariduskäik

2019–2023 Tallinna Tehnikaülikool – PhD  
2016–2019 Politecnico Di Milano, Italy – MSc  
2011–2015 Annamalai University, India – BSc

### Keelteoskus

Hindi emakeel  
Inglise keel kõrgtase  
Itaalia algtase

### Teenistuskäik

2015–2016 praktikant, Indian Institute of Technology, Roorkee, India  
2019–2020 tootmisinsener, Athanacy Engineering Private Limited, India

### Teadustöö välismaal

09.2022 Department of Materials Engineering, Dalarna University, Falun, Sweden  
02.–07.2023 Department of Materials Engineering, Krakow Institute of Technology, Poland

### Osalemine konverentsidel

2023 3rd Korea-Tribology International Symposium 2023, Busan, Korea  
2022 12th International Advances in Applied Physics & Materials Science Congress & Exhibition (APMAS2022) Fethiye-Mugla, Turkey  
2022 20th PLANSEE seminar, Reutte, Austria  
2022 Blended Intensive Programme “Materials Technology and Processes” Esslingen-University of Applied Sciences, Germany  
2022 EPMA’s 20th Powder Metallurgy Summer School, University of Castilla la Mancha, Ciudad Real, Spain  
2022 3rd International Conference on Aspects of Materials Science and Engineering (ICAMSE2022), Punjab, India  
2022 TMS 2022 Annual Meeting & Exhibition California, USA  
2021 14th International Conference on Advanced Computational Engineering and Experimenting (ACEX2021), Malta

**Autasud ja auhinnad**

2023

**Silmapaistva postri auhind**

3rd Korea-Tribology International Symposium (K-TRIB2023),  
Busan, South Korea

2022

**Parima artikli auhind**

3rd International Conference on Aspects of Materials  
Science and Engineering, India

ISSN 2585-6901 (PDF)  
ISBN 978-9916-80-066-9 (PDF)